Abstract volume

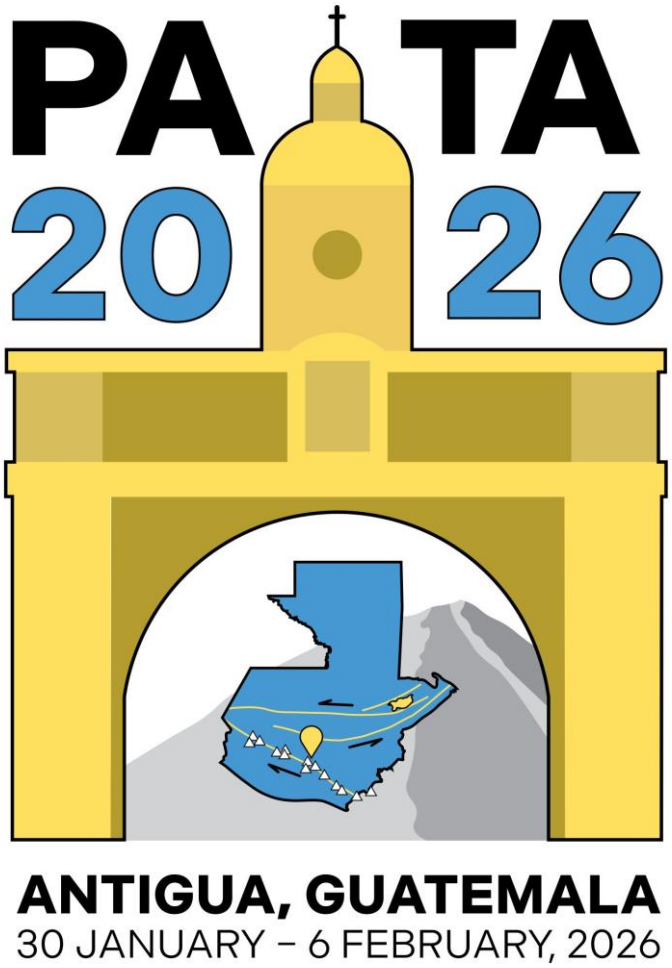

Edited by:
Carla Gordillo
Omar Flores
Christoph Grützner
Tina M. Niemi
Jonathan Obrist-Farner

INQUA TERPRO Project Cascading Hazards and Mitigation (CHAMP)

paleoseismicity.org

Dear participants,

On 4 February 1976, a magnitude 7.5 earthquake ruptured the Motagua Fault, which is part of the North American-Caribbean plate boundary in Guatemala. More than 23,000 people lost their lives and the devastation was huge. On the day 50 years later, we want to commemorate this disaster, and we want to talk about the lessons learned since then.

The International INQUA Meeting on Paleoseismology, Active Tectonics and Archaeoseismology (PATA Days) brings together earthquake scientists from all continents to share latest research in earthquake geology and to discuss the developments in our discipline. A central part of the PATA Days are the joint field trips to active faults and to the sites where the actual research takes place. This idea has always been at the core of the PATA Days since their initiation in 2009.

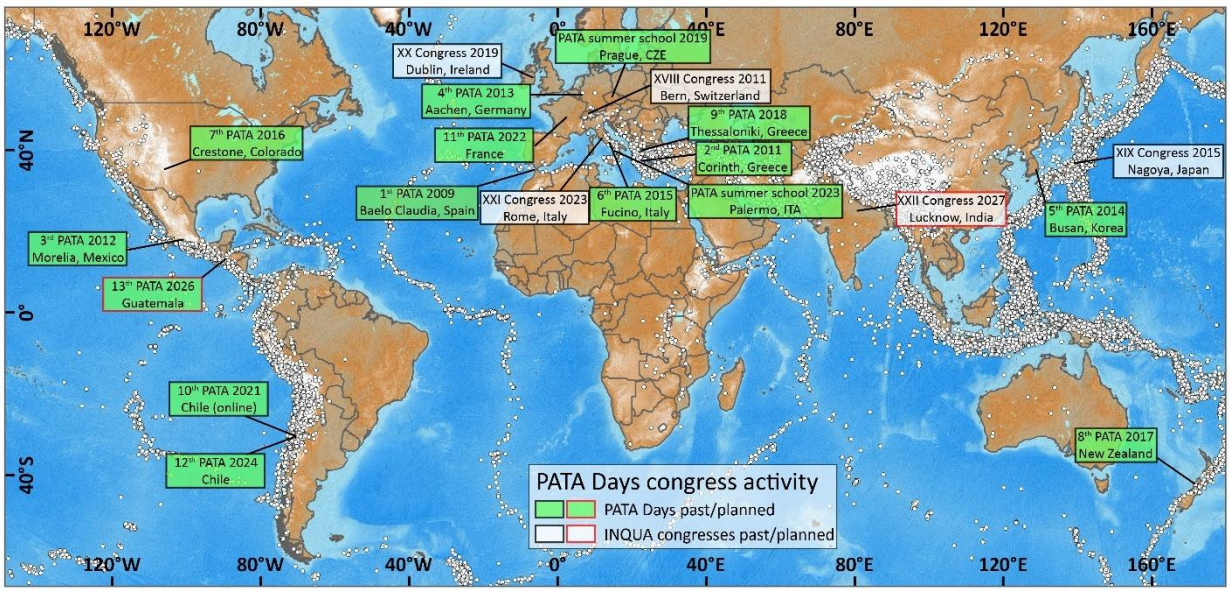

The PATA Days World Map.

The PATA Days are held under the umbrella of INQUA, the International Union for Quaternary Research and its TERPRO Commission (Terrestrial Processes, www.inqua.org). We are grateful for INQUA's continuous support for Early Career Researchers and Researchers from Developing Countries. But most importantly, we are grateful to our entire team for helping to organize this event.

We wish all participants a successful conference, interesting field trips, unforgettable moments, and fruitful discussions.

Your organizing committee:

Carla Gordillo
Omar Flores
Tina M. Niemi
Christoph Grützner
Jonathan Obrist-Farner
Hairo Castellanos
Bridget Garnier

INQUA TERPRO Project Cascading Hazards and Mitigation (CHAMP)

Table of contents

INQUA TERPRO Project Cascading Hazards and Mitigation (CHAMP)

INQUA TERPRO Project Cascading Hazards and Mitigation (CHAMP)

Active tectonics and paleoseismology of Northern Algeria: an overview

Seifeddine Adjiri, Aicha Heddar, Yahia Mohammedi, Abderezzak Tizeraoui Hamoud Beldjoudi

(1) Center of Research in Astronomy, Astrophysics and Geophysics (CRAAG), Bouzareah, Algeria.
Email address of corresponding author: seifeddine.adjiri@gmail.com.

Abstract: *Algeria lies within the western Mediterranean domain, where NW–SE convergence between the African and Eurasian plates generates a complex system of active compressive and transpressive structures. This tectonic framework is expressed by moderate to strong seismicity, including damaging earthquakes such as El Asnam 1980 (Ms 7.2) and Boumerdes 2003 (Mw 6.9). Seismic activity is mainly accommodated within three domains: the Algerian margin, where several active offshore structures have been identified, the Tellian Atlas, which is folded and faulted by active structures shaping seismogenic basins extending east–west along the coastline, and the Saharan Atlas to the south, which also records significant activity. Despite the high seismicity in the area, the lack of paleoseismological studies remains a significant gap. This presentation aims to provide an overview of active tectonics in Algeria, summarising the main structural features, the seismic activity, and recent advances in identifying seismogenic sources, while emphasising the need to refine seismic hazard assessments.*

Key words*: Northern Algeria, Seismicity, Active tectonics, Paleoseismology, Faults*

INTRODUCTION AND SEISMOTECTONIC SETTING

Northern Algeria is situated along the Africa–Eurasia tectonic plate boundary at the southern margin of the Western Mediterranean Sea, constituting a key segment of the Maghrebides orogen in Northwest Africa (Durand-Delga, 1969; Fig. 1a). The ongoing oblique convergence between these two plates, estimated at approximately 5 mm/yr (e.g., Bougrine et al., 2019), makes this area a locus of significant active deformation and frequent seismic activity. This deformation is distributed within a diffuse, 50–100 km wide E–W corridor encompassing the Tell Atlas fold-and-thrust belt and extending northward into the offshore domain (Meghraoui and Pondrelli, 2012; Fig. 1b). The convergence is primarily accommodated by right-lateral transpression, inducing coeval shortening and strike-slip structures.

In Central and Western Algeria, the tectonic regime is dominated by active thrust fault systems and associated folding. The Late Pleistocene shortening rate across the Tell Atlas is estimated at 2.2 mm/yr, based on cumulative shortening in the Chelif Basin (Meghraoui and Pondrelli, 2012). The seismogenic potential of these thrusts has been demonstrated by large-to-moderate earthquakes, such as the 1980 El Asnam (Mw 7.3; Ouyed et al., 1981) and the 2003 Zemmouri-Boumerdès (Mw 6.8; e.g., Delouis, 2004) events. In Eastern Algeria, deformation exhibits strain partitioning, with strike-slip mechanisms inland—such as along the North Constantine Fault, where slip rates reach 2.3 mm/yr (Bougrine et al., 2019)—and thrusting offshore (e.g., the 2021 Mw 6.0 Béjaïa earthquake).

Despite this clear seismogenic potential, characterizing active faults in Northern Algeria poses significant challenges, primarily due to the prevalence of blind thrust faults and the long recurrence intervals of characteristic events. To address these uncertainties, multiple approaches have been initiated over the past few decades. These include the expansion of the Algerian Digital Seismic Network (ADSN) to improve earthquake relocation and source characterization (Yelles-Chaouche et al., 2013), the installation of the permanent Algerian GNSS network (REGAT; Yelles-Chaouche et al., 2019), and the launch of major offshore reconnaissance projects to map active structures along the Algerian margin (e.g., Déverchère, 2003).

Parallel to these national-scale initiatives, regional studies utilizing tectonic geomorphology (Boudiaf, 1996), coastal deformation (Maouche, 2010), and active tectonics analysis (Meghraoui and Pondrelli, 2012, and references therein) have significantly enhanced our understanding of active faulting in Northern Algeria. Furthermore, high-resolution characterization of specific fault systems has been accomplished using paleoseismology. Despite the scarcity of recent surface ruptures, successful paleoseismic investigations have deciphered past earthquake records and provided critical data for key structures. These methods have been applied onshore using classical trenching—notably on the El Asnam Fault, the Sahel Fault (near Algiers), and the Tessalla Fault in the Oranie region—and offshore through the analysis of turbidite deposits.

The aim of this short paper is to provide an overview of active tectonics and paleoseismic studies in Algeria. We summarize the main structural features and seismic activity and review recent advances in identifying seismogenic sources through onshore and offshore paleoseismology, emphasizing the need to refine seismic hazard assessments in this complex transpressional domain.

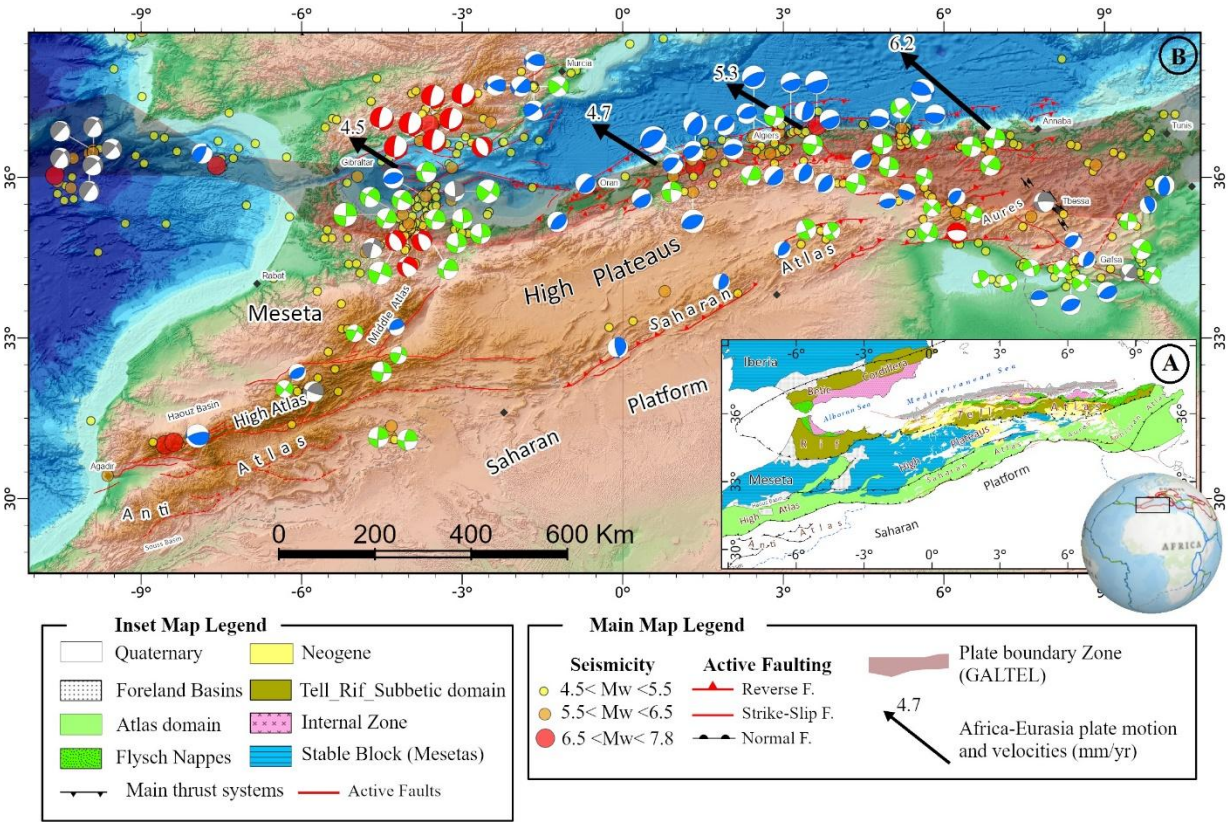

Figure 1: *Tectonic and seismotectonic setting of the Ibero-Maghreb region. (a) Regional tectonic map of the Alpine orogeny in North Africa showing the main tectonic domains (after Durand-Delga, 1969) and the intra-montane Neogene-Quaternary basins. (b) Seismotectonic map of Northwest Africa displaying active and potentially active fault systems within the Eurasia-Africa plate convergence zone. Seismicity (Mw > 4.5) is sourced from the USGS catalog (1908–2025) and focal mechanisms from CSEM (1980–2023). Active faults are derived from the CRAAG database for Algeria and the QAFI database for the Alboran domain. The map also shows the GALTEL diffuse plate boundary (brown strip; Meghraoui and Pondrelli, 2012) and Africa-Eurasia convergence vectors (Bougrine et al., 2019).*

MAIN ACTIVE TECTONICS DOMAINS

Active tectonics in Northern Algeria encompass a broad region divided into distinct tectonic domains: the Algerian margin, the Tell Atlas, and the Saharan Atlas. These domains accommodate the Africa-Eurasia convergence through varying deformation styles and rates. In general, strain rates are highest in the north and decrease southward. The tectonic regime is primarily dominated by thrust faulting and associated folding in the Western and Central parts, whereas a significant strike-slip component characterizes the eastern sector. This section provides an overview of these tectonic domains, highlighting the principal active faults and characteristic seismicity patterns within each.

The offshore domain

The offshore domain corresponds to the Algerian margin, interpreted as a passive margin originally formed in the back-arc setting of the Tethyan subduction zone and subsequently inverted by ongoing Eurasia–Africa convergence (e.g., Déverchère et al., 2005; Yelles-Chaouche et al., 2009; Medaouri et al., 2014). High-resolution bathymetric mapping, combined with seismic reflection and refraction surveys and tectonostratigraphic analysis indicates a multiphase tectonic evolution during the Neogene–Quaternary. The margin exhibits a complex structural style, including reactivated extensional structures and salt-related deformation. However, the dominant active structures are ENE–WSW to E–W-trending thrust faults and associated fault-propagation folds (Déverchère et al., 2005; Domzig, 2006). These thrusts generally dip southward and show clear evidence of Late Quaternary reactivation. The 2003 Zemmouri–Boumerdès earthquake (Mw 6.8) remains the most striking instrumental example of the seismic potential of this offshore thrust system (Fig. 2a). The rupture occurred entirely offshore along the foot of the Algiers–Boumerdès margin (Déverchère et al., 2005; Strzerzynski et al., 2021), on a fault striking N070° and dipping approximately 40° to the south (Delouis, 2004). This event was highlighted by significant coseismic coastal uplift reaching 0.5 m (Meghraoui et al., 2004; Yelles et al., 2004) and induced a minor tsunami recorded along the northern Mediterranean coast. Several historical earthquakes are now also considered to have been generated offshore, as evidenced by their association with Mediterranean tsunamis. Notable examples include the 1790 Oran (Io IX) and the 1856 Djidjeli (Io X) earthquakes. The recent 2021 Béjaïa earthquake (Mw 6.0), located in the eastern offshore sector, further confirms the ongoing activity of these systems.

The Tell Atlas domain

The Tell Atlas fold-and-thrust belt constitutes the primary accommodation zone for a significant fraction of the Africa–Eurasia convergence. While active deformation is diffuse across the belt, seismotectonic records indicate a concentration of activity within the post-nappe, intra-montane Neogene-Quaternary basins, oriented E–W to ENE–WSW, such as the Chelif, Mitidja, and Constantine basins (Fig. 1a). In the western and central Tell Atlas, the structural style is dominated by NE–SW trending, right-stepped en échelon thrust systems and associated fault-related folds that deform Quaternary deposits within and along the basin margins (Meghraoui, 1988). The Chelif Basin in Western Algeria stands out as one of the most active basins in the Western Mediterranean, having hosted several major historical and instrumental earthquakes. Most notably, the 1980 El Asnam earthquake (Mw 7.3) remains the largest recorded event in the Western Mediterranean, producing a 36 km surface rupture with a maximum vertical slip of 6 m (Meghraoui, 1988). This event was associated with a NE–SW trending, north-dipping fault-related fold that induced extensive surface deformation, including metric-scale extrados normal faulting along the active El Asnam fold axis (Fig. 2b). Further east, the Mitidja Basin near Algiers is considered the most active basin in Central Algeria. Its boundaries are defined by active thrust faults that have hosted frequent seismic activity, including major historical events such as the Algiers earthquakes of 1365 (Io = X) and 1716 (Io = IX), and the 1825 Blida earthquake (Io = X–XI) (e.g., Harbi et al., 2015). This basin appears to exhibit structural continuity with the offshore domain. For instance, the 2003 Zemmouri–Boumerdès earthquake (Mw 6.8) was generated by a NE–SW trending, south-dipping offshore thrust fault, which is interpreted as the offshore extension of the Mitidja Basin's southern boundary fault system.

In the Eastern Tell Atlas, the deformation style transitions to a dominance of E–W dextral (right-lateral) and NE–SW sinistral (left-lateral) strike-slip faulting onshore, generating frequent damaging moderate-magnitude seismicity (Abacha, 2015). The North Constantine Fault represents the most prominent strike-slip system in northeast Algeria; it extends approximately 100 km and accommodates a slip rate of ~2.4 mm/yr, as inferred from geodetic measurements (Bougrine et al., 2019). This fault system is associated with the Guelma pull-apart basin, which induces local normal faulting events. The main segment of the fault, however, generates pure right-lateral strike-slip mechanisms, as observed during the 2017–2020 seismic sequences (Bendjama et al., 2021). The conjugate NE–SW system comprises an array of sinistral strike-slip faults associated with multiple historical and instrumental events, including the 1985 Constantine (Ms 6.0) and the 2006 Laalam (Mw 5.0) earthquakes (Abacha, 2015, and references therein). This onshore strike-slip regime contrasts with the compressional style observed along the Northeast Algerian margin, where active ENE–WSW trending thrust faults have been identified and mapped, generating multiple offshore earthquakes.

Saharan Atlas domain

The Saharan Atlas, located farther inland to the south of the Tell Atlas, represents an intracontinental mountain belt positioned between two stable domains: the High Plateaus to the north and the Saharan Platform to the south (Fig. 1a). The northern limit of this domain is bounded by the North Atlas Fault, while its southern boundary is defined by the South Atlas Fault (SAF). The SAF is a major fault system composed of en échelon north-dipping thrusts and related folds, segmented by NW–SE trending strike-slip faults. Although the Saharan Atlas is generally less active than the northern domains and exhibits more diffuse seismicity, it occasionally records moderate to strong earthquakes (e.g., Harbi et al., 2015). This is particularly true along its central and eastern segments, where significant events such as the 1869 (Io = IX) and the 2016 Biskra (Mw 5.2; Wimpenny et al., 2023) earthquakes have occurred. These events were recorded along the eastern segment of the SAF, a zone characterized by strong Pleistocene deformation involving both thrust and strike-slip faulting (Outtani et al., 1995). Furthermore, the occurrence of the 2023 Al Haouz earthquake (Mw 6.8) in the analogous High Atlas system highlights the significant seismogenic potential of this intracontinental belt, emphasizing the critical need to integrate it into seismic hazard assessments for Northern Algeria.

PALEOSEISMOLOGY

Paleoseismological studies in Algeria were pioneered following the devastating El Asnam earthquake of October 10, 1980 (Mw 7.3), focusing primarily on the seismically active Central Tell region. These investigations have successfully established a chronology of Holocene seismic ruptures along major active fault systems in the Chelif and Mitidja basins, both onshore and offshore (Fig. 3a).

The 1980 El Asnam event provided the first extensively documented example of active compressive tectonics in North Africa, characterized by complex coseismic deformation involving folding, thrusting, and secondary extrados normal faulting (King and Vita-Finzi, 1981). While preliminary trenching was initiated (Fig. 3a, 1) during post-seismic microzonation studies (WCC, 1983), the foundational paleoseismological reference for the region was established by Meghraoui (1988). This detailed study involved the excavation and analysis of multiple trenches across the active fault trace (e.g. Fig. 3b). Through the analysis of deformed sedimentary units—specifically buried paleosols and colluvial wedges—and radiocarbon dating, Meghraoui (1988) identified nine paleo-earthquakes over a period of approximately 7,300 years. The results revealed an irregular seismic cycle characterized by clusters of activity separated by periods of quiescence. While the long-term average recurrence interval was estimated at 1,061 years, the clustering behavior suggests significantly shorter intervals during active episodes. Furthermore, the analysis of cumulative deformation yielded a slip rate of 0.4 to 0.6 mm/yr on the El Asnam fault itself. When integrated with regional data, this implies a total shortening rate of ~2.2 mm/yr across the Western Tell Atlas (Meghraoui and Doumaz, 1996).

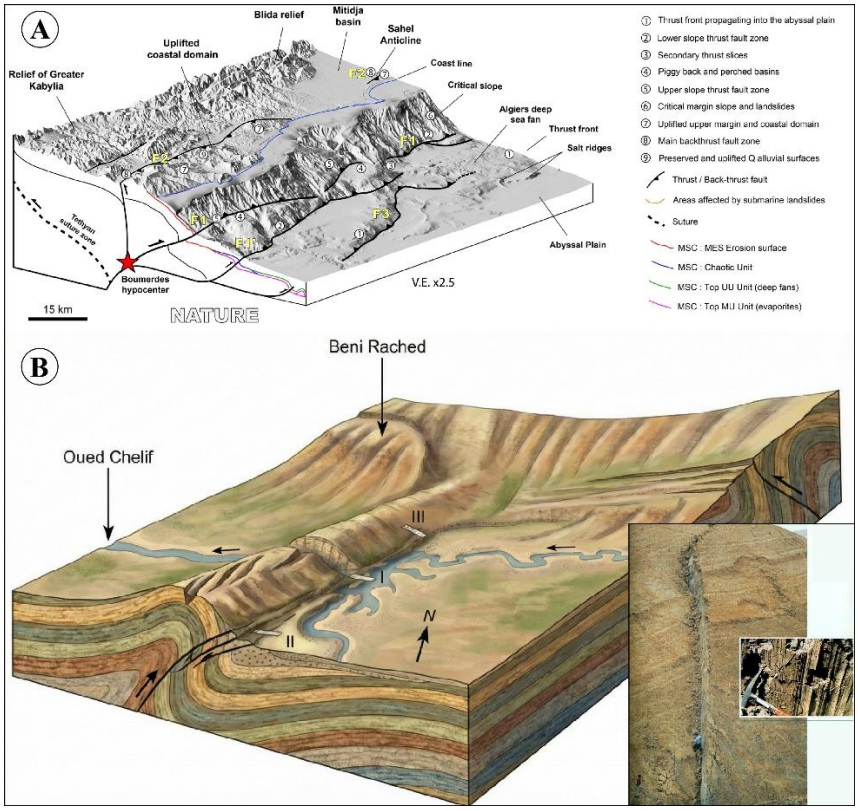

Figure 2: *The major actives structures of northern Algeria. A: The central Algerian margin high resolution DEM showing the structural and sedimentary pattern and the surface processes (Strzerzynski et al., 2021). B: Bloc diagram showing the geomorphologic environment near central segment of the E1 Asnam and the main fault trace at the northeastern end of the rupture zone, with slickensides (Meghraoui, 1988).*

These findings have served as a critical baseline for subsequent syntheses of active tectonics in Northern Algeria and the stress distribution along the Africa–Eurasia plate boundary (Meghraoui and Pondrelli, 2012).

In the northern part of the Mitidja Basin (Fig. 3a, 2), paleoseismological investigations have targeted the Sahel anticline near Algiers. This structure is controlled by a blind reverse fault (Meghraoui, 1988; Maouche et al., 2011) and is covered by thick alluvial deposits, posing significant challenges for direct observation. To overcome this, Heddar et al. (2013) adopted a strategy focused on detecting secondary deformation features. Trenches were excavated across the hanging wall of the Sahel blind thrust to expose extrados faults generated by flexural-slip folding. One trench, located within a small graben-like structure (Fig. 3c), enabled detailed stratigraphic analysis and radiocarbon dating (14C AMS). This approach allowed for the identification of eight rupture events corresponding to both historical and prehistoric earthquakes. Consequently, this study demonstrated that the paleoseismic history derived from secondary extrados faults serves as a reliable proxy for activity on the underlying master thrust, thereby significantly completing the seismic catalog for the Algiers region.

Submarine paleoseismology is a relatively recent field of study in Algeria, despite long-standing evidence that major historical earthquakes—such as Orléansville 1954 (Ms 6.7), El Asnam 1980 (Mw 7.3), and Boumerdès 2003 (Mw 6.8)—can trigger significant underwater turbidity currents (e g., Heezen and Ewing 1955; El-Robrini et al. 1985). Since the 2000s, several geophysical campaigns (e.g., the MARADJA 2003 and 2005 cruises) have facilitated extensive offshore surveys along the Algerian margin (e.g., Déverchère, 2003). The first dedicated offshore paleoseismological study (Fig. 3a, #3) was conducted by Ratzov et al. (2015), based on the analysis of three sediment cores (Fig. 3d) collected off the coast of the area affected by the 1954 and 1980 earthquakes. These cores were retrieved near the location of the 1954 submarine cable break, directly along the path of the turbidity currents triggered by that event. Using multi-proxy analysis—including X-ray imagery, magnetic susceptibility, and grain-size analysis—the study identified between 10 and 25 Holocene turbidites per core. Correlation between these cores revealed a record of 14 major seismic events over the last ~8,000 years, many of which correlate well with events identified onshore along the El Asnam fault. Significantly, the results highlight a pattern of temporal clustering: seismic events appear to occur in groups of 3 to 6 ruptures with relatively short recurrence intervals (approximately 300 to 600 years), separated by longer periods of quiescence lasting ~1.6 kyr. This study demonstrates that offshore paleoseismology not only extends but also refines the knowledge provided by terrestrial trenching, particularly regarding the frequency and clustering of major earthquakes along the central Algerian margin.

In summary, while paleoseismological research has yielded critical data, it remains geographically concentrated in two main terrestrial areas (the Chelif and Mitidja basins) and the central segment of the offshore margin (turbidite

records). However, other regions—including the West (Oran), the East (Eastern Tell), and the Saharan Atlas—exhibit promising potential for active tectonic studies. A comparable, comprehensive paleoseismological program is required in these areas to refine the national seismic hazard assessment.

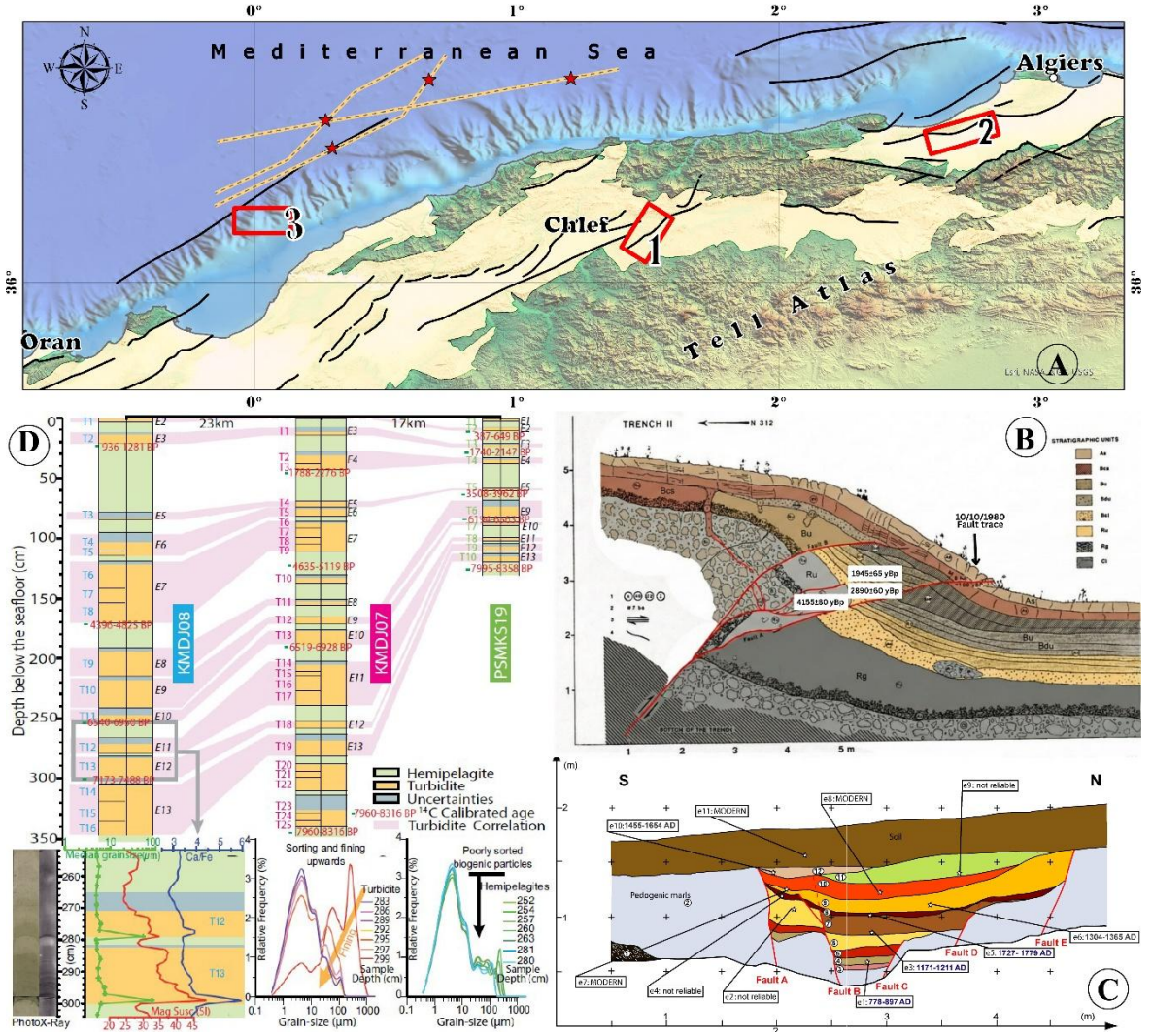

Figure 3: *A: Location map of the different paleoseismology studies realised in northern Algeria, 1:El Asnam fault, 2: Northern part of the Mitidja basin, 3: Chlef offshore area; orange lines are submarine cables, stars are breaks after the 1954 earthquake. B: One of the trenches realised in El Asnam fault related fold structure (Meghraoui, 1988). C: The Sahel trench (Heddar et al., 2013). D: Offshore results (Ratzof et al., 2015).*

CONCLUSION

Northern Algeria represents a key segment of the boundary between the African and Eurasian plates, where active tectonics reflects the long-term and ongoing convergence, expressed through a complex compressional and transpressional structures. This active deformation is essentially accommodated by reverse, thrusts faulting commonly related to folding structures, and strike-slip faulting, which crosscut the Algerian margin, the Tell Atlas and adjacent Neogene basins, and the intracontinental Saharan Atlas. This tectonic framework results in a segmented belt of active structures that control both seismicity distribution and surface deformation. Despite the high seismic risk that characterises this region, the long-term behaviour of many active structures remains poorly constrained due to the limited spatial coverage of palaeoseismic studies. This gap highlights a strong potential for future research based on integrated approaches combining terrestrial and offshore palaeoseismology, high-resolution offshore and onland geophysics, geomorphology, geodesy (GNSS) and advanced chronological methods. Enlarging these multidisciplinary studies within the framework of collaborative exchanges will not only improve seismic risk assessment in Algeria, but also provide crucial information on the geodynamics of diffuse boundaries between tectonic plates and transpressive systems across the western Mediterranean.

REFERENCES

Abacha I (2015) Étude de la sismicité de la région nord-est de l'Algérie, Thèse de Doctorat, l'Université Ferhat ABBAS - Sétif 1. http://dspace.univ-setif.dz:8888/jspui/handle/123456789/1802. Thèse de Doctorat, l'Université Ferhat ABBAS - Sétif 1. http://dspace.univ.setif.dz:8888/jspui/handle/123456789/1802

Bendjama H, Yelles-Chaouche A, Boulahia O, et al (2021) The March 2017 earthquake sequence along the E-W-trending Mcid Aïcha-Debbagh Fault, northeast Algeria. Geosciences Journal 25:697–713. https://doi.org/10.1007/s12303-020-0059-y

Boudiaf A (1996) Étude sismotectonique de La région d'Alger et de la Kabylie (Algérie) : Utilisation des modèles numériques de Terrain (MNT) et de La télédétection pour La reconnaissance d structures tectoniques actives : Contribution a l'évaluation de L'aléa sismique. Doctorat, Thèse de Doctorat, Languedoc University, France

Bougrine A, Yelles-Chaouche AK, Calais E (2019) Active deformation in Algeria from continuous GPS measurements. Geophys J Int 217:572–588. https://doi.org/10.1093/gji/ggz035

Delouis B (2004) Slip distribution of the 2003 Boumerdes-Zemmouri earthquake, Algeria, from teleseismic, GPS, and coastal uplift data. Geophys Res Lett 31:L18607. https://doi.org/10.1029/2004GL020687

Déverchère J (2003) MARADJA cruise, RV Le Suroît

Déverchère J, Yelles K, Domzig A, et al (2005) Active thrust faulting offshore Boumerdes, Algeria, and its relations to the 2003 Mw 6.9 earthquake. Geophys Res Lett 32:n/a-n/a. https://doi.org/10.1029/2004GL021646

Domzig Anne (2006) D'éformation active et récente, et structuration tectonosédimentaire de la marge sous-marine algérienne. Thèse Doctorat Université de Bretagne Occidentale

Durand-Delga M (1969) Mise au point sur la structure du Nord-Est de la Berbérie. Publ Serv Géol Algérie N° 39:89–131

El-Robrini M, Gennesseaux M, Mauffret A (1985) Consequences of the El-Asnam earthquakes: Turbidity currents and slumps on the Algerian margin (Western Mediterranean). Geo-Marine Letters 5:171–176. https://doi.org/10.1007/BF02281635/METRICS

Harbi A, Sebaï A, Benmedjber M, et al (2015) The algerian homogenized macroseismic database (267-1989): A Deeper insight into the algerian historical seismicity. Seismological Research Letters 86:1705–1716

Heddar A, Authemayou C, Djellit H, et al (2013) Preliminary results of a paleoseismological analysis along the Sahel fault (Algeria): New evidence for historical seismic events. Quaternary International 302:210–223. https://doi.org/10.1016/j.quaint.2012.09.007

Heezen BC, Ewing M (1955) Orléansville Earthquake and Turbidity Currents. Am Assoc Pet Geol Bull 39:2505–2514. https://doi.org/10.1306/5CEAE2E6-16BB-11D7-8645000102C1865D

King GCP, Vita-finzi C (1981) Active folding in the Algerian earthquake of 10 October 1980. Nature 1981 292:5818 292:22–26. https://doi.org/10.1038/292022a0

Maouche S (2010) Tectonique active et géodynamique le long de l'Atlas Tellien: Etude des soulèvements côtiers. Thèse doctotat, , USTHB, Alger

Maouche S, Meghraoui M, Morhange C, et al (2011) Active coastal thrusting and folding, and uplift rate of the Sahel Anticline and Zemmouri earthquake area (Tell Atlas, Algeria). Tectonophysics 509:69–80. https://doi.org/10.1016/j.tecto.2011.06.003

Medaouri M, Déverchère J, Graindorge D, et al (2014) The transition from Alboran to Algerian basins (Western Mediterranean Sea): Chronostratigraphy, deep crustal structure and tectonic evolution at the rear of a narrow slab rollback system. J Geodyn 77:186–205. https://doi.org/10.1016/j.jog.2014.01.003

Meghraoui M (1988) Géologie des zones sismiques du Nord de l'Algérie : paléosismologie, tectonique active et synthèse sismotectonique. Thèse de Doctorat es Science, Université de Paris-Sud, Centre d'Orsay

Meghraoui M, Doumaz F (1996) Earthquake-induced flooding and paleoseismicity of the El Asnam, Algeria, fault-related fold. J Geophys Res Solid Earth 101:17617–17644. https://doi.org/10.1029/96JB00650

Meghraoui M, Maouche S, Chemaa B, et al (2004) Coastal uplift and thrust faulting associated with the M w = 6.8 Zemmouri (Algeria) earthquake of 21 May, 2003. Geophys Res Lett 31:L19605. https://doi.org/10.1029/2004GL020466

Meghraoui M, Pondrelli S (2012) Active faulting and transpression tectonics along the plate boundary in North Africa. Annals of Geophysics 55:955–967. https://doi.org/10.4401/ag-4970

Outtani F, Addoum B, Mercier E, et al (1995) Geometry and kinematics of the South Atlas Front, Algeria and Tunisia. Tectonophysics 249:233–248. https://doi.org/10.1016/0040-1951(95)00022-F

Ouyed M, Meghraoui M, Cisternas A, et al (1981) Seismotectonics of the El Asnam earthquake. Nature 292:26–31. https://doi.org/10.1038/292026a0

Ratzov G, Cattaneo A, Babonneau N, et al (2015) Holocene turbidites record earthquake supercycles at a slow-rate plate boundary. Geology 43:331–334. https://doi.org/10.1130/G36170.1

Strzerzynski P, Dominguez S, Boudiaf A, Déverchère J (2021) Tectonic Inversion and Geomorphic Evolution of the Algerian Margin Since Messinian Times: Insights From New Onshore/Offshore Analog Modeling Experiments. Tectonics 40:. https://doi.org/10.1029/2020TC006369

WCC (Woodward Clyde Consultants): 1984, Seismic microzonation of Ech-Cheliff region, Algeria. Report prepared for C.T.C., Algiers, 1, CTC, Algeria, 145 p.

Wimpenny S, Craig T, Blackwell A (2023) Lower-Crustal Normal Faulting and Lithosphere Rheology in the Atlas Foreland. J Geophys Res Solid Earth 128:e2023JB028090. https://doi.org/10.1029/2023JB028090

Yelles K, Lammali K, Mahsas A, et al (2004) Coseismic deformation of the May 21st, 2003, M w = 6.8 Boumerdes earthquake, Algeria, from GPS measurements. Geophys Res Lett 31:n/a-n/a. https://doi.org/10.1029/2004GL019884

Yelles-Chaouche A, Allili T, Alili A, et al (2013) The new Algerian Digital Seismic Network (ADSN): towards an earthquake early-warning system. Advances in Geosciences 36:31–38. https://doi.org/10.5194/adgeo-36-31-2013

Yelles-Chaouche A, Domzig A, Déverchère J, et al (2009) Plio-Quaternary reactivation of the Neogene margin off NW Algiers, Algeria: The Khayr al Din bank. Tectonophysics 475:98–116. https://doi.org/10.1016/j.tecto.2008.11.030

Yelles-Chaouche A, Lammali K, Bellik A, et al (2019) REGAT: A permanent GPS network in Algeria, configuration and first results. Heliyon 5:. https://doi.org/10.1016/j.heliyon.2019.e01435

INQUA TERPRO Project Cascading Hazards and Mitigation (CHAMP)

paleoseismicity.org

Geomorphic expression and near-surface structure of a low-displacement intra-Alpine strike slip fault – a case study in Switzerland's Engadine Line

Baltes, Sebastian (1), Virginia Toy (1), Friedrich Hawemann (1), Marco Vernier (1), Stephen Michalchuk (1), Mara Weiler (1), Steven Smith (2), Paul Herwegh (3)

(1) Institut für Geowissenschaften, J.-J.-Becher-Weg 21, 55128 Mainz, Germany. Email: sbaltes@students.uni-mainz.de
(2) 249 Strada Cantonale, 7602 Casaccia, Switzerland.
(3) Institut für Geologie, TU Bergakademie Freiberg, Bernhard-v.-Cotta-Straße 2, 09599 Freiberg, Germany.

Abstract: *We studied the surface geomorphology and bedrock structure around the Engadine Line (EL) in southeast Switzerland. We focused on the area south of the Maloja Pass and Lake Sils and Lake Silvaplana. The surveyed structures suggest that the fault zone displays classical Riedel-shear geometry. Overall, the fault zone strikes 058°, and principal displacement occurs across an en echelon array of vertical, 042°-striking brittle faults with synthetic Riedel-shear orientations and sub-horizontal striations indicating pure strike slip. Adjacent units are folded around E-W-trending, sub-horizontal axes, also consistent with a Riedel shear system. This structure is characteristic of a very immature fault system and is consistent with comparatively low displacement. This finding highlights the importance of detailed mapping to characterize the neo-tectonics of the fault zone.*

Key words*: Engadine Line, Riedel-shear, Neo-tectonics*

GEOLOGICAL SETTING

The Engadine Line (EL) is an active NE striking transform fault in SE Switzerland, Grisons (Fig. 2a). In the area around Maloja Pass and lakes Silser and Silvaplana, (Schmid & Froitzheim, 1994), found that offset of older tectonic contacts demonstrate the fault in this area has accommodated only 2.8 km of sinistral slip since the Oligocene. This displacement varies with distance along the EL, reaching a maximum of 3.2 km at S-chanf.

Recent work has demonstrated that the EL is an active fault. Cores from Lake Silvaplana contain turbidite deposits resulting from massive slope failure that indicate there have at least been four significant seismic events in the region in the last 1400 years (Bellwald et. al., 2023). The largest local event in seismic catalogues is a M_w 3.4 on 23 February 1978 in Silvaplana (Fäh et al., 2003). Historic records reveal nearby events in 1917 and 1927 (at St. Moritz) that generated ground shaking of MM IV-V. The Bormio area, 15 km distant from Engadine, has a predicted potential maximum ground shaking hazard of MM XII (Galli et al., 1994). There is anecdotal evidence of historic records of a larger earthquake near Chiavenna (15km SW of the studied area) in the 1700s.

There are also exposed fault rocks in the bed of the Orlegna River (Fig. 1), meaning that this is one of only a handful of sites globally offering unique insight into the relationship of slip mechanics to the structure and composition of fault rocks on an active structure.

FIELD OBSERVATIONS

Fault-related features in the Inn Valley

The surface trace of the fault is decorated by active Quaternary features such as shutter ridges, truncated river terraces, scarps and possible sag-ponds (Fig. 2). In the bed

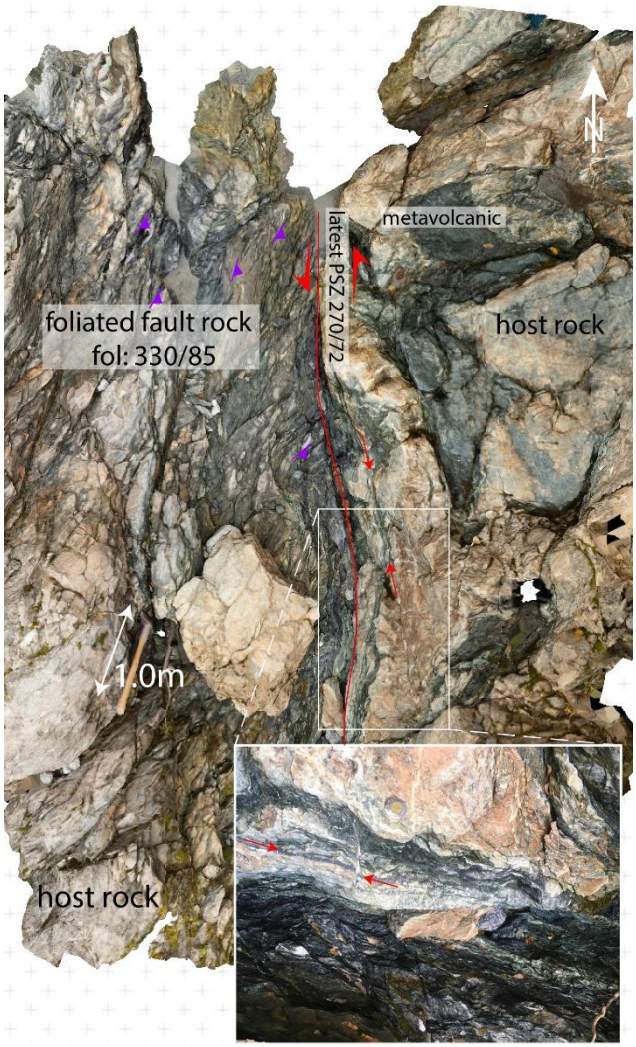

Figure 1: *3D model of outcropping fault rocks in Orlegna River bed. A ductile foliation in metabasic host rock is cross-cut by a discrete brittle 'latest principal slip zone PSZ'. Parallel to this is a cm-thick black layer with random fabric and injection veins.*

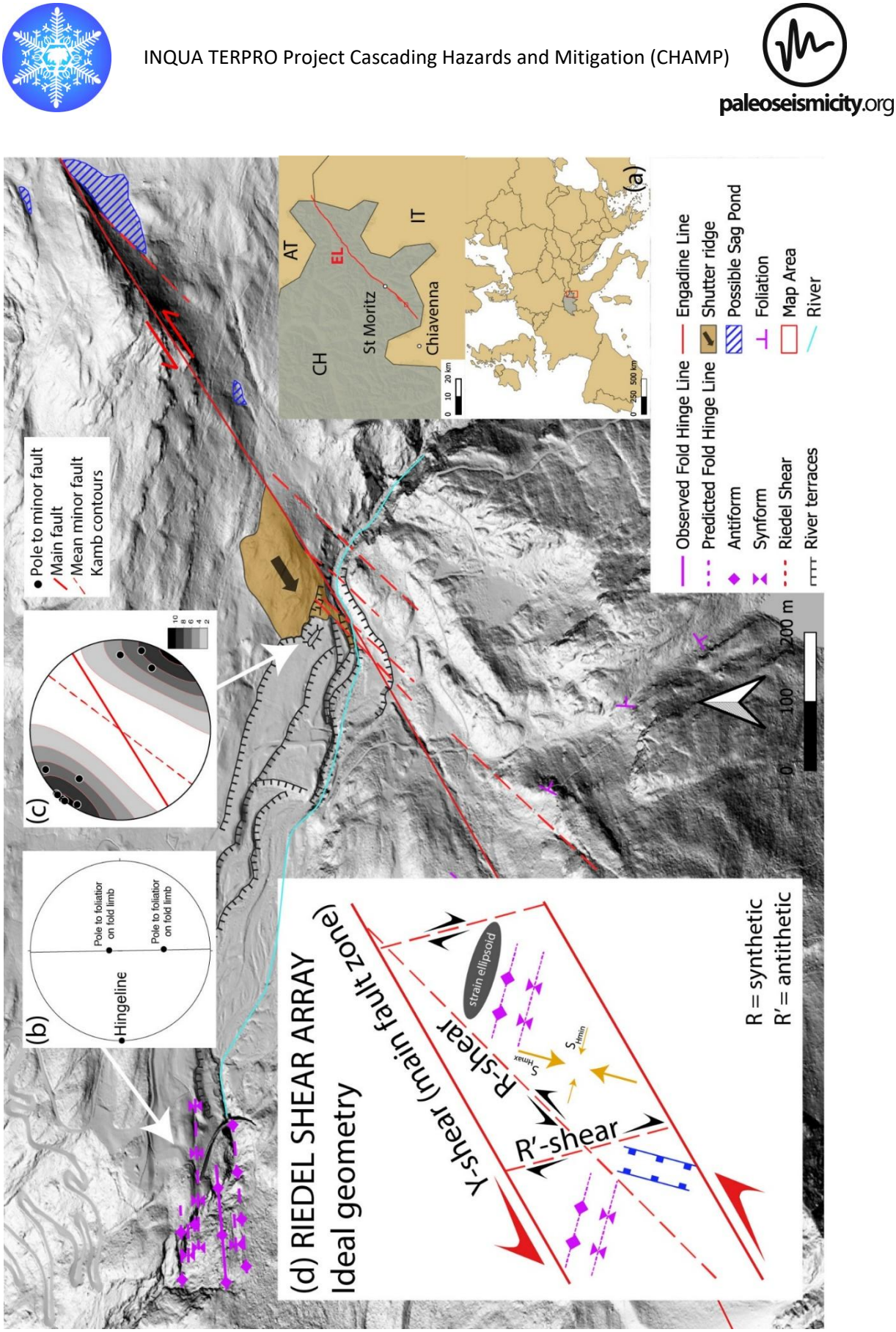

Figure 2: *Overview map based on a LiDAR map of the Inn Valley (Data ©SwissTopo), illustrating geomporphic features and bedrock structure discussed in the text. Insets: (a) overall location (Data ©EuroGeographics). Inset stereonets are equal area, lower hemisphere and display (b) Fold and (c) Minor fault orientations. (d) is an ideal Riedel shear geometry for the major orientation of the EL.*

of the offset Orlegna river, we observe various fault-related rocks, including a c. 1.5 m thick zone of distinctly foliated material and a c. 1 cm thick dark black layer with random internal fabric and injection veins that may be an ultracataclasite or pseudotachylyte (Fig. 1).

Drumlins

A characteristic feature of the topography of the valley are linear drumlins (Fig. 3). Existing geological maps show small faults on the planar sides of these features suggesting they are structurally controlled. Field observations demonstrate that the planar sides, including more gently dipping surfaces at the base of these sides, have glacial striations. Furthermore, in many cases, the drumlins are parallel to minor fold hinge lines, and upstanding parts correlate to more resistant lithologies e.g. in fold cores.

MICROSCOPIC ANALYSIS

Polished petrographic thin sections of the fault rock were analyzed using a TESCAN scanning electron microscope (SEM) equipped with Oxford Instruments detectors at Johannes Gutenberg University, Mainz. Backscattered electron (BSE) images and energy dispersive X-ray spectroscopy (EDS) analyses of chemistry were acquired. The step size for maps was 1 µm. Data were processed using ©Oxford's AZtecOne software.

The results of these analyses (Fig. 4) indicate cataclastic zones that cut at a high angle to foliation and juxtapose foliated micaschists (with a spaced foliation defined by layers of quartz + white mica) and dolomite. The sub-rounded fragments of dolomite are typically wrapped by mm/sized, intact, white mica grains likely derived cataclastically from the micaschist, but there are also areas of fine grained white mica and small euhedral sulfides.

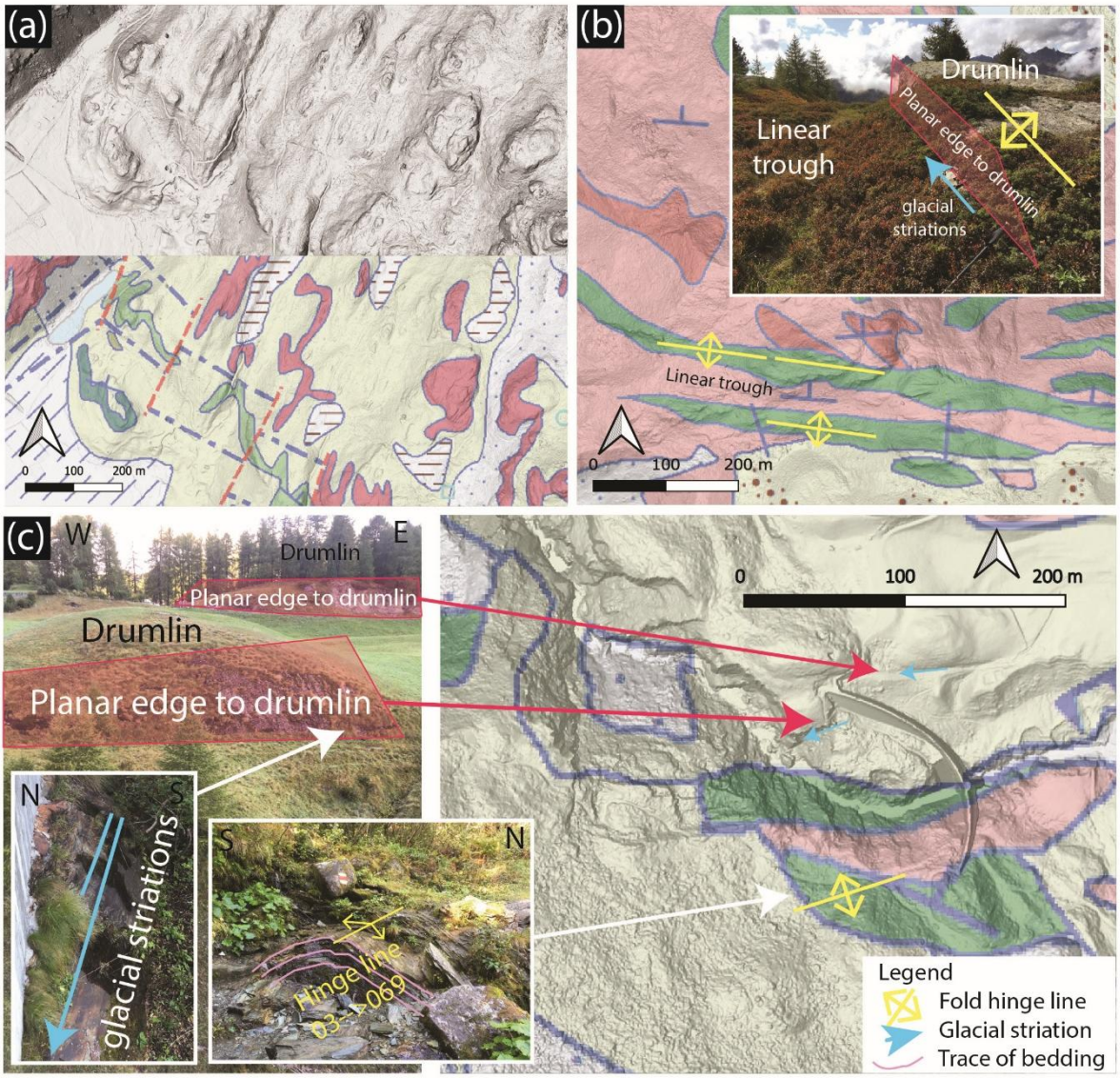

Figure 3: *(a) Illustration of topographic expression of drumlins in LiDAR and geological map data derived from ©SwissTopo. Active faults are here mapped as red lines (dashed where inferred) and different coloured polygons reflect bedrock lithology. (b) Field observations illustrating association of drumlins with fold structures. (c) Field observations illustrating drumlins and striated margins.*

DISCUSSION

Field expression of the EL in the Inn Valley

The observed minor fault and fold orientations are broadly consistent with the predictions of a Riedel shear geometry, as illustrated in Fig. 2(d). We suggest that due to its relatively small (km-scale) displacement, the EL has only generated a zone of distributed structures consistent with this system in the near-surface. It is unknown if a single, discrete fault plane exists at depth, but this should be a target for future investigations.

Drumlins

The presence of glacial striations on the steep side surfaces of drumlins as well as the sloping lower sides, indicates these features pre-date the last glaciation of the valley. Furthermore, the association with fold orientations, including more resistant lithologies in fold cores, indicates the drumlin shapes are controlled by the underlying bedrock structure, rather than by recently active faults.

Fault rock composition and predicted behaviour

The foliated fault rocks we have observed and sampled so far are similar in character to those typically observed on creeping faults such as the San Andreas (Lockner et al., 2011) and potentially the Southern Alpine Fault (Barth et al., 2013), particularly in being dominated by a matrix of foliated, weak micaceous material (Ikari et al., 2011). We expect that the ultracataclasite or pseudotachylyte layer observed and sampled from the Orlegna River outcrop (Fig. 1) preserves evidence of shallower, possibly seismic-rate slip but further microstructural analysis of these samples is still required.

CONCLUSIONS

These preliminary observations of the EL illustrate it is an immature fault zone with a Riedel shear geometry and sets of smaller structures. Our work highlights the importance of detailed and careful mapping, taking account of both geomorphic features and bedrock structure to characterize the neo-tectonics of fault zones. Future joint investigation of the geomorphic expression of faulting and associated fault rocks, coupled with geodetic data analysis is recommended.

Acknowledgements

We sincerely appreciate advice and information provided by Francesco Arrigoni and Allesio Conforto from Universitá degli Studi di Milano Statale about the historic earthquake catalogue.

REFERENCES

Barth, N. C., C. Boulton, B. M. Carpenter, G. E. Batt, and V. G. Toy. 2013. Slip Localization on the Southern Alpine Fault, New Zealand. Tectonics 32 (3): 620–40. https://doi.org/10.1002/tect.20041.

Bellwald, B., Nigg, V., Fabbri, S.C., et al., 2023, Holocene seismic activity in south-eastern Switzerland: Evidence from the sedimentary record of Lake Silvaplana. Sedimentology 71. John Wiley & Sons Ltd on behalf of International Association of Sedimentologists, 116-151. https://doi.org/10.1111/sed.13131

Fäh, D., Giardini, D., Bay, F. et al., 2003. Earthquake Catalogue of Switzerland (ECOS) and the related macroseismic database. Eclogae Geologicae Helvetiae 96, 219-236, https://doi.org/ 10.1007/s00015-003-1087-0.

Galli, P., Magri, L., Mucciarelli, M., et al., 1994. Studi Seismici in Alta Valtellina. I Quaderni Dell'ismes, 336, 69pp.

Ikari, Matt J., Chris Marone, and Demian M. Saffer. 2011. On the Relation between Fault Strength and Frictional Stability. Geology 39 (1): 83–86. https://doi.org/10.1130/G31416.1

Lockner, David A., Carolyn Morrow, Diane Moore, and Stephen Hickman. 2011. Low Strength of Deep San Andreas Fault Gouge from SAFOD Core. Nature 472 (7341): 82–85. https://doi.org/10.1038/nature09927.

Schmid, S. M., Froitzheim, N., 1993. Oblique slip and block rotation along the Engadine line. Eclogae Geologicae Helvetiae 86 (2). Birkhäuser Verlag, 569-593. https://doi.org/10.1038/nature09927

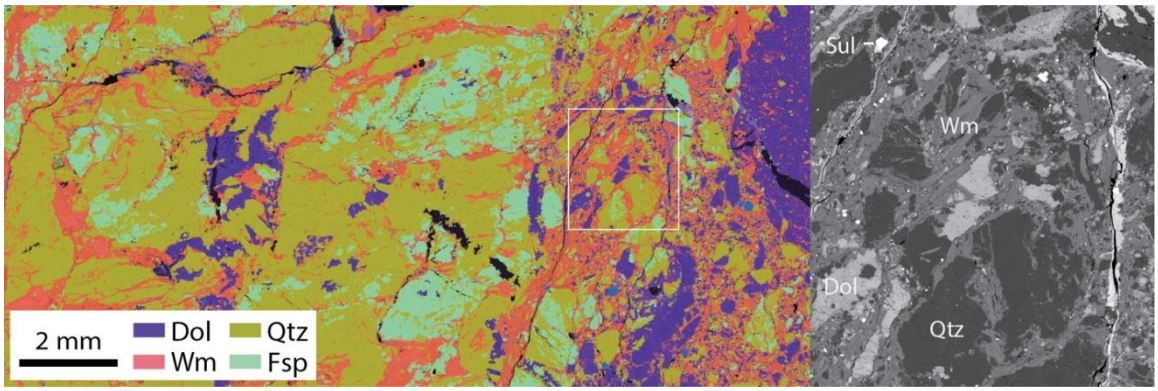

Figure 4: *Composite EDS element maps of a foliated fault rock from the Orlegna River. At left is a foliated mica schist with albite clasts, layers of quartz and white mica. At right are dominantly fragments of dolomite, embedded in a matrix of white mica. Enlargement BSE map highlights the large and surprisingly intact grains of white mica that dominate the matrix of the cataclasite.*

INQUA TERPRO Project Cascading Hazards and Mitigation (CHAMP)

Holocene slip rates on the Santa Cruz Mountains section reveals temporal and spatial consistency for Northern San Andreas Fault, CA

Blisniuk, Kimberly (1), Katherine Guns (2), Roland Burgmann (2)

(1) *Department of Geology, San José State University, San Jose, CA, 95192, USA*
(2) *Department of Earth and Planetary Science, University of California, Berkeley, Berkeley, CA, 94708*
(3) United States Geological Survey, Moffett Field, CA

Abstract: *Field observations and high-resolution topography data combined with 10Be exposure dating on offset landforms indicate higher than expected fault slip rates and seismic hazard potential on the Santa Cruz Mountain section of the northern San Andreas Fault in the San Francisco Bay Area. Geomorphic mapping in Sanborn County Park near Saratoga reveals a progression of alluvial fans and debris flows dextrally offset from their upstream sources by 55 ± 10 m, 170 ± 20 m and 320 ± 20 m, respectively. Surface-exposure dating of large sandstone boulders in these deposits, which are derived from the Tertiary Vaqueros Formation, reveals three distinct depositional ages, ranging from 2.8 ± 1.3 ka, 7.7 ± 0.9 ka, and 12.3 ± 1.5 ka (2σ), respectively. Combining observed offsets with depositional ages indicates an average slip rate of 24.8 ± 3.0 mm/yr on this section of the San Andreas Fault, which is higher than the previously assumed rate of 17 ± 4 mm/yr. This higher slip rate on the fault suggests potentially higher seismic risk for this section of the San Andreas Fault and that slip may remain relatively constant for the northern San Andreas Fault from the North Coast to the Santa Cruz Mountain section.*

Key words: *San Andreas Fault slip rates*

INTRODUCTION

The transform plate boundary between the Pacific and North America plates is made up of a system of strike-slip faults that cut urban northern California into crustal blocks. The movement of these blocks past one another produces earthquakes, one of the greatest natural hazards affecting northern California. Seismically active faults here include the (1) Concord—Green Valley—Calaveras, (2) Rodger's Creek—Hayward, (3) Northern San Andreas, and (4) San Gregorio Faults, all of which define the Northern San Andreas Fault System (Fig. 1). Of these faults, the Northern San Andreas Fault (NSAF), comprised of the North Coast, Peninsula, and Santa Cruz Mountain sections (Fig. 1), is one of the best-studied and seismically active faults in the region, with fast slip rates and a large historic earthquake occurring as recently as 1906 A.D., (Mw7.9) (e.g. Lawson, 1908; Song et al., 2008). Despite multiple previous fault slip-rate studies completed along the NSAF (e.g., Hall et al, 1999; Grove and Niemi, 2005), data gaps still exist along the ~470 km length of the fault, because steep terrain, mass wasting, vegetation, and urban development have generally made slip rate estimates challenging to obtain. Yet, obtaining these data is important because slip rates directly feed into deformation models used to estimate earthquake probability in a region (e.g. UCERF3, Fields et al., 2015). Especially, since the NSAF appears locked, there is no evidence for shallow creep and there is very little microseismicity on the fault.

Published geologic, geomorphic, and paleoseismic data on the NSAF suggest slip rates from 13 mm/yr to 35 mm/yr, at various locations and time intervals along fault strike (e.g., Hall et al., 1999; Grove and Niemi, 2005). On the North Coast section of the fault, slip rates determined over late Pleistocene timescales since ~30 ka and ~200 ka suggest rates from 17 mm/yr up to 35 mm/yr (Grove and Niemi, 2005). These rates are similar, within their respective uncertainties, to Holocene slip rate estimates at this same location of at least 21 to 25 mm/yr since ~1 ka (Grove and Niemi, 2005). On the Peninsula section of the fault, Holocene slip rate estimates appear to slow to 13 to 21 mm/yr, but overlap narrowly at 21 mm/yr with the North Coast section (e.g., Hall et al., 1999). The observed slowing of geologic slip rates from the North Coast section to the Peninsula section is similar to geodetic block models of fault slip for the NSAF, which indicate 20 to 23 mm/yr and 13 to 17 mm/yr for the North Coast and Peninsula sections, respectively (e.g., d'Alessio et al., 2005; Evans et al., 2012). These data suggest a kinematic model where slip rate decreases southward along the NSAF as the fault enters the urban areas surrounding the Peninsula and Santa Cruz Mountain sections. Accordingly, fault slip is transferred westward to the San Gregorio Fault and eastward to the Calaveras and Hayward faults (Johnson et al., 2009). In this paper, we estimate slip rates over three different Holocene timescales on the Santa Cruz Mountain section of the NSAF at Sanborn County Park in Saratoga, CA, a section of the fault where no published slip rate data exist, to better characterize the temporal and spatial patterns of fault slip for the NSAF. With this data we infer an alternative kinematic model where fault slip rate remains steady and constant on the entire length of the NSAF from the North Coast to the Santa Cruz Mountains sections over Holocene timescales. In this kinematic model, seismic hazard remains the same for the length of the NSAF, while it may be reduced on the San Gregorio Fault.

METHODS

To determine ages of the displaced landforms, a relative stratigraphy for observed alluvial fans was developed following the nomenclature of Bull (1991). This stratigraphy is based on surface morphology, which includes inset geometry, the presence or absence of bar-

and-swale micro-topography, the degree of fan dissection, the degree of weathering of sandstone boulders, and overall texture of the surface observed from high-resolution digital topography data and field observations. Based on fan nomenclature of Bull (1991), older alluvial fan surfaces are classified as Qf2, intermediate aged surfaces are mapped as Qf3, and the youngest alluvial surfaces are classified as Qf4 (Bull, 1991). Additionally, we apply the indices "a" and "b" to an alluvial fan classification to indicate older and younger fans, respectively (e.g. Bull, 1996). Absolute ages of offset alluvial fans in this study are constrained with cosmogenic ^{10}Be concentration within surface clasts. All ^{10}Be surface-exposure dates were processed at Stanford University's cosmogenic radionuclide laboratory following the procedures summarized in Blisniuk et al. (2012) and final dates are calculated using the online exposure age calculator formerly known as the CRONUS-Earth online exposure age calculator using version 3.0 (Balco et al., 2008).

RESULTS

Through surface exposure geochronologic constraints and detailed site mapping, we establish a timeline for deposition and subsequent dextral offset for a progression of alluvial fans and debris flows along the NSAF at Sanborn County Park near Saratoga, CA (Fig. 2, Fig. 3, Fig. S1). Alluvial fans here contain large quartz-rich sandstone boulders that are derived from the Tertiary Vaqueros Sandstone Formation (Tvq), which is located within the upper reaches of the Santa Cruz Mountains. Tvq is exposed as bedrock ~500 m west of the fault in the larger stream catchments of Todd Creek, Service Road Creek, and Aubrey Creek (e.g., Brabb et al., 2000; Stoffer, 2005) (Fig. 2). Along the hillslopes adjacent to the fault are Tertiary mudstones of the San Lorenzo Formation (Tsl). The presence of Tsl along the adjacent hillslopes and of Tvq boulders and alluvium at the mouths of the creeks allow us to characterize and correlate alluvial fan units across the NSAF because the source of Tvq must be one of these larger drainages (Fig. 2).

Four distinct alluvial fan units are identified, these units from oldest to youngest are Qf2, Qf3a, Qf3b and Qf4. Qf2 is the oldest and topographically highest surface mapped. These surfaces often contain random yet abundant large Tvq boulders. West of the fault, preserved Qf2 is located at elevations ranging from 440 to 450 m and is distinguished in the field by its elevated, planar topographic expression. East of the fault, Qf2 surfaces are located at 440 to 446 m in elevation and are distinguished by their rounded mound-like topographic expression. Inset and incised into Qf2 are Q3a and Q3b alluvial surfaces. Qf3a and Qf3b surfaces are the most extensive surfaces in the field and are characterize by a hummocky and rough surface morphology. These surfaces exhibit little to no topographic smoothing and contain many debris flow levee bars of Tvq boulders. Qf3a is distinguished from Qf3b in the field by the more weathered appearance of Tvq boulders on the Qf3a surface, the presence of more random Tvq boulders, as well as a varying direction of imbrication of these boulders within debris flow bars. Qf3b surfaces contain many debris flow deposits that are more dominated by boulders and large cobbles than Qf3a deposits. Qf4 are the youngest surface deposits offset by the NSAF. These surfaces are characterized by fresh debris flows deposits, which consist of sharp, well-delineated, and linear Tvq-boulder-rich deposits. Results of ^{10}Be surface exposure geochronology (Table 1) also indicate the presence of four distinct geomorphic surfaces, ranging in age from Qf4 = 2.4 ± 1.3 ka (N=8), Qf3b = 7.7 ± 0.9 ka (N=7), Qf3b =

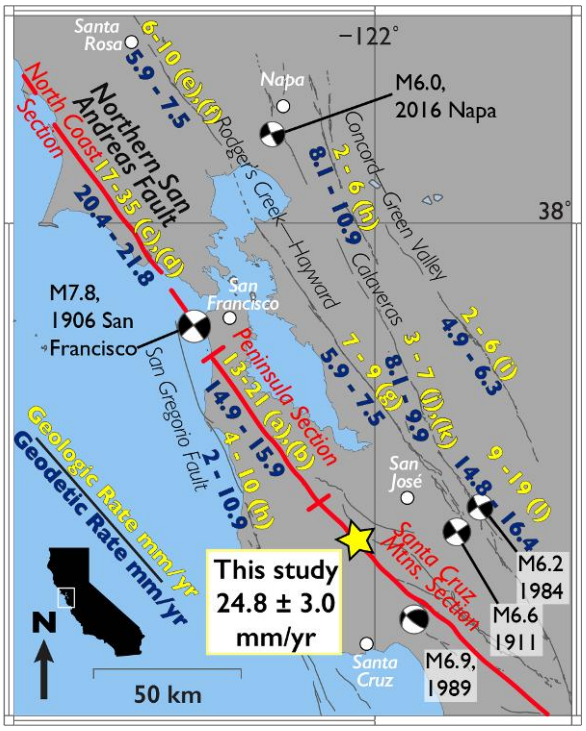

Figure 1: *Regional fault map of the San Francisco Bay Area, California; Faults modified from the USGS Quaternary Fault Database, Northern San Andreas Fault shown in red, while other active faults are shown in black. Focal Mechanisms plotted and labeled for all ≥M6.0 earthquakes since 1900 in the USGS Earthquake catalog, with focal mechanism data from Wang et al. (2009). Estimated geologic and geodetic fault slip rates are given and cited as (a) Hall (1984), (b) Hall et al. (1999), (c) Niemi and Hall (1992), (d) Grove and Niemi (2005), (e) Budding et al. (1991), (f) Schwartz et al. (1992), (g) Lienkaemper and Borchardt (1996), (h) Borchardt et al. (1999), (i) Sawyer and Unruh (2002), (j) Kelson et al. (1996), (k) Simpson et al. (1999), and (l) Kelson et al. (1998). All geodetic slip rates are plotted from Evans et al. (2012).*

12.3 ± 1.5 ka (N=7), and Qf2 = 19.5 ± 3.3 ka (N=2) (Fig. 2;). We interpret these ages to represent four discrete episodes of fan emplacement and subsequent displacement (Fig. 3; t=1, t=2, t=3 and t=4), which allows for the reconstruction and measurement of displacement across the NSAF.

The oldest offset surface preserved along the NSAF at the study site is Qf2 (Fig. 3; t = 1). This surface is mapped west of the fault in Todd, Service Road and Aubry Creeks, as high terraces, and near the mouths of Service Road Creek and Aubry Creek, as raised rounded mound-like deposits (**Fig. 2**). Two surface exposure ages from boulders on a

Qf2 terrace surface in Service Road Creek yield a mean age of 19.5 ± 3.3 ka. The preserved extent of these deposits is limited, therefore reconstructing their original depositional location involves much more uncertainty than for more recent deposits, and for this reason we do not include the Qf2 offset and age in our final slip rate calculations. Here, we infer a maximum (550 m) and minimum (440 m) offset based on aligning a major drainage to the north of Todd Creek, which allows for Qf2 east of the fault to align near a source drainage (Fig. S3E). This realignment infers that Qf2 located at the mouth of Service Road Creek is sourced and was deposited by Todd Creek, and that the Qf2 deposit near the mouth of Aubry Creek was deposited by Service Road Creek (Fig. 3; Fig. S3E). Combining the age of Qf2 with its displacement suggest a slip rate of 25.2 ± 3.4/2.8 mm/yr since ~20 ka.

Following aggradation and subsequent displacement of Qf2 is the emplacement of Qf3a (Fig. 3; t = 2). The Qf3a surface is the most extensive surface present at the Sanborn site. Qf3a is mapped west of the NSAF in Todd Creek and Aubry Creek and east of the fault in front of Service Road Creek and as a shutter ridge at the mouth of Aubry Creek. Sandstone boulders (N=7) from the surface of Qf3a yield an average surface age of 12.3 ± 1.5 ka. Offset reconstructions of Qf3a realigns two streams that are incised into Qf3a across the NSAF. The larger incised stream is located south of Todd Creek and is presently beheaded (Fig. 2). The second stream has been recently captured by Aubry Creek along the NSAF in a left deflection. Directions of boulder imbrication as well as the direction of major stream incision indicate that aggradation of the Qf3a surface from Todd Creek occurred at an angle from northwest to southeast, rather than directly northeast, or the direction of range incision. This is most likely because dextral motion had blocked the mouth of Todd Creek with a high bedrock block of Tertiary Undifferentiated Sediments, forcing deposition of sediment and stream incision to go around this bedrock block (Fig. 3, t = 2). Realignment of Qf3a across the fault in this way requires an average of 320 m of offset (Fig. 2 blue dashed lines, Fig. S3D). We interpret Qf3a to be the last surface to be deposited by Todd Creek before a new downstream channel dextrally offset from the north captured its flow. The minimum offset of ~300 m aligns the beheaded stream incised into Qf3a with the south channel wall of Todd Creek. The maximum offset reunites the Qf3a surfaces across both sides of the fault at Todd Creek (Fig. S3D). This reconstruction also aligns the Qf3a shutter ridge and the second stream located at the mouth of Aubry Creek to its source, Service Road Creek. Combining the age of Qf3a with these offsets suggest a slip rate of 26.0 ± 4.3/3.5 mm/yr since ~13 ka (Table 1). The next youngest surface to aggrade is Qf3b, which is preserved in and at the mouths of Service Road Creek and near Aubry Creek (Fig. 3; t = 3). Surface exposure ages of seven boulders from Qf3b yield a ^{10}Be exposure model age of 7.7 ± 0.9 ka. Mapped offsets of two different Qf3b surfaces indicates 170 ± 20 m of displacement. The maximum offset reconstruction of 190 m realigns the preserved extent of the Qf3 surface on either side of the fault at the mouths of both Service Road and Aubry creeks. Combining the age of Qf3b with its displacement suggest a slip rate of 22.1 ± 4.5/3.7 mm/yr since ~8 ka.

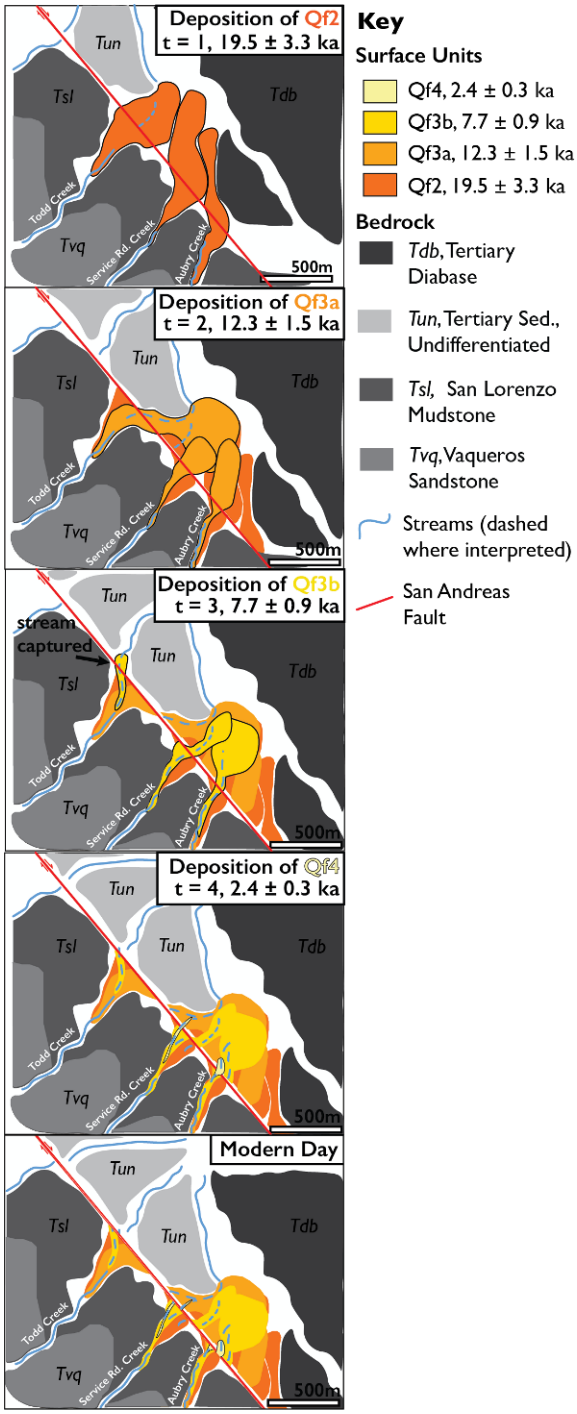

Figure 2: *Schematic reconstruction of proposed depositional history and fault motion of mapped alluvial fans along the northern San Andreas Fault at Sanborn County Park, see text for details.*

The youngest offset surface to aggrade at Sanborn County Park, Qf4, is observed in and at the mouths of Service Road Creek and Aubry Creek (Fig. 3; t = 4). Surface exposure dating of boulders, 2 from Service Road Creek

and 5 from Aubry Creek (N=7), indicate emplacement at 2.4 ± 0.3 ka. Qf4 is measurably offset in Aubry Creek, where a linear debris flow bar of imbricated Tvq boulders is dextrally displaced by 55 ± 10 m. The maximum of 65 m aligns the debris flow (Qf4) across the NSAF. The minimum offset of 45 m realigns a channel that is incised parallel to the Qf4 deposit across the fault (Figs. 2 and S3B). These offsets combined with the 2.4 ± 0.3 ka age of the debris flow indicates a slip rate of 22.9 ± 6.1/5.1 mm/yr.

REFERENCES

Balco, G., Stone, J.O., Lifton, N.A., and Dunai, T.J., 2008, A complete and easily accessible means of calculating surface exposure ages or erosion rates from ^{10}Be and ^{26}Al measurements: *Quaternary Geology*, v. 3, p 174-195, https://doi.org/10.1016/j.quageo.2007.12.001.

Blisniuk, K., Oskin, M., Fletcher, K., Rockwell, T., and Sharp, W., 2012, Assessing the reliability of U-series and 10Be dating techniques on alluvial fans in the Anza Borrego Desert, California: *Quaternary Geochronology*, https://doi.org/10.1016/j.quageo.2012.08.004

Borchardt, G., Synder, D.L., & Wills, C.J., 1999, Holocene Slip Rate of the Concord Fault at Galindo Creek in Concord, California, National Earthquake Hazards Program Final Technical Report, Contract# 1434-HQ-97-GR-03102.

Brabb, E.E., Graymer, R.W., and Jones, D.L., 2000, Geologic map and map database of the Palo Alto 30'x60' quadrangle, California: U.S. Geological Survey, Miscellaneous Field Studies Map MF-2332, 1:100,000 scale.

Budding, K.E., Schwartz, D.P., and Oppenheimer D.H., 1991, Slip Rate, Earthquake Recurrence, and Seismogenic Potential of the Rodgers Creek Fault Zone, Northern California: Initial Results: *Geophysical Research Letters*, v. 18, no. 3, p. 447-450.

Bull, W.B., 1991, Geomorphic Responses to Climate Change: *Oxford University Press*, New York.

d'Alessio, M.A., Johanson, I.A., Bürgmann, R., Schmidt, D.A., and Murray, M.H., 2005, Slicing up the San Francisco Bay Area: Block kinematics and fault slip rates from GPS-derived surface velocities: *JGR*, v. 110, B06403, https://doi.org/10.1029/2004JB003496.

Evans, E.L., Loveless, J.P., and Meade, B.J., 2012, Geodetic constraints on San Francisco Bay Area fault slip rates and potential seismogenic asperities on the partially creeping Hayward fault: *JGR*, v.117, no. B03410, https://doi.org/10.1029/2011JB008398.

Evans, E.L., 2018, A Comprehensive Analysis of Geodetic Slip-Rate Estimates and Uncertainties in California: *BSSA*, 108(1), 1-18, https://doi.org/10.1785/0120170159

Field, E.H., and 2014 Working Group on California Earthquake Probabilities, 2015, UCERF3: A new earthquake forecast for California's complex fault system: U.S. Geological Survey 2015–3009, 6 p., https://dx.doi.org/10.3133/fs20153009.

Fumal, T.E., 2012, Timing of Large Earthquakes during the Past 500 Years along the Santa Cruz Mountains Segment of the San Andreas Fault at Mill Canyon, near Watsonville, California: *BSSA*, v.102, no. 3, p.1099-1119, https://doi.org/10.1785/0120110161.

Gold, R. D., Cowgill, E., Arrowsmith, J R., Gosse, J., Chen, X., and Wang, X.-F. (2009), Riser diachroneity, lateral erosion, and uncertainty in rates of strike-slip faulting: A case study from Tuzidun along the Altyn Tagh Fault, NW China, *J. Geophys. Res.*, 114, B04401, doi:10.1029/2008JB005913.

Grove, K. and Niemi, T.M., 2005, Late Quaternary deformation and slip rates in the northern San Andreas fault zone at Olema Valley, Marin County, California: *Tectonophysics*, v. 401, p. 231-250, https://doi.org/10.1016/j.tecto.2005.03.014.

Hall, N.T., 1984, Holocene History of the San Andreas Fault Between Crystal Springs Reservoir and San Andreas Dam, San Mateo County, California: *BSSA*, v. 74, no. 1, p. 281-299.

Hall, N.T., Wright, R.H., and Clahan, K.B., 1999, Paleoseismic studies of the San Francisco Peninsula segment of the San Andreas fault zone near Woodside, California: *Journal of Geophysical Research*, v. 104, no. B10, p. 23215-23236.

Kelson, K.I., Simpson, G.D, Lettis, W.R., and Haraden, C.C., 1996, Holocene slip rate and earthquake recurrence of the northern Calaveras fault at Leyden Creek, northern California: *Journal of Geophysical Research*, v. 101, no. B3, p. 5961-5975.

Kelson, K.I., Baldwin, J.N., and Randolph, C.E., 1998, Late Holocene slip rate and amounts of coseismic rupture along the central Calaveras fault, San Francisco Bay area, California: Final Technical Report submitted to the National Earthquake Hazard Reduction Program, 26 p., William Lettis & Associates, Inc., Walnut Creek, Calif.

Lawson, A.C., 1908, The California Earthquake of April 18, 1906: Report of the State Earthquake Investigation Commission, Volume I, Carnegie Institution of Washington: Washington, D.C.

Lienkaemper, J.J. and Borchardt, G., 1996, Holocene slip rate of the Hayward fault at Union City, California: *Journal of Geophysical Research*, v. 101, no. B3, p. 6099-6108.

Niemi, T.M, and Hall, N.T., 1992, Late Holocene slip rate and recurrence of great earthquakes on the San Andreas fault in northern California: *Geology*, v. 20, p. 195-198.

Pollitz, F., Evans, E., Hearn, E., Johnson, K., Milner, K, Murray, J. R., Shen, Z-K, Zeng, Y., and Hatem, A. E., 2022, Geodetic deformation model results and corrections for use in U.S. National Seismic Hazard Model 2023: U.S. Geological Survey data release, https://doi.org/10.5066/P9MUPHM4.

Sawyer, T.L. & Unruh, J.R., 2002, Holocene Slip Rate Constraints for the Northern Greenville Fault, Eastern San Francisco Bay Area, California: Implications for the Mt. Diablo Restraining Stepover Model: Abstract T62F-03 presented at the American Geophysical Union Fall Meeting, San Francisco, CA.

Schwartz, D.P., Pantosti, D., Hecker, S., Okumura, K., Budding, K.E., Powers, T., Borchardt, G., Hirschfeld, S.E., Lienkaemper, J.J., McClellan, P. and Wong, I.G., 1992, Late Holocene behavior and seismogenic potential of the Rodgers Creek fault zone, Sonoma County, California: In Proceedings of the second conference on earthquake hazards in the eastern San Francisco Bay Area: California Department of Conservation, Division of Mines and Geology Special Publication, v. 113, p. 393-398.

Simpson, G.D., Baldwin, J.N, Kelson, K.I., and Lettis, W.R., 1999, Late Holocene Slip Rate and Earthquake History for the Northern Calaveras Fault at Welch Creek, Eastern San Francisco Bay Area, California: *BSSA*, v. 89, no. 5, p. 1250-1263.

Toppozada, T.R., and Borchardt, G., 1999, Re-evaluation of the 1836 "Hayward Fault" and the 1838 San Andreas Fault Earthquakes: *BSSA*, 88(1), 140-159.

Wang, Q., Jackson, D.D., and Kagan, Y.Y., 2009, California Earthquakes, 1800-2007: A Unified Catalog with Moment Magnitudes, Uncertainties, and Focal Mechanisms: *SRL*, v. 80, no. 3, https://doi.org/10.1785/gssrl.80.3.446.

Wells, D.L., and Coppersmith, K.J., New Empirical Relationships among Magnitude, Rupture Length, Rupture Width, Rupture Area, and Surface Displacement: *BSSA*, 84(4), 974-1002.

Zechar, J.D. and Frankel, K.L., 2009, Incorporating and reporting uncertainties in fault slip rates: *JGR*, v. 114, no. B12407, https://doi.org/10.1029/2009JB006325

INQUA TERPRO Project Cascading Hazards and Mitigation (CHAMP)

Automated detection and spacing analysis of fracture networks from LiDAR point clouds: implications for distributed surface deformation along the San Ramón Fault, Chile.

Nicolas Campillay (1), Gabriel Easton (1), Sofía Rebolledo (1), Ignacio Gutiérrez (1), Marisol Lara (1), José González (1)

(1) Department of Geology, Faculty of Physical and Mathematical Sciences (FCFM), University of Chile, Santiago, Chile. E-mail: nicolas.campillay@uchile.cl.

Abstract: *Surface rupture associated with active faults commonly involves a combination of localized slip along principal fault strands and distributed brittle deformation affecting surrounding rock volumes. Quantifying the geometry and intensity of this distributed deformation remains challenging due to limited field accessibility and scale dependence of traditional measurements. We present an automated workflow for the remote detection, classification, and spacing analysis of fracture networks derived from high-resolution terrestrial LiDAR point clouds, applied to a bedrock outcrop of the San Ramón Fault (SRF) (central Chile). The method integrates geometric attributes derived from point-cloud surface normals with density-based unsupervised clustering (HDBSCAN) to identify coherent fracture families. Results identify four classes, one of them being consistent with the distributed damage-zone architecture measured in the field, providing first-order geometric constraints on surface deformation at the outcrop scale.*

Key words*: active fault, LiDAR, clustering, surface deformation.*

INTRODUCTION

Rapid urban expansion into piedmont areas of mountain ranges worldwide implies increased exposure to active fault zones. Understanding subsurface faulting and surface rupture is therefore essential for reducing seismic hazards that may affect nearby populations and civil infrastructure.

Surface rupture associated with active faults is commonly expressed as a combination of localized slip along principal fault strands and distributed brittle deformation affecting surrounding rock volumes. Quantifying the geometry and intensity of this distributed deformation remains challenging due to limited field accessibility, the scale dependence of traditional measurements, and the substantial time required for detailed structural data acquisition using conventional field-based approaches.

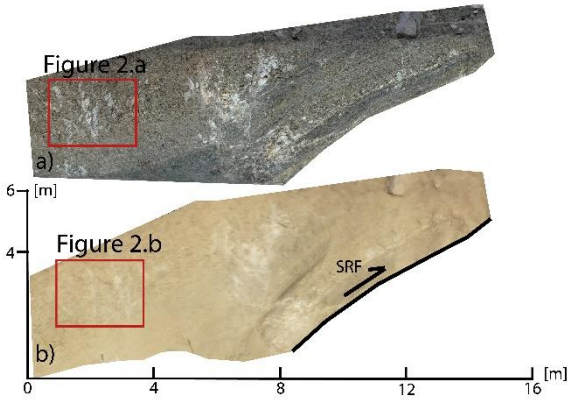

Figure 1: *a) Bedrock outcrop of San Ramón Fault. b) Processed terrestrial LiDAR point cloud used in this study.*

Here we present an automated workflow for the remote detection, classification, and spacing analysis of fracture networks derived from high-resolution terrestrial LiDAR point clouds, applied to a well-exposed anthropogenic bedrock outcrop of the San Ramón Fault (SRF), an active fault located along the western flank of the Andes in Santiago, Chile (Vargas et al., 2014). The outcrop is located within the hanging wall of the SRF and is characterized by a dominant orientation of Dip/Dip direction = 41°/62°. Two main fracture sets, previously identified through detailed field-based structural mapping and displaying fault-related geometric characteristics such as planar continuity and persistence, are present at the site: F1 with Dip/Dip direction = 90°/270°, and F2 with Dip/Dip direction = 73°/340°. The method integrates geometric attributes derived from point-cloud normals with density-based unsupervised clustering (HDBSCAN) to identify coherent discontinuity families without a priori orientation constraints.

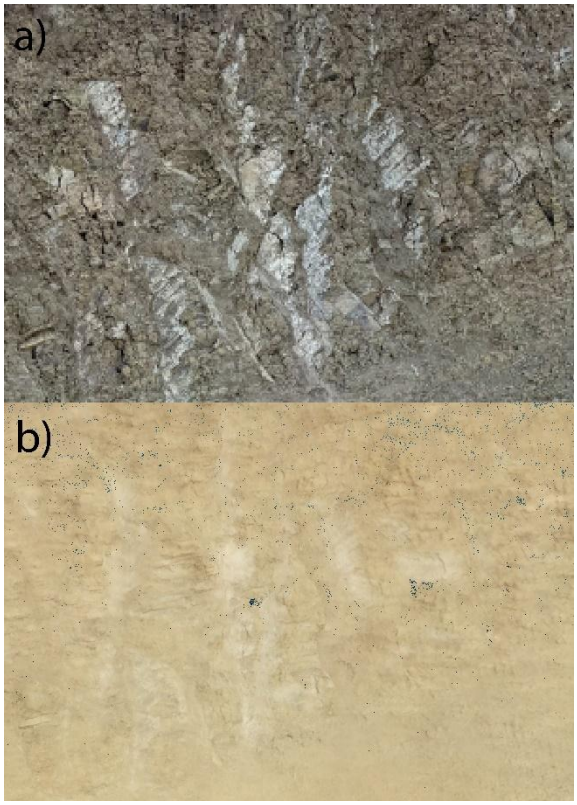

Figure 2: *a) Inset of bedrock outcrop of San Ramón Fault. b) Inset of the terrestrial LiDAR point cloud from Figure 1, showing the main fracture set and the achieved point density (~440,000 pts/m²).*

METHODOLOGY

Data acquisition and preprocessing

Terrestrial LiDAR data were acquired using a Leica BLK360 G1 laser scanner, a compact TLS sensor capable of acquiring up to 360,000 points per second. The scanner was deployed at 14 scan positions to fully capture the geometry of the outcropping fault-related bedrock surface. Individual scans were first aligned and registered into a single point cloud and subsequently georeferenced using differential GPS measurements (Figure 1 and 2). The merged dataset was then filtered to remove noise and non-relevant points, resulting in a final point cloud consisting of approximately 800,000 points, with a global registration error of 0.008 m (Figure 1). Using CloudCompare sofware, geometric attributes were computed for each point, including surface normals (Nx, Ny, Nz) and orientation parameters (Dip and Dip Direction). The enriched point cloud was then exported as a .txt file, preserving the spatial coordinates and derived attributes for subsequent analysis.

Data analysis and clustering

The analysis of the exported .txt file, containing point coordinates, surface normals, and orientation parameters, was performed using the Hierarchical Density-Based Spatial Clustering of Applications with Noise (HDBSCAN) algorithm. HDBSCAN is an unsupervised clustering method that groups data based on local density while explicitly identifying noise and outliers (Campello et al., 2015). The algorithm constructs a hierarchy of density-based clusters and selects the most stable cluster configurations across multiple spatial scales.

Two key parameters control the clustering behavior: min_cluster_size, which defines the minimum number of points required for a cluster to be considered valid, and min_samples, which controls the strictness of the density definition and influences the classification of noise. In this study, point-cloud surface normals were used as the primary input features for clustering, allowing the identification of discontinuity families based on geometric similarity rather than spatial proximity alone. The clustering was performed using min_cluster_size = 10,000 and min_samples = 100, values selected to ensure robust identification of large-scale, structurally meaningful fracture sets.

Normal spacing between discontinuities

Normal spacing between discontinuities was quantified following the methodology proposed by Mammoliti et al. (2022**)**. For each identified fracture set, inter-discontinuity distances were calculated along the mean normal direction of the cluster, allowing objective estimation of fracture spacing independent of scanline orientation. This approach enables consistent comparison of spacing statistics across different fracture families and provides a quantitative measure of brittle damage intensity within the fault-related damage zone.

RESULTS

Data analysis reveals four classes identified by the HDBSCAN algorithm, together with an additional noise class. The number of points assigned to each class and their geometric characteristics are summarized in Figures 3, 4 and Table 1.

Table 1: *HDBSCAN algorithm results and normal spacing between discontinuity.*

Class	N° points	Dip_mean	Dip std.	DipDir mean	DipDir std.	Mean spacing	Max spacing
-1	697,142	60.3°	10.2	303.7°	23.5	NA	NA
0	39,194	32.3°	3.4	309.0°	13.1	0.31 m	0.74 m
1	13,554	60.4°	1.8	279.0°	2.1	0.39 m	3.89 m
2	13,901	52.7°	1.8	290.1°	1.9	0,15 m	0.7 m
3	36,211	57.2°	3.5	296.3°	3.4	0.05 m	0.3 m

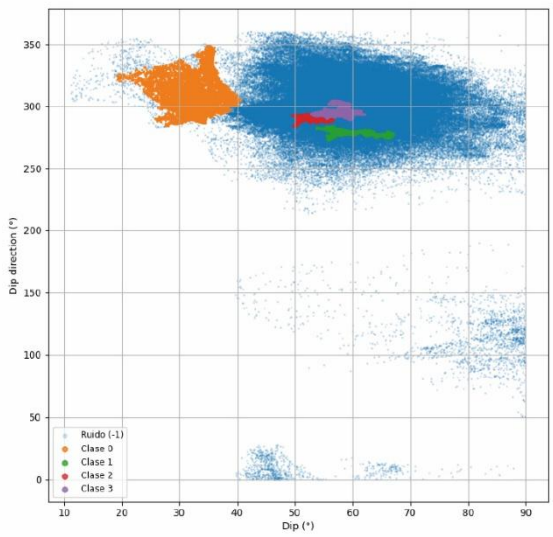

Figure 3: *Dip–dip direction diagram showing fracture families identified using HDBSCAN clustering. The plotted points represent a subsample of the complete point-cloud dataset.*

DISCUSSION

When comparing the classes identified by HDBSCAN with field data and direct outcrop observations, only Class 1 shows a consistent correspondence in terms of dip and dip direction whit F1 (Figure 4). In contrast, Class 0 is associated with colluvial deposits derived from the outcrop surface, while Classes 2 and 3 cannot be identified in the field as genuine structural discontinuities. This highlights that HDBSCAN may erroneously identify planar features that do not represent real discontinuities, such as debris patches or natural slope surfaces (Menegoni et al., 2019).

Conversely, one fracture family recognized in the field (F2) was not detected by HDBSCAN. This discrepancy is likely related to the choice of algorithm input parameters. In particular, this fracture set may exhibit higher internal variability and therefore does not meet the density and stability requirements imposed by the clustering criteria (e.g., *min_cluster_size*), resulting in its classification as noise rather than as a distinct cluster.

The fracture set identified by HDBSCAN (Class 1) likely represents brittle deformation produced by multiple slip events of the San Ramón Fault (SRF), rather than being associated solely with the most recent event. This class constitutes one of the structural sets defining the secondary deformation architecture of the SRF. Because this fracture network is expressed at the surface, it is expected that future surface-rupture events may preferentially exploit and follow this pre-existing geometric and spatial pattern, at least at the outcrop scale.

Acknowledgements: Thanks to Projects Fondecyt 1241021, Fondecyt 1230350 and CHAMP (Cascading Hazards and Mitigation Project).

REFERENCES

Campello, R. J. G. B., Moulavi, D., Zimek, A., & Sander, J. (2015). Hierarchical Density Estimates for Data Clustering, Visualization, and Outlier Detection. *ACM Transactions on Knowledge Discovery from Data*, *10*(1), 1-51. Article 5. https://doi.org/10.1145/2733381

Mammoliti, E.; Di Stefano, F.; Fronzi, D.; Mancini, A.; Malinverni, E.S.; Tazioli, A. A Machine Learning Approach to Extract Rock Mass Discontinuity Orientation and Spacing, from Laser Scanner Point Clouds. Remote Sens. 2022, 14, 2365. https://doi.org/10.3390/rs14102365

Menegoni, N., Giordan, D., Perotti, C., & Tannant, D. D. (2019). Detection and geometric characterization of rock mass discontinuities using a 3D high-resolution digital outcrop model generated from RPAS imagery–Ormea rock slope, Italy. *Engineering geology*, *252*, 145-163.

Vargas, G., Klinger, Y., Rockwell, T. K., Forman, S. L., Rebolledo, S., Baize, S., Lacassin, R & Armijo, R. (2014). Probing large intraplate earthquakes at the west flank of the Andes. Geology, 42 (12), 1083-1086.

INQUA TERPRO Project Cascading Hazards and Mitigation (CHAMP)

Investigating continental-scale deformation and fault coupling in northern central America using Sentinel-1 InSAR

Cosenza-Muralles, Beatriz (1), Cécile Lasserre (2), Giorgio Gomba (3), Francesco De Zan (3), Charles DeMets (4), Marianne Métois (2), and Hélène Lyon-Caen (5)

(1) Universidad de San Carlos de Guatemala, Instituto de Investigación en Ciencias Físicas y Matemáticas, Escuela de Ciencias Físicas y Matemáticas, Mixco, Guatemala (bcosenza@ecfm.usac.edu.gt)
(2) Laboratoire de Géologie de Lyon: Terre, Planètes et Environnement (LGLTPE), Université Claude Bernard Lyon 1
(3) German Aerospace Center (DLR)
(4) Department of Geoscience, University of Wisconsin-Madison
(5) Laboratoire de Géologie, CNRS, École Normale Supérieure Paris, PSL University

Abstract: *Tectonic deformation in northern Central America, driven by the interactions between the Cocos, Caribbean, and North America plates, is accommodated by the Motagua and Polochic left-lateral faults, grabens south of the Motagua Fault, the Middle America subduction zone, and right-lateral faults along the Middle America volcanic arc. Major earthquakes associated with these structures include the 1976 MW 7.5 Motagua and 2012 MW 7.5 Champerico events. To investigate current deformation in this setting, we use Sentinel-1 radar images covering most of Guatemala, El Salvador and western Honduras to obtain the line-of-sight velocity fields, which we subsequently decompose into horizontal and vertical components. While in overall agreement with GNSS data and elastic block models for the region, the high-resolution InSAR data brings new information, highlighting spatial variations across main faults, including a creeping segment along the Motagua fault, slip partitioning within the Caribbean plate wedge and possible coupling variations along the subduction interface.*

INQUA TERPRO Project Cascading Hazards and Mitigation (CHAMP)

Strain accumulation along the Motagua Fault: a creeping segment in the context of the 1976 earthquake

Cosenza-Muralles, Beatriz (1), Cécile Lasserre (2), Farès Mokhtari (2), Giorgio Gomba (3), Francesco De Zan (3), Charles DeMets (4), and Hélène Lyon-Caen (5)

(1) Universidad de San Carlos de Guatemala, Instituto de Investigación en Ciencias Físicas y Matemáticas, Escuela de Ciencias Físicas y Matemáticas, Mixco, Guatemala (bcosenza@ecfm.usac.edu.gt)
(2) Laboratoire de Géologie de Lyon: Terre, Planètes et Environnement (LGLTPE), Université Claude Bernard Lyon 1
(3) German Aerospace Center (DLR)
(4) Department of Geoscience, University of Wisconsin-Madison
(5) Laboratoire de Géologie, CNRS, École Normale Supérieure Paris, PSL University

Abstract: *The Motagua Fault, a major structure accommodating the relative motion between the North American and Caribbean plates, generated a 230-km-long rupture with an average displacement of ~1.08 m during the devastating 1976 earthquake. Slip varied significantly along strike, reaching a maximum of 3.40 m. In the months following the earthquake, afterslip was documented along most of the fault, also showing spatial variations. These observations suggest that the Motagua Fault exhibits not only stick-slip behavior but also aseismic creep. Using Sentinel-1 radar imagery, we derived line-of-sight velocity fields for the region surrounding the fault, which we decomposed into vertical and fault-parallel horizontal components to analyze along-strike slip-rate variations. The unprecedented high-resolution InSAR data reveal a ~40 km-long creeping section along the fault. We discuss the along-strike variations in creep in relation to local geology, as well as the coseismic slip and afterslip distribution associated with the 1976 earthquake.*

INQUA TERPRO Project Cascading Hazards and Mitigation (CHAMP)

paleoseismicity.org

The Saga of Grindavík II: Mapping Concealed Active Graben Faults and Fissures in Iceland Using Electrical Resistivity

De Pascale, G.P. (1)

(1) Faculty of Earth Sciences, University of Iceland, Askja Building, 102, Reykjavik, Iceland

Abstract: *On November 11, 2023, an intense seismic swarm was coincident with fault slip along graben faults in and around the Town of Grindavík in Southwest Iceland. An ~5 km wide graben with abundant normal faults slipped in this area with extensive extension that was also manifested by opening of mode I fissures (i.e. pure opening) that caused hundreds of millions of dollars of damage and one fatality. Importantly, many faults were obscured at the surface due to the built environment or due to a till layer. To map these subsurface hazards, electrical resistivity techniques were used. The resistivity technique was excellent as conducts poorly and thus high resistance areas were oftentimes correlated with subsurface faults and fissures that were then validated with trenching. Resistivity surveys worked best in this instance and helped target subsurface faults and fissures that could be addressed for risk mitigation.*

Key words*: Fault Mapping, Active faults, Resistivity, Iceland, Graben*

INTRODUCTION

Structural geology and tectonic investigations and research and document plate-boundary geological deformation. After the unrest that started in October 2023 near Grindavík as noted with abundant seismicity, we undertook field investigations starting on Nov 10th to document and understand the nature of faults and fissures and associated deformation. Early in the field investigations it was clear to the field team that a graben or fault bounded depression was approximately 5 km wide at the surface formed (Figure 1), along normal faults, both in and around the town of Grindavík. All of this was summarized in the publication by De Pascale et al. (2024). One key finding was the this was dominantly a tectonic event with seismicity coincident with faulting (De Pascale et al., 2024).

METHODS

Electrical resistivity is a geophysical technique to take ground measurements and is related to Ohm's Law where: voltage = current times resistance (or V=IR). For ground investigations, we can calculate resistance as R=V/I, and the resistivity is related to geological parameters like mineralization and fluid contents, temperature, porosity, and presence of voids. By measuring an electric field at a known current, it is possible to calculate the resistance of the total volume of material between the transmitter and receiver to the depth of detection limit of the transmitter signal (Loke and Barker, 1996). Because voids, like lava tubes or fissures or faults are often free of materials, that is are open (i.e. air instead of rock or sediments), they have correspondingly high resistivity values which makes resistivity the gold standard technique for void detection. Thus, using resistivity surveys across a site, stratigraphy, lithology, and voids can be detected. This technique, which is also common for geothermal exploration and characterisation of hydrothermal zones was used successfully for both subsurface cave mapping (e.g. Weissling and White, 2008), as well as for lava tube mapping in the Canary Islands near the Corona Volcano (e.g. Torrese et al., 2021). Capacitive coupled electrical resistivity - measures the electrical properties of rock and soil without cumbersome galvanic electrodes used in traditional resistivity surveys.

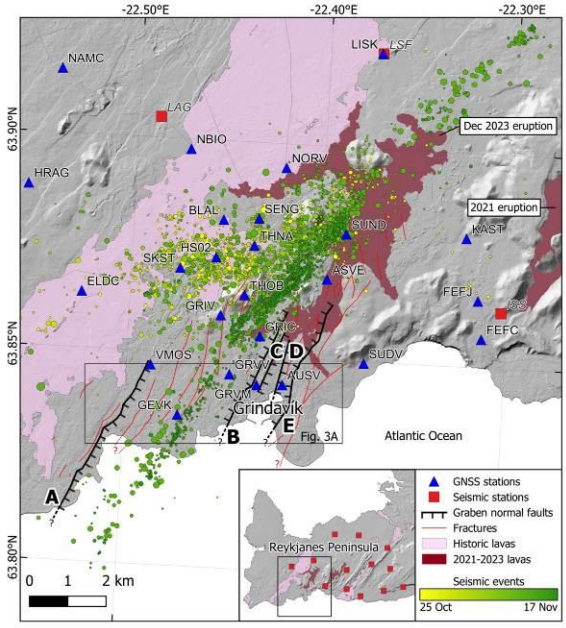

Figure 1: *Map of the field area in Grindavik in Southwest Iceland. Epicenters of earthquakes between 25 October and 17 November 2023 shown in yellow to green with size corresponding to magnitude. Seismic and GPS stations are shown with the former labeled in italic. Note that THOB is the Mt. Thorbjörn station. Sundhnúkur cone row is located along and crossing the SUND station. Lavas produced in the last volcanic period are shown in pink, 2021–2023 lavas in deep red. Main graben faults that slipped in November 2023 A-E are labeled as mapped by De Pascale et al., 2024. Figure modified after the publication by De Pascale et al., 2024.*

A simple coaxial cable array with a transmitter (Tx) and receiver (Rx) sections are pulled along the ground (Figures 2 and 3). Data acquisition is much faster than the DC

resistivity technique and provides accurate stratigraphy/lithology/fracture mapping. For calibration of the system, the resistivity system was used over known cracks, faults, voids, that were documented by De Pascale et al. (2024) to see the response of the system. As expected, the highest resistivity values were encountered (oftentimes with values 1 to 2 orders of magnitude higher than non-fractured areas) at the surface. In Grindavík, an OhmMapper resistivity system was used for the duration of the investigation (Figure 2). Survey points were marked out on the ground with a tape measure and survey paint, and GPS waypoints were taken at each survey location to correlate with the geophysical data. All GPS points were saved as KMZ/KML files for viewing in Google Earth or GIS systems. Note that 0 on the resistivity profiles is the start of line. Thus -10 in any GPS line is 10 m to the west of start points, and thus -20 is 20 m before the start of the survey line. Generally most surveys were taken over known fractures as found through surface mapping, however geophysical anomalies as indicated by ground penetrating radar (GPR) along all of the roads in Grindavík were also investigated by electrical resistivity methods. Surveys were collected to maximum depth of investigation (i.e. where signal was lost) by repeating surveys with varied distances between the transmitter and receivers. In general the closer to the harbour or coastline in Grindavík, the more shallow the maximum depth of resolution of the system which is due to the influence of seawater which is relativity conductive and thus with loss of signal. The electrical resistivity data were data were reduced using the DataMap 2000 software (Geometrics, 2001), and plotted as pseudosections (geometrical view of the measured apparent resistivity data set) while inversion models (i.e. shows true resistivity for each model block, calculated independent of the resistivities of the surrounding model blocks) were completed using the two-dimensional inversion software RES2DINV (Loke and Barke, 1996; Loke, 1999). Data were plotted in a pseudosection, where the depth scale is calculated as a function of the separation between the dipoles.

Figure 2: *Field photograph showing the resistivity system survey crossing surface fractures in central Grindavik in 2024.*

Results and Interpretations

During surveys, surface cracks or faults were noted in the field (as previously mapping using field mapping and drone mapping; e.g. De Pascale et al., 2024) including what GPS point the survey encountered these cracks for correlation of the survey observations along with the subsurface resistivity observations. All of the results of the resistivity surveys are found in Appendix A, B, and C. However for demonstrative purposes, a profile of Route 427 (Austervegur), was undertaken at the start of the geophysical investigation to see the subsurface characteristics of the faults and fissures mapped by De Pascale et al. (2024) in the eastern graben along the eastern side of Grindavík. This profile is fairly long (>300 m long), and had a subsurface penetration of ~5 m depth (Figures 3 and 4) and show a clear correlation between the surface fractures and faults and fissures mapped at the surface (Figure 5).

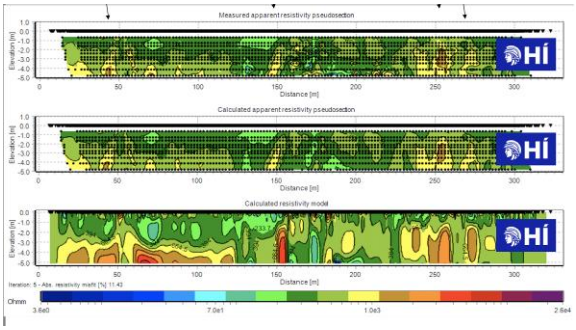

Figure 3: *Resistivity pseudosections, with the measured resistivity at the top, and model outputs of the apparent resistivity in the middle and the calculated resistivity model at the bottom for route 427 in Grindavík (Austervegur) from near the retirement home towards the eastern entrance of town. Resistivity values are in Ohm-m. Please note that there are orders of magnitude difference in values as shown with colours. Yellow and red and orange are much more resistant. These are coincident with the main fault zones D and E shown on the map in Figure 1 (2024).*

Resistivity values ranged from less than 10 Ohm-m, to over $1X10^5$ in the surveys were undertook and there were clear correlations between high resistivity values and known surface faulting and fissures as well as in many areas that the GPR system showed anomalies. Meetings were undertaken to compare resistivity values with GPR values and later with magnetic data and during these meetings, areas that had correspondingly high resistance values were compared with these other methods, although the method with the least uncertainty was shown to be the resistivity system for detection of faults and fissures in the subsurface. Field validation was also critical and was undertaken using fault trenching as well as drilling in key areas where critical infrastructure such as underground electrical lines or water lines were crossing the faults and fissures (e.g. Figure 3)

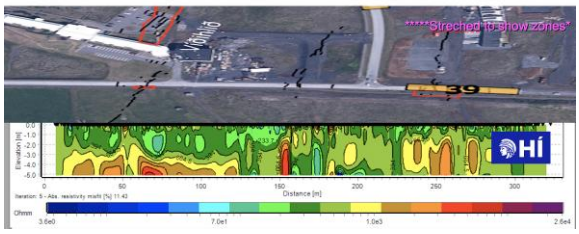

Figure 4: *Comparison of the resistivity model (from Figure 3) with the map showing faults at the surface to show the 1:1 correlation between surface cracking and high resistance zones. Please note that there are also bedrock highs in areas in the models that also show up as relatively higher zones of resistance. Please note that the map at the top is stretched to scale the model and map at the same scale. This shows the utility of electrical resistivity values. Please note that the zone at station 155 m was excavated and there was a open bedrock fissure there that was field validated coincident with the red coloured – high resistivity area below ~2 m depth. A photograph of this can be seen in Figure 5.*

Importantly, at the key site shown in Figure 4, there were open fractures (Figure 5), that opened in November 2023 in the subsurface that had a potential to collapse during future fault motions, earthquakes, or due to settlement that were then excavated for mitigation. In this case the fissures were opened and then infilled with rubble to reduce the likelihood of collapse and thus risk to the buried critical infrastructure there.

Figure 5: *Field photograph by G. De Pascale showing a subsurface horizontally open fissure in bedrock as shown in the locations near station 150 on the horizontal axis in Figure 9 and 10. Please note that during the fixing of the road here, it provided an important opportunity for subsurface insight here as well as validation of the nature of the high resistivity values which in this instance are due to an open fissure at about 2 m below road level. Please note that the photo was taken at road level and the excavator was digging down to fix infrastructure in the subsurface and mitigate the fractures here (aka fill them in so that they did not collapse during future earthquakes). Please note that the zone at station 155 m was excavated and there was open bedrock fissure there that was field validated coincident with the red coloured – high resistivity area below ~2 m depth.*

In conclusion, faults and fissures that opened and slip during the 2023 unrest in Grindavík Iceland caused considerable damage to the built environment. Subsurface, yet open voids from a few centimetres to over a meter wide were oftentimes concealed but a thin, centimetre to metre thick layer of till, marine clay, or construction materials. In order to mitigate hazards of these open voids, electrical resistivity surveys were undertaken that help identify problematic areas that could then be targeted for mitigation. Ultimately, along extensional plate boundaries like where mid-oceanic ridges come onshore like in Iceland or in East Africa, future extensional events will also likely have concealed faults and fissures that can be accurately detected using resistivity methods, even where concealed at the surface.

Acknowledgements: That to the people and Town of Grindavík for access. Thanks for field assistance from E. Mac, E. Owens, D. Forester. This research was supported by Iceland Civil Defence. Thanks for additional field and subsurface to colleagues from Verkis and ISOR. This work was also supported by a grant from Reykjavik Energy (VOR).

REFERENCES

De Pascale, G. P., Fischer, T. J., Moreland, W. M., Geirsson, H., Hrubcová, P., Drouin, V., et al. (2024). On the move: 2023 observations on real time graben formation, Grindavík, Iceland. Geophysical Research Letters, 51, e2024GL110150. https://doi.org/10.1029/2024GL110150

Geometrics, Inc. (2001) Data Map User Guide 29006-01, Rev 3.0, Manual 2900701, 55 pp., San Jose, Calif.

Loke, M. H. (1999), RES2DINV ver. 3.42, Geolectrical Imaging 2D & 3D, User Manual, Richmond Hill, Ont., Canada.

Loke, M. H., and R. Barker (1996), Rapid least-squares inversion of apparent resistivity pseudo-sections using a quasi-Newton method, Geophys. Prospect., 44, 131–152.

Torrese, P., Pozzobon, R., Rossi, A., Unnithan, V., Sauro, F., Borrmann, D., Lauterbach, H., and Santagata, T., 2021. Detection, imaging and analysis of lava tubes for planetary analogue studies using electric methods (ERT). Icarus, 357, I114244. https://doi.org/10.1016/j.icarus.2020.114244

Weissling, B. and White, Kemble. 2008. Electrical Resistivity Imaging as a tool for Assessing Endangered Karst Invertebrate Habitat. Fast Times, magazine for Near-Surface Geophysical Sciences, v 13, N. 4. p.31-35.

INQUA TERPRO Project Cascading Hazards and Mitigation (CHAMP)

Active west-vergent Andean orogeny and potential for large earthquakes along the San Ramon Fault in Santiago, central Chile

Easton, Gabriel (1), Juan Carlos Báez (2), Sergio Ruiz (3), José González Alfaro (3), Sofia Rebolledo (1), Sebastián Arriola (2), Sebastián Barra (2), Carolina Valderas (2), Angelo Villalobos (1), Luisa Pinto (1), Sergio Barrientos (2)

(1) Departamento de Geología, Facultad de Ciencias Físicas y Matemáticas, Universidad de Chile. geaston@uchile.cl
(2) Centro Sismológico Nacional, Universidad de Chile
(3) Departamento de Geofísica, Facultad de Ciencias Físicas y Matemáticas, Universidad de Chile

Abstract:
The San Ramón Fault is an active fault system located at the west Andean thrust front in central Chile. The fault is along the Andean piedmont in the eastern border of Santiago, capital city of the country. From seismic network and geodetic monitoring improved during the last decade, we assessed seismic activity and present-day deformation along the fault system. We found two main north-south oriented domains of microseismicity: one located between 10-20 km depth just below the Andes beside Santiago, and another one located ca. 30 km to the east, at depths between 5-15 km, both compatible with major west-vergent thrust geological structures. Results from geodetic measurement from continuous and campaign stations reveal a sharp decrease in west-east velocities in the mountain front area, which we interpret as locking of the San Ramón Fault at shallow depths in the crust, suggesting potential for major earthquakes along this fault system.

***Key words**: West Andean front, active orogeny, San Ramón Fault, Santiago, Chile.*

INQUA TERPRO Project Cascading Hazards and Mitigation (CHAMP)

A long-term slip rate and total offset estimate for the Motagua Fault, Guatemala

Ebell, Hannes (1), Christoph Grützner (1), Tina Niemi (2), Sumiko Tsukamoto (3), Jeremy Maurer (4)

(1) Institute of Geosciences, Friedrich-Schiller University Jena, Jena, Germany. christoph.gruetzner@uni-jena.de
(2) Earth and Environmental Sciences, University of Missouri-Kansas City, Kansas City, MO, USA
(3) LIAG Institute for Applied Geophysics, Hannover, Germany
(4) Geology and Geophysics, Missouri University of Science and Technology, Rolla, MO, USA

Abstract: *The Motagua Fault in Guatemala is part of the plate boundary between the North American and Caribbean plates. The long-term slip rate and the total offset of the fault are poorly constrained so far. We analyzed morphological markers of total offset such as rivers and ridges, using TanDEM-X digital elevation data with 12 m resolution and own airborne LiDAR elevation datasets in some places. Sinistral offsets found in the Motagua Fault Zone range from several hundred meters to over 10 km, with larger displacements being much less frequent. The total offset does not exceed 18–39 km. The data imply that recent activity is mainly concentrated on the strand that ruptured in the 1976 earthquake, while past activity shifted between different strands, creating a wide multi-stranded fault zone. Using OSL dating of offset river terraces at the Rio El Tambor site, we measure a slip rate of ca. 3-5 mm/a for the active strand of the Motagua Fault. This is in line with previous estimates and geodetic rates.*

Acknowledgements: *This project was conducted as part of the Guatemala GeoHazards IRES program that is funded by an NSF Grant OISE-2153715 to Niemi and a DFG project 529303576 "Active tectonics of the Caribbean-North American plate boundary in Guatemala" to Grützner.*

INQUA TERPRO Project Cascading Hazards and Mitigation (CHAMP)

Investigating evidences of Quaternary fault reactivation in Southwest Iberia, Portugal

Figueiredo, P.M. (1), Ressurreição, R. (2), Custódio, S. (1), Tsukamoto, S. (3)

(1) Instituto Dom Luiz, Science Faculty, University of Lisbon, Portugal. pmfigueiredo@fc.ul.pt.
(2) Laboratório Nacional de Energia e Geologia, Cartografia Geológica, Alfragide, Portugal
(3) Leibniz Institute for Applied Geophysics, Geochronology, Hannover, Germany

Abstract:

Southwest Portugal is close to the European-African plate boundary, and to Mw~8 1755 epicenter. It has seismicity and shows Quaternary deformation through NNE-SSW faults and uplifted marine terraces contrasting with neighboring areas. Recent geophysical and geodetic data highlighted a positive gravimetric anomaly consistent with the uplifted area, limited inland by a misunderstood 90 km NW-SE structure, that only matches a known fault for ~50 km. The remaining -40 km is considered to be an inherent structure, not active, despite a noticeable and prominent scarp in the landscape. We present a preliminary analysis based on 50 cm high-resolution lidar and Plio-Quaternary data, indicating evidence of subtle geomorphic deformation in a wide area, to be investigated combining geology, geophysics and geochronology methods.

This work is supported by Fundação para a Ciência e Tecnologia, FCT, I.P./MCTES through national funds (PIDDAC): UID/50019/2023, LA/P/0068/2020, UID/50019/2025 https://doi.org/10.54499/LA/P/0068/2020 and https://doi.org/10.54499/UID/PRR/50019/2025 and by the European Union (SEISMO-REACT, GA101211167).

***Keywords**: Quaternary activity, seismogenic sources, low strain deformation, cryptic structures, SW Iberia*

INQUA TERPRO Project Cascading Hazards and Mitigation (CHAMP)

paleoseismicity.org

Pleistocene-Holocene fault activity and offset valleys along the southern Mariánské Lázně Fault, Czechia, central Europe

Flašar, Jan (1), Tábořík, Petr (1), Štěpančíková, Petra (1), Yaneva, Marlena (2), Donkova, Yordanka (2), Kalchev, Radoslav (2)

(1) Institute of Rock Structure and Mechanics, Czech Academy of Sciences, V Holešovičkách 94/41, Praha 8, Czechia, email: flasar@irsm.cas.cz
(2) Geological institute, Bulgarian Academy of Sciences, Bonchev str. 24, Sofia, Bulgaria

Abstract: *The Mariánské Lázně Fault (MLF) in western Czechia is probably the most active fault zone within the intraplate Bohemian Massif. While its northern segment is known for Holocene surface ruptures, the timing and nature of movements along the southern MLF remain uncertain. The site near Nová Hospoda, where distinct offset valleys are exceptionally well preserved despite the humid temperate climate and intense periglacial solifluction during the Pleistocene, provides rare evidence of very young deformation. Although a nearby paleoseismological trench (made 2023) revealed late Pleistocene and no clear Holocene displacement, the valley morphology strongly suggests post-Last Glacial Maximum movement. Electrical resistivity tomography and ground-penetrating radar surveys were conducted to identify sedimentary infill suitable for subsequent dating and to characterize the subsurface structure. Determining the precise age and style of recent fault activity at Nová Hospoda is crucial for understanding MLF segmentation, late Quaternary kinematics, and intraplate seismic hazard in the Bohemian Massif.*

Key words*: Mariánské Lázně Fault, offset valleys, Holocene fault activity, geophysical methods.*

INTRODUCTION

The Mariánské Lázně Fault (MLF) is one of the most prominent tectonic structures (Fig. 1) of the Bohemian Massif (Czechia, Central Europe), forming the eastern boundary of the Cheb–Domažlice Graben (Špičáková et al., 2000, Špaček et al., 2022). Although intraplate, the MLF shows significant Cenozoic activity. Geomorphological and structural indicators of recent deformation can be followed along its entire length (Flašar & Štěpančíková, 2022); however, the most active parts are separated by distances exceeding 50 km. The northern part has produced Holocene surface-rupturing earthquakes (Štěpančíková et al., 2019), whereas the southern part is characterized by segment with clearly visible offset valleys and a well-defined scarp (Fig. 2).

Recent paleoseismological trenches at Kopanina and Horka (northern MLF) and at Nová Hospoda (southern MLF) demonstrate that seismic behaviour can vary significantly even between adjacent segments (Štěpančíková et al., 2025). The northern MLF borders the Cheb Basin, a region typified by recurrent earthquake swarms, mantle-derived CO_2 degassing, and Quaternary volcanism (Fischer et al., 2014; Štěpančíková et al., 2025), all indicating ongoing deformation and crustal fluid activity. In contrast, although the southern MLF experienced the historical 1902 Přimda earthquake (Fischer et al., 2014) and displays strong geomorphic evidence of activity, the 2023 Nová Hospoda trench revealed only late Pleistocene deformation.

This inconsistency may reflect segmentation that halts rupture propagation, differences in fault geometry and orientation, variations in crustal stress accumulation, or erosion/burial of Holocene surface evidence. Understanding segmentation and behavioural variability along the MLF is essential for reconstructing Pleistocene–Holocene landscape evolution and improving seismic hazard assessment.

The present study reports first results from new geophysical surveys conducted as a preparatory step for further paleoseismological trenching. The main goal was to characterize sedimentary infill in offset valleys across the

Figure 1: *Digital elevation model showing the striking morphology along the Mariánské Lázně fault - pointed by red arrows.*

southern MLF and identify sites suitable for detailed paleoseismic investigation, complementing previous work at the nearby Nová Hospoda trench.

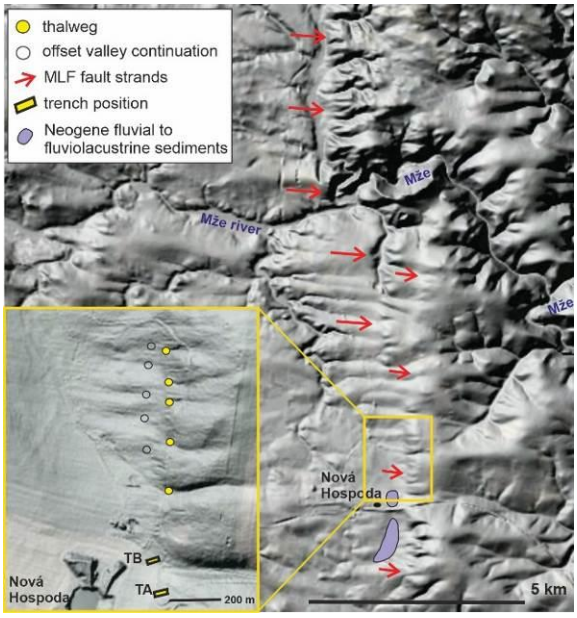

Figure 2: *Digital elevation model with MLF traces, trench site and offset valleys.*

METHODS AND RESULTS

Eight geophysical profiles (100–250 m long) were acquired along and across the proposed fault trace in order to get both cross sections and longitudinal profiles of the offset valleys, which are made along the particular part of the fault. Two complementary methods were used: electrical resistivity tomography (ERT) and ground-penetrating radar (GPR), both were used in the same profiles (Fischer et al., 2012).

The surveys confirm the presence of sedimentary infill in several of the investigated valleys. ERT profiles reveal distinct resistivity contrasts on the eastern (upslope) side of the fault consistent with thicker sediment accumulations (2-4 m), and GPR data support this interpretation by showing layered to chaotic reflections typical of fluvial to colluvial deposits. Sedimentary bodies were also identified on the western (downslope) side of the fault, although thinner (1-2m), suggesting more complex sediment routing and valley development than inferred from surface morphology alone (Fig. 3).

Although the continuity and origin of individual sediment units cannot be resolved solely from geophysical data, the surveys successfully identify multiple localities where sediment thickness and configuration appear suitable for targeted trenching. The profiles also indicate that the fault trace may be more complex or segmented at a local scale, providing valuable structural constraints for follow-up paleoseismological research.

DISCUSSION

It is probable—based mainly on the initial terrain-morphology analyses—that two generations of offset valleys are present: two larger main valleys offset by approximately 40 meters, and around twenty smaller erosion gullies offset by 3–5 meters. This pattern likely reflects two phases of landscape evolution or, alternatively, two periods of movement along the fault. The main valleys may be of late Pleistocene age, whereas the smaller gullies could be Holocene in age. The preliminary results suggest that the thicker infill of larger valleys could be offset, but the situation is not clear regarding the smaller gullies.

Despite clear geomorphic indications of valley offset and active tectonics, the initial geophysical data do not yet constrain the scale of displacement. A key limitation is that ERT and GPR cannot reliably differentiate among fluvial, deluvio-fluvial, and slope-derived sediments, which often share similar physical properties (Fischer et al., 2012). This restricts the ability to quantify offsets or interpret the stratigraphy in terms of earthquake history.

Nevertheless, the reconnaissance survey fulfils its primary objective: identifying locations with sufficient sediment accumulation and favourable geometry for paleoseismological trenching. Paleoseismology remains essential for determining the age, style, and recurrence of past surface-rupturing earthquakes along the MLF (Štěpančíková et al., 2019).

The results indicate that the fault zone is structurally complex and may be segmented at a finer scale than suggested by regional geomorphology. Such segmentation could influence rupture propagation (Zielke & Klinger, 2025) and may explain why late-Pleistocene activity is documented at the Nová Hospoda site (approximately 500 m to the south), whereas Holocene ruptures have not yet been detected.

The next research phase will focus on detailed trenching at newly identified sites between the offset valleys north of Nová Hospoda. These investigations aim to refine the segmentation model of the southern MLF, determine whether Holocene surface-rupturing earthquakes occurred but left limited preservation, and evaluate the possibility of past multi-segment ruptures. Ultimately, integrating geomorphology, geophysics, and paleoseismology will improve understanding of the seismotectonic behaviour of the region and support more robust seismic-hazard assessments in western Czechia.

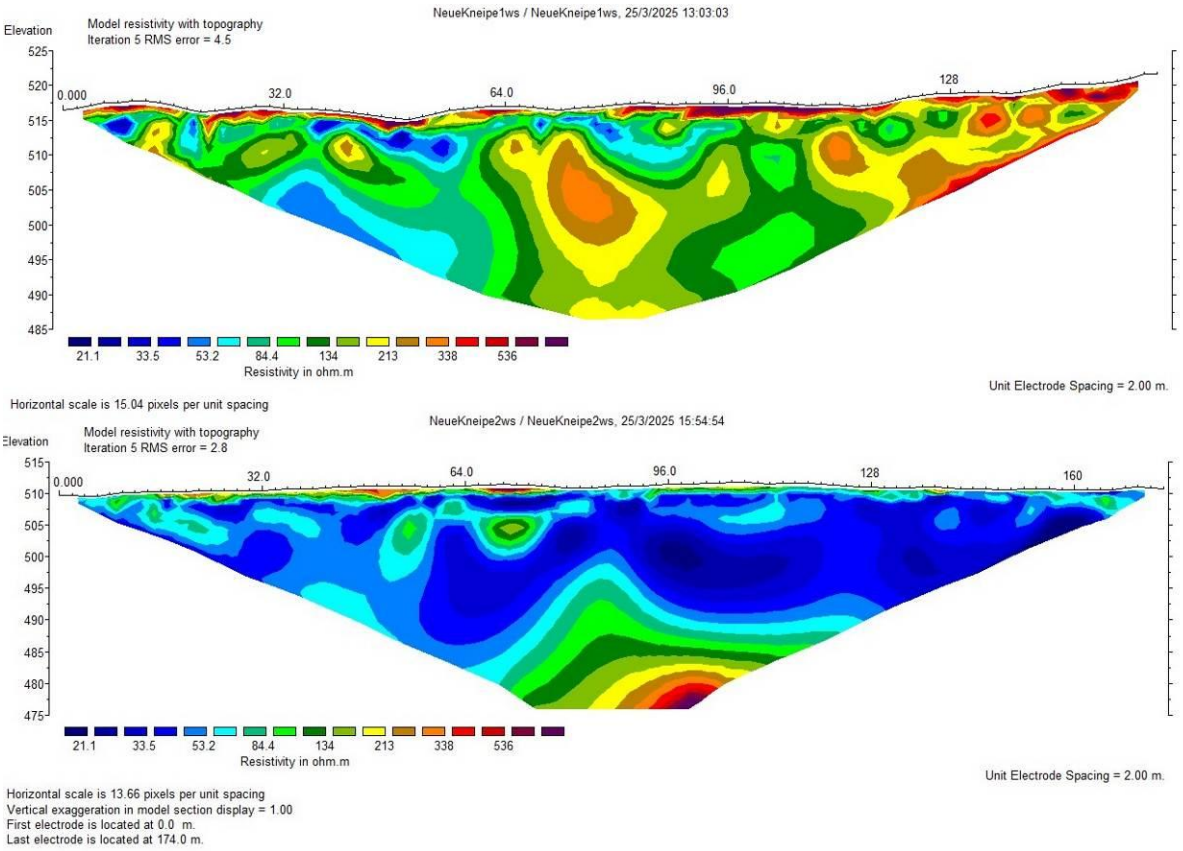

Figure 3: *Comparison between two ERT profiles along the MLF crosscutting the valleys: eastern side of the fault (top), western side of the fault (bottom). Note that the orientation of the profies is south-north.*

Acknowledgements: The research was supported by the Czech Academy of Sciences/Bulgarian Academy of Sciences: Mobility Plus Project no. BAS-25-10. and by the Johannes Amos Comenius Programme (P JAC), project No.CZ.02.01.01/00/22_008/0004605, Natural and anthropogenic georisks.

REFERENCES

Fischer, T., 2012. Imaging the Mariánské Lázně Fault (Czech Republic) by 3-D ground-penetrating radar and electric resistivity measurement. *Studia Geophysica et Geodaetica*, 56(2), pp. 285–299. https://doi.org/10.1007/s11200-012-0825-z

Fischer, T., Horalek, J., Hrubcová, P., Vavryčuk, V., Bräuer, K., & Kämpf, H., 2014. Intra-continental earthquake swarms in West-Bohemia and Vogtland: A review. *Tectonophysics*, 611, pp. 1–27. https://doi.org/10.1016/j.tecto.2013.11.001

Flašar, J. and Štěpančíková, P., 2022. Geomorphological evidence of tectonic activity of the Mariánské Lázně Fault (Czech Republic) and its influence on stream network evolution. *Acta Geodynamica et Geomaterialia*, 19(1), pp. 5–25. https://doi.org/10.13168/AGG.2021.0039

Špaček, P., Štěpančíková, P. and Prachař, I., 2022. Faults of the Bohemian Massif – Source of Analytical Data on Main Faults and Faulted Areas with Seismogenic Potential. https://doi.org/10.48790/mwf4-sh44

Špičáková, L., Uličný, D., & Koudelková, G., 2000. Tectonosedimentary evolution of the Cheb Basin (NW Bohemia, Czech Republic) between Late Oligocene and Pliocene: A preliminary note. *Studia Geophysica et Geodaetica*, 44(4), pp. 556–580. https://doi.org/10.1023/A:1021819802569

Štěpančíková, P., Fischer, T., & Horalek, J., 2019. Active tectonics in the Cheb Basin: Youngest documented Holocene surface faulting in Central Europe. *Tectonophysics*, 760, pp. 1–17. https://doi.org/10.1016/j.tecto.2018.11.016

Štěpančíková, P., Stemberk, J., Tábořík, P., Fischer, T., Findžová, L., & Valenta, J., 2025. Discovering the Čirá–Kopanina Fault: Bridging the Gap between Surface Evidence and Seismic Activity. *Lithosphere*, 2024. https://doi.org/10.2113/2024/lithosphere_2024_192

Zielke, O. and Klinger, Y., 2025. Past earthquakes in continental settings—A geomorphologic perspective. In: A. Elliott and C. Grützner, eds. *Understanding Past Earthquakes*. Cham: Springer, pp. 99–141. https://doi.org/10.1007/978-3-031-73580-6_5

INQUA TERPRO Project Cascading Hazards and Mitigation (CHAMP)

Evidence of Upper Pleistocene-Holocene tectonic activity along the Longhere-Fadalto-Cadola line (eastern Southern Alps, NE Italy)

Franceschet, Angela (1,2), Poli Maria Eliana (2), Patricelli Giulia (2), Paiero Giovanni (2), Marchesini Andrea (2), Abu Zeid Nasser (3)

(1) University of Trieste, Department of Life Science. angela.franceschet@phd.units.it.
(2) University of Udine, Department of Agricultural, Food, Environmental and Animal Sciences.
(3) Teamgeofisica.ceg: Centro di Elaborazione dati Geofisici (Ferrara, Italy).

Abstract: *We made paleoseismological investigations on the eastern part of the Bassano-Valdobbiadene Thrust Auct., i.e. the left lateral Longhere-Fadalto-Cadola transpressive fault. The study area lies at the Pliocene-Quaternary front of the eastern Southern Alps, a S-SE verging active thrust-and-fold belt characterized by moderate to high seismic hazard and risk, where some historical earthquakes registered Mw ≥ 6. The Bassano-Valdobbiadene Thrust Auct. extends with NE-SW trending at the base of the Venetian Prealps, where the Jurassic-Cretaceous carbonate succession overthrusts the Palaeozoic Turbidites and Miocene Molasse. In the framework of the National Seismic Microzonation Project, we carried out a paleoseismological study following preliminary morphotectonic and geophysical investigations, to assess the recent activity and capability of Longhere-Fadalto-Cadola transpressive fault. The paleoseismological trenches, dug on upper Pleistocene-Holocene sediments, reveal clear evidences of recent tectonic activity, possibly related to the 1873 Alpago earthquake (Imax X MCS, Mw 6.3).*

Key words*: Paleoseismology, transpressive fault system, seismic hazard, eastern Southern Alps, NE Italy.*

INTRODUCTION

The eastern Southern Alps (ESA) is a S-verging fold-and-thrust belt, evolving from the middle Miocene up to the Present. Their development occurred in the Neogene-Quaternary time interval (Doglioni & Bosellini, 1987; Castellarin et al., 1992; Fantoni et al., 2002), related to the Neoalpine compressional event. The ESA present architecture largely results from the interaction between the Jurassic-Cretaceous continental rifting and the change in plate kinematics occurred at the end of the early Cretaceous. During the Mesozoic, the former Triassic-Jurassic platform was split into NNE-SSW-trending structural blocks, bounded by normal faults (Bosellini, 1973). When extension ended, a convergence between Adria-Africa and Europe lithosphere plates started. This compressional regime controls the evolution of the Alps up to their present setting, and the Mesozoic normal faults were frequently reactivated and inverted during the Neogene contractional events (Castellarin & Cantelli, 2000; Doglioni, 1992; Galadini et al., 2005). The major deformation phases in the external Venetian Prealps occurred during the Messinian-Pliocene ("Adriatic phase" on Castellarin & Cantelli, 2000) under NW-SE-oriented maximum horizontal stress. This contractional phase activated major thrust system, such as the Bassano-Valdobbiadene, Polcenigo-Montereale, Cansiglio and Montello-Conegliano thrust-systems (Castellarin & Cantelli, 2000). This tectonic phase is still active, and during Pliocene and Quaternary it caused the propagation of the external front toward the piedmont venetian plain that represents its foreland (Galadini et al., 2005; Caputo et al., 2010; Fig. 1).

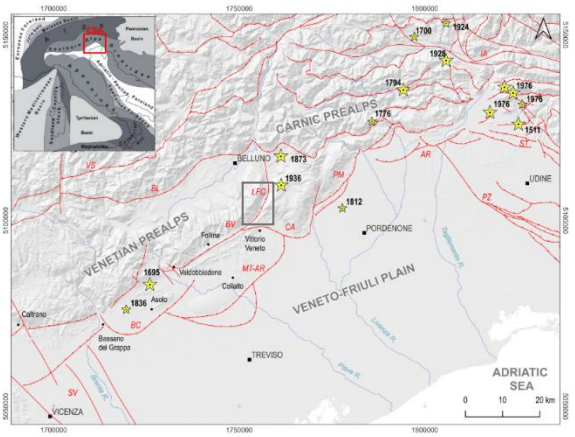

Figure 1: *Structural sketch map of the eastern Southern Alps (SR: EPSG 6708). Yellow stars indicate the historical and instrumental M ≥ 5.5 earthquakes that hit ESA during the last millennium (Rovida et al., 2022). Legend: BC: Bassano-Cornuda Th.; BL: Belluno Th; BV: Bassano-Valdobbiadene Thrust-system; CA: Cansiglio Th.; LCF: Longhere-Fadalto Cadola line; MT-AR: Montello-Arcade Th.; PM: Polcenigo-Montereale Th. The black box notes the study area of Fig. 2.*

Between Bassano del Grappa and Vittorio Veneto localities, most of the late Miocene to Pleistocene deformation at the ESA front is accommodated by the Bassano-Valdobbiadene (BV) and Montello thrust-systems (Castellarin & Cantelli, 2000). The BV Th. tectonic activity continued up to the Holocene and the strain field obtained from geodetic data (horizontal GPS and terrestrial vertical levelling data) indicated that the BV Th. is the structure with the highest seismogenic potential in the Venetian Prealps (Barba et al., 2013). In particular, within the study area, the left-lateral closure of the Bassano-Valdobbiadene thrust (i.e. the Longhere-Fadalto-Cadola line), overthrusts the Jurassic-Cretaceous calcareous units on the Palaeocene turbiditic sequences and Miocene Molasse (Antonelli et al., 1990) along the inherited western border

between the Friuli Carbonatic Platform, in the east, and Belluno basin, in the west (Fig. 2).

From the seismological point of view, the area experienced several M ≥ 5.5 earthquakes over the last millennium (Rovida et al., 2022; Fig. 1). In particular, the Alpago-Vittorio Veneto-Cansiglio Mt. area was affected by two strong events: the 29th June 1873 (I_{max} X MCS e M_w 6.3) Alpago earthquake and the 18th October 1936 (I_{max} VIII MCS e M_w 6.1) Cansiglio earthquake. While the 1936 event is attributed to the Cansiglio source (Sirovich & Pettenati, 2004; Galadini et al., 2005; Burrato et al., 2008), Galadini et al. (2005) associated the 1873 event of Alpago to the Polcenigo-Montereale seismogenic source, but it cannot be ruled out that the seismogenic source of this seismic event could be associated to the Longhere-Fadalto-Cadola transpressive fault.

Goals and Methods

In the framework of the Vittorio Veneto Seismic Microzonation Project a series of seismotectonic investigations in the Lapisina valley were carried out along the possible surficial expression of the Longhere-Fadalto-Cadola fault trace, following the Geological map of Italy, sheet 063 Belluno (Costa et al., 1996; Fig. 2).

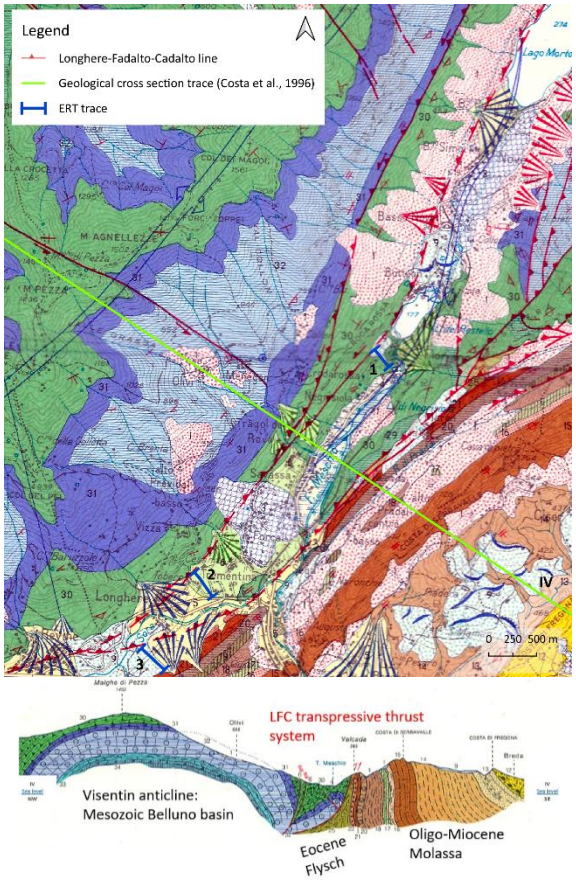

Figure 2: *Geological map and geological cross section (n. IV, green line) of the Lapisina valley (from 063 "Belluno" sheet of the Carta Geologica d'Italia at the 1:50000 scale). (Costa et al., 1996). Blue lines are Electrical Resistivity Tomography (ERT) investigations and illustrate the trench sites.*

Our research investigated the recent activity of the Longhere-Fadalto-Cadola line and its possible relationship with the 1873 Alpago earthquake (Imax = X MCS, Mw = 6.3).

We adopted a multidisciplinary approach combining morphotectonic analysis, geophysical survey and paleoseismological study. Using 1-m resolution LiDAR-derived Digital Elevation Model (DEM), provided by the Provincia of Treviso, we identified some morphological anomalies along the Longhere-Fadalto-Cadola line, potentially linked to its recent tectonic activity (i.e. offset of geomorphic markers, slope breaks, tilted surfaces, drainage anomalies, land-surfaces suspended over the present valley bottom. Subsequently, Electrical Resistivity Tomography (ERT) surveys were achieved to image the shallow subsurface and to better identify the near-surficial fault traces (Fig. 3 and Fig. 5).

Based on morphological and geophysics results, we selected some trench sites across the possible surface trace of the LFC line. Paleoseismological trench walls were cleaned, mapped at 1:10 scale thanks to a 1 x 1 m string grid, and documented with orthomosaics and 2D models. Radiocarbon samples collected from the trench units were dated at Beta Analytic to constrain the age of the deposits.

Paleoseismological trenches

Vittorio Veneto 1 - Pian della Torre locality

The first trench was dug on the "Pian della Torre" terrace, located ≈40 m above the present Lapisina Valley, on the SE slope of the Visentin Mt. (Fig. 2). From the geological point of view the eastern slope of the Visentin Mt. corresponds to the eastern limb of the carbonatic anticline (Costa et al., 1996; Fig. 2). Moreover, the geomorphological map (Pellegrini, 2000) indicate that the terrace consists of fluvioglacial deposits related to the late stages of Piave Glacier retreat after the Last Glacial Maximum (LGM). At the base of the relief, a wide detrital talus is present. ERT data revealed a lateral resistivity contrast in Late Glacial sediments (Fig. 3). We dug a 22 m-long and 2.5 m-depth paleoseismological trench across this anomaly.

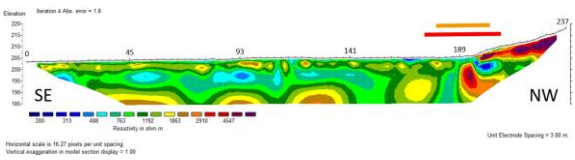

Figure 3: *Electrical Resistivity Tomography (ERT1) investigation of "Pian della Torre", Vittorio Veneto. The red line indicates the main resistivity anomaly while the orange one notes the trench trace.*

The trench exposed kame deposits (13-16 ka BP), overlaid by anthropogenic fills. Clast lithology reflects the Fadalto landslide source area, whose first activation occurred between the Late Glacial and the final glacier retreat, around 16 ka BP (Pellegrini & Surian, 1996; Pellegrini et al., 2006). The composition of the clasts without dolomites and other Triassic lithology typical of the upper Piave catchment, confirms a local sediment provenance. Therefore, we can suppose that the age of the "Pian della Torre" deposits is subsequent the Fadalto landslide. Deposits show a sub-horizontal setting typical of alluvial

sedimentation. Conversely, the NW sector of the trench shows tilted gravels, dipping SE at 50-60°. Moreover, a middle-high angle SE-verging reverse fault (300/55) affects units B and C with a vertical throw of about 10-15 cm (Fig. 4), indicating post-LGM surface deformation.

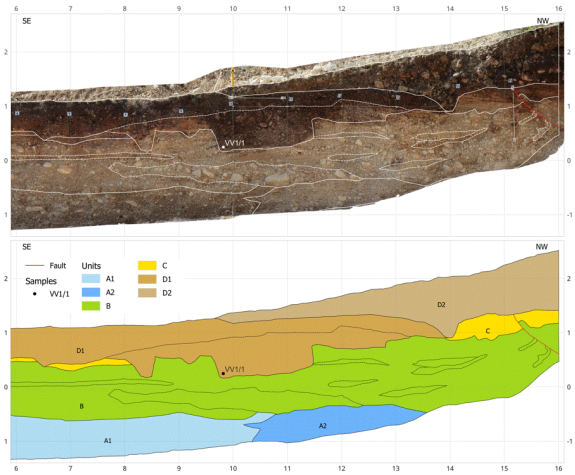

Figure 4: *Paleoseismological log of Trench of Pian della Torre Street (Vittorio Veneto). In the NW sector a SE-verging thrust-fault displaces the kame deposits of Upper Pleistocene age.*

Vittorio Veneto 2 - Cesana Street

ERT investigations acquired across a pronounced morphological scarp near the locality of Cesana revealed significant subsurface resistivity contrasts (Fig. 5). Geological and geomorphological maps (Costa et al., 1996; Pellegrini, 2000) attribute this scarp to fluvial erosion, affecting LGM glacial and fluvio-glacial deposits. However, since this morphological scarp coincides with the Longhere-Fadalto-Cadola line trace as mapped in the CARG-063 Belluno sheet, we verified whether the scarp could also be related to the recent tectonic activity of the LFC line. Here we dug a paleoseismological trench, 12 m-long.

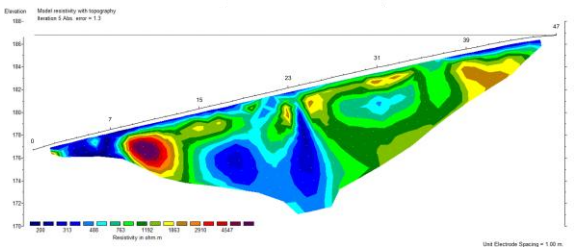

Figure 5: *Electrical Resistivity Tomography (ERT2) investigations of "Cesana Street", Vittorio Veneto. The red line notes the main resistivity anomaly while the orange one notes the trench trace.*

The about 2,5 m-high trench wall exposed alluvial and fluvioglacial deposits, overlaid by agricultural soil, that locally contains anthropogenic fills, with some artefacts. No radiocarbon datable samples were found. However, post-LGM fan deposits are cut and displaced by a high-angle reverse fault that propagates up to the base of the agricultural soil, whose involvement cannot be excluded. The vertical throw observed is at least 0.21 m, testifying post-LGM tectonic activity of the LFC line.

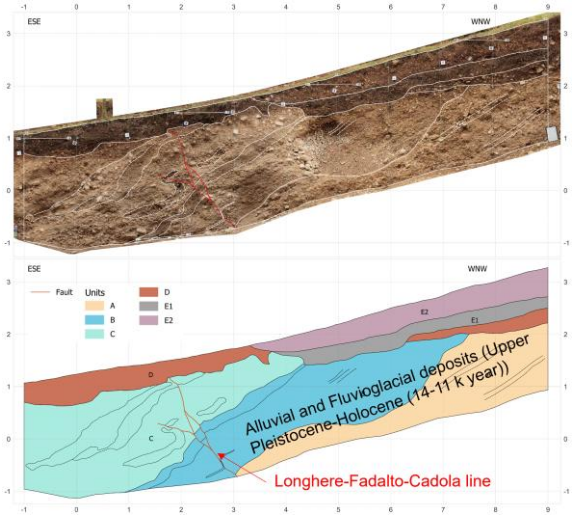

Figure 6: *Paleoseismological Trench of Cesana Street (Vittorio Veneto). A high-angle reverse fault cut and displace Upper Pleistocene-Holocene fan deposits, propagating up to the base of the agricultural soil, whose involvement cannot be excluded.*

Vittorio Veneto 3 - Longhere locality

Near Longhere locality, a third trench exposed very interesting evidence of both seismically induced liquefaction and fault-related deformation. In the northern sector, Late Glacial sands and gravels, belonging to fluvioglacial units A and B (16-13 ka cal BP), quickly change in bedding attitude: from S-vergent lower angle dip to high angle (340/85) close to the northern scarp (Fig. 7a).
Southernmost, sands and gravels rich in matrix (unit C) registered strong paleoliquefaction events. They are overlaid by a colluvial deposit (unit D) radiocarbon dated between 3103-2923 cal BP and 2423-2341 cal BP (Fig. 7b).

Figure 7: *(a) Evidence of fault-related deformation: sands and gravels of the fluvioglacial units A and B with high angle (340/85) close to the northern scarp; (b) Evidence of seismic shaking: sand and gravels liquefactions (unit C) on the south part of the excavated wall.*

DISCUSSION AND CONCLUSION

Results from presented paleoseismological trenches testify the activity of the Longhere-Fadalto-Cadola line during the post-LGM period. Late Glacial deposits are deformed and displaced even if we cannot rule out that also the ploughed soil could be affected by deformation (see for example Vittorio Veneto 2, Cesana trench). In this context, the absence of historical deposits precludes the possibility to associate observed deformation with a historical event.

Nevertheless, according to the Italian Technical Commission for Seismic Microzonation (2015) and the ITHACA guidelines (ISPRA, 2022), a fault showing evidence of activation within the last 40 ka is classified as active. The Longhere-Fadalto-Cadola line meets this criterion at all investigated sites, with significant implication for the high local seismic hazard.

At present, no historical earthquake is conclusively associated with the LFC line. According to the Italian earthquake catalogues, the most recent earthquake happened in the study area, possible referable to this fault, is the 1873 Alpago's earthquake (Mw 6.3). Although the event is currently attributed to the Polcenigo-Montereale system, our new paleoseismological evidence does not exclude the possibility that the LFC line activated during the 1873 earthquake. Further investigations are required to validate this hypothesis, in order to constrain the seismogenic source of the 1873 Alpago's earthquake.

Overall, the results highlight the relevance of the LFC line as an active structure in the Venetian Prealps and underscore its possible contribution to the high seismic hazard of the area.

Acknowledgements: This work was carried out thanks to the support of the Vittorio Veneto Municipality in the framework of the National Project of Macroseismic Zonation: active and capable faults – FAC

REFERENCES

Antonelli, R., Barbieri, G., Dal Piaz, G. V., Dal Pra, A., De Zanche, V., Grandesso, P., Mietto, P., Sedea, R., & Zanferrari, A., 1990. *Carta Geologica del Veneto alla scala 1:250000.* (S. R. per il territorio Regione veneto & Università degli Studi di Padova, Eds.). Firenze: S.E.L.C.A.

Barba, S., Finocchio, D., Sikdar, E., & Burrato, P., 2013. Modelling the interseismic deformation of a thrust system: Seismogenic potential of the Southern Alps. *Terra Nova*, *25*(3), 221–227. https://doi.org/10.1111/ter.12026

Battista Pellegrini, G., Surian, N., & Albanese, D., 2006. Landslide activity in response to Alpine Deglaciation: the case of the Belluno prealps (Italy). In *Geogr. Fis. Dinam. Quat* (Vol. 29).

Bosellini, A., 1973. Modello geodinamico e paleotettonico delle Alpi Meridionali durante il Giurassico-Cretacico. Sue possibili applicazioni agli Appennini. Accordi B. (Ed.), Moderne vedute sulla geologia dell'Appennino. *Acc. Naz. Lincei*, *183*, 163–205.

Burrato, P., Poli, M. E., Vannoli, P., Zanferrari, A., Basili, R., & Galadini, F., 2008. Sources of Mw 5+ earthquakes in northeastern Italy and western Slovenia: An updated view based on geological and seismological evidence. *Tectonophysics*, *453*(1–4), 157–176. https://doi.org/10.1016/j.tecto.2007.07.009

Caputo, R., Poli, M. E., & Zanferrari, A., 2010. Neogene-Quaternary tectonic stratigraphy of the eastern Southern Alps, NE Italy. *Journal of Structural Geology*, *32*(7), 1009–1027. https://doi.org/10.1016/j.jsg.2010.06.004

Castellarin, A., & Cantelli, L., 2000. Neo-Alpine evolution of the Southern Eastern Alps. *Journal of Geodynamics*, *30*, 251–274.

Castellarin, A., Cantelli, L., Fesce, A. M., Mercier, J. L., Picotti, V., Pini, G. A., Prosser, G., & Selli, L., 1992. Alpine compressional tectonics in the Southern Alps. Relationships with the N-Apennines. *Ann. Tectonicae*, *6*, 62–94.

Castellarin, A., Nicolich, R., Fantoni, R., Cantelli, L., Sella, M., & Selli, L., 2006. Structure of the lithosphere beneath the Eastern Alps (southern sector of the TRANSALP transect). *Tectonophysics*, *414*(1–4), 259–282. https://doi.org/10.1016/J.TECTO.2005.10.013

Commissione tecnica per la microzonazione sismica, 2015. *Linee guida per la gestione del territorio in aree interessate da Faglie Attive e Capaci (FAC), versione 1.0*.

Costa, V., Doglioni, C., Grandesso, P., Masetti, D., Pellegrini, G. B., & Tracanella, E., 1996. Foglio 063 "Belluno" e Note Illustrative. Carta Geologica d'Italia alla scala 1:50000. *Memorie Descrittive Della Carta Geologica d'Italia*, 1–74.

Doglioni, C., 1992. Relationships between Mesozoic extensional tectonics, stratigraphy and Alpine inversion in the Southern Alps. *Eclogae Geol. Helv.*, *85/1*, 105–126.

Doglioni, C., & Bosellini, A., 1987. Eoalpine and mesoalpine tectonics in the Southern Alps. *Geologische Rundschau*, *76/3*, 735–754.

Fantoni, R., Barbieri, C., Catellani, D., Castellarin, A., Di Giulio, A., & Pessina, C., 2002. The record of south-Alpine events in the Venetian foreland and foredeep. *Geol. Palaont. Mitt. Innsbruck*. https://www.researchgate.net/publication/275532356

Galadini, F., Poli, M. E., & Zanferrari, A., 2005. Seismogenic sources potentially responsible for earthquakes with M ≥ 6 in the eastern Southern Alps (Thiene-Udine sector, NE Italy). In *Geophysical Journal International* (Vol. 161, pp. 739–762). https://doi.org/10.1111/j.1365-246X.2005.02571.x

Pellegrini, G. B., 2000. Carta geomorfologica d'Italia alla scala 1:50000: Foglio 063 Belluno e note illustrative. *Servizio Geologico d'Italia. Regione Veneto*, 141.

Pellegrini, G. B., & Surian, N., 1996. Geomorphological study of the Fadalto landslide, Venetian Prealps, Italy. *Geomorphology*, *15*(3–4), 337–350. https://doi.org/10.1016/0169-555X(95)00079-K

Rovida, A., Locati, M., Camassi, R., Lolli, B., Gasperini, P., Antonucci, A., Azzaro, R., Bernardini, F., D'amico, S., Ercolani, E., Rossi, A., Tertulliani, A., & Meletti, C., 2022. *Catalogo Parametrico dei Terremoti Italiani (CPTI15), versione 4.0*. Istituto Nazionale Di Geofisica e Vulcanologia (INGV). https://doi.org/10.13127/cpti/cpti15.4

ISPRA, 2022. ITHACA–ITaly HAzard from CApable faults. Inventario delle Faglie Capaci in Italia. Guida alla consultazione e all'utilizzo. *Servizio Geologico d'Italia*, 33.

Sirovich, L., & Pettenati, F., 2004. Source inversion of intensity patterns of earthquakes: A destructive shock in 1936 in northeast Italy. *Journal of Geophysical Research: Solid Earth*, *109*(10). https://doi.org/10.1029/2003JB002919

INQUA TERPRO Project Cascading Hazards and Mitigation (CHAMP)

Fault Throw Evolution Across Multiple Time Scales in the Aremogna–Cinque Miglia Fault System (Italy)

Francescone, Marco (1), Alberto Pizzi (1), Arthur Delorme (2), and Yann Klinger (2)

(1) Department of Engineering and Geology, University of Chieti-Pescara, Italy, marco.francescone@unich.it
(2) Université Paris Cité, Institut de physique du globe de Paris, CNRS, F-75005 Paris, France

Abstract: *The Aremogna–Cinque Miglia Fault System (ACMFS), in the Central Apennines (Italy), is an exceptionally well-preserved active normal fault system that offers key insights into long-term fault evolution. This study combines geological, geomorphological, and paleoseismological data to quantify displacements over three timescales: long-term (~1-2 Myr), mid-term (post-Last Glacial Maximum, ~18 kyr), and short-term (recent paleoearthquakes). Analyses of topography, geological sections, and fault scarps reveal cumulative throws up to ~1500 m in the Aremogna sector and ~1000 m in the Cinque Miglia sector. Post-LGM offsets reach ~20 m, mainly along Cinque Miglia faults, while trench data show coseismic displacements up to 0.8 m. The similarity between long- and mid-term profiles suggests that the ACMFS has acted as an integrated system through multiple seismic cycles, now approaching complex linkage. Structural inheritance controls segmentation and displacement patterns. These results constrain fault growth and scaling, indicating potential earthquakes up to M6.5, with implications for regional seismic hazard.*

Keywords*: active tectonics; fault displacement; hard-linkage*

INTRODUCTION

Long-term fault scarps form from the cumulative displacement of multiple earthquakes and therefore provide key insights into deformation processes—specifically, where past ruptures ended and how they evolved. Precisely defining the spatial extent of coseismic ruptures is crucial for accurately estimating earthquake magnitudes, conducting seismic hazard analysis, informing engineering design, and ensuring public safety. However, there is a lack of datasets that allow us to determine whether the observed pattern remains consistent over time and, if so, for how long. Our findings contribute to a more comprehensive understanding of how normal fault systems evolve across different time scales and how their structural complexities modulate this evolution.

FAULT SYSTEM BACKGROUND

The Aremogna-Cinque Miglia Fault System (ACMFS) is located along the NW-SE seismogenic belt that accommodates NE-extension within the axial zone of the Central Apennines chain, characterized by widespread historical seismicity. The overall normal fault system bounds intermontane basins: the Aremogna plain at an average elevation of 1450-1500 m a.s.l. to the south, and the Cinque Miglia basin (1250 m a.s.l.) to the north, filled by glacial-fluvioglacial and alluvial-lacustrine deposits, respectively. The southwest-dipping Aremogna Fault (AF) and Cinque Miglia Fault (CMF) in the southeastern Abruzzo region (Central Apennines – Italy) are two fault domains composed of multiple and anastomosing strands of ~6 km and ~8 km length, respectively.. They are connected by a complex relay zone between the two subparallel overlapping faults, giving an overall length of 16 km of ACMFS shows NW-SE to N-S trending scarps displacing Pleistocene-Holocene deposits (Fig. 1).

The presence of low-angle structures in the CMF, such as the 30°-dipping Mount Rotella fault, also suggests possible positive inversion of a Mesozoic structure during orogenesis. In turn, there is evidence that these faults have experienced a negative inversion during the Quaternary. This behaviour is commonly observed in the Central Apennines (Calamita et al., 2011; Falcucci et al., 2018).

PALEOSEISMICITY

The Aremogna-Cinque Miglia Fault System is one of the first active fault systems in the central Apennines for which a seismic potential was inferred by paleoseismological trenching (Frezzotti M. & Giraudi C., 1989; D'Addezio et al. 2001; Brunamonte et al., 2001). Timing of the paleoearthquakes is based on radiocarbon dating and stratigraphic relations. The most recent event is constrained between 800 B.C. and 1030 A.D., possibly closer to the youngest part of the interval; the penultimate between 3735 and 2940 B.C., with the younger part of the interval preferred; the oldest event is constrained between 3540 B.C. and 7000 B.P., possibly between 6500 and 7000 B.P. Considering all the fault sections that slip during large surface faulting events, the authors estimate that the average recurrence intervals range from 2140 to 5080 years, and the vertical slip per event ranges from 0.3 to 1 m. The Holocene vertical slip rate ranges from 0.1 to 0.5 mm/yr.

Although the Catalogue of Strong Italian Earthquakes (Guidoboni et al., 2018; 2019) includes the most significant events that occurred over the past two millennia, none can be directly linked to the ACMFS. However, the possibility that one of these earthquakes occurred during the September 1349 earthquake sequence and was produced by this fault should be considered.

In this context, and because the ACMFS is one of the few fault systems in the Apennines with a clearly defined surface trace, understanding its seismic behavior is critically important.

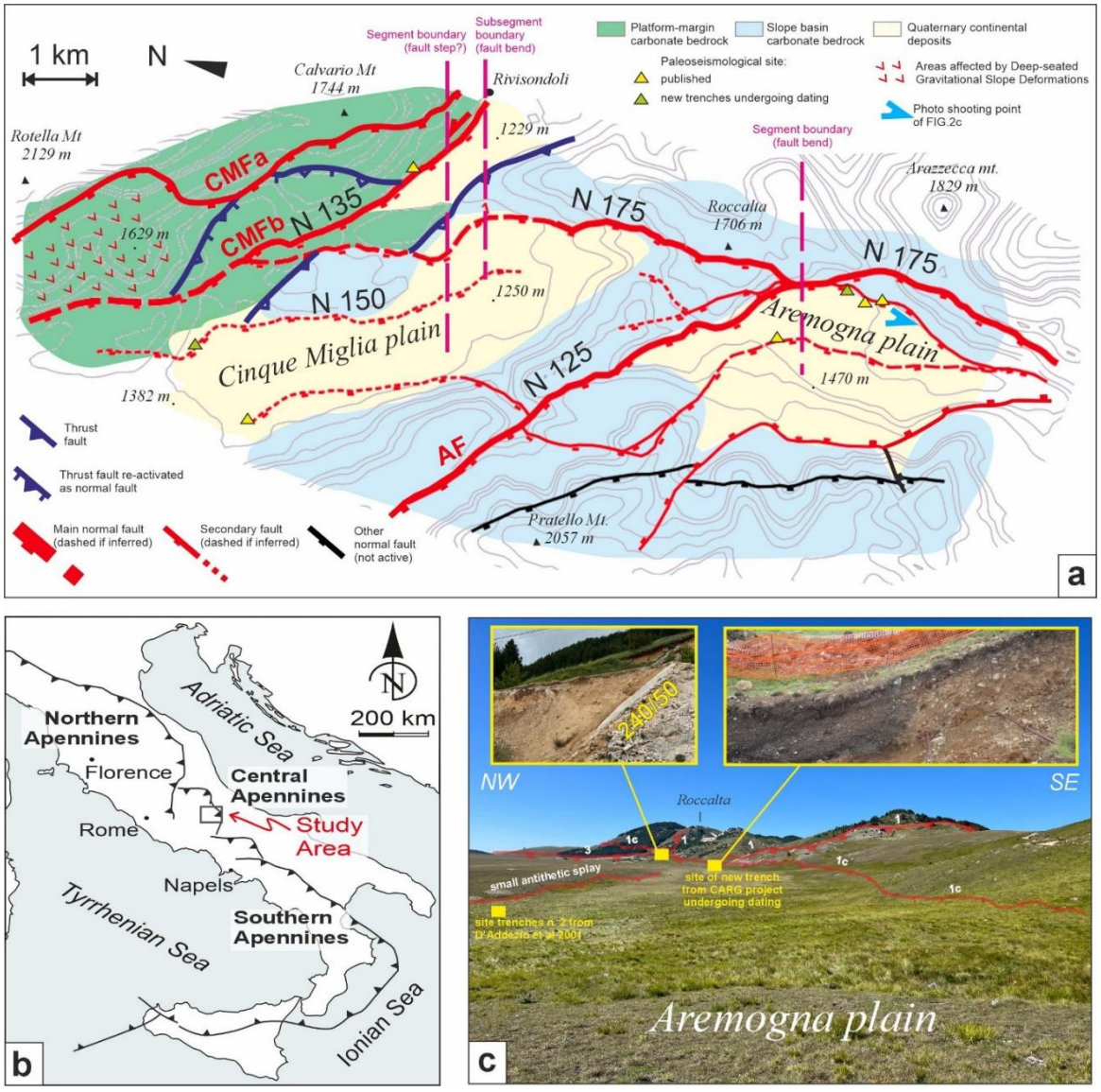

Figure1: *a) Simplified geologic map of the Aremogna-Cinque Miglia Fault System. Strikes of the faults are expressed on each main trace. b) Location box of the study area. c) Photo view from south to north of the main faults of the eastern Aremogna plain. The shooting point is shown on panel (a).*

METHODS

Our approach combines high-resolution topographic analysis, detailed field mapping, and paleoseismological trenching to reconstruct the fault's activity (i.e., throws) across different timescales, enabling comparisons and evaluating the fault system's evolution. To study the ACMFS in detail, we divided the fault system into two main fault domains that display connected fault traces and complex structural features. These domains are the Aremogna fault system (AF - south) and the Cinque Miglia fault system (CMF - north), consisting of both synthetic and antithetic faults, along with nine associated fault traces (ranging from 4 to 11 km long). We identified fault domains showing evidence of activity by integrating fieldwork data, published geological maps, paleoseismology, structural geology, and high-resolution imagery, including Google Earth and a 5-meter-resolution DEM.

RESULTS AND DISCUSSION

We reconstructed the evolution of the ACMFS from its onset in the Early Quaternary to the present using vertical-throw data. For the mid-term, to avoid overestimation, we chose cumulative displacement from the best-constrained topographic profile, which has low offset measurement errors. Finally, we implied the highest throws for each sector, so the obtained values are to be considered the maximum throw for each segment (Fig. 2).

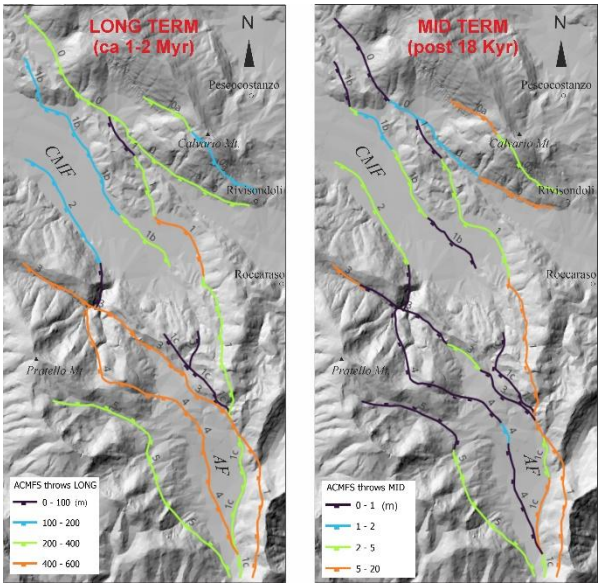

Figure 2: *Maps of the cumulative tectonic throw evolution through time: on the left long-term (ca 1-2 Myr) throw, on the right mid-term (post 18 Kyr) throw. The color scales show the range of vertical displacement at each time frame.*

The results indicate that segments with high geological displacement but without post-LGM activity are mainly located at high elevations (i.e., AF domain). In contrast, faults associated with the highest mid-term throws are generally located at lower elevations (CMF). This observation suggests that the most recently activated segments are located on the footwall of the faults that were formerly active, probably during an earlier stage of the extension, or that the two main domains were overlapped, suggesting there might be a shift of the activity at least for about 18 ky and a hard-linkage evolution.

To assess how mid-term throw rates relate to the long-term evolution of the fault system, we also compared the long-term throw curve for the ACMFS, assuming that the mid-term throw rates remained constant throughout the entire period of fault activity during the Quaternary. The comparison indicates that, under these assumptions, the long-term throw is generally consistent, especially in the overlap zone.

The model of fault evolution presented here shows the extent of the surface expression (~16 km), which allows us to infer an expected magnitude of M6.5 for the event, according to empirical relations in the literature (Wells and Coppersmith, 1994). We also inferred that the contribution of displacement from secondary faults exceeds 33% of the total amount, highlighting rupture processes that occur over wide areas around active faults, which are difficult to detect in the field.

CONCLUSIONS

Comparing fault displacements across different time scales is key to understanding the evolution of a fault system (Puliti et al., 2020). The present-day setting of ACMFS shows geological offsets that transition smoothly from the cumulated lower displacement in the northern part of the system (~1000 m) to the cumulated higher displacement in the south (~1500 m). This slightly asymmetric distribution of displacement suggests that an overlap breaching zone connects the faults.

Inheritance from reverse faults or older normal faults may play a significant role in the formation and growth of extensional structures at depth. It could have important implications for empirical relationships between the geometries and dimensions of surface faulting, providing also indications for those investigating seismic hazards.

REFERENCES

Calamita, F., Satolli, S., Scisciani, V., Esestime, P., & Pace, P. (2011). Contrasting styles of fault reactivation in curved orogenic belts: Examples from the central Apennines (Italy). GSA Bulletin, 123(5–6), 1097–1111. https://doi.org/10.1130/B30276.1.

Falcucci, E., Gori, S., Bignami, C., Pietrantonio, G., Melini, D., Moro, M., et al. (2018). The Campotosto seismic gap in between the 2009 and 2016–2017 seismic sequences of central Italy and the role of inherited lithospheric faults in regional seismotectonic settings. Tectonics, 37, 2425–2445. https://doi.org/10.1029/2017TC004844.

Frezzotti M., & Giraudi C. (1989). Evoluzione geologica tardo-pleistocenica ed olocenica del Piano di Aremogna (Roccaraso-Abruzzo): Implicazioni climatiche e tettoniche. Memorie Della Società Geologica Italiana, 42, 5–19.

D'Addezio, G., Masana, E., & Pantosti, D. (2001). The Holocene paleoseismicity of the Aremogna-Cinque Miglia Fault (Central Italy). In Journal of Seismology (Vol. 5).

Brunamonte, Michetti, Serva, & Vittori. (1991). Evidenze Paleosismologiche nell'Appennino Centrale ed implicazioni neotettoniche. Studi Geologici Camerti.

Guidoboni E., Ferrari G., Mariotti D., Comastri A., Tarabusi G., Sgattoni G., Valensise G. (2018) - CFTI5Med, Catalogo dei Forti Terremoti in Italia (461 a.C.-1997) e nell'area Mediterranea (760 a.C.-1500). Istituto Nazionale di Geofisica e Vulcanologia (INGV). https://doi.org/10.6092/ingv.it-cfti5.

Guidoboni E., Ferrari G., Tarabusi G., Sgattoni G., Comastri A., Mariotti D., Ciuccarelli C., Bianchi M.G., Valensise G. (2019), CFTI5Med, the new release of the catalogue of strong earthquakes in Italy and in the Mediterranean area, Scientific Data 6, Article number: 80 (2019). https://doi.org/10.1038/s41597-019-0091-9.

Puliti, I., Pizzi, A., Benedetti, L., Di Domenica, A., & Fleury, J. (2020). Comparing Slip Distribution of an Active Fault System at Various Timescales: Insights for the Evolution of the Mt. Vettore-Mt. Bove Fault System in Central Apennines. Tectonics, 39(9). https://doi.org/10.1029/2020TC006200.

Wells, D. L., & Coppersmith, K. J. (1994). New empirical relationships among magnitude, rupture length, rupture width, rupture area, and surface displacement. Bulletin of the seismological Society of America, 84(4), 974-1002.

INQUA TERPRO Project Cascading Hazards and Mitigation (CHAMP)

Interplay Between Tectonics and Surface Processes in the Landscape Evolution of the Colca Region, Peru

Gaidzik, Krzysztof (1), Andrzej Tyc (1), Swann Zerathe (2), Julien Carcaillet (2), Marta Woszczycka (1), María Teresa Ramírez-Herrera (3), Carlos Benavente (4), Justyna Ciesielczuk (1), Laurence Audin (2)

(1) Institute of Earth Sciences, University of Silesia in Katowice, Sosnowiec, Poland. krzysztof.gaidzik@us.edu.pl
(2) ISTerre, Université Grenoble Alpes, 1381 rue de la Piscine, 38610 Gieres, France.
(3) Laboratorio de Tsunamis y Paleosismología, Universidad Nacional Autónoma de México, Mexico City, Mexico.
(4) Instituto Geológico Minero y Metalúrgico (INGEMMET), Lima, Peru.

Abstract: *The Colca region represents a unique natural laboratory for studying landscape evolution driven by the interplay of tectonic and volcanic activity, fluvial erosion, mass-wasting processes, lithological variability, karst development, glacial processes, and climatic influences. Here, we adopt a multidisciplinary approach to understand the mutual feedbacks between these interacting processes. Our findings reveal strong coupling among tectonic, volcanic, and surface processes: paleoseismological and archeoseismological evidence indicates potential for large damaging earthquakes; active faults exert a primary control on the hydrothermal system; Coulomb stress-transfer modeling confirms a predominantly tectonic origin for most earthquakes;* ^{10}*Be–derived basin-averaged erosion rates vary among sub-basins, from the upper plateau and broad valley to the deeply incised canyon and piedmont basins; incision rates reveal the combined effects of tectonic uplift and mass wasting, including temporary river damming and ephemeral lake formation; and karst development, including travertine deposition and cave formation, is closely linked to the region's volcanic and tectonic activity.*

Key words*: landscape evolution, incision, erosion, uplift, active tectonics, Andes*

INQUA TERPRO Project Cascading Hazards and Mitigation (CHAMP)

Ground-Based Remote Sensing for Enhanced Paleoseismic Characterization of Trenches and Fault Scarps in Tectonically Complex Areas of Spain and Italy

Gallego-Montoya, John (1), María Ortuño (1), Lucilla Benedetti (2), Moritz Kirsch (3), Magali Riesner (2), David Garcia-Sellés (1), Samuel Thiele (3), Eduardo García-Meléndez (4), Marc Ollé-López (1), Júlia Molins-Vigatà (1)

(1) RISKNAT Group, GEOMODELS, Departament de Dinàmica de la Terra i de l'Oceà, Facultat de Ciències de la Terra, Universitat de Barcelona, Barcelona, Spain. Email: jj.gallego.montoya@ub.edu
(2) Aix Marseille University, CNRS, IRD, INRAE, CEREGE, Aix-en-Provence, France
(3) Helmholtz-Zentrum Dresden-Rossendorf, Helmholtz Institute Freiberg for Resource Technology, Freiberg, Germany
(4) Research Group Environmental Geology, Quaternary and Geodiversity (QGEO), Universidad de León, León, Spain

Abstract: *Ground-based remote sensing provides new perspectives in paleoseismology by enhancing fault characterization and reducing interpretative uncertainty. This study applies portable multi-sensor hyperspectral imaging combined with LiDAR and high-resolution photogrammetry to characterize paleoearthquake events and deformation structures in trenches, outcrops, and exhumed fault scarps across diverse tectonic regions in Spain and Italy, including the Eastern Betics Shear Zone, the Central Pyrenees, and the Central Apennines. The objectives are to improve paleoseismic trench interpretation, identify subtle deformation features commonly overlooked in conventional logging to enhance event-horizon recognition, and analyze mineralogical and spectral variations along exhumed fault rock scarps to detect alteration patterns linked to differential exposure and progressive exhumation. Results show that hyperspectral analysis reveals features difficult to observe with the naked eye, including fault-related surface deformation, centimeter-scale soft-sediment deformation, and spectral mineralogical variations expressed as zones of differential weathering along exposed fault surfaces. This multi-sensor approach demonstrates broad applicability and transferability across contrasting tectonic settings, strengthening event reconstruction and reducing interpretative uncertainty.*

Key words*: Advances in Paleoseismology; Ground-Based Remote Sensing; Hyperspectral Data; Paleoearthquake Event recognition.*

INTRODUCTION

Paleoseismology extends seismic records beyond historical archives, providing foundational parameters for seismic hazard assessment. Conventional trench and bedrock-scarp studies, however, face persistent challenges and sources of uncertainty: (i) subtle deformation is easily masked by surface processes, (ii) dating precision is limited by poor correlation of sampled units, and (iii) post-field validation is often impossible due to access restrictions and trench back-filling.

Recent advances in ground-based remote sensing now offer centimeter-scale, multi-sensor datasets formerly unattainable. Pioneer studies (Ragona et al., 2006; Kirsch et al., 2019) demonstrated that hyperspectral data can significantly reduce interpretative uncertainties in paleoseismic investigations by revealing deformation structures not visible to the naked eye. The increasing portability, reduced cost, and improved accessibility of ground-based hyperspectral cameras, combined with the development of open-source processing software (Thiele et al., 2021), create favorable conditions for broader application and methodological refinement across diverse tectonic environments.

Here, we integrate hyperspectral, LiDAR, and photogrammetric data from trenches, outcrops, and exhumed fault scarps across three seismically active and tectonically contrasting regions of Spain and Italy: the Eastern Betics Shear Zone, the Central Pyrenees, and the Central Apennines. Our objectives are to refine paleoearthquake interpretation by detecting subtle deformation features that escape visual logging and to analyze mineralogical and morphological indicators along exhumed fault-rock surfaces to assess patterns of differential exposure and progressive exhumation. Together, these goals extend hyperspectral methods (already proven in trenches) to outcrop soft-sediment deformation and exhumed fault scarps for the first time, yielding a more robust and reproducible framework for characterizing paleoearthquake evidence in complex tectonic settings.

TECTONIC AND GEOLOGICAL SETTING

The Western Mediterranean is a natural laboratory of active tectonics, where Africa–Eurasia convergence and Tethyan slab rollback drive collision, back-arc extension, and strike-slip faulting that have fragmented and reactivated faults. Historical and archaeological records document high-intensity earthquakes since pre-Roman times, while palaeoseismic data reveal variable fault geometries and slip rates since the Late Pleistocene (García-Mayordomo et al., 2012; Faure Walker et al., 2021). We focus on three representative regions (*Figure 1A*).

(i) Eastern Betics Shear Zone (SE Spain). A transtensional corridor (1.5 mm/yr) with oblique thrusting and left-lateral slip. The Alhama de Murcia Fault is the region's major seismogenic structure. It has produced several damaging earthquakes since 1500 AD (Martínez-Díaz et al., 2019), including the Mw 5.2 Lorca earthquake in 2011. The study site lies at the La Tercia trench (*Figure 1B*), where at least four ancient events have been documented in the last 40 ka (Gómez-Novel et al., 2022).

(ii) Central Pyrenees (NE Spain). This region exhibits slow post-orogenic extension (0.06–0.08 mm/yr vertical), minor thrust reactivation, isostatic rebound, and gravitational collapse. Historical destructive earthquakes (e.g., Mw ≈ 6.2 Ribagorza 1373, 1923 Vielha) left coseismic environmental signatures (Ortuño et al., 2008; Larrasoaña et al., 2010). The Sort site is located on a low-energy fluvial terrace of laminated fine-grained Quaternary deposits, Noguera Pallaresa River (*Figure 1C*).

(iii) Central Apennines (Italy). This region is dominated by an extensional regime (2–3 mm/yr, NW-SE), where some of the most destructive earthquakes in Italy occurred: 1349 and 1703 Norcia–L'Aquila, 1915 (Mw 7) Fucino, 2009 (Mw 6.3) L'Aquila, and the 2016–17 earthquake sequence. Our study focuses on the southern Fucino fault system, specifically the San Sebastiano fault, where a 7-m-high exhumed limestone bedrock scarp along the Giovenco River valley has been characterized (*Figure 1D*). Cosmogenic ^{36}Cl dating reveals at least five seismic exhumation events preserved on the fault surface, clustered around 4 and 11 ka, associated with repeated earthquake sequences (Benedetti et al., 2013).

METHODS

This study builds upon the workflow proposed by Kirsch et al. (2019). We first conducted conventional paleoseismological fieldwork. Terrestrial LiDAR (Optech ILRIS-3D) and photogrammetric data (Nikon D850, 45.7 MP) were acquired. Point clouds were generated and processed in Agisoft Metashape and CloudCompare for orthophotos and digital elevation models. Hyperspectral imagery was collected using SPECIM FX10 (400–1000 nm) and FX17 (900–1700 nm) at Sort and San Sebastiano, and AISA Fenix 1K (400–2500 nm) at La Tercia, all from distances of 5–10 m and with spatial resolutions of 4–8 mm. Radiometric correction, illumination modeling, and geometric co-registration with LiDAR/photogrammetry point cloud were performed using the hylite package (Thiele et al., 2021), enabling reflectance retrieval and projection of the hyperspectral cube onto 2-3D surfaces. Additional processing included spectral smoothing, empirical line correction, dimensionality reduction (Minimum Noise Fraction—MNF and Principal Component Analysis—PCA), mineral-sensitive band ratios, and the generation of false-color composites for lithological and structural discrimination within a multilayer visualization workflow.

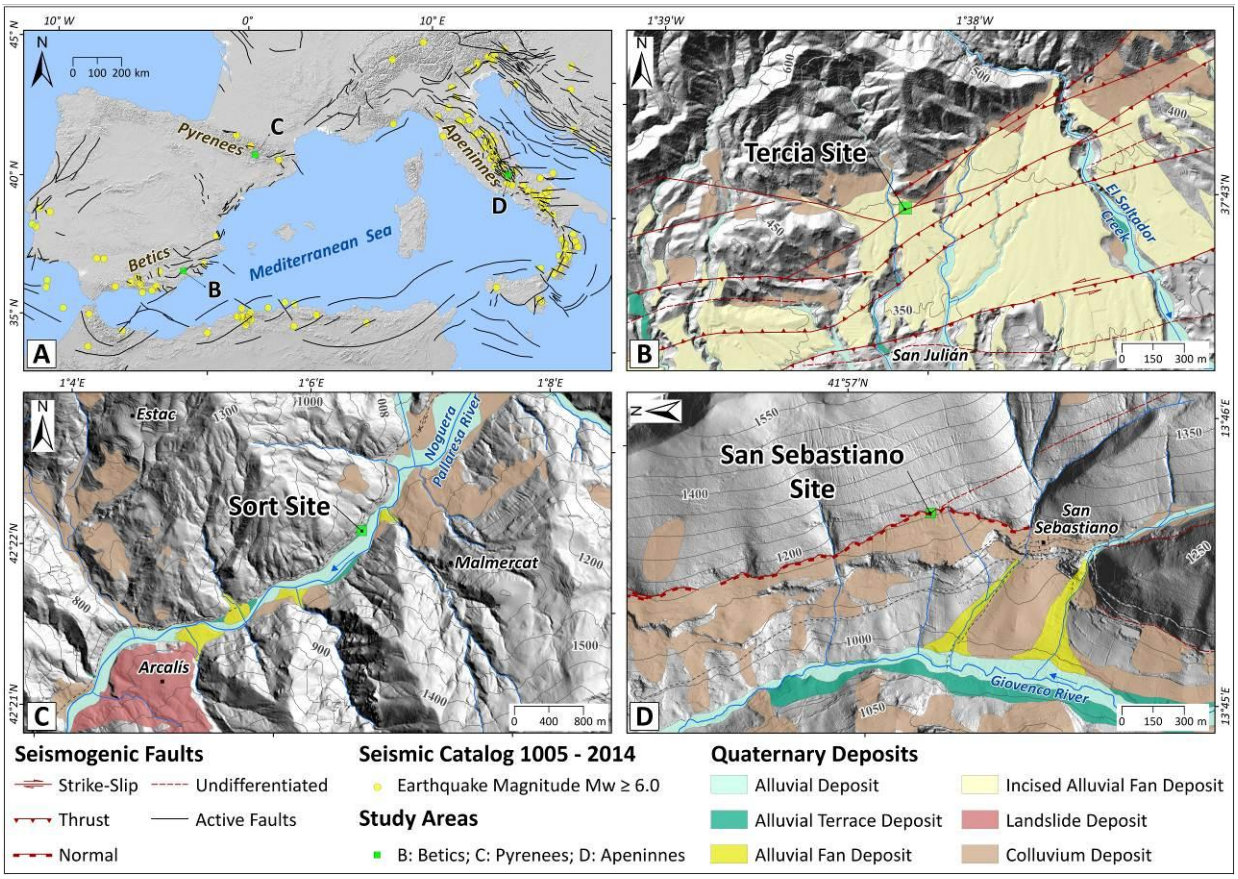

Figure 1: *A. Location of study sites in seismically active areas of the western Mediterranean. Active faults and earthquakes Mw ≥ 6.0 (1005–2014) compiled from the European Seismic Hazard Model (Basili et al., 2020), Benedetti et al. (2013), the QAFI and Fault2SHA databases (García-Mayordomo et al., 2012; Faure Walker et al., 2021). B. La Tercia trench on the northern segment of the Alhama de Murcia Fault, previously studied by Gómez-Novel et al. (2022); mapping adapted to the 5 m DEM (IGN, 2022). C. Sort site in the Noguera Pallaresa River basin; Quaternary deposit mapping modified from the 1:25,000 Ripoll sheet (ICGC, 2018) and the 5 m DEM (IGN, 2022). D. San Sebastiano fault scarp; mapping adapted from the 1:25,000 Scano sheet (Italian Geological Survey, 2008) and the 1 m LiDAR DEM (MASE, 2021).*

For the Tercia and Sort sites, field logs were compared with stacked hyperspectral data to refine stratigraphic boundaries, identify fractures, and classify centimeter-scale deformation features. At the San Sebastiano scarp, 10 cm-radius Regions of Interest spaced every 25 cm were extracted along vertical profiles from mineral band ratios. Mean and normalized index values were plotted to detect abrupt changes in slope and trend; these breaks were identified both visually and with the BottomUp segmentation algorithm (Truong et al., 2020; Llinares et al., 2025). Additional data (point spectra, Schmidt-hammer strength and surface roughness; Zielke et al., 2022) were collected but are not presented here; they will be used to correlate vertical mineralogical variability with the ^{36}Cl exhumation history (Benedetti et al., 2013).

RESULTS AND CONCLUSIONS

At least three paleoearthquake events during the past 34,000 years were identified in the La Tercia trench, confirming a surface-rupturing event <15 ka (Figure 2A).

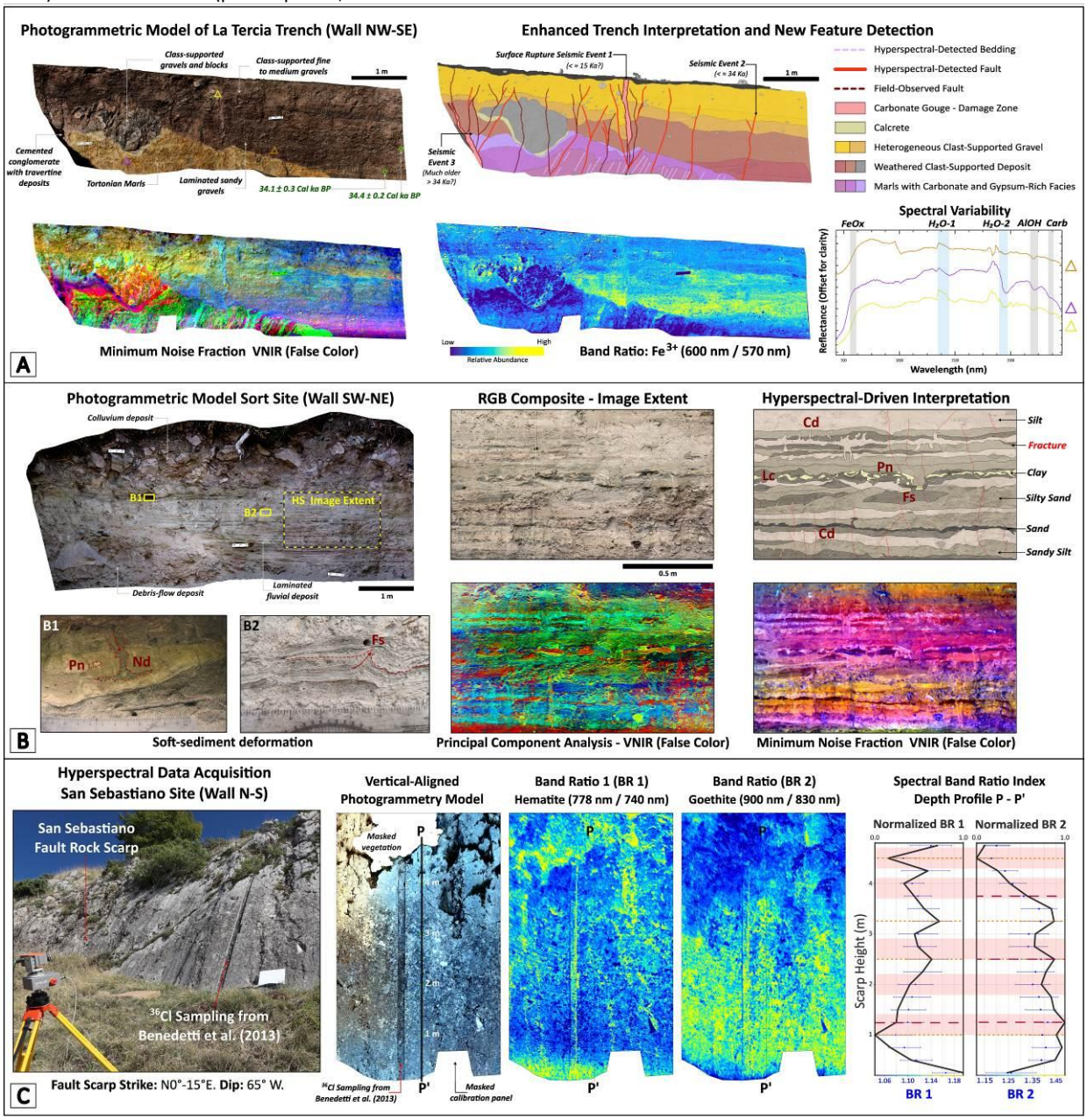

Figure 2: *A. La Tercia hyperspectral-enhanced paleoseismic interpretation. Photogrammetric model vs. false-color MNF-VNIR and iron-band-ratio images; orange, purple, and yellow triangles mark spectral variability across distinct stratigraphic units. B. Sort outcrop: photogrammetric model with yellow-boxed area for soft-sediment photos B1 and B2; yellow dashed line shows hyperspectral coverage. MNF- and PCA-VNIR composites highlight clay/silt/sand packages and soft-sediment structures (Pn = pseudonodule, Nd = Neptunian dike, Cd = clastic dike, Fs = flower structure, Lc = load cast). C. San Sebastiano scarp: acquisition, vertically-aligned model; hematite (BR1) and goethite (BR2) band indices (raw ±1σ blue, normalized black) along profile P–P'. Orange points and dark-red dashes mark visual and BottomUp slope-breaks; red transparent bands show ^{36}Cl-dated exhumation clusters (Benedetti et al., 2013).*

Hyperspectral iron, gypsum, and carbonate indices reveal 30–40 cm of vertical throw along the dominant left-lateral fault, resolving reverse-component flexures and discontinuous fault traces associated with strike-slip offset. Centimeter-scale stratigraphy in the basal marls and mineral gradients within the damage zone are now distinguishable, reducing uncertainty in unit contacts and fault-trace geometry while refining and validating previous interpretations (Gómez-Novel et al., 2022).

Spectral-dimensionality reduction and false-color composites (*Figure 2B*) resolve centimeter-thick laminae of sand, silt, and clay previously indistinguishable by color or texture, enabling horizontal tracing of liquefacted horizons within rhythmic alternations of competent beds and liquefiable sands. Soft-sediment deformation (load casts, pseudonodules, clastic and Neptunian dikes, and flower structures) indicates deposition in a low-energy aquatic environment that was abruptly subjected to high-energy and shear forces, leading to liquefaction, sediment injection, loading, and brittle failure of unconsolidated layers, likely attributable to seismic shaking rather than gravity alone. These findings demonstrate the potential of hyperspectral data to refine correlations between soft-sediment deformation and earthquake events.

Limestone-dominated San Sebastiano scarp (*Figure 2C*) shows alteration products that are spectrally active at 400–1700 nm; consequently, FX10/17 cameras effectively capture hematite/goethite band-ratio variability despite lacking the 2340 nm carbonate absorption feature. Band-ratio indices highlight spatial variability along the scarp, delineating four spectral zones (0–1, 1–2.5, 2.5–3.25, and 3.25–4.5 m) whose slope breaks changes align reasonably well with some ^{36}Cl-dated exhumation clusters (0–1.2, 1.2–2, 2–2.7, 2.7–3.9, and 3.9–4.5 m; Benedetti et al., 2013). Although these correlations are promising, broader spectral coverage and combined roughness/strength analyses are required to strengthen interpretations of scarp rupture. A comparative assessment of hyperspectral sensors confirms that 400–1700 nm systems can substantially advance paleoseismology by enabling more detailed and reproducible investigations.

Acknowledgements: This research was supported by the TREAD Project, funded by the European Union under the Horizon Europe program through the Marie Skłodowska-Curie Actions Doctoral Networks – Grant Agreement No. 101072699.

REFERENCES

Basili, R., Danciu, L., Carafa, M. M. C., Kastelic, V., Maesano, F. E., Tiberti, M. M., Vallone, R., Gracia, E., Sesetyan, K., Atanackov, J., Sket-Motnikar, B., Zupančič, P., Vanneste, K., & Vilanova, S. (2020). Insights on the European Fault-Source Model (EFSM20) as input to the 2020 update of the European Seismic Hazard Model (ESHM20). *EGUsphere*, *2020*, 1-32. doi:10.5194/egusphere-egu2020-7008

Benedetti, L., Manighetti, I., Gaudemer, Y., Finkel, R., Malavieille, J., Pou, K., Cushing, E. M., & Keddadouche, K. (2013). Earthquake synchrony and clustering on Fucino faults (Central Italy) revealed by in-situ ^{36}Cl exposure dating. *Journal of Geophysical Research: Solid Earth*, *118*(9), 4948-4974. doi:10.1002/jgrb.50307

Faure Walker, J. P., Boncio, P., Pace, B., Roberts, G., & Benedetti, L. (2021). Fault2SHA Central Apennines database and structuring active fault data for seismic hazard assessment. *Scientific Data*, *8*, 87. doi:10.1038/s41597-021-00868-0

García-Mayordomo, J., Insua-Arévalo, J. M., Martínez-Díaz, J. J., Jiménez-Díaz, A., Martín-Banda, R., Martín-Alfageme, S., Álvarez-Gómez, J. A., Rodríguez-Peces, M., Pérez-López, R., Rodríguez-Pascua, M. A., & others. (2012). The Quaternary Active Faults Database of Iberia (QAFI v. 2.0). *Journal of Iberian Geology*, *38*(2), 285-302. doi:10.5209/rev_JIGE.2012.v38.n2.39253

Gómez-Novell, O., Ortuño, M., García-Mayordomo, J., Insua-Arévalo, J. M., Rockwell, T. K., Baize, S., & others. (2022). Improved geological slip-rate estimations in the complex Alhama de Murcia Fault zone (SE Iberia) and its implications for fault behaviour. *Tectonics*, *41*, e2022TC007465. doi:10.1029/2022TC007465

Kirsch, M., Lorenz, S., Zimmermann, R., Andreani, L., Tusa, L., Pospiech, S., Jackisch, R., Khodadadzadeh, M., Ghamisi, P., & Unger, G. (2019). Hyperspectral outcrop models for palaeoseismic studies. *Photogrammetric Record*, *34*, 385–407. doi:10.1111/phor.12300

Larrasoaña, J. C., Ortuño, M., Birks, H. H., Valero-Garcés, B., Parés, J. M., Copons, R., & Bordonau, J. (2010). Palaeoenvironmental and palaeoseismic implications of a 3700-year sedimentary record from proglacial Lake Barrancs (Maladeta Massif, Central Pyrenees, Spain). *Palaeogeography, Palaeoclimatology, Palaeoecology*, *294*(1-2), 83-93. doi:10.1016/j.palaeo.2009.10.009

Llinares, M., Gassier, G., Viseur, S., & Benedetti, L. (2025). A new inversion algorithm (PyMDS) based on the Pyro library to use chlorine 36 data as a paleoseismological tool on normal fault scarps. *Applied Computing and Geosciences*, *25*, 100234. doi:10.1016/j.acags.2025.100234

Martínez-Díaz, J., Alonso-Henar, J., Insua-Arévalo, J., Canora, C., García-Mayordomo, J., Rodríguez-Escudero, E., Álvarez-Gómez, J., Ferrater, M., Ortuño, M., Masana, E. (2019). Geological evidences of surface rupture related to a seventeenth century destructive earthquake in Betic Cordillera (SE Spain): constraining the seismic hazard of the Alhama de Murcia fault. *J. Iber. Geol, 45*. doi:10.1007/s41513-018-0082-2

Ortuño, M., Queralt, P., Martí, A., Ledo, J., Masana, E., Perea, H., & Santanach, P. (2008). The North Maladeta Fault (Spanish Central Pyrenees) as the Vielha 1923 earthquake seismic source: recent activity revealed by geomorphological and geophysical research. *Tectonophysics*, *453*(1-4), 246-262. doi:10.1016/j.tecto.2008.05.015

Ragona, D., Minster, B., Rockwell, T., & Jussila, J. (2006). Field imaging spectroscopy: A new methodology to assist the description, interpretation, and archiving of paleoseismological information from faulted exposures. *Journal of Geophysical Research: Solid Earth*, *111*, B06205. doi:10.1029/2006JB004267

Thiele, S. T., Lorenz, S., Kirsch, M., Contreras Acosta, I. C., Tusa, L., Herrmann, E., Möckel, R., & Gloaguen, R. (2021). Multi-scale, multi-sensor data integration for automated 3-D geological mapping. *Ore Geology Reviews*, *136*, 104252. doi:10.1016/j.oregeorev.2021.104252

Truong, C., Oudre, L., & Vayatis, N. (2020). Selective review of offline change point detection methods. *Signal Processing*, *167*, 107299. doi:10.1016/j.sigpro.2019.107299

Zielke, O., Benedetti, L., Mai, P. M., Fleury, J., Rizza, M., & Viseur, S. (2022). Bedrock fault roughness resolves slip increments of large earthquakes: Case studies from Central Italy. *Tectonophysics*, *838*, 229502. doi:10.1016/j.tecto.2022.229502

INQUA TERPRO Project Cascading Hazards and Mitigation (CHAMP)

Past Site Use Impacts the Pedogenic Age Estimation of Alluvial Fan Deposits in the Simi Valley Area of Southern California: A Cautionary Tale

González, Tania (1)

(1) Earth Consultants International, 1642 East Fourth Street, Santa Ana, CA 92701-5148 USA. Email: tgonzalez@earthconsultants.com

Abstract: *We conducted fault trenching studies for a property previously used as a fruit orchard and chicken farm inferred to be bisected by the Holocene Simi fault. The 172-m-long, 3.35- to 5.5-m-deep trench extended nearly the entire site length. A ~0.75-m-thick calcic (Btk) soil horizon 1.25 m below the ground surface in the northern, medial alluvial fan surface was traced the entire trench length as a marker bed, confirming a lack of near-surface faults through the site. In the distant portion of the fan, at the trench's south end, the horizon was less well-developed and buried by 5.1 m of alluvium and younger soils. Given its degree of development, the Btk horizon was initially interpreted as a Pleistocene relict soil. However, radiocarbon dating returned ages of about 3.4 ka, requiring reconsideration of the soil's pedogenic history and deeper fault analyses. Past land uses likely contributed to the unexpected rapid soil development.*

Key words*: Pedogenesis, radiocarbon dating, fault study, agricultural impacts*

INTRODUCTION

A fault study was required to evaluate whether a property proposed for residential development in Simi Valley, California, is underlain by the Simi fault. If the fault were found, setbacks would be required to avoid placing residences across the Holocene-active traces. Because the State of California considers a fault active if it has moved at least once in the past 11.7 ka, to confirm sites are not underlain by active faults, fault studies need to show the Holocene sediments are not faulted. Trenches should ideally expose Holocene and late Pleistocene deposits. Where the Holocene section is too deep, other methods such as drilling or cone penetration tests (CPTs) can be used to correlate the stratigraphy across the area of interest (CGS, 2018).

Simi fault

The Simi fault is a >65° N-dipping reverse, or reverse-oblique fault delineating the N boundary of the Simi Valley. The fault is the E half of an approximately 32–48 km-long zone of faults and folds extending W to the city of Camarillo (Fig. 1). From W to E, the major faults comprising this zone are the Springville, Santa Rosa and Simi faults (S-SR-SFZ). These faults and associated folds are the result of N-S-directed crustal shortening that began in the Plio-Pleistocene (DeVecchio et al., 2012) and is still ongoing today, posing a seismic hazard to the region.

Paleoseismic studies along the S-SR-SFZ have shown evidence of Holocene displacement. González & Rockwell (1991) measured a displacement of 0.65–1.1 m per event, a recurrence interval of 720–2,200 years, and a slip rate of 0.5–0.9 mm/yr along the Springville fault. In western Simi Valley, ~3.5 km W of the study site, Hitchcock et al. (2003) inferred the most recent surface-rupturing event on the Simi fault occurred between 1.2 ka and <4.9 ka, resulting in ~1–1.5 m of vertical and 2–2.5 m of total left-lateral oblique displacement, respectively. They also calculated a Holocene slip rate of ~1 mm/yr. DeVecchio et al. (2012) inferred a minimum slip rate of 0.8–1.4 mm/yr, and a recurrence interval of 715–1,100 years along the Simi fault zone.

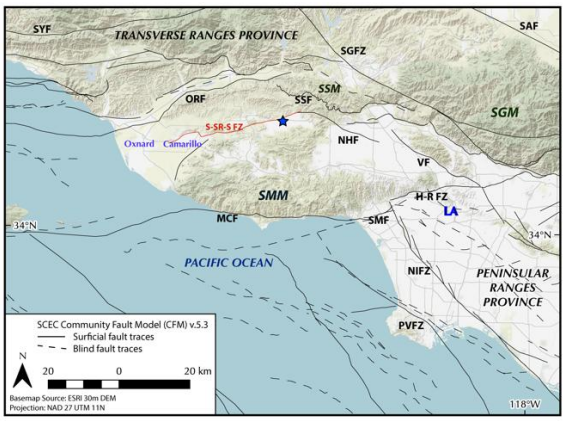

Figure 1: *DEM-based map showing study site location (blue star) relative to the city of Los Angeles (LA, in blue), significant mountain ranges (SMM–Santa Monica Mountains, SGM–San Gabriel Mountains, SSM–Santa Susana Mountains), and faults (SYF–Santa Ynez fault, SGFZ–San Gabriel fault zone, SAF–San Andreas fault, ORF–Oakridge fault, SSF–Santa Susana fault, S-SR-SFZ–Springville-Santa Rosa-Simi fault zone (in red), NHF–Northridge Hills fault, VF–Verdugo fault, MCF–Malibu Coast fault, SMF–Santa Monica fault, H-RFZ–Hollywood-Raymond fault zone, NIFZ–Newport-Inglewood fault, and PVFZ–Palos Verdes fault zone).*

Historical uses of the site

Historical information on the property is based from a review of vintage aerial photographs and county records, with some data confirmed by the local historical society. By the 1920s, the property, as most of the surrounding area, was planted with orchards, likely lemon and orange trees. In 1937, a residential structure and detached garage were built near the southeast corner of the property, and by 1945, five ~24-m-long and ~8-m-wide structures aligned E-W and parallel to each other had been built to the NW of the house (Fig. 2). These structures, built on concrete slabs, housed chickens; the property became a well-known egg ranch in the region. Dozens of fruit and ornamental trees

were present throughout the property in between the structures. It is not known when the ranch ceased operations, but the structures were demolished and most of the trees were removed in 2022, a few weeks before the fault study began.

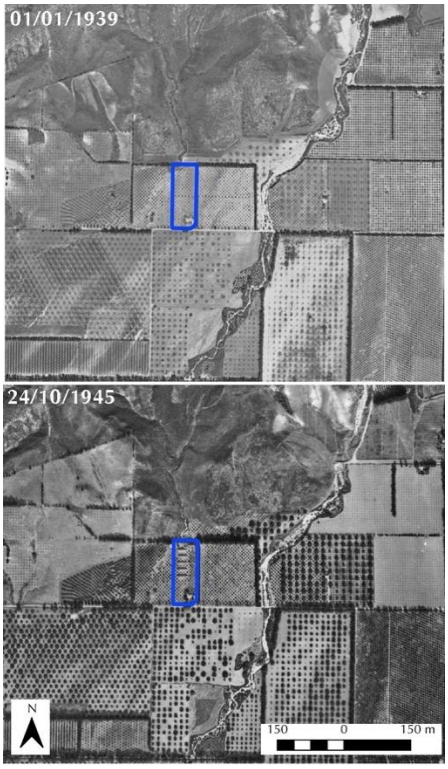

***Figure 2**: 1939 (top) and 1945 (bottom) aerial photographs of the study site (blue rectangle) showing orchards, residential structure near SE corner, and chicken houses built between 1939 and 1945 in the northern two-thirds of the site. Site is on the N side of the Simi Valley, at the base of the Santa Susana Mountains. Dry Canyon Wash is ~170 m E of the site.*

FAULT STUDY

The field investigation first involved the excavation and logging of an ~172-m-long trench extending in a SE direction nearly the full length of the site, across the inferred location of the Simi fault. The trench was 3.35–5.5 m deep, and benched for safety (Figs. 3 & 4).

The study site is located on a slightly elevated, gently SW–sloping (±2°) infilled alluvial fan surface. Ephemeral streams used to flow in a W-SW direction across the site before Dry Canyon Wash, the main stream to the E, was channelized (Fig. 2). The area has a semi-arid Mediterranean climate with mean annual precipitation of ~30–46 cm and average annual temperature of ~16°C.

Geologic and soil units exposed in trench

The trench exposed a series of dm- to m-thick fining-upward alluvial fan and fluvial (channel and overbank) deposits, often capped by now-buried soils. These soils indicate pulses of sedimentation were followed by depositional hiatuses that allowed for soil formation. Each of these hiatuses lasted decades to maybe a few thousand years. The soils were recognized by their darker colors indicative of organic accumulation; horizonation; accumulation of secondary clay as films on ped faces, bridges between grains, and coatings on clasts; calcification; and bioturbation. Alluvial fan packages typically have sharp erosional contacts with the buried soils immediately below, and the A horizons that used to cap these soils are truncated or removed altogether. The fluvial sections include coarse basal gravels, nested channels, and often display abrupt, scoured and irregular contacts with the underlying sediments or soils.

***Figure 3**: View to the NW of the northern ~130 m (425 ft) of the W wall of the trench showing ~1.5-m-high benches. level line and stations (in feet) on the bottom bench. The dark soil horizon near the level line is the main subject of this paper. The E wall was logged in detail.*

The trench exposed a truncated buried soil we traced nearly the full length of the exposure. At Sta. 60 (~18 m), the top of the soil was ~1.25 m below the ground surface, whereas at Sta. 550 (~168 m) the same soil was buried by 5.1 m of younger sediments and soils. In some trench sections, this buried soil had been incised into and removed by younger fluvial deposits, but by using both trench walls, we were able to show continuity of the soil along the full length of the trench south of Sta. 60. Continuous layers below the depth of the scoured-out soil in the northern 18 m of the trench showed there were no near-surface faults in the northern portion of the trench either. Thus, this buried soil was a key marker bed that demonstrated the deposits exposed were not impacted by faulting.

In the northern third of the trench, to about Sta. 140 (~43 m), the ~0.76-cm-thick buried soil horizon was described as a brown to dark grayish brown (10YR 4/2.5 when moist (m), 10YR 5/2 when dry (d), using Munsell soil color notation) sandy clay to clay with few thin very dark grayish brown (10YR 3/2 m, 10YR 4/3 d) clay films on ped faces and common to many moderately thick clay films bridging grains, strong coarse prismatic breaking to strong fine to medium angular blocky soil structure, many to continuous moderate thick calcium carbonate coatings on ped faces, and many calcium carbonate filaments and common nodules (Gile et al.'s, 1966 carbonate deposition Stage II-III). Given these characteristics, the soil was labelled as a calcic (Btk) horizon (Fig. 5, left photo).

This same buried soil near the bottom of the southern half of the trench, from about Sta. 200 to Sta. 551 (~61 to 168 m), was described as a dark grayish brown to brown (10YR 4/2.5-4/3 m, 10YR 6/2-6/3 d) sandy clay with strong medium to coarse angular blocky soil structure breaking to moderate to strong fine angular blocky structure, very few thin to no clay films bridging grains, and common thin

calcium carbonate coatings on ped faces and forming thin filaments and few nodules (Stage I; Fig. 5, right photo).

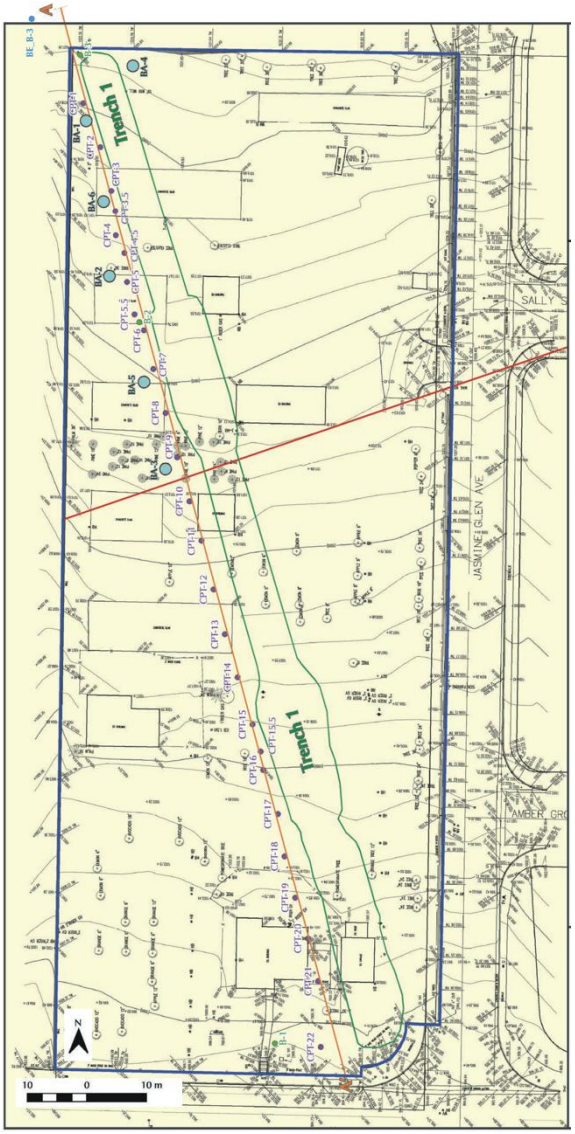

***Figure 4**: Site plan (blue boundary) showing trench outline in green, CPTs with purple dots, large-diameter bucket augers (BAs) with light blue dots, and small-diameter hollow stem borings (Bs) with green dots. The WSW-trending red line through the site is the inferred location of the Simi fault as show on the State-issued fault map. Orange line shows cross-section prepared using the CPT and borehole data.*

Using the soil development index (SDI) method of Harden & Taylor (1983) and soil-age regressions for the southern California area (Dolan et al., 1997), we estimated the Btk soil horizon near the N-end of the trench has been exposed to soil forming processes for a minimum of ˜4.6 ky (using the non-normalized SDI values) with a median, preferred estimate of ˜14.3 ky. The characteristics of the same soil in the central and southern portions of the trench yielded a minimum of ˜3.9 ky of exposure to soil-forming processes at the ground surface before burial, with a mean estimate of ˜12.3 ky. The Stage II-III calcium carbonate concentration at >1.5-m-depth supported the Pleistocene, mean age estimates as the preferred values. We reasoned the differences in the Btk soil in different trench sections are a function of depth: the soil near the N end is a relict soil likely still under the influence of soil-forming factors, whereas the same soil farther S is buried too deeply, and had stopped developing as a soil at some point in the past.

***Figure 5**: Close-up photographs of the same Btk soil horizon at Station 85, W wall (left) and Station 500, E wall (right), below the white flags/line. Note differences in soil structure and abundance of calcium carbonate. Green flag in the photo on the right marks location where charcoal was collected (but not dated).*

Under this scenario, the >14-ka age for the relict soil represented our preferred age estimate for the unit. We argued the trench had exposed late Pleistocene sediments, satisfying the California depth requirements for fault studies. Furthermore, given the short recurrence interval for the Simi fault, if the fault extended through the area trenched, we should have seen faulted deposits. We thus concluded we had cleared the site of Holocene-active faults.

The reviewer, however, requested we confirm our findings with numerical age dating. Two small charcoal fragments collected from the upper section of the buried soil in the S-end of the trench were analyzed by Beta Analytic. The radiocarbon dating results returned calibrated calendar ages (CCAs) of ˜3.4 ka (Table 1). Given the past agricultural use of the property, modern carbon contamination was a concern. Beta's dating experts indicated pre-treatment of the charred samples removed any modern carbon, and stood by the ˜3.4 ka-age results. This conclusion was also supported by the very similar ages for the two samples, which were collected >46 m apart along the length of the trench. Based on these findings, even if we assumed these dates reflect the age of burial rather than the age of the soil, we could not conclusively show that the trench was deep enough to expose pre-Holocene sediments. This required us to conduct additional, deeper studies to expose demonstrably Pleistocene sediments.

The additional studies included drilling 3 small-diameter hollow-stem auger borings (Bs), emplacement of 26 CPTs, and drilling and down-hole logging 6 large-diameter borings (Bas; Fig. 4). The CPTs paralleled the trench and covered the entire length of the study site, extending the depth of exploration to between 11.9 and 30.5 m.

Table 1: Radiocarbon Dating Results

Beta No.	Location (depth in m)	Type of Material	CRA[1]	CCA[2]
629940	T-1, Sta. 339West (4.0)	Charred material	3130 ± 30	3409–3319 (64.7%); 3304–3247 (25.7%); 3445–3423 (5%)
629941	T-1, Sta. 491West (4.1)	Charred material	3160 ± 30	3451–3339 (92.1%); 3285–3272 (3.3%)
654904	BA[3]-3 (9.1-11.3)	Alkali soluble organics	7390 ± 30	8330–8165 (85.5%); 8092–8040 (9.9%)
654905	BA-3 (9.1-11.3)	Alkali insoluble organics	8610 ± 30	9678–9530 (95.4%)
634821	B[4]-1(21-21.3)	Organic sediment	23740 ± 90	28062–27695 (95.4%)

[1] Conventional Radiocarbon Age in years before present (yBP). [2] Calendar Calibrated Age in years before AD 1950
[3] BA = Large-diameter bucket auger [4] B = Small diameter hollow-stem boring

To further assess the potential for modern carbon contamination, a bulk sample from a paleosol in BA-3 at ~9–11-m depth was analyzed for both alkaline soluble (humic) and insoluble fractions, with radiocarbon dates obtained for each fraction. The humic fraction returned a CCA of ~8.25 ka; the alkaline-insoluble fraction, ~9.6 ka (Table 1). The two results are similar, suggesting little to no contamination from modern carbon, and further confirming the reliability of the ~3.4 ka age results for the younger soil. Moreover, humic ages are thought to more closely date the burial of soil surfaces (Dalsgaard & Odgaard, 2001; Kristiansen et al., 2003) so we assume sample 654904 dates the burial of this soil, and sample 654905 is a better estimate of the age of the soil, with the difference between the ages suggesting the paleosol at ~9–11-m depth was exposed to soil-forming processes at the ground surface, prior to burial, for about 1.35 ky.

To define the Holocene-Pleistocene (H-P) boundary, we relied on the radiocarbon-dated units (Table 1) to calculate approximate rates of sedimentation for the alluvial fan deposits at different depths. Using the ~3.4-ka burial age of the soil described before, we calculated a depositional rate for the sediments in the uppermost 4 m of ~1.2 m/ky. Using this rate, the H-P boundary would occur at a depth of ~14 m. The burial age of ~8.25 ka for the top of the 9-–11-m-depth paleosol yields a sedimentation rate of 1.09 m/ky, and a depth for the H-P boundary of ~12.8 m. Thus, these two results independently indicated a depth for the H-P boundary of ~13.5 m. A sediment sample collected at a depth of ~21 m was dated to ~28 ka, indicating that Pleistocene sediments occur within the depth explored.

Distinctive units observed in the Bs and BAs were correlated to the CPT curves, and these data combined were used to construct a cross-section that showed several sedimentary packages and paleosols extend unfaulted nearly the full length of the study area. A ~5.5-m vertical step in Pleistocene alluvial fan deposits in the NW corner of the site, between borings BA-4 and B-3 (Fig. 5), suggested the Simi fault is located at or just N of the study area. The reviewing geologist approved our study.

CONCLUSIONS

Numerical ages obtained for the buried soil exposed in the trench originally interpreted as late Pleistocene suggest that this soil formed at a faster rate than similar soils in other southern California locales. The illuviation of clay, development of prismatic structure and significant accumulation of secondary calcium carbonate appear to be related to the site's historical uses, including irrigation of the orchard (Ortiz et al., 2022) and accumulation of calcium carbonate-rich chicken manure. Thus, past agricultural uses of a site need to be carefully considered when using soil-stratigraphic methods to estimate the age of deposits.

Acknowledgements: Property owners and developers John Proia and Louis Santor commissioned the study and kindly allowed this publication. Taylor Bogdanovich, Clay Kelty, Maria Herzberg, Yannick Wirtz and Eldon Gath assisted with various phases of the study. Dave Howe, Director, Strathearn Historical Park & Museum, provided confirmation of historical data.

REFERENCES

California Geological Survey (CGS), 2018 [Revision], Earthquake Fault Zones | A Guide for Government Agencies, Property Owners / Developers, and Geoscience Practitioners for Assessing Fault Rupture Hazards in California: *Special Publication 42*, 83p. + plates.

Daalsgard, K. & Odgaard, B.V., 2001, Dating sequence of buried horizons of podzols developed in wind-blown sand at Ulfborg, Western Jutland: *Quaternary International* 78, 53-60.

DeVecchio, D.E., Keller, E.A., Fuchs, M., & Owen, L.A., 2012, Late Pleistocene structural evolution of the Camarillo fold belt: Implications for lateral fault growth and seismic hazard in southern California: *Lithosphere* 4(2), 91-109.

Dolan, J.F., Sieh, K., & Rockwell, T.K., 2000, Late Quaternary activity and seismic potential of the Santa Monica fault system, Los Angeles, California: *Geological Society of America Bulletin* 112(10), 1559-1581.

Gille, L.H., Peterson, F.F., & Grossman, R.B., 1966, Morphological and genetic sequences of cabonate accumulation in desert soils: *Soil Science* 101, 347-360.

González, T. & Rockwell, T.K., 1991, Holocene activity of the Springville fault in Camarillo, Transverse Ranges, Southern California; preliminary observations. In *Engineering Geology along the Simi-Santa Rosa Fault System and Adjacent Areas, Simi Valley to Camarillo Ventura, California* (Blake, T.F. ed): Southern California Section Association of Engineering Geologists, Annual Field Trip Guidebook 2, 369-383.

Harden, J.W. & Taylor, E.M., 1983, A quantitative comparison of soil development in four climatic regimes: *Quaternary Research* 28, 342-359.

Hitchcock, C.S., Lindvall, S.C., Treiman, J.A., Weaver, K.D., Helms, J.G., Lettis, W.R., & Simpson, G.D., 2003, Paleoseismic investigation of the Simi fault at Arroyo Simi, Simi Valley, CA: Evidence of timing of Late Holocene earthquakes on the Simi-Santa Rosa fault zone: *Statewide California Earthquake Center* Contribution #723, https://central.scec.org/publication/723.

Kristiansen, S.M., Dalsgaard, K., Holst, M.K., Aaby, B. & Heinemeier, J., 2003, Dating of prehistoric burial mounds by 14C analysis of soil organic matter fractions: *Radiocarbon* 45(1), 101-112.

Ortiz, A.C., Jin, L., Ogrinc, N., Kaye, J., Krajnc, B. & Ma, L., 2022, Dryland irrigation increases accumulation rates of pedogenic carbonate and releases soil abiotic CO_2: *Scientific Reports* 12, 464.

INQUA TERPRO Project Cascading Hazards and Mitigation (CHAMP)

Linking Surface Uplift and Upper-Plate Extension in the Forearc of Northern Chile: Insights from Quaternary active deformation in the Mejillones Peninsula

González, Gabriel (1), Ian Del Rio (1), Yerko González (1), José González-Alfaro (2), Luis Astudillo (3), Gabriel Easton(2)

(1) CIGIDEN, Departamento de Ciencias Geológicas, Universidad Católica del Norte, Email: ggonzale@ucn.cl,
(2) Departamento de Geología, Facultad de Ciencias Físicas y Matemáticas, Universidad de Chile.
(3) Escuela de Ciencias del Mar, Pontificia Universidad Católica de Valparaíso, Chile.

Abstract:
The relationship between surface uplift and upper-plate faulting provides fundamental insights into how convergent margins partition strain. In northern Chile, the hyperarid Mejillones Peninsula preserves Pleistocene marine terraces and eolian deposits displaced by normal faults, enabling direct quantification of coeval uplift and extension. We investigate whether uplift and slip rates are dynamically linked, reflecting forearc flexure driven by megathrust segmentation. Geomorphic mapping, structural analysis, and new OSL ages from K-feldspar in marine and eolian sediments, combined with $^{40}Ar/^{39}Ar$ single-crystal fusion ages from volcanic ash layers, constrain Quaternary deformation. Dated shoreline markers show a marked acceleration in uplift after MIS 19 and later after MIS 11. Uplift rates increase northward, coinciding with a 24 m north-to-south decrease in the highest wave-cut notch over 24 km, indicating southward tilting of ~0.1° and spatial segmentation of Quaternary uplift. The uplift pattern is mirrored by a similar gradient in fault slip rates along the Mejillones Fault, demonstrating mechanical coupling between upper-plate extension and surface uplift. We propose that the spatiotemporal evolution of deformation reflects a local deep structural control of the plate margin. These results highlight that deep subduction-zone architecture exerts first-order control on forearc deformation and megathrust segmentation along the northern Chile margin.

***Keywords**: Northern Chile, subduction zones, surface uplift,fault slip rate, Quaternary tectonics*

INTRODUCTION

In active continental margins, the partitioning of strain between the megathrust and upper-plate faults controls patterns of surface uplift and forearc deformation. Unraveling the relationship between uplift and fault slip rates is essential for understanding the mechanical behavior of convergent margins. Establishing this relationship remains challenging, as both integrate deformation over different spatial and temporal scales.

The hyperarid forearc of northern Chile offers an exceptional natural laboratory. On the Mejillones Peninsula, well-preserved Pleistocene marine terraces and eolian deposits are displaced by active normal faults, allowing simultaneous measurement and dating of uplifted and faulted geomorphic markers. Previous work suggests that the coexistence of uplift and extension reflects persistent segmentation on the subduction interface that inhibits the propagation of large megathrust ruptures (Victor et al., 2011). Structure in the downgoing slab, such as fracture zones or ridges (Maksymowicz, 2015), may localize deformation and influence spatial variation in uplift.

We evaluate whether uplift and normal faulting are dynamically linked, meaning higher uplift rates coincide with faster fault slip. We also test if deformation has migrated spatially across the peninsula and explore whether these upper-plate processes reflect deeper structural controls on margin behavior. To evaluate this, we integrate geomorphic analyses with new geochronological constraints from OSL dating of K-feldspar in eolian and marine deposits and $^{40}Ar/^{39}Ar$ single-crystal fusion ages from volcanic ash layers. These dated and deformed deposits provide a direct basis for quantifying Quaternary deformation rates.

GEOMORPHOLOGICAL, STRATIGRAPHICAL, AND STRUCTURAL SETTINGS

The Mejillones Peninsula is shaped by three major east-dipping normal faults, the Mejillones, Caleta Herradura, and La Rinconada faults, which bound the Morro Mejillones, Morro Jorgino, and Morro Moreno horsts and three associated half-grabens that host the Pampa Mejillones, Pampa Herradura, and Pampa Aeropuerto strandplains (González et al., 2003) (Fig. 1). These surfaces tilt toward their respective bounding faults, forming rollover structures expressed by beach ridges that cross topographic contours. The horsts preserve two groups of marine terraces recording Pliocene emergence and Pleistocene uplift (Binnie et al., 2016). A group of high terraces in Morro Mejillones (360–600 m asl) includes an ash dated at 3.25 ± 0.17 Ma (Marquardt, 2005), and a group of 5 to 6 lower terraces, which yields ^{10}Be ages of ~480–269 ka (Binnie et al., 2016). Morro Jorgino hosts a similar sequence of lower terraces, ranging from 10 to 270 m above sea level (asl). Both groups of terraces are separated by a prominent paleo-coastal cliff exposed on both horsts.

Neogene stratigraphy consists of the Miocene Caleta Herradura Formation, the Pliocene La Portada Formation, and the Pleistocene Mejillones Formation (Ferraris and Di Biase, 1978; Krebs et al., 1992). The Caleta Herradura Formation comprises ~260 m of marine deposits dating to the early–late Miocene. The La Portada Formation (~70 m thick) contains ash layers dated at ~4.2–2.9 Ma, with Sr isotope ages near 1.6 Ma (Marquardt, 2005; Victor et al., 2011). The Mejillones Formation unconformably overlies La Portada and forms

beach-ridge sequences, with basal ash dated at 0.79 ± 0.03 Ma (Marquardt, 2005). Ortlieb et al. (1996c) identified several beach ridges of the Mejillones Formation containing a mollusk association typical of the Panamic Province of the coast of Peru. Ortlieb et al. (1996c) defined this association as a thermally anomalous molluscan assemblage (TAMA). According to Ortlieb et al. (1996), this fauna migrated from lower latitudes to the Mejillones Peninsula during the MIS (Marine Isotopic Stage) 11 (420-370 ka). Eastern alluvial deposits locally interfinger with these marine sediments.

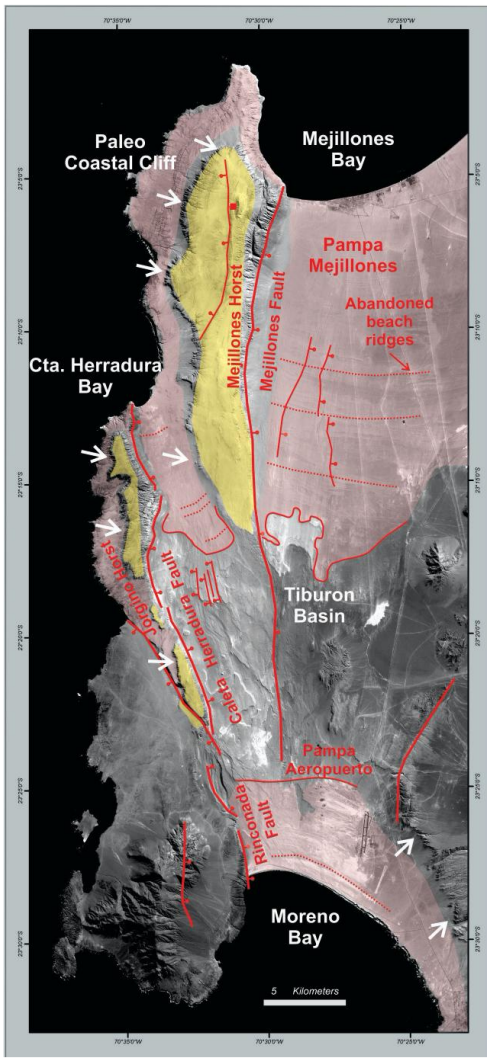

Figure 1: *Satellite image showing the Mejillones Peninsula and main structural and morphological features. Yellow polygons depict Pliocene deposits and pink polygons the distribution of Pleistocene marine deposits.*

The Mejillones Fault generates a cumulative scarp up to ~500 m high, active since at least the Miocene (Cortés et al., 2012), decreasing southward over ~40 km and extending ~10 km offshore (Vargas et al., 2011). Additional north–south faults form scarps up to ~6 m in Pampa Mejillones. Offsets of alluvial fans along active fronts reach ~15 m, with ^{10}Be surface exposure ages of ~15–59 ka (Cortés et al., 2012).

METHODS

To constrain the timing of deformation and sedimentation on the Mejillones Peninsula, we combined luminescence and isotopic dating with detailed structural analysis along the main faults.

OSL Dating

Optically Stimulated Luminescence (OSL) dating was applied to K-feldspar grains from eolian and marine sediments displaced by Quaternary faulting. Equivalent doses were measured using post-IR IRSL protocols (Buylaert et al., 2009, 2012), which reduce fading and provide reliable ages. Sample preparation followed standard mineral separation under red light, and measurements were performed on Risø TL/OSL systems with infrared diodes and a ^{90}Sr/^{90}Y beta source.

^{40}Ar/^{39}Ar Dating

Single-crystal ^{40}Ar/^{39}Ar analyses of feldspar and biotite from ash layers within marine strata and terrace deposits supplied independent age constraints for sediment deposition and subsequent uplift.

Structural Analysis and Slip Rates

Topographic profiles across the Mejillones and Caleta Herradura faults were obtained using differential GPS and drone photogrammetry to quantify cumulative offsets of terraces and alluvial fans. Slip rates were calculated by dividing measured vertical displacements by the OSL and ^{40}Ar/^{39}Ar ages.

RESULTS

Onset of the Quaternary uplift

The earliest emergence of the Mejillones Peninsula is recorded by the highest marine terrace on the northern Mejillones Horst, where a volcanic tephra yields a ^{40}Ar/^{39}Ar age of 3.25 ± 0.17 Ma at ~580 m asl (Marquardt, 2005). This implies a long-term uplift rate of ~0.18 ± 0.01 m/kyr and indicates that initial uplift during the Pliocene was slow and spatially restricted to the northernmost part of the peninsula. In contrast, a correlative high terrace on the southern Mejillones Horst lies at ~250 m asl and is carved into La Portada Formation strata. Ash layers immediately below this terrace, dated at 3.44 ± 0.02 Ma (biotite) and 3.67 ± 0.02 Ma (sanidine), confirm that the central parts of the peninsula remained submerged at that time. The emergence of the Jorgino Horst likely occurred later in the Pliocene.

In the Tiburón Basin, the basal contact of the Mejillones Formation truncates the La Portada Formation, marking the earliest Quaternary emerged surface in the graben. Shoreface to backshore facies with a gypsum horizon, and closely clustered ^{40}Ar/^{39}Ar ages yield an average of 755 ± 41 ka,

defining the timing of the marine transgression, represented by the strata of the Mejillones Formation, and the onset of the graben uplift that subsequently produced the beach ridge sequence.

Temporal variation of the uplift rates

The Mejillones Formation preserves late Quaternary uplift through extensive strandplains confined to the half-grabens (Pampa Mejillones, Pampa Herradura, and Pampa Aeropuerto). Beach ridges composed of pebble- to boulder-sized clasts exhibit offlap geometries, indicating coastal regression driven by eustatic sea-level fall modulated by tectonic uplift. Seven major, although degraded, shoreline scars (Scar 1 to Scar 7) cut across ridge sequences (Victor et al., 2011).
The highest beach ridges near Cuenca del Tiburón (~198 m asl) overlie the ash dated at 755 ± 41 ka, demonstrating that ridge formation and tectonic emergence began after MIS 19. A pIRIR age of 204.6 ± 20.3 ka near Scar 2 (60–120 m asl) indicates formation between MIS 7 and MIS 19. U-series ages from Pampa Aeropuerto show that warm-water TAMA fauna are associated with MIS 11 (~420 ka), whereas cold-water assemblages reflect MIS 9 (~310–280 ka) (Ortlieb et al., 1996; Victor et al., 2011). At La Rinconada, pIRIR ages of ~250–242 ka date the transgression that culminated in Scar 2 during MIS 7, and alluvial deposits dated at 92–87 ka cap Scar 1 (MIS 5e).

Uplift rates in Pampa Mejillones were determined along its eastern margin, where vertical fault displacement is minimal. Scar elevation versus age relationships reveal a marked acceleration after MIS 11, from ~0.08 m/kyr before MIS 11 to ~0.38 m/kyr afterward.

On the horsts, uplift is recorded by a staircase of marine terraces that formed synchronously with the strandplains. Mapping identifies six terraces correlated to MIS 19–MIS 9a. Their geometry indicates limited disruption by normal faulting (contra Binnie et al., 2016). Uplift-rate histories derived from terrace elevations and MIS ages show a clear acceleration after MIS 19: from ~0.14 ± 0.01 m/kyr to ~0.30 ± 0.04 m/kyr on the northern Mejillones Horst, and ~0.29 ± 0.04 m/kyr on the Jorgino Horst.

Spatial segmentation of uplift and forearc tilting

The highest wave-cut notch along the western flanks of Morro Mejillones and Morro Jorgino decreases in elevation by 24 m over ~24 km southward, revealing forearc tilting of ~0.1°.
This spatial gradient has persisted since the Pliocene, evidenced by elevation differences between correlative high terraces (~580 m north vs. ~250 m south). These observations indicate long-term segmented uplift and differentiated forearc flexure along the peninsula.

Normal faulting synchronous with Quaternary uplift

Shoreline scars within Pampa Mejillones show progressively greater tilting from older to younger markers, reflecting the continued development of a rollover structure above the Mejillones Fault. Slip-rate estimates derived from the tilting of shoreline scars and their corresponding MIS ages reveal a systematic northward increase. In the southern sector, fault slip during MIS 17 yields a very low rate of approximately 0.02 ± 0.08 m/kyr, whereas the central segment records a rate of ~0.18 ± 0.02 m/kyr. The highest activity is observed in the northern sector, where slip rates of ~0.29 ± 0.04 m/kyr are associated with MIS 9c shoreline deformation. This spatial trend closely mirrors the uplift-rate variations documented along the peninsula, demonstrating that upper-plate extension and vertical forearc uplift are mechanically coupled processes.

Farther south, in Pampa Aeropuerto, only the youngest Isotopic stages preserved are MIS 9c and 9a beach ridges, suggesting either a decrease in uplift or that normal faulting has accommodated most of the vertical motion, thereby limiting the emergence of younger coastal markers.

Additional evidence of temporal variability in fault slip is recorded in the Tiburón Basin, where a volcanic ash dated at 3.44 ± 0.02 Ma (biotite) and 3.67 ± 0.02 Ma (sanidine) is vertically displaced by ~48–50 m along the Mejillones Fault. Using the mean age of 3.56 Ma, the resulting long-term slip rate of ~0.014 m/kyr confirms that normal faulting during the early uplift stage was very limited. This extremely slow Pliocene slip contrasts sharply with the faster Quaternary rates, demonstrating that fault activity intensified as uplift propagated and accelerated toward the northern peninsula.

DISCUSSION

The earliest uplift of the Mejillones Peninsula occurred during the Pliocene and was restricted to the northernmost sector, as evidenced by the higher elevation of the oldest marine terrace in the Mejillones Horst and the minimal fault displacement recorded in the Tiburón Basin. This stage was characterized by very low slip rates on the Mejillones Fault (~0.014 m/kyr) and slow uplift (~0.18 m/kyr), suggesting limited tectonic forcing on the upper plate during this initial phase.
Later uplift began after the final marine transgression at ~755 ka and developed the well-defined terrace staircase along the borders of the horsts, marking the onset of accelerated emergence. The first major acceleration occurred during MIS 19 and subsequently propagated southward, initiating uplift in the central peninsula after MIS 11. This diachronous evolution demonstrates that uplift did not occur uniformly along strike, but rather migrated spatially through time.

The persistent north–south gradient in terrace elevations and the 24 m of vertical difference in the highest wave-cut notch reveal long-term southward tilting of the forearc on the order of ~0.1°. This gradient, sustained since the Pliocene, indicates that uplift has been persistently segmented. The Mejillones Fracture Zone (Maksymowicz, 2015), a NE–SW-trending

structure being subducted obliquely relative to the convergence direction, offers a plausible mechanism for this spatial pattern. Its progressive southeastward migration beneath the upper plate likely transfers differential strain to the forearc, driving the observed temporal and spatial variations in uplift. This deep-seated tectonic control explains why uplift initiated in the north and later propagated toward the southeast, producing a segmented forearc high that acts as a stable, long-term feature of the subduction margin.

Normal faulting along the Mejillones Fault intensified during the late Quaternary, with slip rates increasing from <0.1 m/kyr in the south to ~0.3 m/kyr in the north. This along-strike gradient mirrors the spatial pattern of uplift rates and tilting, indicating that upper-plate extension and vertical forearc deformation are mechanically linked. These findings support a deformation model in which strain is increasingly accommodated by normal faults as uplift accelerates. This behavior is consistent with megathrust segmentation that inhibits the southward propagation of large ruptures (Victor et al., 2011), focusing permanent deformation within the upper plate above a persistently decoupled fault patch. Although some authors have proposed that uplift in northern Chile is driven primarily by coseismic events (Melnick et al., 2016), our long-term observations show that cumulative slip across the upper plate is dominated by the sustained migration of a tectonic uplift domain rather than transient earthquake-cycle displacements.

REFERENCES

Binnie, A., Dunai, T.J., Binnie, S.A., Victor, P., González, G., Bolten, A., 2016. Accelerated late quaternary uplift revealed by 10Be exposure dating of marine terraces, Mejillones Peninsula, northern Chile. Quaternary Geochronology, 36, 12-27, doi: 10.1016/j.quageo.2016.06.005.

Buylaert, J.P., Murray, A.S., Thomsen, K.J., Jain, M., 2009. Testing the potential of an elevated temperature IRSL signal from K-feldspar. Radiation Measurements, 44(5-6), 560-565, doi: 10.1016/j.radmeas.2009.02.007.

Ferraris, F. & Di Biase, F., 1978. Carta Geológica de Chile, Hoja Antolagasta, Región de Antofagasta. *Instituto de Investigaciones Geológicas,* No. 30, 49 p.

Cortés J., González G., Binnie, S. A., Robinson, R., Freeman, S.P.H.T., Vargas G., 2012. Paleoseismology of the Mejillones Fault, northern Chile: Insights from cosmogenic 10Be and optically stimulated luminescence determinations. Tectonics, 31, TC2017, doi: 10.1029/2011TC002877.

González, G., Cembrano, J., Carrizo, D., Macci, A., Schneider, H., 2003. The link between forearc tectonics and Pliocene–Quaternary deformation of the Coastal Cordillera, northern Chile. Journal of South American Earth Sciences, 16(5), 321-342, doi: 10.1016/S0895-9811(03)00100-7.

Krebs, W. N., Aleman, A. M., Padilla, H., Rosenfeld, J. H., & Niemeyer, H. (1992). Age and paleoceanographic significance of the Caleta Herradura diatomite, Península de Mejillones, Antofagasta, Chile. *Andean Geology*, *19*(1), 75-81.

Maksymowicz, A. (2015). The geometry of the Chilean continental wedge: Tectonic segmentation of subduction processes off Chile. Tectonophysics, 659(2015), 183–196. https://doi.org/10.1016/j.tecto.2015.08.007

Marquardt, C., 2005. Déformations Néogénes le long de la Côte Nord du Chili (23°-27° S). In: Avant-Arc des Andes Centrales; PhD thesis, Lab. des Mec. Et Tranferts en Geol. Univ. Toulouse III-Paul Sabatier, Toulouse, France, 212 pp.

Melnick, D., 2016. Rise of the central Andean coast by earthquakes straddling Moho. Nat. Geosci. 9, 401–407. https://doi.org/10.1038/ngeo2683.

Ortlieb, L., Diaz A., Guzman, N., 1996c. A warm interglacial episode during oxygen isotope stage 11 in northern Chile. Quaternary Science Reviews, 15(8–9), 857–871, doi: 10.1016/S0277-3791(96)00062-5.

Vargas, G., Palacios, C., Reich, R., Luo, S., Shen, C., González, G., 2011. U-series dating of co-seismic gypsum and submarine paleoseismology of active faults in Northern Chile (23ºS). Tectonophysics, 497(1-4), 34-44, doi: 10.1016/j.tecto.2010.10.017.

Victor, P., Sobiesiak, M., Glodny, J., Nielsen, S.N., Oncken, O., 2011. Long-term persistence of subduction earthquake segment boundaries: evidence from Mejillones Peninsula, northern Chile. Journal of Geophysical Research: Solid Earth, 116, 22, doi: 10.1029/2010JB007771

INQUA TERPRO Project Cascading Hazards and Mitigation (CHAMP)

Microseismicity and Quaternary deformation along the Puerto Aldea Fault, north-central Chile

González-Alfaro, José (1), Bertrand Potin (1, 2), Constanza Ulloa (3), Sergio Ruiz (1), Gabriel Easton (3), Cristina Ortega (3),Carolina Gutiérrez (2)

(1) Department of Geophysics, University of Chile, Blanco Encalada 2002, Santiago, Chile. Email: josgonal@uchile.cl
(2) Tomos, Santiago, Chile
(3) Department of Geology, University of Chile, Plaza Ercilla 803, Santiago, Chile

Abstract: *The Puerto Aldea Fault (PAF) constitutes the main Quaternary geological structure in coastal north-central Chile. This normal fault exhibits a 60–70 km-long trace, encompassing both subaerial and submarine expressions. Vertical displacements of 2–5 m in Pliocene–Pleistocene units, suggest that crustal earthquakes of Mw ~7.0 may have ruptured the area during the recent geological past. Following the 2015 Mw 8.3 Illapel earthquake, a significant increase in upper-crustal seismicity was observed in the PAF area. In 2022, a field campaign installed 10 temporary broadband seismological stations that recorded microseismic activity over a 7-month period. From the 9,605 detected events, 3,724 occurred in the upper crust (<25 km depth), of which 2,295 were located inland. These results indicate that the recorded microseismicity could be associated with the PAF and likely reflects ongoing upper crustal deformation, offering valuable insights into how the fault operates on both geological and present-day timescales.*

Key words: *Quaternary normal fault, tectonic geomorphology, seismology, subbottom acoustic profiles, subduction margin.*

INQUA TERPRO Project Cascading Hazards and Mitigation (CHAMP)

Remote Sensing-based Geohazard Assessment in Kambarata, Kyrgyzstan

Greenough, Emma (1), Richard Walker (1), Benedict Johnson (1), Max Van Wyk De Vries (2), Ekbal Hussain (3)

(1) Department of Earth Sciences, University of Oxford, Oxford, UK. emma.greenough@reuben.ox.ac.uk
(2) University of Cambridge, Department of Geography, CB2 3EN, UK
(3) British Geological Survey, Keyworth, Nottingham, NG12 5GG, UK

Abstract: *The ongoing India-Eurasia continental collision causes significant and widespread seismic activity in central Asia, with approximately 20 mm per year of north-south shortening accommodated by a diffuse network of active faults spanning the Tien Shan and Pamir mountain ranges. The Kambarata 1 hydroelectric power plant in western Kyrgyzstan is currently in pre-construction stage, so there is motivation to accurately determine and mitigate the surrounding hazard associated with active faults and landslides before construction is completed. Here, we use a combination of analyses of field surveys and high-resolution satellite imagery to improve existing fault maps and recognise previously unidentified gravitational and fault-related surface features in the vicinity of the Kambarata 1 site. We explore the uses and limits of different remote sensing analysis techniques, considering both modern and historical imagery as mapping resources, and the use of repeat radar and optical satellite data as the basis of quantitative monitoring techniques.*

INQUA TERPRO Project Cascading Hazards and Mitigation (CHAMP)

The anatomy of a strike-slip plate boundary fault in a pull-apart basin

Grützner, Christoph (1), Tina Niemi (2), Omar Flores (3), Carlos Perez Arias (4), Aleigha Dollens (2), Jeremy Maurer (5) , Jonathan Obrist-Farner (5)

(1) Institute of Geosciences, Friedrich-Schiller University Jena, Jena, Germany. christoph.gruetzner@uni-jena.de
(2) Earth and Environmental Sciences, University of Missouri-Kansas City, Kansas City, MO, USA
(3) Universidad de San Carlos de Guatemala, Guatemala City, Guatemala
(4) Ingeotecnia, Guatemala City, Guatemala
(5) Geology and Geophysics, Missouri University of Science and Technology, Rolla, MO, USA

Abstract: *The Motagua Fault in Guatemala is part of the plate boundary between the North American and Caribbean plates. At the Estanzuela site, the fault-parallel, elongated topographic depression "Laguneta Los Yajes" is about 2 m lower than its surroundings and interpreted as a pull-apart basin. Since it was seasonally filled with water, the surface rupture of the 1976 M7.5 Earthquake could not be mapped precisely here. We trenched the northern topographic scarp to investigate the boundary fault but did not encounter a distinct major shear zone. Instead, we found distributed deformation. Two additional trenches showed the main fault zone in the center of the depression, and additional structures that accommodate distributed shear. We interpret the fault geometry to be a fault bend rather than a stepover, and we document the evidence for off-fault deformation over 80 m around the main strand at this site.*

Acknowledgements: *This project was conducted as part of the Guatemala GeoHazards IRES program that is funded by an NSF Grant OISE-2153715 to Niemi and a DFG project 529303576 "Active tectonics of the Caribbean-North American plate boundary in Guatemala" to Grützner.*

INQUA TERPRO Project Cascading Hazards and Mitigation (CHAMP)

paleoseismicity.org

Spatial and Temporal Clustering of Earthquakes in a Subduction Setting in Central Aotearoa-New Zealand

Humphrey, Jade (1), Andrew Nicol (1), Rob Langridge (2), Andy Howell (1,2), Matiu Prebble (1), Camilla Penney (1), Jaime Delano (3), Giles Ostermeijer (1), Matt Parker (1), Ryosuke Ando (4)

(1) School of Earth and Environment, University of Canterbury, Private Bag 4800, Christchurch, New Zealand. Email: jade.humphrey@canterbury.ac.nz.
(2) Earth Sciences NZ, 1 Fairway Drive, Avalon, Lower Hutt, New Zealand
(3) WSP, PO Box 1482, 67 Cashel Street, Christchurch, New Zealand
(4) University of Tokyo, 7 Chome-3-1 Hongo, Bunkyo City, Tokyo 113-0033, Japan

Abstract: *Spatial and temporal clustering of fault ruptures, occurring as either multi-fault earthquakes or earthquake sequences, pose hazards that are challenging to forecast. In the central Aotearoa-New Zealand plate boundary, comparisons of paleoearthquake and historic earthquake timings for upper-plate and subduction-interface faults reveal that temporal clustering is common. Temporal clustering is most prominent where upper-plate faults are underlain by, and inferred to be connect with, the subduction interface. Clustering is interpreted to be driven by stress transfer promoted by physical fault linkage along strike and with the plate interface at depth. Quantifying earthquake clustering could have important implications for estimates of time-dependent hazards and estimating plausible rupture lengths and requires further investigation.*

Key words*: Earthquake clustering, Hope Fault, central New Zealand, paleoseismology*

INTRODUCTION

Clustering of paleoearthquakes in space and time has been observed on some faults and fault systems, although it remains unclear whether such clustering is the exception or the norm (Stein et al. 1997; Fraser et al. 2010; Benedetti et al. 2013; Humphrey et al. 2025). Clusters of earthquakes in paleo-records may arise due to co-rupture of multiple faults in the same earthquake (i.e. multi-fault earthquakes) or from sequences of earthquakes that are closely spaced in time (e.g., triggered earthquakes). Long records of paleoearthquakes, both along faults and across fault systems, are critical for understanding earthquake clustering behaviour and assessing the resulting seismic hazard.

We explore evidence for temporal clustering of earthquakes along and across the Pacific and Australian plate boundary in central Aotearoa-New Zealand (A-NZ; Fig. 1A). This region is dominated by networks of sub-parallel dextral faults including the Marlborough Fault System (MFS) and North Island Dextral Fault Belt (NIDFB), which are underlain by the Hikurangi subduction interface. In this study, we compare earthquake timings along the plate boundary system for the Alpine, Hope, Kekerengu faults and the southern Hikurangi Subduction interface (Freund 1971; Knuepfer 1984; Van Dissen et al. 1991; Holt et al. 1995; Wallace et al. 2012; Nicol et al. 2017; Hatem et al. 2019; Fig 1B). For our analysis, existing paleoseismic data from these faults was augmented with new paleoseismic data from six trenches and reinterpretations of two published logs on the Hope Fault. We generate a Holocene earthquake record for the Conway section of the Hope Fault (HF-CS), which is the longest on-fault multi-earthquake record for any major plate boundary structure in A-NZ. We then compare our observations from along the plate boundary to results for the Wairarapa, Wellington and Ōhāriu faults across the plate boundary in central A-NZ by Humphrey et al. (2025).

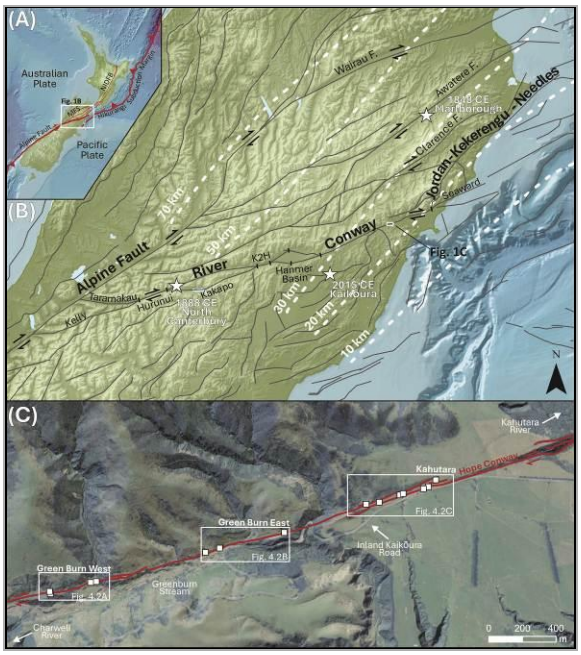

Figure 1: *(A) Tectonic setting of Aotearoa-New Zealand showing main plate boundary structures. The Marlborough Fault System (MFS) forms part of plate boundary in the northern South Island, with faults likely connecting to structures in the North Island Dextral Fault Belt (NIDFB) across the Cook Strait. (B) Major active faults within and near the MFS, with faults and fault sections studied here shown in bold. The depth to the Hikurangi subduction interface is shown in white dashed lines (Williams et al. 2013). Sections of the Hope Fault are as defined in the Community Fault Model (CFM) Version One (Seebeck et al. 2023). "K2H" is the Kakapo 2 Hanmer section, and four sections (Hanmer NW, Hanmer, Hope: Hanmer SW, Hope: Hanmer SE) are collectively labelled here as the Hanmer Basin. The map shows the epicentral locations of the 1848 Mw 7.4-7.7 Awatere, 1888 Mw 7.1 North Canterbury and 2016 Mw 7.8 Kaikōura earthquakes (Downes et al. 2014). (C) The 2.5 km part of the Hope Conway section (HF-CS) that*

is the focus of the paleoseismic investigations in this paper. The Green Burn locality is here divided into Green Burn West and East. For reference, the Charwell and Kahutara rivers are indicated, and the Inland Kaikōura Road labelled. The red lines are the simplified fault traces identified from lidar. Hillshade is layered on top of aerial imagery.

DATA AND METHODS

We excavated five trenches and three pits over three campaigns, reinterpreted (and partly reopened) two trenches and generated age models for six trench sites along 2.5 km of the HF-CS (*Fig. 1C*). These sites were divided into three sites for analysis (Kahutara, Green Burn East and Green Burn West; *Fig 1C*). The Kahutara locality is characterised by a pull-apart basin and included the excavation of four new trenches (Heke Ngahere 1-4: i.e. *Fig 2*). Green Burn East and West are both dominated by shutter ridges and fan and slope processes. One new trench (Mānuka Grove) was excavated at Green Burn East as well as three pits (Pīwakawaka Bush 1-3) at paleochannels that are displaced by the fault. An existing trench (Green Burn East; Hatem et al. 2019) was also partly re-excavated and reinterpreted. The Green Burn West 2 trench (Hatem et al. 2019) at the Green Burn West locality was also reinterpreted.

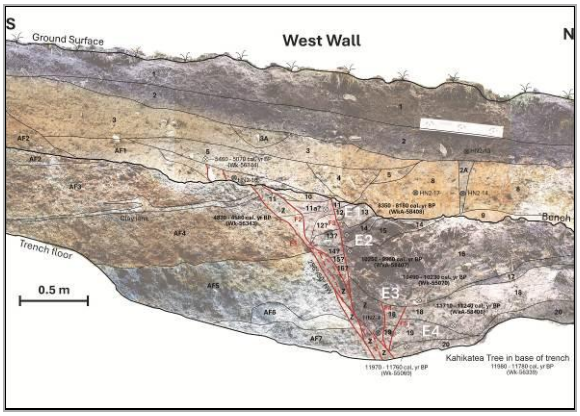

Figure 2: *Heke Ngahere 2 trench from the Kahutara locality. Dark organic rich material is juxtaposed against alluvial fan material across a northwest dipping fault in the southern strand of the pull-apart basin. The oldest basin sample was recovered from this trench at ~12,000 cal. yr BP, revealing that the trenches in this basin may have the potential to generate Holocene records.*

Bulk samples were taken at many of the new trenches and where possible, radiocarbon material with lower residence time (i.e. macrobotanical material such as seeds) was selected and sent for AMS dating. OxCal models were developed for each trench following published methodologies (Lienkaemper et al. 2009; Fraser et al. 2010; Humphrey et al. 2025). We use Probability Density Functions (PDFs) to show the timing of each earthquake derived from the OxCal analysis for each trench along strike (*Fig. 3*) and combined age models for fault segments and faults (*Fig. 4*).

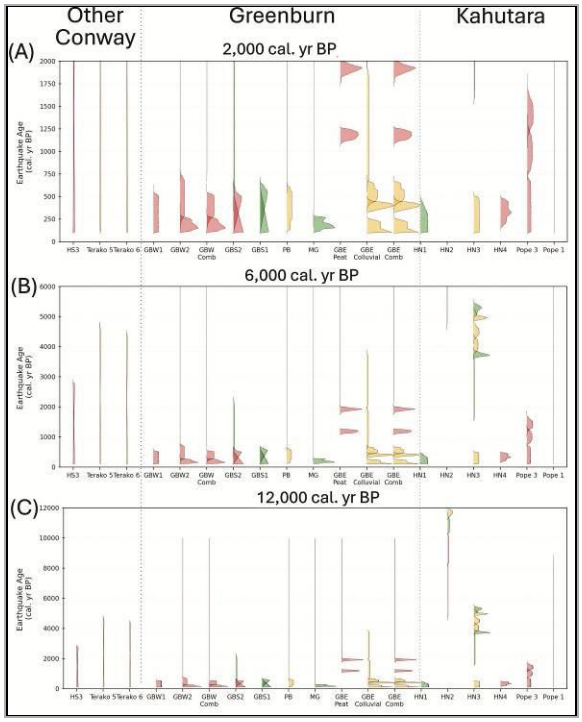

Figure 3: *Probability Density Functions for each trench site and locality plotted along strike west to east for (A) 2,000 cal. yr BP, (B) 6,000 cal. yr BP and (C) 12,000 cal. yr BP. A traffic light system is used to evaluate the quality of evidence used to determine if the event was an earthquake following the New Zealand Paleoseismic Site Database, Version 1.0, where green (A) = strong, yellow (B) = moderate, and red (C) = weak (Litchfield et al. 2023).*

We used the combine function in OxCal to generate a record for the HF-CS (*Fig. 4 – panel 3*). We then compare this combined HF-CS record to earthquakes timings derived from off-fault Alpine Fault records (Howarth et al. 2021), Hope River section trenches (Langridge et al. 2013), Kekerengu Fault trenches (Morris et al. 2023) and lagoons for the southern Hikurangi subduction interface record (Clark et al. 2019; Pizer et al. 2021; Pizer et al. 2023) for the last 2,000 cal. yr BP.

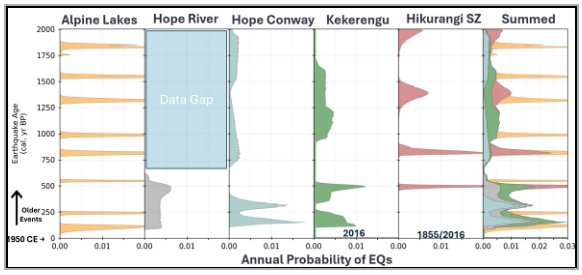

Figure 4: *Comparison of earthquake timings from Alpine Fault lake records (Howarth et al. 2021), Hope River (Langridge et al. 2013), Hope Conway, Kekerengu (Morris et al. 2023) and southern Hikurangi subduction interface (Clark et al. 2019; Pizer et al. 2021; Pizer et al. 2023) for the last 2,000 cal. yr BP. Many faults have poorly constrained records (i.e. wide PDFs) or data gaps (i.e. Hope River) that would be resolved with further trenching or reanalysis of existing data.*

RESULTS

Our trenching uncovered Holocene age material and represents one of the first opportunities in A-NZ to generate an on-fault Holocene record for a major plate boundary fault. We found the record to be discontinuous with inferred complete or partially complete data separated by intervals with little or no earthquake information (*Fig. 3*). There are at least two basin wide unconformities at the Kahutara locality between 2000-4000 cal. yr BP and 6000-8000 cal. yr BP (*Fig. 3*).

For the HF-CS, we determined there had been a total of 12 earthquakes in the last 12,000 cal. yr BP (including the ~4,000 years of no records (*Fig. 4 - Panel 3*). We focus our comparisons to the last 2,000 cal. yr BP where records on other plate boundary structures are more complete. In this period, four earthquakes have occurred on the HF-CS (Fig. 1, Conway section). These earthquakes are estimated to have occurred at the following times: 235 – 120 cal. yr BP (E1), 395 - 250 cal. yr BP (E2), 1325 – 695 cal. yr BP (E3) and 1990 – 1470 cal. yr BP (E4).

DISCUSSION

Along plate boundary clustering

We evaluate potential rupture lengths along the Hope Fault. The 1888 CE North Canterbury Earthquake (*Fig. 1*), ruptured the Hope River segment and terminated west of the HF-CS. The paleoearthquake records from the Hope River are short (< 750 cal. yr BP) and, at present, cannot confidently determine if 1888 CE rupture pattern is the norm. Preliminary results suggest the timings of observed earthquakes Hope River segment do correlate well with HF-CS, which may suggest that there is some temporal clustering between these segments.

The timing of the four earthquakes observed on the HF-CS also overlap with earthquakes recorded on the Kekerengu Fault. It is likely that interaction is occurring along strike between these faults and contributing to the observed clustering. The Kekerengu Fault has an additional rupture during the 2016 CE Kaikōura Earthquake, which included up to 20 upper-plate faults and a partial subduction interface rupture (Litchfield et al. 2018; Mouslopouou et al. 2019). The HF-CS did not rupture in this earthquake despite being within 5 km of other surface ruptures.

The major plate boundary structures, the Alpine Fault and the southern Hikurangi interface, have contrasting earthquake records over the last 2,000 cal. yr BP. The Alpine Fault records derived from lake cores (Howarth et al. 2021) revealed 9 events in the last 2,000 cal. yr BP with a recurrence interval approximately half that of the subduction interface. The interface records are also derived from off-fault sites (Clark et al. 2019; Pizer et al. 2021, 2023), with two probable historic ruptures in 1855 and 2016 CE. The small uncertainties of the Alpine Fault PDFs make the apparent overlap with timings on other faults less visually striking. The variations in both recurrence intervals and uncertainty complicates current methods used to test for overlap between PDFs and further statistical analysis is required to address the clustering significance between these faults.

Across plate boundary clustering

In Humphrey et al. (2025), two of the upper-plate faults (Wairarapa and Wellington faults) exhibited a strong clustering behaviour in a 5,500 year earthquake record. In this across plate boundary system, north of Cook Strait from the Hope Fault (*Fig. 1*), the Hikurangi subduction zone connects at seismogenic depths with these two faults and is thought to facilitate stress interactions and co-rupture during earthquakes that would lead to the strong clustering relationship observed (Humphrey 2025). Timings of earthquakes on the subduction interface also coincided with the timings of studied upper-plate faults in windows of 200-500 years, in >50% of the observed windows (*Fig. 5*). The authors conducted tests and concluded that the observed clustering was likely caused by these interactions and not simply due to Poisson earthquake timings.

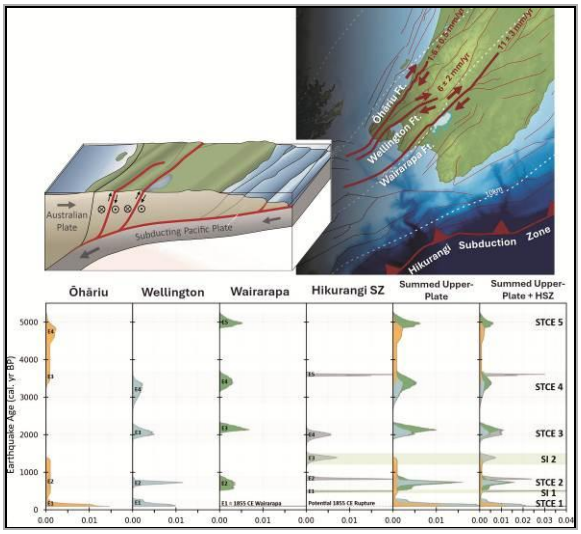

Figure 5: *Earthquake timings produced for upper-plate faults in the lower North Island of A-NZ by (Humphrey et al. 2025). Faults are thought to connect at depths where the subduction interface is likely contributing to the facilitation of stress transfer resulting in the strong clustering patterns observed between upper-plate faults and with the subduction interface.*

In the along fault plate boundary setting, the role of the subduction interface is less clear. The more eastern parts of the Hope (i.e. HF-CS and Seward) and Kekerengu faults, are likely to intersect the subduction interface at seismogenic depths and to be influenced by stress interactions associated with subduction. Stress transfer from the Alpine onto the Hope Fault and other unstudied faults in the MFS is unclear and requires further analysis.

Future work

Discriminating between multi-fault and sequence earthquake models is not currently possible with paleoearthquake records, as these data typically do not

have sufficient temporal resolution (Humphrey et al., 2025). Additional trenching and integration with physics-based earthquake simulator models may improve our understanding of the drivers of earthquake clustering. Further development of testing for earthquake clustering is still required to quantify the frequency of earthquake clustering, particularly for faults or fault systems with varying recurrence intervals, record completeness and certainty. Quantifying earthquake clustering could have important implications for estimates of time-dependent hazards and estimating plausible rupture lengths.

Acknowledgements: We thank the Resilience to Nature's Challenges and the Natural Hazards Commission for funding this research.

REFERENCES

Benedetti L, Manighetti I, Gaudemer Y et al. 2013. Earthquake synchrony and clustering on Fucino faults (Central Italy) as revealed from in situ 36Cl exposure dating. Journal of Geophysical Research: Solid Earth 118: 4948-4974.

Clark KJ, Howarth J, Litchfield N et al. 2019. Geological evidence for past large earthquakes and tsunamis along the Hikurangi subduction margin, New Zealand. Marine Geology 412: 139-172.

Downes G, Dowrick D 2014. Atlas of isoseismal maps of New Zealand earthquakes - 1843-2003. GNS Science Monograph 25 [CD]. Second Ed. ed. Lower Hutt, New Zealand, Institute of Geological and Nuclear Sciences.

Fraser J, Vanneste K, Hubert-Ferrari A 2010. Recent behavior of the North Anatolian Fault: Insights from an integrated paleoseismological data set. Journal of Geophysical Research: Solid Earth 115: 1-27.

Freund R 1971. The Hope Fault a Strike Slip Fault in New Zealand, New Zealand Department of Scientific and Industrial Research.

Hatem AE, Dolan JF, Zinke RW, Van Dissen RJ, McGuire CM, Rhodes EJ 2019. A 2000 Yr Paleoearthquake Record along the Conway Segment of the Hope Fault: Implications for Patterns of Earthquake Occurrence in Northern South Island and Southern North Island, New Zealand. Bulletin of the Seismological Society of America 109: 2216-2239.

Holt WE, Haines A 1995. The kinematics of northern South Island, New Zealand, determined from geologic strain rates. Journal of Geophysical Research: Solid Earth 100: 17991-18010.

Howarth JD, Barth NC, Fitzsimons SJ et al. 2021. Spatiotemporal clustering of great earthquakes on a transform fault controlled by geometry. Nature Geoscience 14: 314-320.

Humphrey JA 2025. Spatial and temporal clustering of large-magnitude earthquakes in the Central Aotearoa-New Zealand plate boundary: a thesis submitted in partial fulfilment of the requirements for the degree of Doctor of Philosophy in Geology at the School of Earth and Environment, University of Canterbury. Unpublished thesis, [University of Canterbury], Christchurch, New Zealand.

Humphrey J, Nicol A, Howell A et al. 2025. Spatial and Temporal Clustering of Large Earthquakes on Upper-Plate and Subduction Thrust Faults Along the Southern Hikurangi Subduction Margin, Aotearoa-New Zealand. Bulletin of the Seismological Society of America: 25.

Knuepfer PLK 1984. Tectonic geomorphology and present-day tectonics of the alpine shear system, South Island, New Zealand (Neotectonics, Faults). Unpublished thesis, University of Arizona.

Langridge RM, Almond PC, Duncan RP 2013. Timing of late Holocene paleoearthquakes on the Hurunui segment of the Hope fault: Implications for plate boundary strain release through South Island, New Zealand. GSA Bulletin 125: 756-775.

Lienkaemper J, Ramsey C 2009. OxCal: Versatile Tool for Developing Paleoearthquake Chronologies-A Primer. Seismological Research Letters 80: 431-434.

Litchfield NJ, Villamor P, Van Dissen RJ et al. 2018. Surface Rupture of Multiple Crustal Faults in the 2016 Mw 7.8 Kaikōura, New Zealand, Earthquake. Bulletin of the Seismological Society of America 108: 1496-1520.

Litchfield N, Humphrey J, Morgenstern R, Langridge RM, Coffey GL, Van Dissen RJ 2023. The New Zealand Paleoseismic Site Database, Version 1.0. Seismological Research Letters 95: 64-77.

Morris P, Little T, Van Dissen R et al. 2023. A revised paleoseismological record of late Holocene ruptures on the Kekerengu Fault following the 2016 Kaikōura earthquake. New Zealand Journal of Geology and Geophysics 66: 342-363.

Mouslopoulou V, Saltogianni V, Nicol A et al. 2019. Breaking a subduction-termination from top to bottom: the large 2016 Kaikōura Earthquake, New Zealand. Earth and Planetary Science Letters 506: 1-10.

Nicol A, Seebeck H, Wallace L 2017. Quaternary Tectonics of New Zealand. Pp. 1-34.

Pizer C, Clark KJ, Howarth J et al. 2021. Paleotsunamis on the southern Hikurangi Subduction Zone, New Zealand, show regular recurrence of large subduction earthquakes. The Seismic Record 1: 75-84.

Pizer C, Clark KJ, Howarth J et al. 2023. A 5000 yr record of coastal uplift and subsidence reveals multiple source faults for past earthquakes on the central Hikurangi margin, New Zealand. GSA Bulletin 136: 2702-2722.

Seebeck H, Van Dissen RJ, Litchfield NJ et al. 2023. The New Zealand Community Fault Model – version 1.0: an improved geological foundation for seismic hazard modelling. New Zealand Journal of Geology and Geophysics 67: 209-229.

Stein RS, Barka AA, Dieterich JH 1997. Progressive failure on the North Anatolian fault since 1939 by earthquake stress triggering. Geophysical Journal International 128: 594-604.

Van Dissen R, Yeats RS 1991. Hope fault, Jordan thrust, and uplift of the seaward Kaikoura Range, New Zealand. Geology 19: 393-396.

Wallace L, Barnes P, Beavan J et al. 2012. The kinematics of a transition from subduction to strike-slip: An example from the central New Zealand plate boundary. Journal of Geophysical Research 117: 1-24.

Williams CA, Eberhart-Phillips D, Bannister S et al. 2013. Revised interface geometry for the Hikurangi Subduction Zone, New Zealand. Seismological Research Letters 84: 1066-1073.

INQUA TERPRO Project Cascading Hazards and Mitigation (CHAMP)

Developing a fault segmentation model for seismic hazard assessment in intraplate regions: insight from the Yangsan Fault system, SE Korea

Kim, Taehyung (1), Jin-Hyuck Choi

(1) Active Tectonic Research Center, Korea Institute of Geoscience and Mineral Resources (KIGAM), Daejeon 34132, Republic of Korea. Email: adrian0305@kigam.re.kr

Abstract: *Fault models are fundamental input data for Seismic Hazard Analysis (SHA). In tectonically active regions, these models are readily constructed from surface ruptures of historical earthquakes. However, in slow-deforming intraplate regions like the Korean Peninsula, constructing fault models is challenging due to the scarcity of surface-rupturing records and the modification of fault traces by erosion. Here, we propose a methodology for identifying the segmentation geometry of strike-slip fault systems in such regions. Our approach utilizes geometric and structural discontinuities as primary criteria, supplemented by along-fault variations in lithology and geomorphology. We apply this method to the Yangsan Fault (YF), a major structure in South Korea. The ~200 km-long YF is divided into 12 to 15 segments, primarily controlled by fault bends. This segmentation correlates well with available paleoseismological data, suggesting that inherited structural geometries control rupture behavior even in slow-deforming settings.*

Key words*: fault segmentation, paleoseismology, intraplate faults, seismic hazard, Yangsan Fault*

INTORDUCTION

Seismic Hazard Analysis (SHA) aims to mitigate the damage from future large earthquakes by assessing ground shaking levels. Fault models, which specify spatial geometry and slip rates, are critical components of SHA (Field et al., 2014). In regions with frequent large earthquakes, such as the Western US or New Zealand, fault models are often based on clear traces of historical surface ruptures (Stirling et al., 2012; Hatem et al., 2022).

However, in slowly deforming intraplate regions, constructing reliable fault models is problematic. Large earthquakes have long recurrence intervals, often exceeding historical records, and erosion rates may outpace tectonic deformation, obscuring active fault traces (Villamor et al., 2012). Despite these challenges, densely populated areas in these regions, such as South Korea, require robust SHA.

This study proposes a systematic workflow to define the segmentation geometry of strike-slip faults in slow-deforming regions where surface rupture traces are indistinct. We employ a multidisciplinary approach combining geological mapping, geophysics, and structural analysis. We demonstrate the efficacy of this method through a case study of the Yangsan Fault (YF), the most prominent seismogenic structure in the southeastern Korean Peninsula.

METHODOLOGY: CRITERIA FOR FAULT SEGMENTATION

We established a procedure to construct fault models based on the premise that large earthquakes rupture along pre-existing crustal-scale fault systems. The workflow involves three main steps: defining the fault trace, identifying segmentation boundaries, and determining segment lengths.

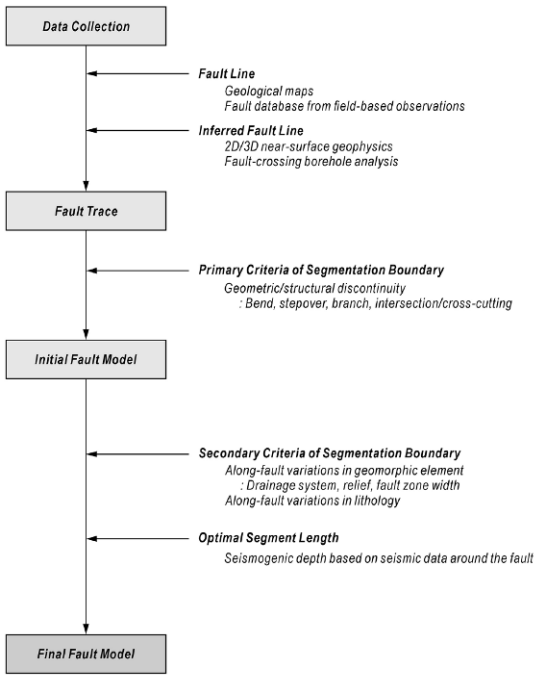

Figure 1: *Workflow for the development of fault models in slow-deforming regions (Kim and Choi, 2024).*

Defining the Fault Trace

In the absence of clear surface ruptures, the fault trace is compiled from geological maps (1:50,000 to 1:1,000,000 scale) and field observations of fault cores. In areas covered by young sediments, multidisciplinary methods

are required. We suggest using geophysical surveys (gravity, electrical resistivity) and borehole drilling to infer fault locations beneath the subsurface by detecting anomalies in basement depth or lithology.

Segmentation Criteria

Once the trace is defined, segmentation is performed using a hierarchy of criteria:

1. Primary Criteria (Geometric/Structural): We identify structural discontinuities that act as barriers to rupture propagation. These include fault bends (changes in strike >5°), stepovers, branches, and intersections (Biasi and Wesnousky, 2017).
2. Secondary Criteria (Lithological/Geomorphic): Along-fault variations in lithology and geomorphic features (drainage systems, topographic relief) are used to refine boundaries. These variations often reflect the long-term segmented evolution of the fault.
3. Optimal Segment Length: The minimum length of a segment is constrained by the seismogenic depth derived from local seismicity (Klinger, 2010).

CASE STUDY: THE YANGSAN FAULT

The Yangsan Fault (YF) is a mature, right-lateral strike-slip fault extending approximately 200 km NNE-SSW across the southeastern Korean Peninsula. It has a long evolutionary history since the Cretaceous and shows evidence of Quaternary reactivation (Cheon et al., 2020).

Data Integration and Tracing

We compiled fault traces from published geological maps and refined them using data from paleoseismological trenches and outcrops. In sediment-covered valleys, the fault location was constrained using gravity and electrical resistivity surveys, confirmed by borehole data that pinpointed the fault core zone (Lee et al., 2020; Choi et al., 2021).

Segmentation Results

Applying the proposed criteria, the on-land trace of the YF was initially segmented based on geometric bends (>5°) and branches. We then integrated lithological boundaries and geomorphic anomalies (e.g., changes in stream flow direction controlled by fault relief).

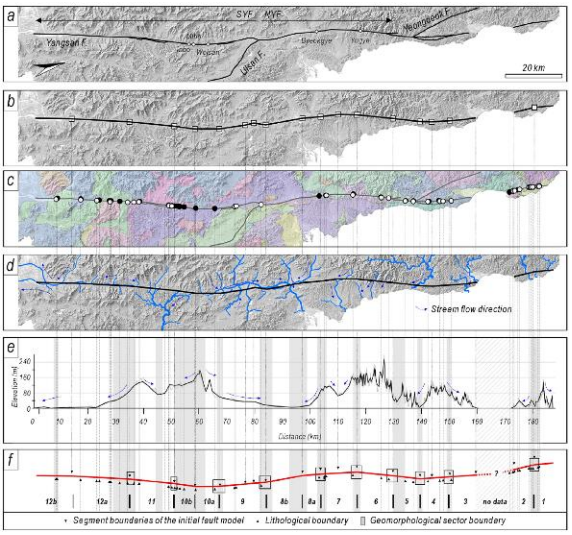

Figure 2: *Final fault model of the Yangsan Fault showing segmentation into 12 major segments.*

The final fault model divides the YF into 12 major segments (some subdivided into sub-segments, totalling up to 15 sections). The lengths of these segments generally correspond to earthquake magnitudes of M 6.0 to 6.9 if ruptured independently, based on empirical relationships (Wells and Coppersmith, 1994).

DISCUSSION

Correlation with Paleoseismicity

To validate our geometric segmentation, we compared the segment boundaries with paleoseismological records. Rupture history analysis reveals that geometric segments often exhibit distinct timing of the Most Recent Event (MRE). For instance, adjacent segments 7 and 8a show consistent MRE timing (<3.2 ka), suggesting they may rupture together, whereas segments 10a and 10b show different rupture histories (MRE 30-17 ka vs. Holocene), implying they act as independent segments (Kim et al., 2023). This confirms that the proposed geometric segmentation reasonably reflects the seismic behavior of the fault.

CONCLUSIONS

We presented a robust methodology for constructing fault models in slow-deforming regions where surface ruptures are rare. By systematically analyzing structural discontinuities and verifying them with lithological and geomorphic data, we successfully defined the segmentation geometry of the Yangsan Fault. This approach provides a necessary framework for performing deterministic and probabilistic SHA in intraplate environments, contributing to better seismic hazard preparedness.

REFERENCES

Biasi, G.P. and Wesnousky, S.G., 2017. Bends and ends of surface ruptures. Bulletin of the Seismological Society of America, 107, 2543-2560.

Cheon, Y., Cho, H., Ha, S., Kang, H.-C., Kim, J.-S., and Son, M., 2019. Tectonically controlled multiple stages of deformation along the Yangsan Fault Zone, SE Korea, since Late Cretaceous. Journal of Asian Earth Sciences, 170, 188-207.

Cheon, Y., Choi, J.-H., Kim, N., Lee, H., Choi, I., Bae, H., Rockwell, T.K., et al., 2020. Late Quaternary transpressional earthquakes on a long-lived intraplate fault: a case study of the Southern Yangsan Fault, SE Korea. Quaternary International, 553, 132-143.

Choi, J.-H., Kobayashi, T., Kim, K.J., Ryoo, C.-R., Shin, Y.H., Lee, S.R., et al., 2021. Research in active tectonics and development of fault segment model for intraplate regions. R&D Report GP2020-014, KIGAM, Daejeon, Korea, 140 p.

Field, E.H., Arrowsmith, R.J., Biasi, G.P., Bird, P., Dawson, T.E., Felzer, K.R., et al., 2014. Uniform California earthquake rupture forecast, version 3 (UCERF3): the time-independent model. Bulletin of the Seismological Society of America, 104, 1122-1180.

Hatem, A.E., Collett, C.M., Briggs, R.W., Gold, R.D., Angster, S.J., Field, E.H., and Powers, P.M., 2022. Simplifying complex fault data for systems-level analysis: earthquake geology inputs for US NSHM 2023. Scientific Data, 9, 506.

Kim, T. and Choi, J.-H., 2024. Segmentation geometry of strike-slip fault systems in slow-deforming regions: a proposed method and case study of the Yangsan Fault, South Korea. Geosciences Journal, 28(5), 625-645.

Kim, T., Choi, J.-H., Cheon, Y., Lee, T.-H., Kim, N., Lee, H., et al., 2023. Correlation of paleoearthquake records at multiple sites along the southern Yangsan Fault, Korea: insights into rupture scenarios of intraplate strike-slip earthquakes. Tectonophysics, 854, 229817.

Klinger, Y., 2010. Relation between continental strike-slip earthquake segmentation and thickness of the crust. Journal of Geophysical Research: Solid Earth, 115, B07306.

Lee, S.R., Kobayasi, T., Ko, L.S., Ko, H.J., Kwon, S.-K., Kwon, C.W., et al., 2020. Research on Geologic hazard assessment of large fault system- focusing on central region of the Yangsan Fault. KIGAM R&D Report NP2018-017, KIGAM, Daejeon, Korea, 502 p.

Stirling, M., McVerry, G., Gerstenberger, M., Litchfield, N., Van Dissen, R., Berryman, K., et al., 2012. National seismic hazard model for New Zealand: 2010 Update. Bulletin of the Seismological Society of America, 102, 1514-1542.

Villamor, M.P., Capote, R., Stirling, M.W., Tsige, M., Berryman, K.R., Martinez-Diaz, J.J., and Martín-González, F., 2012. Contribution of active faults in the intraplate area of Iberia to seismic hazard: the Alentejo-Plasencia Fault. Journal of Iberian Geology, 38, 85-111.

Wells, D.L. and Coppersmith, K.J., 1994. New empirical relationships among magnitude, rupture length, rupture width, rupture area, and surface displacement. Bulletin of the Seismological Society of America, 84, 974-1002.

INQUA TERPRO Project Cascading Hazards and Mitigation (CHAMP)

Displacement and Slip Distribution along Fossil and Active Faults: A Framework for Interpretation and Hazard Assessment

Young-Seog Kim (1), Jin-Hyuk Choi (2), Kwangmin Jin (2)

(1) Major of Environmental Geosciences, Pukyong National University, Busan 48513, Republic of Korea. *ysk7909@pknu.ac.kr.
(2) Korea Institute of Geoscience and Mineral Resources, Daejeon 34123, Republic of Korea

Abstract: *Displacement and coseismic slip variations along faults are essential for understanding fault evolution, rupture dynamics, and seismic hazard, yet structural and geomorphic complexities often obscure such measurements. To address these challenges, this study proposes a concise, multi-proxy framework that integrates geomorphic, stratigraphic, and paleoseismic evidence, supported by insights from the analysis of fossil- and active-fault systems. The framework emphasizes the fundamental controls on displacement and slip distribution; fault type, geometry, linkage, and maturity, incorporating quantitative analyses with high-resolution geomorphic markers. Illustrative examples demonstrate how normalized slip patterns on active ruptures distinguish true rupture barriers from compensating linkage zones, and how displacement–distance (d–x) data reveal cumulative slip increments and strain partitioning between faulting and folding. Contrasting post-depositional and syn-depositional d–x signatures further aid in reconstructing faulting chronology and sedimentation interactions. By reducing interpretive uncertainty in data-limited environments, the framework improves estimates of slip per event, recurrence intervals, and maximum earthquake magnitudes. Ultimately, this approach enhances the reliability of seismic hazard assessment and strengthens our understanding of long-term fault behaviour.*

Key words*: Fault displacement, Co-seismic slip distribution, Fault evolution, Paleoseismology, Hazard assessment.*

1. INTRODUCTION

Accurate analysis of variation in fault displacement and coseismic slip is fundamental for understanding fault evolution, earthquake behaviour, and seismic hazard. These parameters illuminate kinematic history, segmentation, and rupture dynamics, yet they remain difficult to constrain where surface evidence is obscured. The absence of key beds or piercing points, erosion of colluvial wedges, strain partitioning onto secondary structures, and ductile overprints or reactivation commonly obscure true offsets.

Despite such challenges, improving methods for analysing slip distributions is essential for reducing uncertainties in estimates of earthquake magnitude and recurrence. This study outlines a concise framework for evaluating displacement and coseismic slip in active and fossil faults. Built on insights from exhumed fault systems, the framework employs integrated approaches to address slip heterogeneity origins, improve paleoseismic interpretation under data-limited conditions, and underpin more robust seismic hazard assessments.

2. CONCEPTUAL FRAMEWORK FOR FAULT DISPLACEMENT AND SLIP ANALYSIS

Our framework employs a multi-proxy strategy informed by fossil-fault investigations and emphasizes the fundamental controls governing slip distribution: fault type, three-dimensional geometry, faulting history, linkage style, and structural maturity.

Slip patterns reflect interactions between fault kinematics and regional stress. Distinct fault types produce characteristic displacement profiles, while geometric complexity—curvature, bends, and step-overs—modulates deformation and rupture propagation. Segment linkage further influences slip transfer, acting either as barriers or zones of concentration. Fault maturity also shapes displacement patterns.

Given the challenge of obtaining direct offset measurements, an integrated approach involving high-resolution topography, DEMs, and detailed surface mapping is applied. Offset channels, scarps, and stratigraphic markers such as dated terraces or alluvial fans serve as effective markers for cumulative displacement.

Because deformation is distributed across both brittle and ductile components, quantifying strain partitioning within fault cores and damage zones is essential. Fracture analyses, fault-rock characterization, and mapping of strain gradients help constrain total displacement beyond that recorded on a single trace. Additionally, defining the geometry and intensity of the damage zone improves understanding of how strain is disseminated across secondary structures.

By synthesizing these elements, the proposed framework reduces uncertainties inherent in slip-distribution analysis, enhances the proper interpretation of fault systems in complex or data-poor settings, and contributes to more reliable seismic hazard evaluation, including improved estimates of potential magnitudes and event numbers.

3. ILLUSTRATIVE EXAMPLES OF SLIP DISTRIBUTION AND FAULTING HISTORY

3.1. Normalized Slip Distributions on Earthquake Surface Ruptures

Figure 1 presents the along-fault variations in coseismic slip of the 1957 M 8.1 Gobi-Altay, Mongolia, earthquake surface rupture (Choi et al., 2012), an exemplary case for understanding coseismic deformation patterns.

Figure 1a presents the horizontal and vertical offset data, averaged along the rupture to capture spatial variability. Rupture sections where offset is locally high or low reflect

structural or rupture-process complexities. Figure 1b shows the interpolated slip distributions, producing a smoothed, continuous profile that reveals the overall slip distribution. This result highlights characteristic patterns, such as rainbow-shaped distributions for strike-slip faults, and helps identify zones of localized or distributed slip. Figure 1c displays the net slip, obtained by combining horizontal and vertical components. As the total displacement along the surface rupture, net slip provides the most comprehensive measure of coseismic deformation. Figure 1d compares net slip with the plunge of net slip (α). This relationship clarifies along-strike variations in slip-vector orientation and shows the role of linkage zones. Only two linkage zones exhibit pronounced slip troughs that act as actual barriers of lateral rupture propagation, whereas others show slip compensation rather than termination. These observations emphasize that geometric complexities vary in their capacity to impede rupture propagation.

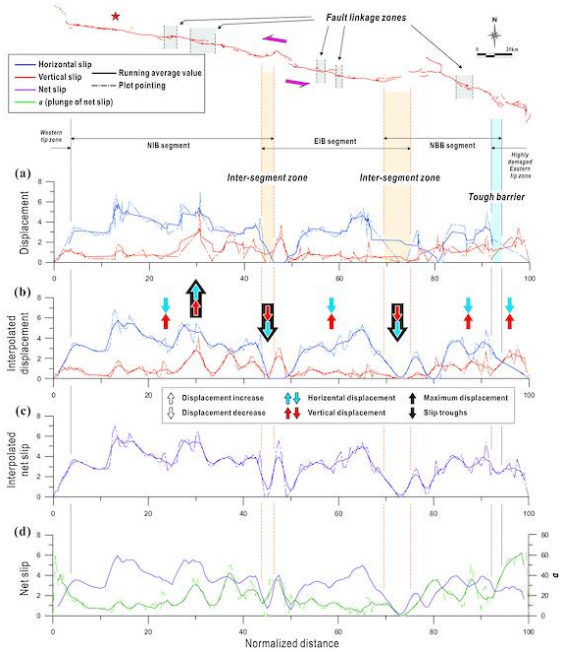

Figure 1: *Normalized slip distributions along the 1957 Gobi-Altay, Mongolia, earthquake surface rupture (Choi et al., 2012). (a) Horizontal and vertical slip data sampled by running average value. (b) Interpolated slip distributions. (c) Net slip data calculated using horizontal and vertical slip amounts. (d) Comparison between net slip distribution and plunge of net slip (α value). Only two fault linkage zones, which show slip troughs, act as barriers, whereas slip compensation is common at fault linkage zones.*

3.2. Displacement-Distance (d–x) Data for Cumulative Offset

Figure 2 presents displacement–distance (d–x) data from the southern (a) and northern (b) walls of a reverse fault, illustrating how cumulative displacement is quantified through offsets of a specific geological unit (Kim et al., 2011). Each point on the d–x plot represents the displacement of that unit across the fault. Although the two profiles are not identical, they display similar overall trends, indicating consistent long-term slip behaviour despite local variations. Both profiles exhibit distinct step-like patterns, interpreted as displacement cumulated by past fault activity or changes in slip rate. These steps likely reflect the integrated slip of multiple earthquake events over geological timescales.

The data also reveal patterns related to fault-related folding. While folding displacement remains broadly constant along the fault, it shows a slight inverse correlation with total displacement, suggesting that some strain is diverted into folding, particularly near fault tips where rupture propagation is terminated. Importantly, folding-related displacement is excluded from the calculation of total fault displacement to ensure that the d–x profiles represent discrete fault slip alone. This separation of deformation components is essential for accurate kinematic interpretation.

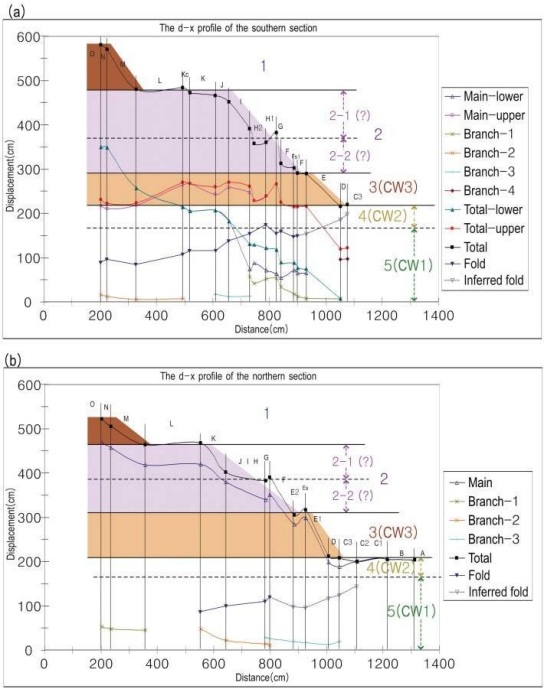

Figure 2: *Displacement–distance (d–x) data for the southern (a) and northern (b) walls (Kim et al., 2011). The two profiles are not identical, but the general trends are similar. It should be noted that the trends show several step-like features that indicate cumulative displacement. The displacements accommodated by fault-related folding are generally constant along the fault. However, the displacements slightly increase in inverse proportion to the total displacement, which may indicate that some of the displacement associated with faulting is accommodated by folding at fault tips. The displacement accommodated by fault-related folding is not included in the amount of the total displacement. Distance is measured from the unconformity contact between the Tertiary volcanic rock and marine terraces. Displacement represents the measured offset of a unit across a fault along the fault traces.*

3.3. Contrasting Models of Faulting History

Figure 3 contrasts post-depositional and syn-depositional faulting models, each producing distinct displacement–distance (d–x) signatures. In the post-depositional model (Fig. 3a), faulting occurs after sedimentation, and the d–x profile of a once-continuous layer exhibits an irregular

slope reflecting variations in slip magnitude or along-strike behaviour (Kim et al., 2011).

In contrast, the syn-depositional model (Fig. 3b) involves fault motion during sediment accumulation. Older layers experience greater cumulative offset, resulting in a generally steeper d–x profile at the erosion surface. Although both models may show irregular trends due to complexities in fault propagation, the steepened profile is a remarkable indicator of recurrent slip during deposition. Distinguishing between these two patterns is essential for reconstructing tectono-sedimentary evolution and identifying persistently active structures.

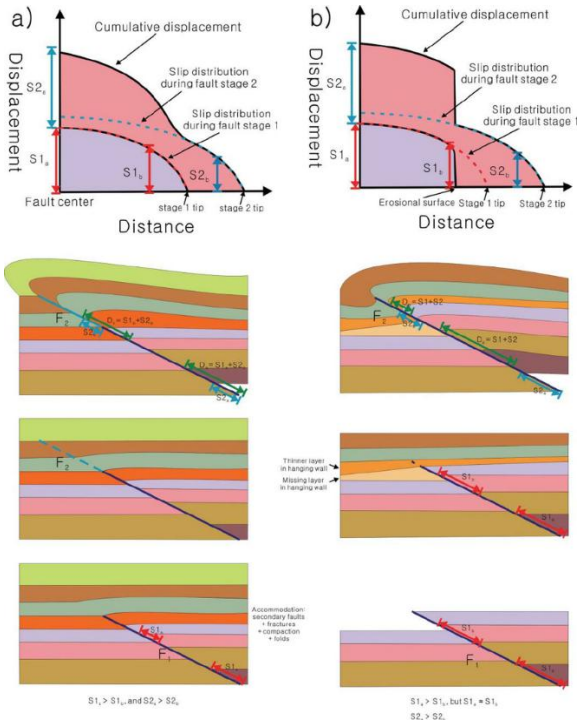

Figure 3: *Two contrasting models of faulting history (Kim et al., 2011). (a) Post-depositional fault model and related d–x profile. (b) Syn-depositional fault model and related d–x profile. Although both profiles show irregular slopes, syn-depositional faulting produces a steeper profile at the erosion surface.*

4. DISCUSSION AND IMPLICATIONS FOR HAZARD ASSESSMENT

The integrated framework, combining insights from fossil-fault studies with geomorphic and stratigraphic proxies, provides a systematic approach for interpreting fault displacement and coseismic slip distributions. Analysis of active ruptures (Fig. 1) helps distinguish true rupture barriers from linkage zones exhibiting slip compensation, improving seismic segmentation models. Interpretation of cumulative d–x data (Fig. 2) clarifies long-term slip behaviour, revealing step-like increments related to past events and the partitioning of strain between discrete faulting and folding.

By reducing uncertainties through multi-proxy evidence and quantitative brittle–ductile strain partitioning, this framework improves the characterization of displacement in environments lacking direct trench exposures. It enables more reliable estimates of slip per event, recurrence intervals, and long-term rupture characteristics, which are key inputs for probabilistic seismic hazard assessments. Improved understanding of slip heterogeneity supports better constraints on maximum earthquake magnitudes and cumulative displacement histories, enhancing the robustness of seismic hazard evaluations, particularly in intraplate settings where fault activity is subtle.

5. CONCLUSION

Accurate characterization of variation in fault displacement and coseismic slip is essential for interpreting fault mechanics and seismic hazard. The proposed framework integrates geomorphic and stratigraphic surrogates with quantitative analyses of deformation partitioning to address common data limitations. Through the combined evaluation of slip distributions, cumulative d–x behaviour and faulting history models, the approach clarifies sources of slip variability and improves paleoseismic reconstruction. Ultimately, it contributes to more reliable assessments of rupture potential, earthquake magnitudes, and event frequencies, thereby strengthening seismic hazard mitigation efforts.

Acknowledgements: This research was supported by a grant(2022-MOIS62-001(RS-2022-ND640011)) of National Disaster Risk Analysis and Management Technology in Earthquake funded by Ministry of Interior and Safety (MOIS, Korea).

REFERENCES

Choi, J.-H., Jin, K., Enkhbayar, D., Davvasambuu, B., Bayasgalan, A., & Kim, Y.-S., 2012. Rupture propagation inferred from damage patterns, slip distribution, and segmentation of the 1957 MW 8.1 Gobi-Altay earthquake rupture along the Bogd fault, Mongolia. *Journal of Geophysical Research*, 117, B12401.

Kim, Y.-S., Peacock, D.C.P., & Sanderson, D.J., 2004. Fault damage zones. *Journal of Structural Geology*, 26, 503-517.

Kim, Y.-S., Kihm, J.-H., & Jin, K., 2011. Interpretation of the rupture history of a low slip-rate active fault by analysis of progressive displacement accumulation: an example from the Quaternary Eupcheon Fault, SE Korea. *Journal of the Geological Society, London*, 169, 273-288.

Revisiting the Mw6.6 1968 Meckering, Australia, slip distribution using optical correlation

Klinger, Y. (1), A. Delorme (1), L. Zhang (1) and T. King (2)

(1) Université Paris Cité, Institut de physique du globe de Paris, CNRS, Paris France
(2) Geoscience Australia, Camberra, Australia

Abstract: *The 1968 Mw6.6 Meckering earthquake, Australia, is a typical intracontinental earthquake affecting a slow deformation region. The general deformation pattern indicates dominant thrusting with some component of dextral lateral offset. A post-earthquake field survey allowed to get the rupture trace and some sense of the slip distribution along strike, mostly based on survey of human-made features (roads, fences...) Here, taking advantage of recent advances in optical image correlations, especially in the ability to constrain common tight points between old diachronic air photographs, we compute differential topography between images acquired in 1962 and 1972 to recover detail of the vertical slip distribution. Massive changes did occur during the decade between the two periods of image acquisition, due to farming and reallocation of land use. This makes optical correlation for horizontal displacement more complicated and we could only recover measurements along long-term permanent features such as paved road.*

INQUA TERPRO Project Cascading Hazards and Mitigation (CHAMP)

paleoseismicity.org

Paleoseismicity of the Rieti Basin (Central Apennines, Italy): insights on faults interaction and multisegment ruptures

Livio, Franz A. (1), Anna M. Blumetti (2), Valerio Comerci (2), Maria F. Ferrario (1), Marco Caciagli (3), Pio Di Manna (2), Luca Guerrieri (2), Kathleen Nicoll (4), Marco Pizza (1), Argelia Silva Fragoso (1), Emanuele Scaramuzzo (1), Frank Thomas (1), Giorgio Tringali (1), Alessandro M. Michetti (1,6)

(1) Università degli Studi dell'Insubria, Como, Italy.
(2) ISPRA, Geological Survey of Italy, Roma, Italy.
(3) Istituto Nazionale di Geofisica e Vulcanologia, Sezione di Bologna, Italy.
(4) University of Utah, Salt Lake City, Utah USA.
(5) Università degli Studi di Milano, Italy.
(6) Istituto Nazionale di Geofisica e Vulcanologia, Sezione Osservatorio Vesuviano, Napoli, Italy.

Abstract: *The Rieti Basin is a typical example of a rhombohedral tectonic basin within the basin-and-range system of Central Apennines (Italy). Although largely overlooked in paleoseismological research, this area is crucial for understanding how the present-day extensional regime generates high-angle, intersecting basin-bounding normal faults. We excavated 17 paleoseismological trenches along the normal faults bordering the Rieti Basin and identified evidence of 6–15 paleoearthquakes that ruptured these faults during the last ~20 kyr. We found that during sequences of rupture events, which can reach a maximum magnitude Mw 6.5, a consistent spatial and temporal pattern is followed. These results suggest that, for the Rieti Basin, stress transfer among surrounding faults may have played a key role in controlling the spatio-temporal sequence of earthquakes.*

Key words*: Central Italy, extensional tectonics, paleoseismology, Coulomb Stress Transfer*

INTRODUCTION

The Central Apennines in Italy represent one of the most studied regions worldwide for active tectonics and paleoseismology, providing a benchmark dataset for extensional domains and seismic hazard assessment (e.g., Roberts and Michetti, 2004; Galli et al., 2008, 2011; Roberts et al., 2025). Despite extensive research, the Rieti Basin—a fault-bounded intermountain depression in the axial sector of the Apennines—remains relatively underexplored. This basin, shaped by Plio-Quaternary extensional tectonics, is characterized by a box-shaped alluvial plain bounded by two sets of nearly orthogonal normal faults. Previous studies identified Late Pleistocene–Holocene seismicity with slip rates of 0.2–0.4 mm/yr (Michetti et al., 1995), yet key questions persist regarding fault interactions and earthquake rupture scenarios. Between 2020 and 2022, new investigations funded by the Italian Government included 17 paleoseismic trenches, 52 radiometric dates, and geophysical surveys along urbanized fault zones. These data revealed multiple paleoearthquakes over the last ~20 kyr and enable reconstruction of fault slip rates, event chronology, and rupture patterns. We present a space-time paleoseismological diagram to evaluate single versus multi-fault rupture sequences, contributing to improved seismic hazard models for the region.

GEOLOGICAL SETTING

The Rieti Basin lies within the Central Apennines, a region that evolved from a Meso-Cenozoic passive margin into a fold-and-thrust belt during Neogene westward subduction

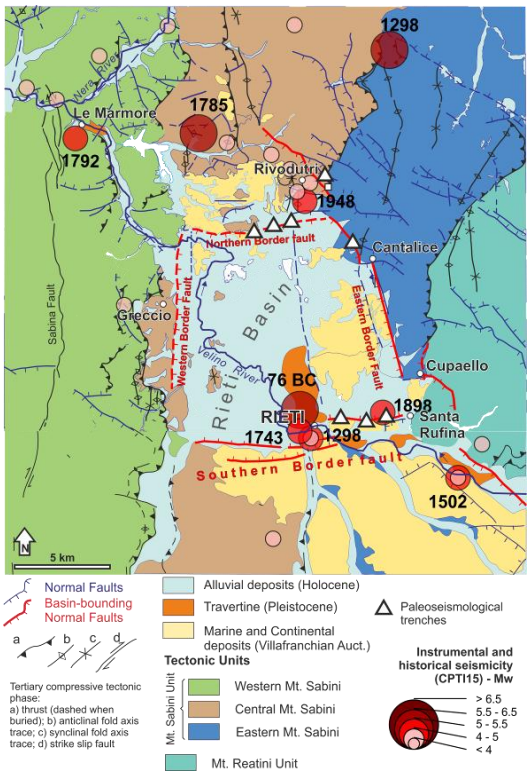

Figure 1: *Geological setting of the Rieti Basin area.*

of the Adriatic plate. Its current setting reflects eastward migration of the accretionary wedge and back-arc extension, producing strong normal faulting earthquakes. The basin belongs to the Umbria-Marche Pelagic Domain, composed of Jurassic–Paleogene carbonates and marls stacked in thrust sheets over an inherited rifted margin

with complex fault patterns. Today, it forms a box-shaped topographic depression bounded by Quaternary normal faults, shaped by extensional tectonics and regional uplift during the Quaternary.

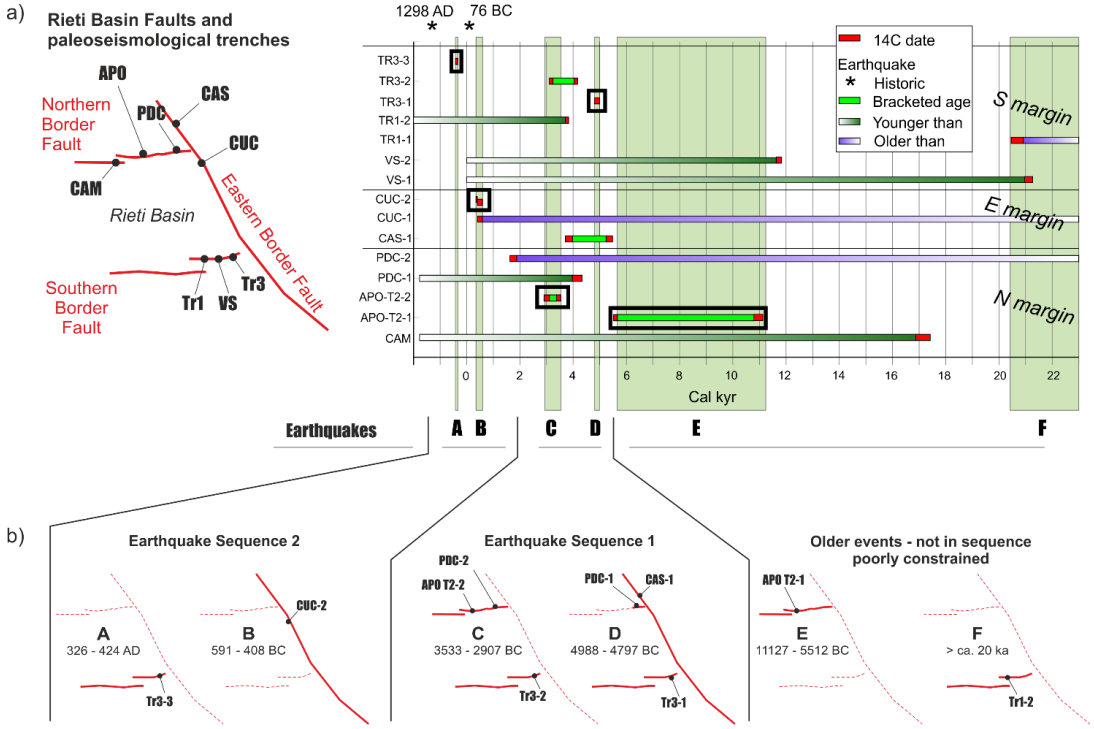

Figure 2: *a) Space-time diagram at the basin scale; on the ordinates the acronym of the earthquakes recognized in each trench; each horizontal bar represents the temporal constraints to the occurrence of each earthquake; black boxes indicate well-constrained events, and the green transparent bars are highlighting possible correlations across trenches; b) summary of the sequence of fault ruptures along the basin-bounding faults, based on well-constrained events (thick continuous lines indicate fault ruptures; thin dashed lines, not assessed).*

Early Pleistocene subsidence was controlled by the eastern border fault, creating a half-graben and thick alluvial deposits, later displaced by hundreds of meters during Middle Pleistocene faulting with slip rates of 0.2–0.4 mm/yr. Regional uplift redirected river systems (Guerrieri et al., 2006), while later tectonics produced an orthogonal fault network. The Pleistocene warm climatic phases favored travertine deposition, notably the Le Marmore platform that dammed the Velino River and accelerated sedimentation in the plain. During the Pleistocene and Holocene, erosional/depositional processes proved more effective than tectonics in shaping the basin's landscape, with deposition rates being greater than fault slip rates. Our investigations focused on three border fault areas during a post-seismic reconstruction program. Historical seismicity includes major events in 76 BCE and 1298, plus several destructive earthquakes within 40 km, and moderate events in 1785, 1898, and 1948, confirming the basin's significant seismic hazard.

METHODS

We applied a multidisciplinary approach to investigate three study areas along the northern, eastern, and southern border faults of the Rieti Basin, combining geophysical prospecting and paleoseismological trenching. Electric Resistivity Tomography (ERT) and Ground Penetrating Radar (GPR) profiles were acquired across major fault strands using high-resolution strategies and processed through advanced inversion and filtering techniques to achieve detailed subsurface imaging. Trench documentation employed photogrammetry, LiDAR scanning, and Structure-from-Motion workflows, with stratigraphic descriptions following international standards to reconstruct deformation history.

A total of 17 trenches were excavated, 13 suitable for paleoseismic analysis, yielding 52 radiocarbon samples calibrated with IntCal20 and integrated with previous trenching data for chronological consistency.

RESULTS

We compiled paleoseismic evidence from newly excavated trenches and previous studies by Michetti et al. (1995), recalibrating all radiocarbon dates using the IntCal20 curve and synthesizing them in a space-time diagram. The diagram shows calibrated age ranges for each event, highlighting five well-constrained earthquakes (Events A–E) and one less-constrained event (F). These events do not overlap in time, suggesting distinct ruptures, though correlations across different trench sites remain speculative due to dating uncertainties. Event A just before the 326 - 424 CE at the SE margin, with no clear historical match, though its age may be consistent with the 76 BCE earthquake reported in historical catalogs. Event B is tightly constrained on the eastern margin at 591–351 BCE, possibly involving multiple fault splays. Between 3–5 kyr BCE, widespread faulting affected all basin margins: Event C (3533–2907 BCE) and Event D (4988–4797 BCE) represent two separate ruptures likely involving the entire 21 km Rieti Basin Fault, consistent with large

displacements exceeding 50 cm and magnitudes around Mw 6.5. Event E, broadly dated between 11127–5664 BCE, activated the northern margin, while Event F predates 20 kyr BP and affected the southern margin. Overall, seven earthquakes are bracketed in time, with recurrence intervals of several millennia, aligning with global patterns for faults of similar length and slip rate.

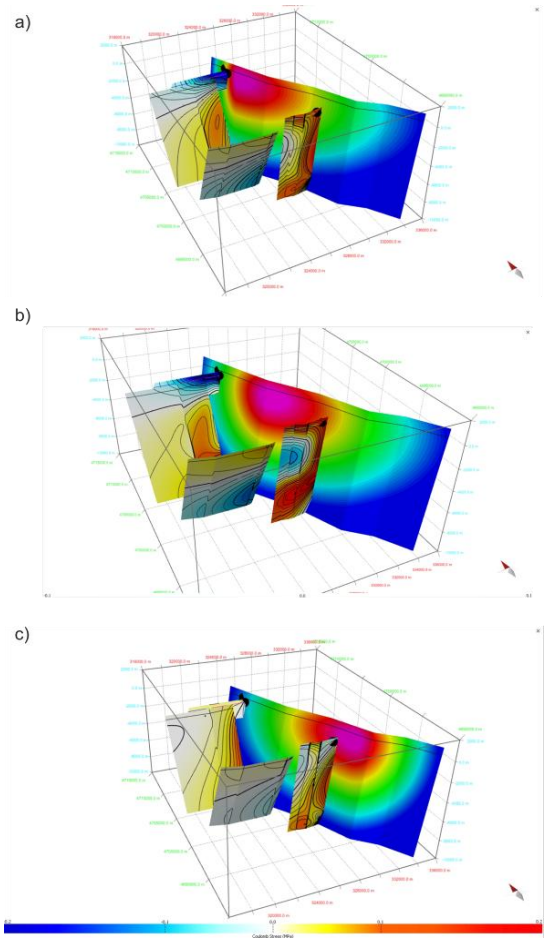

Figure 3: *– results from the CSS modeling investigating how a tapered slip on the principal fault could promote slip on the adjacent structures. Panels a-c show different slip distribution along the Eastern Border Fault (max Displacement fixed at 1 m).*

When considering only well-constrained events, two major earthquake sequences emerge: Sequence 1 began with rupture of the eastern and southern faults around 4988–4797 BCE and ended with northern and southern ruptures around 3533–2907 BCE; Sequence 2 started with an eastern fault rupture between 591–408 BCE and concluded with southern fault movement between 326–424 CE. These findings underscore the potential for multi-fault ruptures and a significant seismic hazard in the Rieti Basin. Under simplified assumptions and boundary conditions, and considering the fundamental geometry of the modeled faults, our analysis indicates that the along-strike distribution of slip on the eastern border fault exerts the primary control on Coulomb Stress transfer (CSS) affecting the adjacent faults (Fgiure 3). The northern and southern boundary faults exhibit minor stress accumulation in their shallow sectors as a consequence of displacement along the eastern border fault.

Notably, the simulation of a slip event analogous to the D earthquake identified through paleoseismological investigations suggests a modest increase in stress on the southern border fault. This finding is consistent with paleoseismological evidence indicating coeval movement of the southern fault during the same seismic episode.

CONCLUSIONS

We here present the first comprehensive paleoseismic characterization of the Rieti Basin in Central Italy, based on 17 newly excavated trenches. We identified and dated up to 15 surface-rupturing earthquakes over the last 20000 years, revealing a previously undocumented tectonic history. The spatial and temporal distribution of these events suggests a recurring rupture pattern starting on the Eastern Border Fault and followed by activity on the northern or southern faults, consistent with the basin's orthogonal fault architecture. Our findings indicate that the maximum credible earthquake could reach Mw 6.5, though chronological resolution limits distinguishing single large ruptures from clustered sequences. These results highlight the importance of paleoseismic studies for seismic hazard assessment in densely populated regions and advocate for similar investigations in other urbanized fault zones.

REFERENCES

Galli, P., Castenetto, S., and Peronace, E.: The macroseismic intensity distribution of the 30 October 2016 earthquake in central Italy (Mw 6.6): Seismotectonic implications, Tectonics, 36, 2179–2191, https://doi.org/10.1002/2017TC004653, 2017.

Galli, P., Galderisi, A., Martino, M., Scarascia Mugnozza, G., and Bozzano, F.: The coseismic faulting of the San Benedetto tunnel (2016, Mw 6.6 central Italy earthquake), in: Tunnels and Underground Cities: Engineering and Innovation Meet Archaeology, Architecture and Art, edited by: Peila, Viggiani and Celestino, 805–811, Taylor & Francis Group, London, ISBN 978-1-138-38865-9, 2020.

Guerrieri, L., Comerci, V., Ferreli, L., Pompili, R., Serva, L., Brunamonte, F., and Michetti, A. M.: Geological evolution of the intermountain Rieti basin (Central Apennines), Mapping Geol. in Italy, SELCA, 123–130, 2006.

Michetti, A. M., Brunamonte, F., Serva, L., and Whitney, R. A.: Seismic hazard assessment from paleoseismological evidence in the Rieti Region (Central Italy), Perspect. Paleoseismol., Assoc. Eng. Geol. Bull., Special Publ., 63–82, 1995

Roberts, G. P., Iezzi, F., Sgambato, C., Robertson, J., Beck, J., Mildon, Z. K., Papanikolaou, I., Michetti, A. M., Faure Walker, J. P., Mitchell, S., Meschis, M., Shanks, R. P., Phillips, R., McCaffrey, K., Vittori, E., Visini, F., and Iqbal, M.: Characteristics and modelling of slip-rate variability and temporal earthquake clustering across a distributed network of active normal faults constrained by in situ 36Cl cosmogenic dating of fault scarp exhumation, central Italy, J. Struct. Geol., 195, 105391, https://doi.org/10.1016/j.jsg.2025.105391, 2025.

Roberts, G. P., and Michetti, A. M.: Spatial and temporal variations in growth rates along active normal fault systems: an example from the Lazio–Abruzzo Apennines, central Italy, J. Struct. Geol., 26, 339–376, 2004.

INQUA TERPRO Project Cascading Hazards and Mitigation (CHAMP)

Paleoseismic evidence for recurrent large earthquakes along the Polochic-Motagua Fault System, Guatemala

McEnaney, Trenton N. (1), Jonathan Obrist-Farner (1), Tina M. Niemi (2), Omar Flores Beltetó (3), Aleigha Dollen (2), Francisco Gomez (4), Jeremy Mauer (1), Carlos Pérez Arias (5)

(1) Geology and Geophysics, Missouri University of Science and Technology, Rolla, MO 65409 USA
(2) Earth and Environmental Sciences, University of Missouri-Kansas City, 5110 Rockhill Road, Kansas City, MO 64110 USA
(3) Universidad de San Carlos de Guatemala, Guatemala City, Guatemala
(4) Department of Geological Sciences, University of Missouri, Columbia, MO 65211 USA
(5) Ingeotecnia, Guatemala City, Guatemala

Abstract: *The 1976 Motagua Earthquake ruptured over 240 km of the North American–Caribbean plate boundary in Guatemala. Despite its significance and potential for severe societal impacts, the long-term seismic behavior of the Motagua Fault remains poorly limited. We present paleoseismic evidence for up to eight surface-rupturing earthquakes identified in three trenches at Gualán over the past 7,000 years. Radiocarbon dating and stratigraphic analysis indicate a maximum recurrence interval of 885 ± 61 years (95% confidence), with temporal clustering and variable interevent times of 400–1,200 years—patterns consistent with other major transform boundaries. Historical and instrumental data suggest seismic activity resumed in the late 1700s, culminating in the 1976 rupture, potentially indicating renewed seismicity after a prolonged period of quiescence. These results demonstrate that contemporary strain is primarily accommodated by slip along the Motagua Fault, with creep dominating the eastern segment and large earthquakes releasing stress along the western segment.*

Key words*: Motagua Fault · Guatemala · Paleoseismology · Central America ·Earthquake · Trench*

INQUA TERPRO Project Cascading Hazards and Mitigation (CHAMP)

Transient Aseismic Vertical Deformation Across the Steeply-Dipping Pisia-Skinos Normal Fault (Gulf of Corinth, Greece)

Mildon, Zoë K. (1), Manuel Diercks (1,2) , Gerald P. Roberts (3), Joanna P. Faure Walker (4), Athanassios Ganas (5), Ioannis Papanikolaou (6), Vassilis Sakas (7), Jenni Robertson (3), Claudia Sgambato (3), and Sam Mitchell (3)

(1) School of Geography, Earth and Environmental Sciences, University of Plymouth, Plymouth, UK (zoe.mildon@plymouth.ac.uk)
(2) Institute of Earth System Sciences, Leibniz University Hanover, Hanover, Germany
(3) School of Natural Sciences, Birkbeck, University of London, London, UK
(4) Department of Risk and Disaster Reduction, University College London, London, UK
(5) Institute of Geodynamics, National Observatory of Athens, Athens, Greece
(6) Department of Natural Resources Development & Agricultural Engineering, Laboratory of Mineralogy and Geology, Agricultural University of Athens, Athens, Greece
(7) Department of Geology and Geoenvironment, Section of Geophysics and Geothermy, National and Kapodistrian University of Athens, Athens, Greece

Abstract: *Geodetically-derived deformation rates are sometimes used to infer seismic hazard, implicitly assuming that short-term (annual-decadal) deformation is representative of longer-term deformation. This is despite geological observations indicating that deformation/slip rates are variable over a range of timescales. Using geodetic data from 2016 to 2021, we observe an up to 7-fold increase in vertical deformation rate in mid-2019 across the Pisia-Skinos normal fault in Greece. We hypothesize that this deformation is aseismic as there is no temporally correlated increase in the earthquake activity (M > 1). We explore four possible physical mechanisms, and our preferred hypothesis is that the transient deformation is caused by centimeter-scale slip in the upper 5 km of the Pisia fault zone. This is the first observation of shallow tectonic (i.e., not related to human activities) aseismic deformation on a normal fault globally. Our results suggest that continental normal faults can exhibit more variable slip/deformation over shorter timescales than previously observed, and thus care should be taken when utilizing geodetic rates to quantify seismic hazard.*

Key words*: normal faulting, central Greece, aseismic deformation, seismic hazard*

INTRODUCTION

Fault slip rates are fundamental for seismic hazard assessment, yet they vary across timescales from millennia to years (e.g. Friedrich et al., 2003). While long-term (thousands to hundreds of thousands of years) variability is well documented through geological markers such as uplifted terraces and cosmogenic dating, short-term changes are harder to detect.

Geodetic techniques like GNSS and InSAR now allow monitoring of annual to decadal deformation, revealing transient episodes in diverse tectonic settings. For example, in subduction zones, slow slip events lasting weeks to months are common (Schwartz & Rokosky, 2007), while strike-slip faults occasionally exhibit short-lived aseismic creep (Rousset et al., 2016). In extensional regions, transient deformation has been observed but often linked to deep detachment faults (Wernicke et al., 2008) or anthropogenic activity (Pepin et al., 2022).

Seismic hazard assessments that include geological fault-based information, for example from field data of geodetic studies, are becoming more common, e.g. UCERF in California (Field et al., 2017) or the New Zealand seismic hazard map (Gerstenberger et al., 2022). InSAR has been used to derive strain rate maps for faults that are presently in their interseismic phase (e.g. (Bird & Kreemer, 2014; Shen et al., 2007)). This assumes that the strain rate derived over a few years are constant and representative of the longer term strain rate.

Here we use geodetic data from the European Ground Motion Service (EGMS) (Costantini et al., 2021) to study a transient phase of deformation on the Pisia-Skinos normal fault in Greece, which we hypothesise is caused by shallow aseismic slip. This is the first example of potentially a slow slip earthquake on a continental normal fault.

TECTONIC SETTING

The Gulf of Corinth is an active rift accommodating north–south extension since ~5 Ma. Extension occurs on east–west trending normal faults, forming a half-graben with north-dipping faults along the southern coast (Jackson et al., 1982; Roberts & Ganas, 2000). The Pisia-Skinos fault system lies on the Perachora Peninsula at the eastern gulf margin. These faults dip ~60° and ruptured during the 1981 earthquake sequence (M_w 6.7 and 6.4). Previous studies show variable slip rates over thousands of years, inferred from marine terraces (Cooper et al., 2007; Roberts et al., 2009) and cosmogenic dating (Mechernich et al., 2018), but short-term variability remained undocumented until now.

There was a swarm of earthquakes around the Perachora peninsula from 2020-2021 (Michas et al., 2022), where the seismicity began at approximately 5 km, which then deepened and moved to the north-west over time. We explore the temporal relation between this swarm and the deformation we observe.

METHODS

Vertical deformation data was downloaded from the EGMS (https://egms.land.copernicus.eu/), which is derived from Sentinal-1 satellite data. In the study area, deformation data is available from 2016-2021, with a magnitude of deformation given every 6 days for points every 100 m.

The deformation data is analysed spatially around the Pisia-Skinos fault (Figure 1a), and as a N-S profile which is approximately perpendicular to the strike of the fault. Average uplift and subsidence values are calculated for three small areas where there is good coherence and spatial coverage of the data.

The baseline between two permanent GNSS stations, THIV and KORI was analysed over the same time period to provide an additional constraint to the rates of deformation changes.

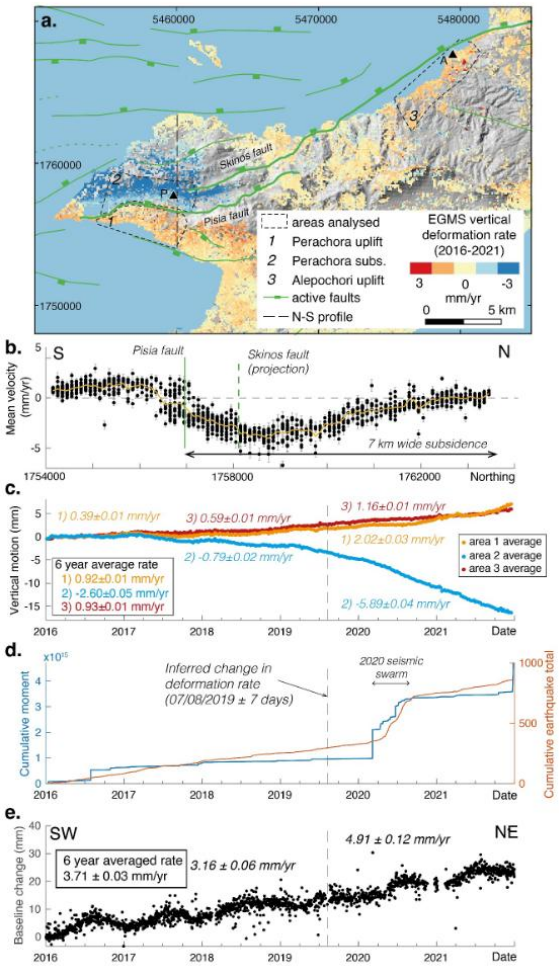

Figure 1: *EGMS deformation data from the Perachora peninsula. a) map of the region. b) Mean rate of vertical deformation across the Pisia fault. c) Time series of three regions analysed. Rates before and after the inferred change are calculated. d) Earthquake activity. e) Time series of GPS baseline change between two nearby stations.*

We use simple modelling to explore the underlying physical mechanism causing the transient phase of deformation. We use Coulomb 3.4 (Toda et al., 2005) to model elastic deformation associated with shallow (0-5 km) slip and deeper slip (15-25 km). We use PSGRN/PSCMP (Wang et al., 2006) to model visco-elastic post-seismic deformation after the 1981 earthquake.

RESULTS

There is a transition from uplift to subsidence that is spatially coincident with the trace of the Pisia-Skinos fault (Figure 1a, b). Around the village of Perachora, the 6-year average uplift rate is 0.92±0.01 mm/yr and the average subsidence rate is -2.60±0.05 mm/yr, this is an uplift/subsidence ratio of ~1/3.

The rate of vertical deformation is non-uniform over the studied time interval (Figure 1c), assuming that there is a single point where the deformation changes, we use piecewise linear regression to constrain the change in deformation to occur on 07/08/2019 (±7 days). There is an up to 7-fold increase in the vertical rate of deformation. There is no temporally correlated increase in the number of earthquakes, nor the cumulative moment released (Figure 1d). The increase in the rate of deformation does not temporally correlate with the onset of the 2020-2021 seismic swarm.

We hypothesise that there are four possible tectonic mechanisms that could explain the vertical deformation observed, and we use simple modelling to explore these.

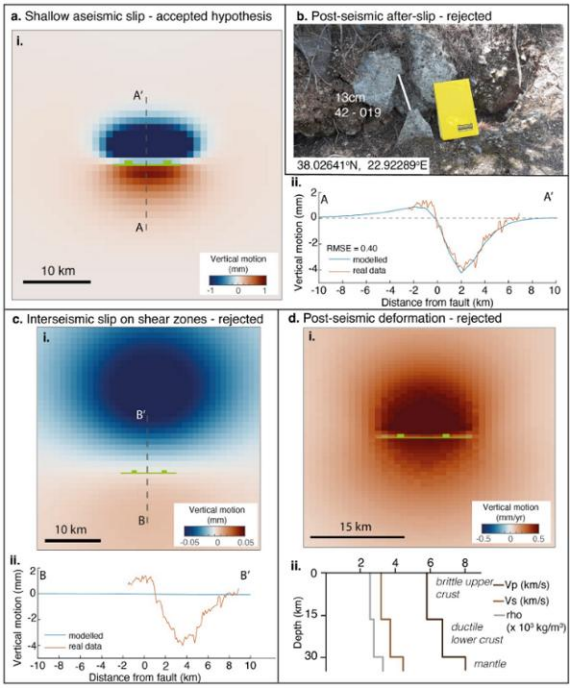

Figure 2: *Possible tectonic mechanisms for the vertical deformation on the Pisia fault. a) Shallow slip (preferred model). b) Photo of the 1981 surface rupture, with no evidence for post-seismic afterslip. c) Interseismic slip on shear zones, however the magnitude and size of deformation does not match observations. d) Post-seismic visco-elastic rebound model, however the pattern of deformation does not match observations.*

Using the elastic half-space model in Coulomb 3.4, we model small magnitude slip (1-10 cm) over a range of depths (0-5 km), aiming to fit the magnitude and wavelength of the deformation observed in the N-S profile (Figure 1b). The best-fit simple model (Figure 2a) has the fault slipping 1.8 cm from 2-4 km depth – while this is not

a full inversion, it gives an indication of the approximate magnitude of slip and depth needed to produce the observed deformation. We believe this is the first observation of a transient shallow slip event or a slow slip event on a continental normal fault.

There is no evidence of an increase in the size of the surface ruptures associated with the 1981 earthquakes (Figure 2b), therefore post-seismic afterslip is unlikely to be causing the vertical deformation observed.

We use the elastic half space model to model slip on an underlying deep shear zone, following the hypothesis of (Cowie et al., 2013). The pattern of uplift and subsidence produced from this model spatially correlates with the fault trace (Figure 2c), but the magnitude of deformation is two orders of magnitude smaller than observed. Therefore, shear zone slip is unlikely to be the causative mechanism.

Using PSGRN/PSCMP, we model the post-seismic deformation expected after 35 and 40 years for a M 6.7 event (i.e. after the 1981 earthquakes), and then calculate the different to get a deformation rate over the time intervals studied (2016-2021). Based on this model, we would expect to see uplift everywhere (Figure 2d), which does not match with our observations.

DISCUSSION

We cannot determine a specific trigger for the onset of the transient elevated rate of deformation. Rate-and-state friction framework can be applied to study earthquake behaviour on faults. One study modelling a normal fault (Biemiller & Lavier, 2017) can replicate both earthquakes and aseismic slip transients. Variations in the fault zone rheology may be the underlying driver, but we cannot readily access the Pisia-Skinos fault at the depths of interest.

Our observation of variations in deformation over annual timescales raises interesting questions for how short-term (annual-decadal) deformation relates to longer-term (hundreds to thousands of years) deformation rates, particularly pertinent if geodetic data is used to infer seismic hazard.

We assume that the rate from 2016-2019 is representative of the steady state rate, and that the rate from 2019-2021 is a transient elevated rate. We can link these observations to the longer term (125 kyrs) record of uplift to attempt to estimate how often these transient phases of deformation might happen. The long term uplift rate is 0.51 mm/yr over 125kyrs (Cooper et al., 2007; Roberts et al., 2009). The coseismic uplift from the 1981 earthquakes was 10 cm (Cooper et al., 2007), and the recurrence interval is 0.9-1.3 kyrs (Mechernich et al., 2018). We assume that the transient phase of deformation lasts between 3 and 10 years. Given these assumptions and uncertainties, we calculate that a transient phase of deformation could occur every 110-1800 years, i.e. longer than satellite geodesy has been available, perhaps explaining why such events haven't been recognised before now.

Our study highlights a potential pitfall of using geodetically derived deformation rates to inform seismic hazard, as it may be difficult to determine whether a geodetic rate is truly representative of "steady state" or whether a transient phase has been captured. This highlights that the occurrence of short-term (annual-decadal) transient phases of deformation merits further investigation

Acknowledgements: This study was funded by NERC Standard Grant (NE/V012894/1, PI—G. Roberts) and UKRI Future Leaders Fellowship (MR/T041994/1, PI—Z. Mildon). M. Diercks is supported by the University of Plymouth, School of Geography, Earth and Environmental Sciences PhD studentship. Spatial analysis and figures made using QGIS v3.16. We thank the Hexagon Smart Net Greece for releasing their GNSS data to A. Ganas.

REFERENCES

Biemiller, J., & Lavier, L. (2017). Earthquake supercycles as part of a spectrum of normal fault slip styles. Journal of Geophysical Research: Solid Earth, 122(4), 3221–3240. https://doi.org/10.1002/2016JB013666

Bird, P., & Kreemer, C. (2014). Revised Tectonic Forecast of Global Shallow Seismicity Based on Version 2.1 of the Global Strain Rate Map. Bulletin of the Seismological Society of America, 105(1), 152–166. https://doi.org/10.1785/0120140129

Cooper, F. J., Roberts, G. P., & Underwood, C. J. (2007). A comparison of 103–105 year uplift rates on the South Alkyonides Fault, central Greece: Holocene climate stability and the formation of coastal notches. Geophysical Research Letters, 34(14). https://doi.org/10.1029/2007GL030673

Costantini, M., Minati, F., Trillo, F., Ferretti, A., Novali, F., Passera, E., et al. (2021). European Ground Motion Service (EGMS). In 2021 IEEE International Geoscience and Remote Sensing Symposium IGARSS (pp. 3293–3296). https://doi.org/10.1109/IGARSS47720.2021.9553562

Cowie, P. A., Scholz, C. H., Roberts, G. P., Faure Walker, J. P., & Steer, P. (2013). Viscous roots of active seismogenic faults revealed by geologic slip rate variations. Nature Geoscience, 6.12(November), 1036–1040. https://doi.org/10.1038/ngeo1991

Field, E. H., Milner, K. R., Hardebeck, J. L., Page, M. T., van der Elst, N., Jordan, T. H., et al. (2017). A Spatiotemporal Clustering Model for the Third Uniform California Earthquake Rupture Forecast (UCERF3-ETAS): Toward an Operational Earthquake Forecast. Bulletin of the Seismological Society of America, 107(3), 1049–1081. https://doi.org/10.1785/0120160173

Friedrich, A. M., Wernicke, B. P., Niemi, N. A., Bennett, R. A., & Davis, J. L. (2003). Comparison of geodetic and geologic data from the Wasatch region, Utah, and implications for the spectral character of Earth deformation at periods of 10 to 10 million years. Journal of Geophysical Research: Solid Earth, 108(B4). https://doi.org/10.1029/2001JB000682

Gerstenberger, M., Bora, S., Brendon, B., DiCaprio, C., Van Dissen, R. J., Atkinson, G. M., et al. (2022). New Zealand National Seismic Hazard Model 2022 revision: model, hazard and process overview. https://doi.org/10.21420/TB83-7X19

Jackson, J. A., Gagnepain, J., Houseman, G., King, G. C. P., Papadimitriou, P., Soufleris, C., & Virieux, J. (1982). Seismicity, normal faulting, and the geomorphological development of the Gulf of Corinth (Greece): the Corinth earthquakes of February and March 1981. Earth and Planetary Science Letters, 57(2), 377–397. https://doi.org/10.1016/0012-821X(82)90158-3

Mechernich, S., Schneiderwind, S., Mason, J., Papanikolaou, I. D., Deligiannakis, G., Pallikarakis, A., et al. (2018). The Seismic History of the Pisia Fault (Eastern Corinth Rift, Greece) From Fault Plane Weathering Features and Cosmogenic 36Cl Dating.

J. Geophys. Res. Solid Earth, 123(5), 4266–4284. https://doi.org/10.1029/2017JB014600

Michas, G., Kapetanidis, V., Spingos, I., Kaviris, G., & Vallianatos, F. (2022). The 2020 Perachora peninsula earthquake sequence (East Corinth Rift, Greece): spatiotemporal evolution and implications for the triggering mechanism. Acta Geophysica, 70(6), 2581–2601. https://doi.org/10.1007/s11600-022-00864-x

Pepin, K. S., Ellsworth, W. L., Sheng, Y., & Zebker, H. A. (2022). Shallow Aseismic Slip in the Delaware Basin Determined by Sentinel-1 InSAR. Journal of Geophysical Research: Solid Earth, 127(2), e2021JB023157. https://doi.org/10.1029/2021JB023157

Roberts, G. P., & Ganas, A. (2000). Fault-slip directions in central and southern Greece measured from striated and corrugated fault planes: Comparison with focal mechanism and geodetic data. Journal of Geophysical Research: Solid Earth, 105(B10), 23443–23462. https://doi.org/10.1029/1999JB900440

Roberts, G. P., Houghton, S. L., Underwood, C., Papanikolaou, I., Cowie, P. A., van Calsteren, P., et al. (2009). Localization of Quaternary slip rates in an active rift in 10 5 years: An example from central Greece constrained by 234 U- 230 Th coral dates from uplifted paleoshorelines. J. Geophys. Res., 114(B10), B10406. https://doi.org/10.1029/2008JB005818

Rousset, B., Jolivet, R., Simons, M., Lasserre, C., Riel, B., Milillo, P., et al. (2016). An aseismic slip transient on the North Anatolian Fault. Geophysical Research Letters, 43(7), 3254–3262. https://doi.org/10.1002/2016GL068250

Schwartz, S. Y., & Rokosky, J. M. (2007). Slow slip events and seismic tremor at circum-Pacific subduction zones. Reviews of Geophysics, 45(3). https://doi.org/10.1029/2006RG000208

Shen, Z.-K., Jackson, D. D., & Kagan, Y. Y. (2007). Implications of Geodetic Strain Rate for Future Earthquakes, with a Five-Year Forecast of M5 Earthquakes in Southern California. Seismological Research Letters, 78(1), 116–120. https://doi.org/10.1785/gssrl.78.1.116

Toda, S., Stein, R. S., Richards-Dinger, K., & Bozkurt, S. B. (2005). Forecasting the evolution of seismicity in southern California: Animations built on earthquake stress transfer. Journal of Geophysical Research, 110(B5), B05S16. https://doi.org/10.1029/2004JB003415

Wang, R., Lorenzo-Martín, F., & Roth, F. (2006). PSGRN/PSCMP - A new code for calculating co- and post-seismic deformation, geoid and gravity changes based on the viscoelastic-gravitational dislocation theory. Computers and Geosciences, 32(4), 527–541. https://doi.org/10.1016/j.cageo.2005.08.006

Wernicke, B., Davis, J. L., Niemi, N. A., Luffi, P., & Bisnath, S. (2008). Active megadetachment beneath the western United States. Journal of Geophysical Research: Solid Earth, 113(B11). https://doi.org/10.1029/2007JB005375

INQUA TERPRO Project Cascading Hazards and Mitigation (CHAMP)

Monitoring slow aseismic slip along faults from InSAR time series: the case example of the Haiyuan fault in China

Mokhtari, Farès (1), Lasserre, Cécile (1), Romain Jolivet (2), Olivier Cavalié (3), Simon Daout (4), Sun Jianbao (5), Marie-Pierre Doin (6), Philippe Durand (7)

(1) LGL-TPE, Univ Lyon, UJM, UCBL, ENSL, CNRS, Lyon, France. Email: cecile.lasserre@univ-lyon1.fr
(2) LG-ENS, PSL Research University, CNRS, Paris, France
(3) CEREGE, Aix-Marseille Univ, CNRS, IRD, INRAE, Coll France, Aix-en-Provence, France
(4) CRPG ENSG, Université de Lorraine, Nancy, France
(5) Institute of Geology, China Earthquake Administration, Beijing, China
(6) ISTerre, Université Grenoble-Alpes, Grenoble, France
(7) CNES, Toulouse, France

Abstract: *Advances in geodetic monitoring have revealed complex interactions between aseismic and seismic slip throughout the seismic cycle. The Haiyuan Fault (northeast China) provides an exceptional setting to study fault slip behavior due to the coexistence of locked and creeping sections. We analyze a 35 km creeping segment located between the 1920 Mw 7.9 rupture and the Tianzhu seismic gap using Sentinel-1 InSAR time series (2014–2020). The average horizontal creep rate reaches up to 5 mm/yr, with along-strike variations. Local subsidence, up to 8 mm/yr, occurs within an extensional relay zone whose morphology and slip behavior are further characterized using Independent Component Analysis. Comparison with ERS and Envisat data reveals persistent creep over 27 years. The enhanced signal-to-noise ratio of Sentinel-1 data highlights intermittent creep behavior with recurrent transient accelerations, providing new insights into the processes controlling fault slip along the Haiyuan Fault.*

Key words*: Fault, creep, InSAR, geodesy, China*

INQUA TERPRO Project Cascading Hazards and Mitigation (CHAMP)

Revisiting Aotearoa New Zealand's Alpine Fault earthquake history: Evidence for three events in the last 500 Years

Newsham, Sophie (1), Nicol, Andrew (1), Lorrey, Andrew (2), Martin, Timothy (3), Howell, Andrew (1), McGrath, Jack (1), Humphrey, Jade (1) Penney, Camilla (1), Sarkawi, Gina (1)

(1) School of Earth and Environment, University of Canterbury, Private Bag 4800, Christchurch, New Zealand. sophie.newsham@pg.canterbury.ac.nz
(2) Principal Scientist - Climate and Environmental Applications, Earth Science New Zealand, Private Bag 99940, Newmarket, Auckland
(3) Independent Forest Ecologist (Independent), Whangarei, New Zealand

Abstract: *Alpine Fault earthquakes are a major contributor to seismic hazard in Aotearoa New Zealand. Earthquake forecast models use 1717 CE as the most recent rupture on the Alpine Fault. Our compilation of dendroseismology and radiocarbon dating of landscape disturbances challenges this conclusion. A systematic review of evidence suggests three significant events in the last 500 years around 1610-1640, 1710-1730 (previously 1717 CE), and 1800-1840. While the 1700s event caused widespread disturbance, evidence for, and dating of, the early 1600s and 1800s events are less common, especially in lake records. These less well-documented 'earthquakes' could comprise multiple moderate-to-large ruptures (M6.5–7.9) rather than a single long rupture. The timing of these three earthquakes and the possibility of Alpine Fault earthquake sequences may modify hazard forecasts and warrant further investigation.*

Key words*: Alpine Fault, New Zealand, earthquake chronology, seismic risk, most recent event*

INTRODUCTION

The Alpine Fault (AF) can produce major earthquakes (≥M8) approximately every 200-300 years and is one of Aotearoa New Zealand's (A-NZ) most significant seismic hazards (e.g. Berryman et al., 2012; Biasi et al., 2015; Cochran et al., 2017; Howarth et al., 2021). Reliable dating of large to great earthquakes on the AF is crucial for seismic risk assessment. The conditional probability (CP) of the central AF rupturing in the next 50 years is about 75% (29–99% at the 95% confidence interval) and anchored to a most recent event (MRE) in 1717 CE (Wells et al., 1999). Uncertainties in earthquake timing, along with evidence of widespread landscape disturbance and the potential for additional AF earthquakes over the past 500 years, challenge the currently accepted earthquake history. This study collates and recalibrates existing datasets to update the 500-year earthquake record on the AF. Our paper shares preliminary results.

DATA AND METHODS

The AF is the longest onshore active fault in A-NZ, extending 800 km. This study focuses on the onshore Northern, Central, and Southern sections of the AF (Fig. 1). Since European settlement in 1840, there have been no large surface-rupturing earthquakes or recorded surface creep on the AF, and stress accumulation is inferred to be released in large to great earthquakes (Mw 7-8+) (Berryman et al., 2012; De Pascale & Langridge, 2012; Sutherland et al., 2007; Yetton et al., 2010).

Our systematic review of published and unpublished AF earthquake timings since 1500 CE, incorporates significant new data, timing uncertainties and builds on earlier reviews (Berryman et al., 1992; Howarth et al., 2018; Yetton et al., 2010). Dates and extents of AF earthquakes are from radiocarbon dating, dendrochronology, and historical records at ~70 sites (Fig. 1). The last comprehensive review of AF earthquake chronologies was in 2018 (Howarth et al., 2018), and an updated review of the literature is timely, given subsequent publications challenging accepted earthquake timings (e.g. Blagen et al., 2022; Langridge et al., 2021, 2025).

Our review of AF earthquake timing uses data categorised by fault section and data type. Most evidence for the timing of AF earthquakes is from radiocarbon dating, which employs three main approaches: on-fault trenches and pits (Berryman et al., 2012; Langridge & Howarth, 2018; Langridge et al., 2012, 2018, 2025; Wright et al., 1998; Yetton, 2002; Yetton et al., 1998), near-fault exposures in river cuttings or fault-bounded, ponded sediments (Cochran et al., 2017; Cooper & Norris, 1990; De Pascale & Langridge, 2012; Norris et al., 2001; Sutherland & Norris, 1995), and off-fault sediments such as lake turbidites (Howarth et al., 2012, 2014, 2016, 2021) and landslide deposits (Almond et al., 2023; Davies & Korup, 2007; Goff et al., 2004; Langridge et al., 2012; Wright, 1999; Yetton et al., 1998). Other datasets include dendrochronology to estimate the ages of tree cohorts on earthquake-related landforms (Blagen et al., 2022; Cullen et al., 2003; Wells, 1998; Wells et al., 2001; Wells & Goff, 2006, 2007), and to identify earthquake-induced tree growth anomalies. Tree-ring growth anomalies underpin the widely cited 1717 CE AF earthquake age (Wells et al., 1999). Historical records, including an 1826 sealer's account of intense shaking in Fiordland (Downes et al., 2005), were also evaluated for potential links to AF rupture. Lichenometry dates for AF earthquakes are debated (Bull, 1996) and not included here.

PRELIMINARY RESULTS

Interpretations suggest at least three large to great (≥~M7) AF earthquakes in the past five centuries at around 1610-1640, 1700-1730, and 1800-1840 CE (e.g., Fig 2). These earthquakes are discussed from oldest to youngest.

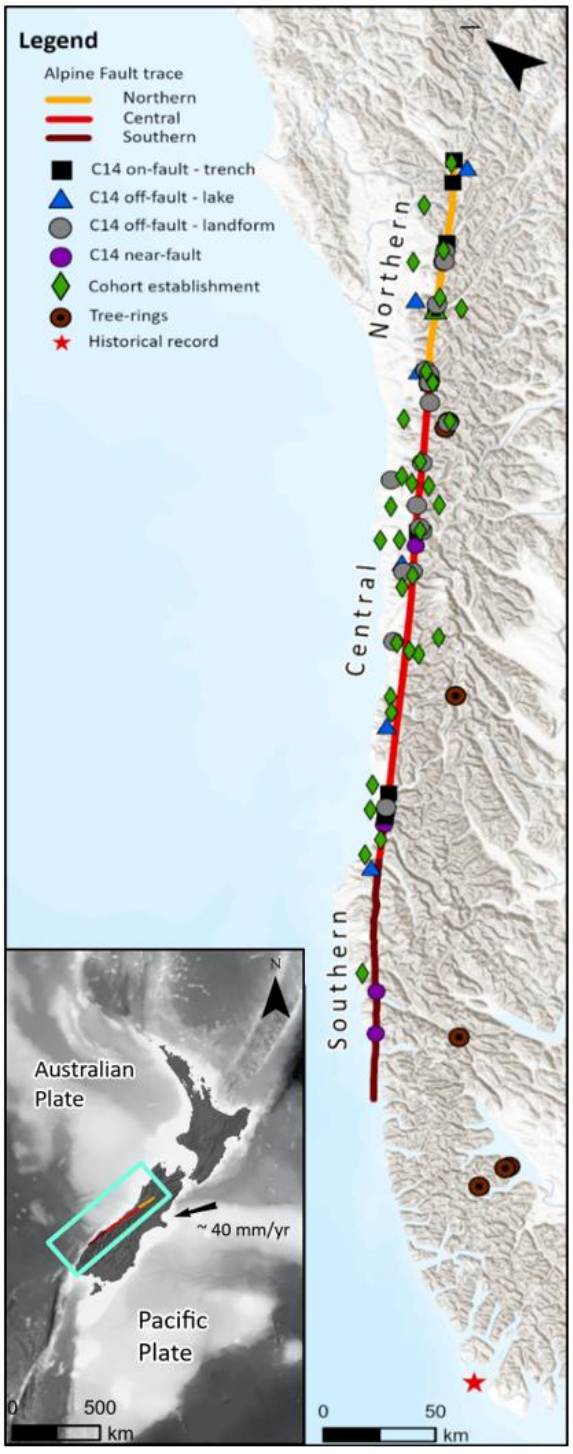

Figure 1: *Map showing Alpine Fault sections and data-source locations along the fault. Inset map shows the tectonic setting of the Alpine Fault.*

The proposed 1610-1640 CE AF earthquake has been identified by multiple authors along ~370 km of the Northern and Central sections (e.g., Fig 2). Cohort establishment ages across multiple sites indicate widespread landscape formation and forest disturbance. A spatially extensive event(s) can be temporally linked to an AF earthquake with on-fault radiocarbon ages; although these ages also overlap with later events, making temporal attribution uncertain. Moreover, near- and off-fault radiocarbon ages of potential coseismic landforms coincide with the timing of cohort establishment for terrace and beach ridge aggradation. Similarly, tree-ring anomalies at three sites also suggest synchronous growth changes during this period. However, the lack of cross-dating reduces our confidence in the precision and origin(s) of these interpretations.

The 1710-1730 CE earthquake is widely recognised and incorporated into hazard models for the Central section (Gerstenberger et al., 2024; Howarth et al., 2021; Orchiston et al., 2018). It produced a 200-380 km long rupture along three fault sections with magnitude ≥M8 (e.g. Howarth et al., 2021; Yetton et al., 1998) (e.g., Fig.2). The timing is based on dendrochronology and radiocarbon ages from trench exposures, near-fault sediment sequences and off-fault landscape disturbance ages. The synchronous timing of tree-ring growth suppressions across multiple sites during 1715-1719 CE provides annual precision for this earthquake (Wells et al., 1999). This event is commonly cited as occurring in 1717 CE and to be the most recent event on the central AF (Howarth et al., 2021; Wells et al., 1999; Yetton et al., 1998). However, this narrow age range is based on a limited number of tree cores and uncertain cross-matching results. Our ±10-year age range for this event represents these uncertainties.

There is extensive evidence for landscape disturbance in 1800-1840 CE (e.g., Fig. 2). On-fault trench data indicate a surface-rupturing event between 1813–1848 CE on the Northern and north-Central sections of the AF, suggesting a minimum rupture length of ~40 km. This on-fault evidence is supported by near- and off-fault radiocarbon ages. Cohort establishment and tree-ring anomalies ages indicate widespread landscape formation and forest disturbance in the early 1800s along the Central section of the fault; however, minimal forest disturbance was observed near the Northern section despite on-fault evidence of fault rupture in this area. Historical accounts, including a sealer's report of severe shaking in 1826 and coastal damage in South Westland, have been linked to either an offshore segment of the AF or the Puysegur subduction thrust (Downes et al., 2005). Based on the evidence, we believe the AF ruptured during this period, though it is unclear if it was the same event reported in 1826.

DISCUSSION

The available data show evidence of varying quality and quantity for three large-to-great earthquakes on the AF since 1500 CE. These earthquakes have been identified in the literature, with particular focus on the 1717 CE event (our preferred age 1710-1730 CE). Given the 20- and 40-year time windows for each earthquake, it is possible, (especially for 1610-1640 CE and 1800-1840 CE events), that the data record sequences of multiple moderate-to-large earthquakes (M6.5–7.9), rather than a single great earthquake, as is widely accepted for 1710-1730 CE.

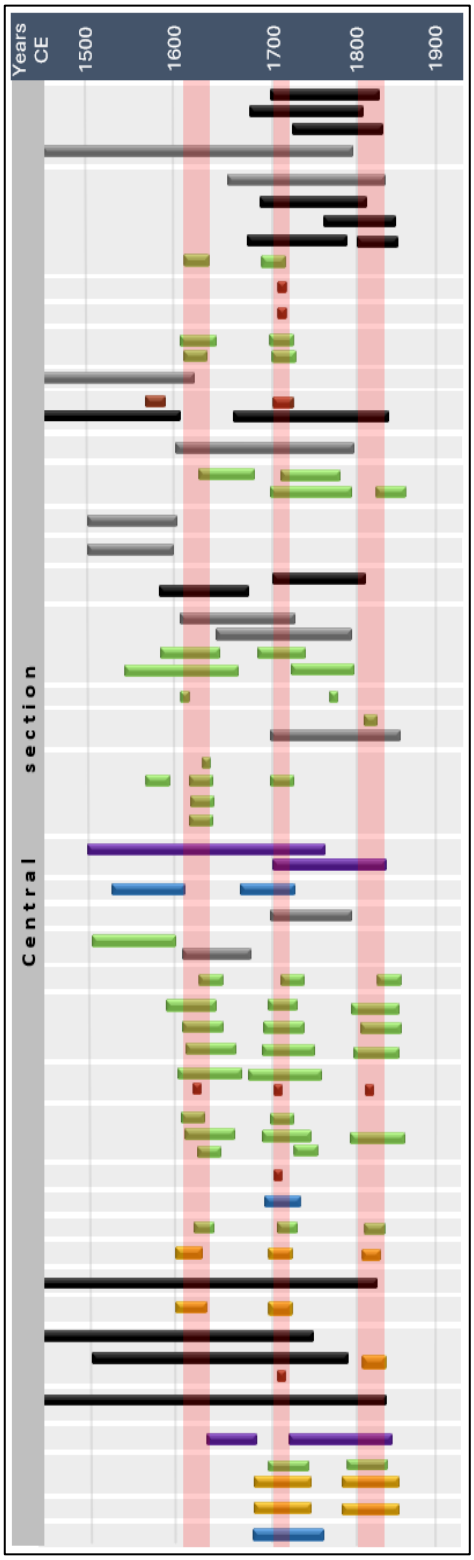

Figure 2: *Evidence for three earthquakes since 1500 CE on the Central section of the Alpine Fault. Age range of interpreted event timings (by the original source) indicated by coloured horizontal bars.Colours as per Legend in Fig 1. Vertical red transparent bars represent our interpreted event timings. See text (Results section)*

Our preliminary conclusions have important implications for AF recurrence intervals. If the three proposed AF earthquakes ruptured the Central section, the average recurrence interval over the last 500 years would be about 160 years, while the average time between these three earthquakes is roughly 100 years. These intervals are up to three times shorter than the commonly cited mean ~200–350 yr recurrence interval for the Southern and Central sections (e.g. Berryman et al., 2012; Biasi et al., 2015; Cochran et al., 2017; Howarth et al., 2018, 2021; Langridge et al., 2021, 2025; Yetton et al., 2010). These differences could indicate that the past 500 years sample a temporal cluster of large earthquakes. Such clustering has been observed on similar strike-slip, plate boundary faults like the San Andreas and North Anatolia faults (e.g. Bulut et al., 2011; Grant & Sieh, 1994). If clustering recently occurred on the AF and the last event was 180-220 years ago (rather than ~300 years), then the CP of large earthquakes on the fault in the next 50 years may change. Further consideration should also be given to whether the sample magnitude or completeness is higher for the last 500 years compared to older earthquakes, whether the dated events record sequences of earthquakes and/or whether some landscape disturbances along the AF were triggered by non-AF events.

We review on-fault, near-fault, and off-fault evidence for three large-to-great earthquakes on the AF in the last 500 years. The timings are estimated to be approximately; 1610-1640, 1710-1730, and 1800-1840 CE. Preliminary interpretations suggest AF rupture behaviour may vary in space and time. The 1710-1730 CE event remains the strongest candidate for a great earthquake, while early 1600s and 1800s events may have been <M8 and/or characterised by sequences. Further chronological modelling and improved age precision are essential to support time-dependent hazard models and improve risk assessment for Aotearoa New Zealand.

Acknowledgements: This work is partially funded by the National Hazards Commission and the University of Canterbury. The authors wish to thank all researchers whose work on the Alpine Fault contributed to this review.

REFERENCES

Almond, P. C., Berryman, K., Villamor, P., Read, S., et al. (2023). Alluvial fan response to Alpine Fault earthquakes on the Westland piedmont, Whataroa, Aotearoa-New Zealand. *Earth surface processes and landforms*.

Berryman, K., Beanland, S., Cooper, A., Cutten, H., et al. (1992, 01/01). The Alpine Fault, New Zealand: Variation in Quaternary structural style and geomorphic expression. *Annales Tectonicae, VI*, 126-163.

Berryman, K., Cooper, A. F., Norris, R., Villamor, P., et al. (2012). Late Holocene rupture history of the Alpine Fault in south Westland, New Zealand. *Bulletin of the Seismological Society of America, 102*(2), 620-638.

Berryman, K. R., Cochran, U. A., Clark, K. J., Biasi, G. P., et al. (2012). Major earthquakes occur regularly on an isolated plate boundary fault. *Science (American Association for the Advancement of Science), 336*(6089), 1690-1693.

Biasi, G. P., Langridge, R. M., Berryman, K. R., Clark, K. J., et al. (2015). Maximum-likelihood recurrence parameters and conditional

probability of a ground-rupturing earthquake on the southern Alpine Fault, South Island, New Zealand. *Bulletin of the Seismological Society of America, 105*(1), 94-106.

Blagen, J. R., Davies, T. R. H., Wells, A., & Norton, D. A. (2022). Post-seismic aggradation history of the West Coast, South Island, Aotearoa/New Zealand; dendrogeomorphological evidence and disaster recovery implications. *Natural hazards (Dordrecht), 114*(3), 2545-2570.

Bull, W. B. (1996). Prehistorical earthquakes on the Alpine fault, New Zealand. *Journal of Geophysical Research: Solid Earth, 101*(B3), 6037-6050.

Bulut, F., Ellsworth, W. L., Bohnhoff, M., Aktar, M., et al. (2011). Spatiotemporal earthquake clusters along the North Anatolian fault zone offshore Istanbul. *Bulletin of the Seismological Society of America, 101*(4), 1759-1768.

Cochran, U. A., Clark, K. J., Howarth, J. D., Biasi, G. P., et al. (2017). A plate boundary earthquake record from a wetland adjacent to the Alpine Fault in New Zealand refines hazard estimates. *Earth and planetary science letters, 464*, 175-188. Cooper, A. F., & Norris, R. J. (1990). Estimates for the timing of the last coseismic displacement on the Alpine Fault, northern Fiordland, New Zealand. *New Zealand Journal of Geology & Geophysics, 33*(2), 303-307.

Cullen, L. E., Duncan, R. P., Wells, A., & Stewart, G. H. (2003). Floodplain and regional scale variation in earthquake effects on forests, Westland, New Zealand. *Journal of the Royal Society of New Zealand, 33*(4), 693-701.

Davies, T. R. H., & Korup, O. (2007). Persistent alluvial fanhead trenching resulting from large, infrequent sediment inputs. *Earth surface processes and landforms, 32*(5), 725-742.

De Pascale, G. P., & Langridge, R. M. (2012). New on-fault evidence for a great earthquake in A.D. 1717, central Alpine Fault, New Zealand. *Geology (Boulder), 40*(9), 791-794.

Downes, G. L., Cochran, U., Wallace, L., Reyners, M., et al. (2005). *EQC project 03/490:* Understanding local source tsunami : 1820s Southland tsunami. Institute of Geological & Nuclear Sciences.

Gerstenberger, M. C., Van Dissen, R., Rollins, C., DiCaprio, C., et al. (2024). The seismicity rate model for the 2022 Aotearoa New Zealand national seismic hazard model. *Bulletin of the Seismological Society of America, 114*(1), 182-216.

Goff, J. R., Wells, A., Chague-Goff, C., Nichol, S. L., et al. (2004). The elusive AD 1826 tsunami, south Westland, New Zealand. *New Zealand Geographer, 60*(2), 28-39.

Grant, L. B., & Sieh, K. (1994). Paleoseismic evidence of clustered earthquakes on the San Andreas fault in the Carrizo Plain, California. *Journal of Geophysical Research: Solid Earth, 99*(B4), 6819-6841.

Howarth, J. D., Barth, N. C., Fitzsimons, S. J., Richards-Dinger, et al. (2021). Spatiotemporal clustering of great earthquakes on a transform fault controlled by geometry. *Nature geoscience, 14*(5), 314-320.

Howarth, J. D., Fitzsimons, S. J., Norris, R. J., & Jacobsen, G. E. (2012). Lake sediments record cycles of sediment flux driven by large earthquakes on the Alpine Fault, New Zealand. *Geology (Boulder), 40*(12), 1091-1094.

Howarth, J. D., Fitzsimons, S. J., Norris, R. J., & Jacobsen, G. E. (2014). Lake sediments record high-intensity shaking that provides insight into the location and rupture length of large earthquakes on the Alpine Fault, New Zealand. *Earth and planetary science letters, 403*, 340-351.

Howarth, J. D., Fitzsimons, S. J., Norris, R. J., Langridge, R., et al. (2016). A 2000 yr rupture history for the Alpine fault derived from Lake Ellery, South Island, New Zealand. *The Geological Society of America Bulletin, 128*(3-4), 627-643.

Howarth, J. D., Cochran, U. A., Langridge, R. M., Clark, K., et al. (2018). Past large earthquakes on the Alpine Fault: paleoseismological progress and future directions. *New Zealand Journal of Geology and Geophysics, 61*(3), 309-328.

Langridge, R. M., Basili, R., Basher, L., & Wells, A. P. (2012). Late Holocene landscape change history related to the Alpine Fault determined from drowned forests in Lake Poerua, Westland, New Zealand. *Natural hazards and earth system sciences, 12*(6), 2051-2064.

Langridge, R. M., & Howarth, J. D. (2018). A new paradigm for Alpine Fault paleoseismicity; the northern section of the Alpine Fault. *GNS Science Miscellaneous Series, 121*.

Langridge, R. M., Howarth, J. D., Coffey, G., Villamor, P., et al. (2025). A multi-event paleoseismic record from the northern Alpine Fault at Marble Hill, Aotearoa New Zealand. *Geomorphology*, 109945.

Langridge, R. M., Howarth, J. D., Cox, S. C., Palmer, J. G., et al. (2018). Frontal fault location and most recent earthquake timing for the Alpine Fault at Whataroa, Westland, New Zealand. *New Zealand journal of geology and geophysics, 61*(3), 329-340.

Langridge, R. M., Villamor, P., Howarth, J. D., Ries, W. F., et al. (2021). Reconciling an early nineteenth-century rupture of the Alpine Fault at a section end, Toaroha River, Westland, New Zealand. *Bulletin of the Seismological Society of America, 111*(1), 514-540.

Norris, R. J., Cooper, A., Wright, T., & Berryman, K. (2001). Dating of past Alpine fault rupture in South Westland. New Zealand Earthquake Commission Report No. 99, 134.

Orchiston, C., Mitchell, J., Wilson, T., Langridge, R., et al. (2018). Project AF8: developing a coordinated, multi-agency response plan for a future great Alpine Fault earthquake. *New Zealand Journal of Geology and Geophysics, 61*(3), 389-402.

Sutherland, R., Eberhart-Phillips, D., Harris, R. A., Stern, T., et al. (2007). Do great earthquakes occur on the Alpine Fault in central South Island, New Zealand? *A Continental Plate Boundary: Tectonics at South Island, New Zealand, 175*, 235-251.

Sutherland, R., & Norris, R. J. (1995). Late Quaternary displacement rate, paleoseismicity, and geomorphic evolution of the Alpine Fault; evidence from Hokuri Creek, South Westland, New Zealand. *New Zealand Journal of Geology & Geophysics, 38*(4), 419-430.

Wells, A. (1998). Landscape disturbance history in Westland, New Zealand: the importance of infrequent earthquakes along the Alpine Fault. Lincoln University.

Wells, A., Duncan, R. P., & Stewart, G. H. (2001). Forest dynamics in Westland, New Zealand: the importance of large, infrequent earthquake-induced disturbance. *The Journal of Ecology, 89*(6), 1006-1018.

Wells, A., & Goff, J. (2006). Coastal dune ridge systems as chronological markers of palaeoseismic activity: a 650-yr record from southwest New Zealand. *The Holocene, 16*(4), 543-550.

Wells, A., & Goff, J. (2007). Coastal dunes in Westland, New Zealand, provide a record of paleoseismic activity on the Alpine Fault. *Geology (Boulder), 35*(8), 731-734.

Wells, A., Yetton, M. D., Duncan, R. P., & Stewart, G. H. (1999). Prehistoric dates of the most recent Alpine Fault earthquakes, New Zealand. *Geology (Boulder), 27*(11), 995-998.

Wright, C. A. (1999). Geology and paleoseismology of the central Alpine Fault, New Zealand University of Otago.

Wright, C. A., Norris, R. J., Cooper, A. F. (1998). Paleoseismic history of the central Alpine Fault. *Geological Society of New Zealand Miscellaneous Publication, 101A*, 249.

Yetton, M. (2002). Paleoseismic investigation for the North and West Wairau Sections of the Alpine Fault, South Island, New Zealand.

Yetton, M., Wells, A., Williams, A., Pinches, et al. (2010). Earthquake rupture history of the Alpine fault over the last 500 years. Geologically Active: Proceedings of 11th International Association for Engineering Geology and the Environment Congress, Auckland,

Yetton, M. D., Wells, A., & Traylen, N. J. (1998). The probability and consequences of the next Alpine Fault earthquake. EQC.

INQUA TERPRO Project Cascading Hazards and Mitigation (CHAMP)

Postojna Cave: speleoseismic evidence of Late Quaternary earthquakes

Novak, Uroš (1), Stanka Šebela (1)

(1) ZRC SAZU Karst Research Institute, Titov trg 2, 6230 Postojna, Slovenia. Email: uros.novak@zrc-sazu.si

Abstract: *This study establishes a paleoseismic record within the Postojna Cave (SW Slovenia) using uranium-thorium geochronology of deformed speleothems located in fault zones. The cave system lies within the dextral strike-slip regime of the NW Dinarides, influenced by the seismogenic Idrija and Predjama Faults. Nine deformed speleothems were sampled and dated from the TM extensometer site in Postojna Cave, revealing three temporal clusters of deformation: 1.4–4.3 ka, 6–8 ka, and 20–23 ka BP. These clusters correspond to previously identified regional paleoseismic events, notably the Holocene seismic phases on the Idrija and Selce Faults. The integration of speleoseismology and fault micro-displacement monitoring demonstrates that cave speleothems preserve reliable records of tectonic activity, confirming episodic seismicity in the NW Dinarides. This represents the first application in Slovenia combining in-cave extensometric monitoring with U-Th-dated speleothem deformation, contributing new insight into fault kinematics and long-term earthquake recurrence in karst environments.*

Key words*: speleoseismology, paleoseismicity, U-Th dating, Postojna Cave, NW Dinarides.*

INQUA TERPRO Project Cascading Hazards and Mitigation (CHAMP)

Deciphering Late Holocene Coastal Deformation and Tsunami Evidence from the Tongoy Wetlands.

Ortega, Cristina (1), José González Alfaro (2), Cristian Calderón (1), Tomás Wistuba (3), Gabriela Barraza (1), Marcelo Vásquez (3), Tomás Donari (3), Gabriel Easton (1)

(1) Departamento de Geología, Facultad de Ciencias Físicas y Matemáticas, Universidad de Chile, cristina.ortega.c@gmail.com.
(2) Departamento de Geofísica, Facultad de Ciencias Físicas y Matemáticas, Universidad de Chile.
(3) Escuela de Geología, Facultad de Ciencias, Ingeniería y Tecnología, Universidad Mayor.

Abstract: *The Tongoy wetlands on the semiarid coast of north-central Chile (~30°S) preserve a valuable record of coastal evolution during the Late Holocene. This study presents the first geomorphological, stratigraphic, and sedimentological results aimed at reconstructing their geological history and evaluating evidence of past seismic and tsunami events. Preliminary observations reveal sedimentary sequences containing high-energy marine deposits interbedded with estuarine and alluvial facies, which may correspond to tsunami-derived inundations deposits. In addition, the spatial distribution of fluvial terraces levels within the wetlands suggests deformation patterns influenced by both the megathrust earthquake cycle and active crustal faults. These findings provide insight into the interaction between tectonic activity, coastal processes, and sedimentary dynamics along the semiarid Chilean margin, contributing to the regional paleoseismic framework and advancing our understanding of Late Holocene coastal evolution in a tectonically active setting.*

Key words*: Paleoseismology, Holocene coastal evolution, Fluvial terrace, Tsunami stratigraphy, Active crustal faults.*

INQUA TERPRO Project Cascading Hazards and Mitigation (CHAMP)

paleoseismicity.org

Displacement patterns and segment interaction in the Ulsan Fault Zone, SE Korea: Insights into fault growth and activity

Park, Kiwoong (1), Sambit Prasanajit Naik (2), Young-Seog Kim (1)

(1) GSGR, Major of Environmental Geology, Pukyong National University, Busan, Korea. pko8108@pukyong.ac.kr.
(2) Department of Petroleum Engineering and Earth Sciences, University of Petroleum and Energy Studies, India

Abstract: *Fault systems grow through the propagation and linkage of individual segments, producing displacement profiles that are important for understanding tectonics and seismic hazard. We examine how offsets at the scale of segments relate to the dynamics of the broader fault network by analyzing the approximately 50 km long, NNW-SSE oriented Ulsan Fault in SE Korea, which remains relatively active despite the generally low seismicity of the region. The fault is subdivided into six segments composed of subparallel reverse strands. We extracted geomorphic vertical separations from swath profiles across valleys oriented perpendicular to the fault and compared them with reported Quaternary offsets to confirm a tectonic signal. Vertical displacement reaches its maximum in two central segments and decreases toward both ends, consistent with widely recognized models of fault growth. Landscape based separations of roughly one to three meters likely underestimate the total cumulative vertical displacement because of ongoing incision and erosion within the valleys. Segments with greater displacement coincide with zones of elevated small magnitude seismicity, linking present-day deformation to long term displacement recorded in the topography. We infer that an active central segment influences the activity of neighboring faults, while the reduced activity in the northern part of the system reflects the diversion of stress, thereby improving the regional assessment of seismic hazard.*

Key words*: Fault displacement pattern, Fault geometry and evolution, Fault segment, Paleoseismology, Ulsan Fault Zone*

1. INTRODUCTION

Fault systems commonly evolve through the growth and linkage of discrete fault segments. As individual segments accumulate slip and interact with neighbouring structures, they develop systematic but spatially variable patterns of displacement along strike that reflect differences in segment maturity, interaction, and strain localization within the fault network (Kim and Sanderson, 2005). Such along-strike variations record where strain is preferentially localized or transferred within a fault network and therefore provide insight into segment maturity, interaction, and potential rupture extent. Understanding the geometric and kinematic relationships among segments is thus a key requirement for characterizing fault behaviour and associated seismic hazard. In intraplate regions, where slip rates are relatively low, recurrence intervals are long, and surface evidence of fault activity is often fragmentary or obscured by sedimentation and erosion, resolving the geometry and kinematics of fault segments is particularly challenging. In such settings, high-resolution LiDAR-derived DEM analyses, detailed geomorphic markers of cumulative displacement, and closely spaced paleoseismic trenching become critical tools for constraining how and where intraplate faults accommodate strain.

Although the Korean Peninsula is located far from major plate boundaries and has traditionally been regarded as a region of relatively low seismicity, recent moderate earthquakes have led to a re-evaluation of this perception. The 2016 Mw 5.5 Gyeongju and 2017 Mw 5.4 Pohang earthquakes, which occurred near the Yangsan and Ulsan faults in SE Korea, demonstrated that intraplate faults in Korea are capable of generating damaging events and underscored the need for detailed paleoseismological and kinematic studies.

The Ulsan Fault Zone (UFZ) is a NNW–SSE-trending, reverse fault extending for ~50 km from Ulsan to Gyeongju. Its existence and overall geometry are inferred from geological mapping, uplifted range-front geomorphology, and geophysical surveys, but direct evidence for Quaternary reactivation is restricted to a limited number of trench and outcrop sites because much of the fault trace is buried beneath thick alluvial deposits. In addition, a set of nearly continuous active faults is developed 4–5 km east of the valley along the mountain front, and these range-front structures, together with the Ulsan fault valley, are commonly referred to as the UFZ in a broader sense. This configuration suggests that shortening is accommodated within an imbricate thrust system rather than along a single discrete surface. This study addresses that need by analysing the segmentation, landscape-derived offset patterns, and available reported slip rate estimates of the UFZ.

2. GEOMORPHOLOGICAL AND GEOLOGICAL SETTING

The eastern Tohamsan range forms a steep mountain front along the Ulsan fault zone, with relief that progressively decreases southward into lower hills and dissected piedmonts. Streams draining the eastern slopes have constructed a series of N–S-oriented confluent alluvial fans along the range front. The fan surfaces can be subdivided into higher, intermediate, and lower levels on the basis of relative elevation, surface morphology, incision depth, and sediment characteristics, recording repeated episodes of fan progradation and river entrenchment during the Quaternary. Fan apices are consistently located at the mouths of bedrock valleys along the eastern range,

indicating that alluvial-fan deposits are sourced from the uplifted footwall block. Triangular facets and steep fault scarps along the range front, together with the large volume of colluvial and alluvial deposits, point to long-lived uplift on N–S to NNW–SSE-striking reverse faults that place the eastern block over the western block under an approximately ENE–WSW-trending maximum horizontal compressive stress.

Bedrock in the study area consists mainly of Cretaceous–Paleogene granite, unconformably overlain by Quaternary alluvial-fan and fluvial deposits (Fig. 1). Tectonically, the UFZ has been interpreted as a multiphase structure that experienced right-lateral strike-slip deformation during Miocene opening of the East Sea and has since been reactivated as a reverse-dominant fault under ENE–WSW compressional regime (Cheon et al., 2023). Throughout the UFZ, numerous Quaternary faults are exposed in the walls of erosional valleys incised into the fan surfaces and mountain slopes, and basement faults are also abundant. These faults are predominantly N–S to NNW–SSE striking and dip mainly eastward (Fig. 1). This fault array provides a structurally complex framework in which active reverse-fault strands, inherited basement structures, and range-front geomorphology can be examined together.

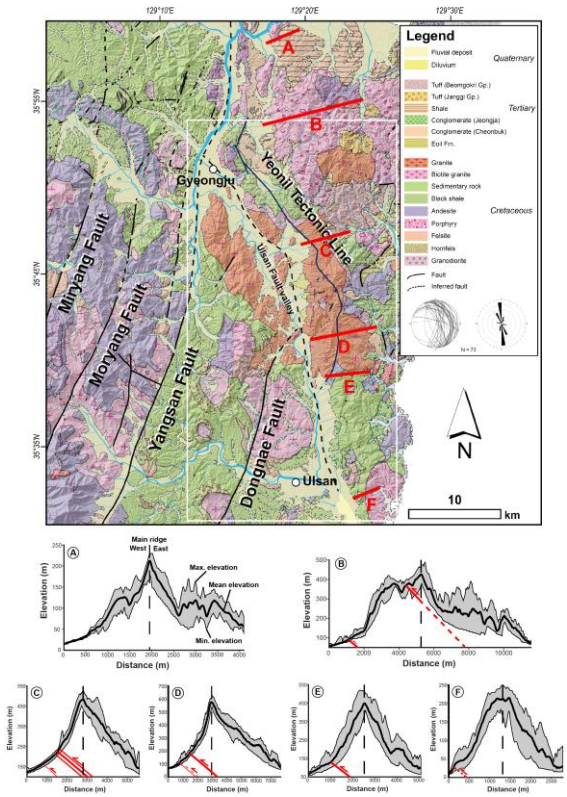

Figure 1: *(a) Geological map of the Gyeongju–Ulsan region showing the Ulsan fault zone and adjacent major faults. Lithologic units and mapped/inferred faults are summarized in the legend, and the stereonet in the inset shows the orientations of faults measured within the study area. Red lines labelled A–F indicate the locations of swath profiles drawn roughly perpendicular to the Ulsan fault zone. (b) Swath profiles A–F extracted along these transects, showing minimum, mean, and maximum elevation across each profile. Red lines along the profiles mark the surface traces of reported Quaternary faults.*

3. METHODS AND RESULTS

To characterize the range-front morphology, we extracted six topographic swath profiles (A–F in Fig. 1) roughly perpendicular to the Ulsan fault valley. The profiles show asymmetric relief, high western slopes facing the UFZ and gentler eastern slopes in the central part of the zone, whereas northern and southern cross-sections display more subdued relief and weaker asymmetry. Along the western side of the central swaths, abrupt breaks in slope and topographic steps coincide with the projected traces of reported Quaternary reverse faults, indicating that the western mountain front has been strongly shaped by repeated uplift on the UFZ rather than by erosional processes alone.

We divided the UFZ into six segments on the basis of changes in strike, gaps and step-overs in mapped fault traces, and the distribution of reported Quaternary faults (Fig. 2a). Some segments are characterized by multiple overlapping strands, whereas others are represented mainly by a single dominant strand in the current surface mapping. This geometry reflects the present state of mapping based on bedrock outcrops and DEM interpretation, and additional strands may be concealed beneath alluvial cover or removed by erosion. In fault-perpendicular valleys, detailed swath profiles were used to identify landscape-derived vertical separations interpreted as cumulative vertical offsets produced by faulting. For each vertical separation, we recorded its along-strike position and strand assignment and then projected all measurements onto a segment-parallel coordinate system. Strand-mean vertical separations typically fall in the range of ~1–3 m, with locally larger values in the central segments where several strands overlap. Because these offsets are measured along actively incising valley floors, they are interpreted as minimum, and thus likely underestimated, values of cumulative vertical displacement that have been partially reduced by fluvial erosion. For each segment, we defined a regular along-strike grid (~0.2 km spacing), interpolated strand-specific offsets onto this grid to obtain continuous vertical-separation profiles, and then summed the contributions of all strands at each grid node to derive a segment-scale cumulative vertical separation profile (Fig. 2b). The resulting cumulative profiles show a typical fault-displacement pattern, characterized by displacement that is strongly concentrated in the central part and tapers toward both tips of the fault (Davis et al., 2005). The Monte Carlo envelopes consistently preserve the central displacement maxima and tipward tapering, suggesting that these features are robust despite local geomorphic complexity and measurement uncertainty.

4. DISCUSSION AND IMPLICATIONS FOR HAZARD ASSESSMENT

The structural and geomorphic analyses indicate that the

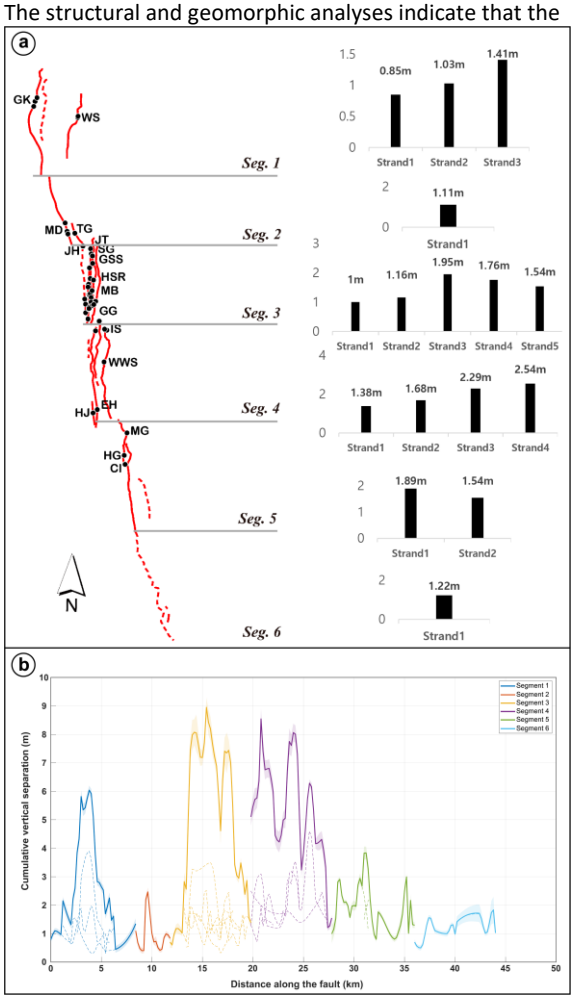

Figure 2: *(a) Map-view geometry of the segmented Ulsan fault showing 6 segments and the mapped reverse fault strands. The histograms to the right summarize the mean landscape-derived vertical separation for each strand within a given segment, based on offsets measured at fault-perpendicular valleys. (b) Along-fault displacement profiles for the 6 segments. Dashed lines denote strand-scale vertical separation profiles, coloured by segment, whereas thick solid lines represent segment-scale cumulative profiles obtained by summing all strands. Shaded envelopes indicate the mean ±1σ range derived from Monte Carlo resampling of the landscape-derived offsets.*

UFZ behaves as a segmented reverse fault system in which deformation is strongly focused in the central part of the fault. For these central segments, we propose a schematic imbricate thrust system that soles into a low-angle basal fault, with multiple reverse fault strands splaying upward to form the observed range-front array and uplift the eastern mountain block (Fig. 3c). The range-front swath profiles further show that major topographic steps and steep western mountain slopes coincide with the projected traces of reported Quaternary reverse faults, indicating that the western mountain front owes much of its present morphology to repeated uplift on the Ulsan fault system rather than to erosional processes alone.

Cumulative vertical separation profiles derived from landscape show pronounced displacement maxima in the two central segments and systematic tapering toward both fault tips. The displacement peaks occur in segments where multiple overlapping reverse-fault strands are mapped, indicating that shortening is accommodated within a relatively wide, strand-rich fault zone in the central part of the UFZ. This spatial correspondence between high cumulative displacement and a broadened multi-strand architecture is consistent with the central segments representing a more structurally evolved and mechanically dominant part of the fault system. Reported slip rate estimates for the Late Quaternary along the UFZ (Choi et al., 2012), on the order of ~0.05–0.2 mm/yr, show higher values in the central part of the fault and lower values toward both tips, a pattern consistent with the cumulative displacement distribution inferred from the landscape-derived offsets (Fig. 3b). The mapped pattern of segments and strands, the concentration of cumulative displacement, and the higher Late Quaternary slip rates in the central part of the UFZ indicate that these central segments currently represent the mechanically dominant portion of the fault zone and plausible loci for future moderate to large ruptures. It is also suggested that larger earthquake events are more likely to involve, and possibly preferentially traverse, the central segments rather than being confined to the low-displacement tips. At the same time, the segmentation pattern implies that rupture lengths may be limited by geometric barriers at some bends, step-overs, or gaps, although multi-segment ruptures remain plausible where segments are closely spaced or linked by overlapping strands.

Regionally, the Ulsan fault zone is embedded within a broader intraplate fault network that includes the Yangsan, Dongnae, and Cheongun faults, and it is likely to interact kinematically with these neighbouring structures. In the central part of the UFZ, the high-displacement segments are located near the part of the northern Dongnae fault where its trace is unclear. In this area, the concentration of cumulative displacement and higher Late Quaternary slip rates suggests that a substantial portion of the strain is accommodated within the UFZ. In segment 2, the UFZ runs very close to the Cheongun fault, and both fault development and cumulative vertical separation on the Ulsan fault are relatively subdued.

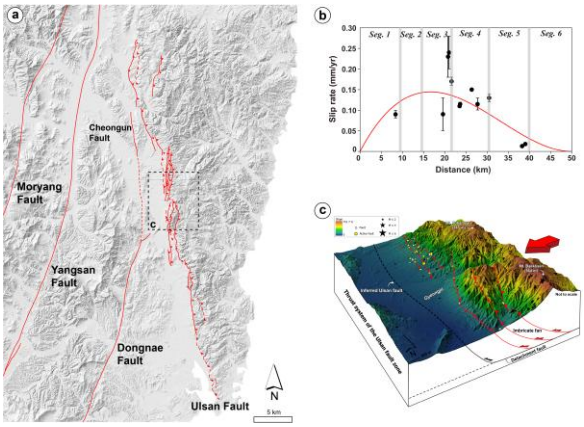

Figure 3: *(a) map showing the geometry of the Ulsan fault zone and neighboring major faults. Red lines denote mapped fault traces, highlighting the segmented and strand-rich structure of the Ulsan fault zone relative to the more linear neighboring faults. (b) Along-strike variation in reported late Quaternary slip rates on the Ulsan fault zone. Red curve is a simple trend line illustrating a broad slip rate maximum in the central part of the fault and tapering toward both tips. (c) Schematic three-dimensional block diagram of the central Ulsan fault zone, illustrating an imbricate thrust system inferred from geomorphic and structural observations.*

We interpret this as indicating that a larger strain may be taken up on the Cheongun fault in this area. Toward the northern end of the UFZ, Quaternary faulting and displacement diminish as the fault approaches the Yangsan fault, implying a progressive transfer of strain accommodation from the UFZ to the northern Yangsan segments. For seismic hazard assessment in SE Korea, where overall seismicity is low but recent earthquakes have demonstrated the potential for damaging intraplate earthquakes, it is therefore important to consider not only the behaviour of individual UFZ segments but also how deformation is partitioned among the adjacent fault system, and to evaluate the possibility of multi-segment rupture scenarios within this linked fault system.

5. CONCLUSION

To clarify how fault segments behave and interact with neighbouring fault systems in a low-strain intraplate setting, we carried out detailed geomorphic analysis and displacement-pattern profiling along the Ulsan Fault Zone in SE Korea. Our results show that cumulative vertical separation and Late Quaternary slip rates are both strongly concentrated in the central part of the UFZ and systematically decrease toward the fault tips, indicating that strain and uplift are preferentially focused in a structurally mature, multi-strand reverse fault that likely overlies an imbricate thrust architecture. The UFZ exemplifies how deformation in intraplate regions can be unevenly localized within specific segments of a linked fault network, underscoring that seismic hazard assessments must account for fault segmentation and system-scale interactions rather than treating individual faults in isolation.

Acknowledgements: This research was supported by a grant(2022-MOIS62-001(RS-2022-ND640011)) of National Disaster Risk Analysis and Management Technology in Earthquake funded by Ministry of Interior and Safety (MOIS, Korea).

REFERENCES

Cheon, Y., Shin, Y. H., Park, S., Choi, J.-H., Kim, D.-E., Ko, K., Ryoo, C.-R., Kim, Y.-S., & Son, M., 2023. Structural architecture and late Cenozoic tectonic evolution of the Ulsan Fault Zone, SE Korea: New insights from integration of geological and geophysical data. *Front. Earth Sci.* 11, 1183329. https://doi.org/10.3389/feart.2023.1183329.

Choi, S.J., Jeon, J.S., Song, K.Y., Kim, H.C., Kim, Y.H., Choi, P.Y., Choi, W.C., Han, J.G., Ryoo, C.R., Sun, C.G., Jun, M.S., Kim, G.Y., Kim, Y.B., Lee, H.J., Shin, J.S., Lee, Y.S., Gi, W.S., Lee, H.K., Song, Y.G., Kim, Y.S., Kang, T.S., Hong, D.G., & Kim, S.K., 2012. Active Fault Map and Seismic Hazard Map. Natural Hazards Mitigation Research Group, National Emergency Management Agency.

Davis, K., Burbank, D. W., Fisher, D., Wallace, S., & Nobes, D. 2005. Thrust-fault growth and segment linkage in the active Ostler fault zone, New Zealand. *Journal of Structural Geology*, 27(8), 1528-1546.

Kim, Y. S., & Sanderson, D. J., 2005. The relationship between displacement and length of faults: a review. *Earth-Science Reviews*, 68(3-4), 317-334.

INQUA TERPRO Project Cascading Hazards and Mitigation (CHAMP)

Holocene faulting along the Budoia-Aviano Thrust (eastern Southern Alps, NE-Italy): insights from a multidisciplinary and multiscale approach

Patricelli, Giulia (1,3), Maria Eliana Poli (1), Emanuela Falcucci (2), Stefano Gori (2), Enzo Rizzo (3), Angela Franceschet (4,1), Giovanni Paiero (1), Andrea Marchesini (1), Davide Russo (3), Fabrizio Mucchi (3), Riccardo Caputo (3)

(1) Department of Agricultural, Food, Environmental and Animal Sciences - University of Udine, 114 via del Cotonificio, 33100 Udine, ITALY. Email: giulia.patricelli@uniud.it
(2) National Earthquake Observatory - Istituto Nazionale di Geofisica e Vulcanologia - Rome, ITALY
(3) Department of Physics and Earth Sciences - University of Ferrara - Ferrara, ITALY
(4) Department of Life Sciences - University of Trieste - Trieste, ITALY

Abstract: *We present a multidisciplinary and multiscale investigation of the Budoia-Aviano Thrust System (BA), located along the Pliocene-Quaternary external front of the eastern Southern Alps (NE Italy). As part of the active SSE-verging Southalpine fold-and-thrust belt, BA accommodates ongoing N-S crustal shortening. The area has experienced at least three M>5.5 historical earthquakes, indicating significant seismogenic potential. Within the NASA4SHA PRIN project, we combined morphotectonic analyses, high-resolution geophysical imaging (deep and shallow ERT, GPR), and palaeoseismological trenching to constrain the geometry and Quaternary evolution of the fault system. The excavated trenches exposed Upper Pleistocene-Holocene deposits displaced by reverse faults, showing evidence of repeated Holocene deformation with a cumulative offset of at least 4.5 m. Here we present one of the two parallel trenches excavated. This integrated approach refines the seismotectonic framework of the eastern Southern Alps and provides essential constraints for assessing the seismic potential of the area.*

Key words*: thrust faulting, morphotectonics, palaeoseismology, multiscale analyses, eastern Southern Alps*

INTRODUCTION

Understanding the geometry and kinematics of active faults is essential for evaluating the seismogenic potential of seismic areas. In the Eastern Southern Alps (NE Italy), low deformation rates and widespread blind thrusting hinder the recognition of active structures, making fault segmentation and slip behavior difficult to constrain. Because surface-rupturing thrusts are rare and geomorphic signals are often subtle or rapidly erased, integrated multiscale approaches are crucial. Particularly, palaeoseismology provides direct constraints on shallow fault geometry, surface-rupture potential, slip rates, and earthquake recurrence (McCalpin et al., 2023), supporting seismic-hazard assessment. In this study, we present a multidisciplinary investigation—up to the palaeoseismological scale—along the Carnic Prealpine front in western Friuli (NE Italy), conducted within the PRIN project NASA4SHA. Our results provide new evidence of Holocene coseismic rupture on the backthrust associated with the S-vergent Budoia-Aviano thrust.

SEISMOTECTONIC SETTING

The study area is located along the active front of the Eastern Southern Alps (ESA), within the western Carnic Prealps of NE Italy. The structural evolution of the Eastern Southern Alps is the result of the collision and indentation of the Adriatic microplate beneath the Austroalpine domain through a multiphase tectonic history. The Dinaric compressional phase, active from the Late Cretaceous to the Middle Eocene (Doglioni and Bosellini, 1987), did not significantly affect the study area. Subsequently, during the SSE-verging Neogene (Neoalpine) compressional phase (Doglioni and Bosellini, 1987; Caputo, 1996; Castellarin and Cantelli, 2000), and particularly from the middle Miocene onward, the study area was progressively involved in the propagation of the SSE-verging fold-and-thrust systems of ESA. Particularly, the outer sector of the Southalpine Front is characterized by large-scale, well-developed fault-propagation anticlines, locally affected by a flat frontal blind segment (Caputo et al., 2010, and references therein), which cause the extensive cropping out of pre-Quaternary units along the Veneto-Friuli Prealps. During the ongoing Pliocene-Quaternary tectonic phase (≈N-S σ_1), several major structural segments developed or propagated, with lateral variations and transfer faults promoting segmentation and partial reactivation of inherited lineaments (Galadini et al., 2005). These structures forming the Frontal Thrust System are responsible for seismicity in the investigated region. Over the last millennium, the Carnic Prealpine western area has experienced three major earthquakes with M > 5.5 (Rovida et al., 2022) (Fig.1). The 1812 M 5.7 event affected the piedmont plain of the Pordenone area. In 1873, the M 6.3 Alpago earthquake produced significant destruction across the Alpago area and the Belluno-Cansiglio region. More recently, the 1936 M 6.1 Cansiglio earthquake heavily impacted the southern Cansiglio area and the Alpago basin. Regarding seismogenesis, while the source of the 1812 earthquake remains uncertain due to its ambiguous macroseismic pattern, the 1873 and 1936 events are attributed to two adjacent seismogenic sources along the Carnic Prealps front—the Polcenigo-Montereale and Cansiglio sources, respectively (Galadini et al., 2005).

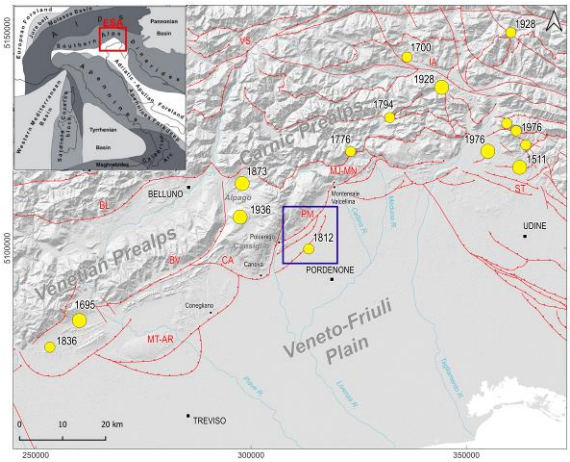

Figure 1: *Structural map of the Eastern Southern Alps with the distribution of* M > 5.5 *historical seismicity (yellow circles) (Rovida et al., 2022). Blue box is the study area. Faults: BL: Belluno th., BV: Bassano-Valdobbiadene th., CA: Cansiglio th., IA: Idrija-Ampezzo fs., MT-AR: Montello-Arcade th., MJ-MN: Monte Jouf-Maniago ts., PM: Polcenigo-Montereale ts., ST: Susans-Tricesimo ts., VS: Valsugana th. SR: EPSG 6708.*

The Polcenigo-Montereale Thrust System

The Polcenigo-Montereale system extends approximately 20 km from the Livenza River to the Cellina Stream, trending SW-NE (Poli et al., 2015). Across strike, the PM system consists of three distinct reverse fault planes: the Polcenigo-Montereale (PM), the Budoia-Aviano (BA), and the Vigonovo (VI) thrusts (Fig. 2).

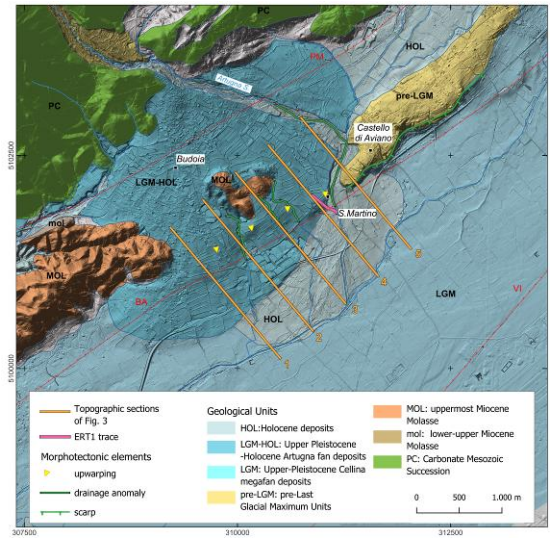

Figure 2: *Geological and morphotectonics on the shaded relief from a 1 m mesh DTM of the study area (Z factor: 7x).*

The entire thrust system underlies the large Cansiglio-Cavallo macro-anticline, formed by the Mesozoic carbonate succession, displaces the Miocene Molasse deposits and propagates upwards progressively affecting the Quaternary units. Several geomorphic indicators are associated with the activity of the Budoia-Aviano thrust (Poli et al., 2015), including deformation of the Upper Pleistocene-Holocene alluvial fan, which appears upwarped, drainage anomalies affecting small streams incising the distal part of the fan near Budoia, a ~25 m-high scarp delimiting the SE side of the Castello di Aviano relief, and the marked deviation of the Artugna River as it approaches Castello di Aviano. In this study, we focus specifically on the portion of the Budoia-Aviano thrust located between the municipality of Budoia and Castello di Aviano locality.

METHODS AND RESULTS

We applied a multiscale approach that integrates geological-morphotectonic mapping, deep and shallow geophysics, and palaeoseismology, allowing us to correlate observations from the scale of the entire thrust system down to its individual splays.

Morphotectonic Analysis

The investigated sector can be divided into three main geomorphological domains (Fig. 2). In the northwestern area, characterized by steep slopes, Mesozoic carbonate platform deposits crop out extensively. The central piedmont sector is dominated by the Upper Pleistocene-Holocene alluvial fan of the Artugna Stream, which is currently entrenched by the stream itself. Locally, isolated hills consisting of uppermost Miocene Molasse and pre-Last Glacial Maximum units. Downstream of the Castello di Aviano relief, the Artugna Stream begins to aggrade, forming the present Holocene alluvial fan, which develops at the interaction zone between the older Upper Pleistocene-Holocene fan and the Last Glacial Maximum (LGM) deposits of the high plain. The southeastern portion of the study area is dominated by the LGM Cellina megafan deposits (Fontana et al., 2014).

For the morphotectonic analysis, we examined the high-resolution (1 m) DTM derived from the LiDAR survey conducted by the Friuli Venezia Giulia Civil Protection between 2006 and 2010, with an average point density of four classified ground points per square meter and freely available from the regional geoportal. In detail, we constructed a series of five evenly spaced (500 m) topographic cross-sections oriented across strike of the Budoia-Aviano thrust, intersecting the distal portion of the Artugna LGM fan (Figs. 2 and 3).

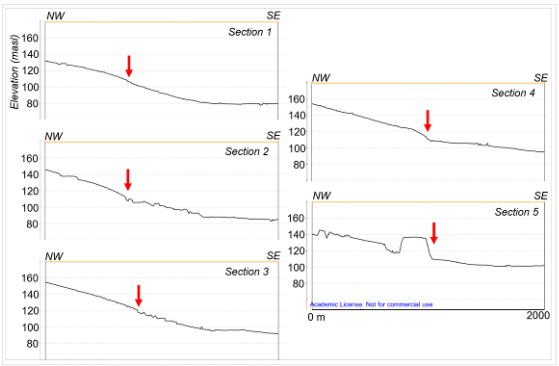

Figure 3: *NW-SE oriented seriated topographic profiles showing the surface anomaly (profile traces in Fig. 2).*

The profiles (Fig. 3), displayed with a 7× vertical exaggeration, clearly highlight a discontinuity in the fan

morphology, separating an upwarped upstream sector from a more regular downstream surface. Section 5 intersects the prominent ~25 m-high scarp bordering the Castello di Aviano high, composed of pre-LGM conglomerates. The N60° orientation of the discontinuity is consistent with the structural trend of the Budoia-Aviano thrust.

Geophysical Survey

To investigate the subsurface discontinuity, a suite of multiscale geophysical surveys was conducted, including deep and shallow electrical resistivity tomographies (DERT and ERT) and ground-penetrating radar (GPR) (Rizzo et al., 2025). The deeper DERT survey imaged the overall structural architecture, clearly resolving the Polcenigo-Montereale (PM) and Budoia-Aviano (BA) fault planes, while higher-resolution shallow ERT and GPR focused on the San Martino locality, where the deep discontinuity aligns with pronounced surface deformation (Fig. 4).

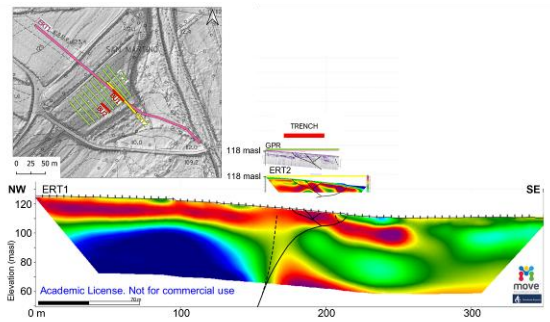

Figure 4: *multiscale geophysical survey conducted at the San Martino di Budoia locality.*

The shallow ERT survey with 5 m spacing (ERT1) imaged the upper ~50 m, revealing a steep discontinuity separating low-resistivity fractured Miocene Molasse to the north from intermediate resistivity LGM deposits to the south. This break propagates upward into a high-resistivity unit interpreted as the Upper Pleistocene-Holocene Artugna alluvial fan. At finer scale, the 1 m spacing survey (ERT2) better resolved the upper ~10 m, dominated by the same high-resistivity fan unit, and revealed several small-scale discontinuities within the alluvial deposits. In parallel with the ERTs, the seriated GPR profiles (300 MHz) detected south-dipping discontinuities disrupting lateral sediment continuity, consistent with ERT anomalies, thereby providing essential constraints for defining the palaeoseismological trench siting strategy.

Palaeoseismology

Based on the results of the morphotectonic and geophysical survey, we conducted a palaeoseismological analysis in the San Martino di Budoia locality (Poli et al., 2025). In this note we present the results of the Budoia2 trench (BU2 in Fig. 4) which exposed late LGM to Holocene deposits of the Artugna alluvial fan (Fig. 5).

Basal Unit A forms a south-dipping stratified body consisting of sandy-matrix gravels. Up-section, Unit A gradually grades upwards into the brown silty-clayey horizon of Unit B, where sub-rounded clasts show weak weathering. Above Unit B, the overlying Unit C consists of a basal medium- to-fine sand body (C1) grading upward to gravels with sand and pebbles. The entire alluvial sequence is overlain by 30-50 cm of ploughed soil.

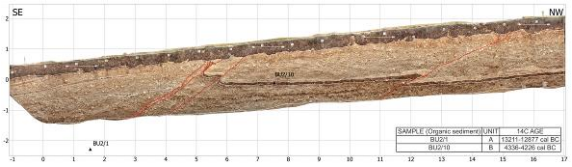

Figure 5*: Interpreted orthomosaic of the western wall of Budoia2 trench, black triangles indicate the C14 dated samples.*

Although the geometry of the alluvial fan bodies indicates a SSE-directed flow, consistent with the site's alluvial dynamics, the lateral continuity of the entire succession is disrupted by the presence of north-verging reverse shear planes. We identified a main damage zone comprised between coordinates 3 and 6 m (Fig. 5, see details in Fig. 6).

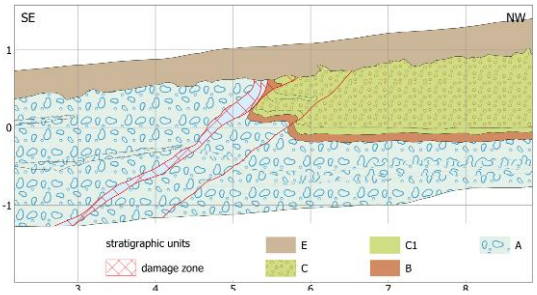

Figure 6: *Interpretation of the Budoia2 trench between coordinates 3 - 8 m.*

The major southern (inner) shear zone is clearly emphasized by the rotation and re-orientation of several gravels and marks the abrupt interruption and the upward dragging of Units B and C against the uplifted Unit A (Fig. 5). The second identified reverse plane, which develops at the footwall of the major one, further displaces the stratigraphic succession at coordinates 4-6 m (Fig. 7a).

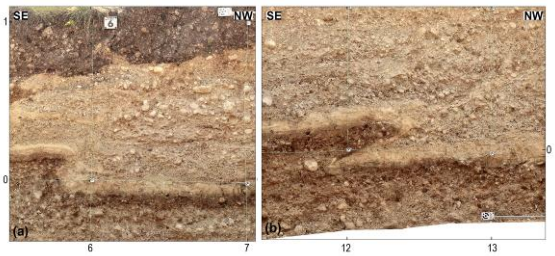

Figure 7: *(a) detail of the secondary reverse plane of the main fault zone; (b) detail of the minor reverse splay between coordinates 11 and 15 m.*

Between coordinates 11 and 15 m an additional intermediate-to-low angle reverse fault plane is present which displaces Units A, B and C1 and propagates upwards, clearly marked by iso-aligned clasts, up to the bottom of the ploughed soil (Figs 5, 8 and Fig. 7b).

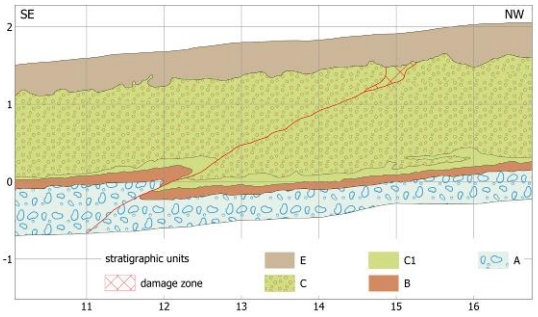

Figure 8: *Interpretation of the Budoia2 trench between coordinates 11 - 16 m.*

DISCUSSION AND CONCLUSIONS

The palaeoseismological analysis conducted across the pronounced morphotectonic evidence referred to the Budoia-Aviano thrust in the San Martino locality revealed a north-verging back-thrust system composed of multiple shear planes, confirming the geometry of the discontinuities imaged by the GPR data. A direct comparison between the radargram and the trench-wall interpretation shows an excellent match of both the stratigraphic geometries and the south-dipping shear planes (Fig. 9). The identified fault-related evidence indicates late Pleistocene-Holocene activity of the reverse fault planes, with vertical offsets of about 25 cm along the secondary plane (measured on the bottom of B unit, between coordinates 11 and 13 m, Fig. 8) and a minimum total displacement of approximately 90 cm (measured on the bottom of Unit B) along the main fault zone (coordinates 4-6 m, Fig. 6). By taking into account the seismic potential of the area documented in historical times (Rovida et al., 2022), the displacement observed on the secondary plane may be attributed to a single post-C1 seismic event. Conversely, for the >90 cm vertical displacement measured along the major shear zone, it is reasonable to assess that the deformation recorded in the trench walls represents a cumulative record of multiple events occurred in the last 6500 years, since the development of Unit B.

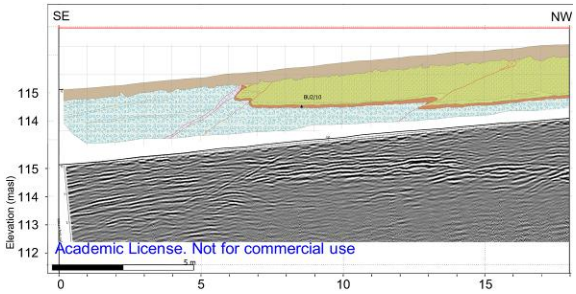

Figure 9: *Comparison between the interpreted western wall of the Budoia2 trench (top, legend in Figs. 6 and 8) and the radargram (bottom).*

Based on the collected data, the multiscale analysis suggests that, in the portion of the Southalpine front between Budoia and Aviano, the deformation is certainly accommodated through folding and coseismic displacement along backthrusts. However, the nature and deformational behavior of the south-verging forethrust, onto which these backthrusts root and which ultimately controls the deformation, still require further investigation.

Acknowledgements: This work was carried out thanks to the support of the Italian PRIN Project (Research Projects of National Interest) NASA4SHA "*Fault segmentation and seismotectonics of active thrust systems: the Northern Apennines and Southern Alps laboratories for new Seismic Hazard Assessments in northern Italy*" (PI R. Caputo).

REFERENCES

Caputo R., 1996. The polyphase tectonics of eastern Dolomites, Italy. *Memorie di Scienze Geologiche* 48, 93-106.

Caputo, R., Poli, M.E., Zanferrari, A., 2010. Neogene-Quaternary stratigraphy of the eastern Southern Alps, NE Italy. *Journal of Structural Geology* 32, 1009-1027. https://doi.org/10.1016/j.jsg.2010.06.004.

Castellarin, A., Cantelli, L., 2000. Neo-Alpine evolution of the Southern Eastern Alps. *Journal of Geodynamics* 30, 251-274.

Doglioni, C., Bosellini, A., 1987. Eoalpine and mesoalpine tectonics in the Southern Alps. *Geologische Rundschau* 76, 735-754.

Fontana, A., Mozzi, P., Marchetti, M., 2014. Alluvial fans and megafans along the southern side of the Alps. *Sedimentary Geology* 301, 150-171. https://doi.org/10.1016/j.sedgeo.2013.09.003.

Galadini, F., Poli, M.E., Zanferrari, A., 2005. Seismogenic sources potentially responsible for earthquakes with M > 6 in eastern Southern Alps (Thiene-Udine sector, NE Italy). *Geophysical Journal International* 161, 739-762. https://doi.org/10.1111/j.1365-246X.205.02571.x.

McCalpin J., Ferrario F., Figueiredo P., Livio F., Grützner C., Pisarska-Jamrozy M., Quigley M., Reicerter K., Rockwell T., Štěpančíková P., Tábořík P., 2023. New developments in onshore paleoseismic methods, and their impact on Quaternary tectonic studies. *Quaternary International* 664, 59-76. https://doi.org/10.1016/j.quaint.2023.03.008.

Poli M.E., Monegato G., Zanferrari A., Falcucci E., Marchesini A., Grimaz S., Malisan P., Del Pin E., 2015. Seismotectonic characterization of the western Carnic pre-alpine area between Caneva and Meduno (NE Italy, Friuli). *DPC-INGV-S1 Project "Base-knowledge improvement for assessing the seismogenic potential of Italy" (D6/a2.1).*

Poli M.E., Patricelli G., Falcucci E., Gori S., Rizzo E., Paiero G., Marchesini A., Franceschet A., Russo D., Boldrin P., Sobbe A., Caputo R., 2025. Recent tectonic activity of the Budoia-Aviano Thrust: the example of the Late Pleistocene-Holocene Artugna alluvial fan (eastern Southern Alps, NE Italy). *Miscellanea INGV* 103, 91-96. https://doi.org/10.13127/misc/103.

Rizzo E., Poli M.E., Patricelli G., Giampaolo V., De Martino G., Mucchi F., Marchesini A., Boldrin P., Bonali F.L., Caputo R., 2025. Deep and Shallow Electrical Resistivity Tomography on the Budoia-Aviano Thrust (NE Italy). *Miscellanea INGV* 103, 75-80. https://doi.org/10.13127/misc/103.

Rovida, A., Locati, M., Camassi, R., Lolli, B., Gasperini, P., Antonucci, A., 2022. Catalogo Parametrico dei Terremoti Italiani (CPTI15), versione 4.0. Istituto Nazionale di Geofisica e Vulcanologia. https://doi.org/10.13127/CPTI/CPTI15.4

Intraplate rupture pattern revealed by lacustrine deposits in northwestern Mongolia

Pinzon, Nicolás (1), Klinger, Yann (1), Duarte, Edward (2), Sabatier, Pierre (2), Jin-Hyuck Choi (3), et al., Baataraa Ga (4)

(1) Université Paris Cité, Institut de Physique du Globe de Paris (IPGP), CNRS, Paris, France
(2) EDYTEM, University Savoie Mont Blanc, CNRS, Le Bourget du lac, France
(3) Korea Institute of Geosciences and Mineral Resources, Daejeon, South Korea
(4) Institute of Astronomy and Geophysics, Ulaanbaatar, Mongolia

Abstract: *Large intraplate earthquakes can occur in unexpected places and can reach devastating magnitudes. However, how these earthquakes accommodate deformation over long–term periods remains unknown, given their rare occurrence. Here, we apply lacustrine paleoseismology to reconstruct the history of large earthquakes along the Bulnay Fault System (BFS) in Mongolia. Sedimentary archives from Mongol Lakes revealed micrometer-scale event deposits triggered by large–to–major earthquakes. We identify four seismic events from sedimentological and geochemical signatures over the last 9 kyr. The most recent corresponds to the great Mw8 1905 earthquake sequence, while the penultimate event appears to be previously undocumented. The tempo of these ruptures suggests that: 1) the Bulnay fault releases strain by episodic independent ruptures along the Bulnay fault and synchronized major events involving the Bulnay and nearby Tsetserleg faults, and 2) the 1905 earthquake-doublet may have marked the onset of a multimillennial period of seismic quiescence along the BFS.*

INQUA TERPRO Project Cascading Hazards and Mitigation (CHAMP)

Paleoseismological constraints on fault linkage and segmentation in the Cinque Miglia–Aremogna fault system, central Italy.

Pizzi, A. (1), Boncio P. (1), Francescone M. (1), Puliti I. (1), Chiarini E. (2), Morelli F. (3), Nirta G. (2), Nocentini M. (2), Piacentini T. (3), Testa A. (1), Pepe M. (1) & Desideri A. (1)

(1) Department of Engineering and Geology, University of Chieti-Pescara, Italy, alberto.pizzi@unich.it
(2) Italian Institute for Environmental Protection and Research (ISPRA), Rome, Italy
(3) Department of Science, University of Chieti-Pescara, Italy

Abstract: *We analysed the geological and structural setting, and paleoseismological record of the Aremogna–Cinque Miglia Fault System (ACMFS), located in the southernmost portion of the active extensional belt of the central Apennines (Italy). A key objective of the study was to test whether the ACMFS may have ruptured synchronously with the Mt. Morrone Fault to the north, for which previous work suggested rupture lengths exceeding 21 km to account for the displacements observed in paleoseismic trenches. We also examined the possible southeastward continuation of the system along the Ortona–Roccamonfina transverse lineament (ORL), which marks the boundary between the central and southern Apennine arcs, to assess whether inherited contractional structures may act as segmentation barriers. Geological and structural mapping, integrated with three paleoseismological trenches across the ACMFS, revealed evidence of at least four Holocene surface-rupturing earthquakes (younger than 3365 BCE). At least one of these events displays an age consistent with a surface-rupturing event recognized along the Mt. Morrone Fault. This temporal overlap suggests a possible "multi-fault system earthquake" involving both structures. On the other hand, the new surface and subsurface geological constraints appear to exclude the "physical continuation" of the ACMFS southeast of the ORL, suggesting that strain is instead accommodated by distinct fault architectures and deformation styles. This supports the view of the ORL as a major structural segmentation boundary.*

Key words*: Active normal faults, segmentation, paleoseimology, Central Apennines.*

INTRODUCTION

Significant advances achieved over the past decades in the mapping of active and capable faults, supported by new technologies in both field acquisition and remote sensing, are clearly evidenced by the proliferation of tectonic maps and dedicated fault databases. Accurate definition of the surface trace of active and capable faults is crucial not only for surface-rupture hazard assessment but also for evaluating seismic potential, which is intrinsically controlled by the length and segmentation of the seismogenic fault.

This is particularly relevant for the active extensional system affecting the axial zone of the Central–Northern Apennines (Italy), characterized by normal fault systems up to ~30 km long with predominantly W-dipping planes, and commonly bounding intramountain basins filled with fluvio–glacio–lacustrine and slope-derived deposits (Fig. 1). However, the 2016–2017 Central Italy seismic sequence, culminating in the October 30th Mw 6.5 mainshock, demonstrated that even well-mapped adjacent fault systems (e.g., the Mt. Vettore–Mt. Bove and Laga Mts. faults), despite clearly defined surface traces from geological and geomorphological data, may interact and rupture synchronously as a "multi-fault system earthquake". Furthermore, the 2016–2017 sequence highlighted how pre-existing cross structures, such as Miocene–Pliocene thrust-ramps inherited from the contractional emplacement of the Apennines thrust-and-fold belt, may act as temporary rupture barriers during the initial events. These structures localized stress accumulation until eventually serving as the nucleation point for the largest Mw 6.5 shock, which ruptured across the barrier itself (e.g., Pizzi et al., 2017). Both observations point out that even high-resolution fault mapping and precise segmentation of the active extensional belt along the Apennine axis are not always sufficient to constrain the maximum expected earthquake on a given fault system.

Given these open issues, we investigated the Aremogna–Cinque Miglia Fault System (ACMFS), located at the southern termination of the Central Apennine arc and at the transition to the Southern Apennines. This system, indeed, exhibits key structural and kinematic similarities with the fault networks activated during the 2016–2017. The study consisted of detailed geological and structural mapping, supported by surveys carried out for the Capracotta sheet of the Geological Map of Italy (Servizio Geologico d'Italia, *in press*). Furthermore, morphotectonic analyses based on high-resolution DEMs, followed by the excavation of three paleoseismological trenches, whose locations were also selected on the basis of geophysical investigations, were performed.

GEOLOGICAL SETTING

The Aremogna-Cinque Miglia normal fault system (ACMFS) is characterized by SW- to W-dipping faults linked by a complex relay zone that developed between two overlapping and nearly parallel segments. The system comprises a series of fault segments trending NW-SE to N-S, which offset Late Pleistocene and Holocene continental deposits. The fault network extends over a total length of ca. 16 km.

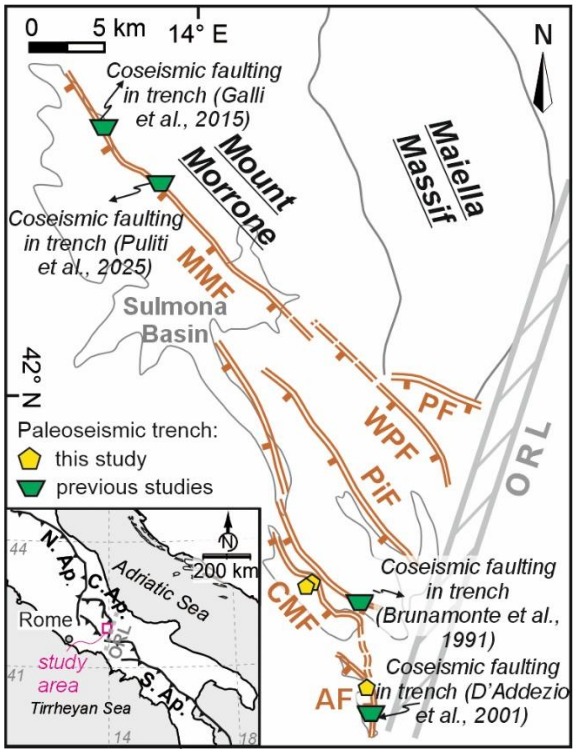

Figure 1: *Main Quaternary SW-dipping normal faults in the outer sector of the southern Central Apennines, with the location of paleoseismological trenches. MMF: Mt. Morrone Fault; PF: Palena Fault; WPF: western Porrara Fault; PiF: Pizzalto Fault; CMF: Cinque Miglia Fault; AF: Aremogna Fault; ORL: Ortona–Roccamonfina transverse lineament. The study area is shown in the inset. N.Ap., C.Ap. and S.Ap. indicate the Northern, Central and Southern Apennines, respectively.*

It is one of the earliest active fault systems in the central Apennines, where seismic potential has been inferred by excavation of paleoseismological trenches
(Frezzotti & Giraudi, 1989; Brunamonte et al., 1991). The normal fault system bounds adjacent intramountain basins: the Aremogna basin to the south (average elevation 1450–1500 m a.s.l.) and the Cinque Miglia basin to the north (≈ 1250 m a.s.l.). Both basins contain glacial–fluvioglacial and alluvial–lacustrine deposits. Detailed geological and geomorphological mapping and stratigraphic surveys reveal, based on the age of displaced continental deposits, the presence of both synthetic and antithetic fault segments showing clear evidence of Quaternary activity. These segments exhibit along-strike variability, en échelon geometry, and step-over/relay zones configuration, consistent with active deformation along the ACMFS.
The Cinque Miglia normal faults consist of segments approximately 6 km long bordering the basin of the same name to the east, with a prevailing NW-SE orientation, but with local E-W and N-S variations. In the central area, the trace is not very clear and lacks outcrops. In contrast, in the northern and southern portions, the fault appears as continuous escarpments up to 3 meters high that displace Quaternary continental deposits, including alluvial and fluvioglacial sediments. In the south-eastern area, the fault plane outcrops to the west and displaces the carbonate succession of scarp-basin limestones, including Pleistocene and Holocene alluvial deposits. A segment of the same sector, about 1.7 km long, crosses the western edge of the plateau in a NW-SE direction. The fault displaces Holocene lacustrine-marsh and alluvial deposits and is marked by continuous escarpments up to 2 meters high. The trace is oriented NW-SE and displaces Holocene alluvial deposits dated to 1370±1000 BCE by D'Addezio et al. (2001) in the authors' paleoseismological study.
The Aremogna fault consists of a series of W-dipping segments with a predominantly (N)NW-(S)SE orientation to the north and N-S towards the south. From the north, the plain branches into two main segments, the first of which can be identified along a narrow depression, elongated NW-SE. The second segment continues in a north-northwest to south-southeast direction, forming a transfer zone between the Aremogna fault and the Cinque Miglia fault, which appears to be partially buried by slope deposits and continues through Holocene alluvial sediments and a carbonate substrate, maintaining an active role in recent tectonic modelling of the area. At its southernmost edge, it branches off into numerous synthetic and antithetic segments to the main structure.

RESULTS, DISCUSSION AND CONCLUSIONS

During surveys of the Capracotta sheet, three paleoseismological trenches were excavated in both sectors of the Aremogna-Cinque Miglia fault system (Fig. 1). In the Aremogna sector, the trench dug at an altitude of 1444 m revealed synthetic and antithetic planes that displace Holocene paleosols, highlighting how the fault activity dissects the topographic surface in at least four events, some of which were confirmed by the previous studies (D'Addezio et al., 2001). Only one of two trenches dug for the Cinque Miglia basin, at an altitude of 1262 m, along a section of the fault bordering the basin, revealed ruptures in the Pleistocene fluvioglacial deposits.

With a benched slot approximately 38 m long in the WSW-ESE direction, 12 stratigraphic units were identified in the Aremogna trench, in the hanging wall and in the footwall. were identified and associated with repeated fault-activation events. The trench showed two normal fault zones. The first (FA), located in the easternmost portion of the trench, consisting of synthetic splays of the primary faults, displaces cemented Quaternary deposits at the FW and Holocene deposits at the HW; the second, is a secondary antithetic plane (FB). Based on stratigraphic and structural observations on both walls of the trench, at least four faulting events have been identified, highlighted by the occurrence of three colluvial wedges and by the later displacement of the younger colluvial wedge.

The Cinque Miglia trench is approximately 54 m long. It reveals a deformation zone in its central sector, expressed by a near-vertical fissure filled with colluvial soil. We interpret this feature as likely related to surface-faulting event(s). However, the absence of well-defined stratigraphic markers—due to the dominance of massive alluvial gravel throughout the trench—did not allow the identification of clearly offset reference horizons. The stratigraphy exposed in the trenches across the Aremogna and Cinque Miglia basins cannot be unequivocally correlated between the different sites, with the exception of the oldest units (fluvioglacial gravel cones). These deposits consistently post-date the Last Glacial Maximum (LGM) and accumulated between ~18,000 and 12,000 years ago. Therefore, paleoearthquake horizons can only be correlated across the trenches by integrating the existing chronological constraints from the literature with those obtained in this study.

Despite the uncertainties affecting both the radiometric dating and the precise placement of event horizons within the

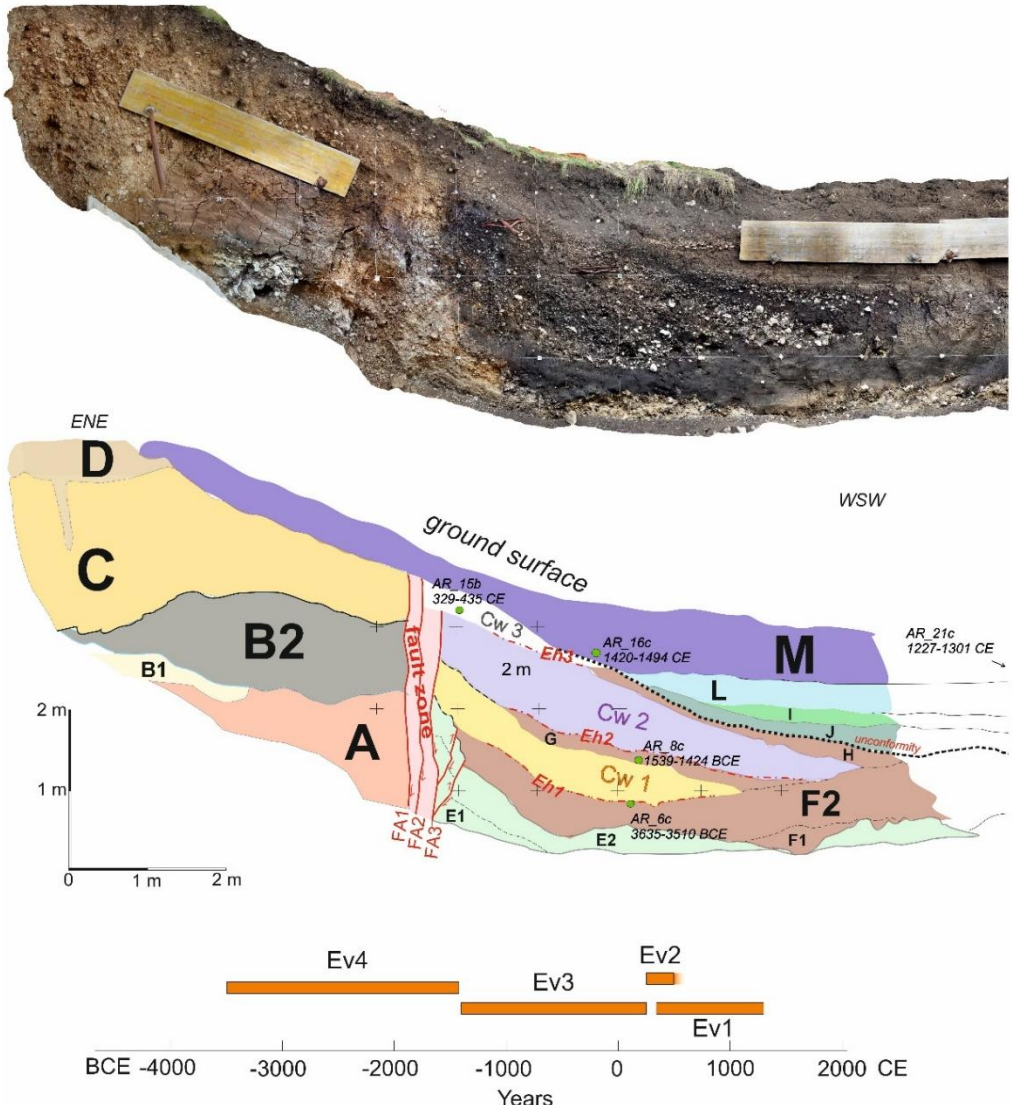

***Figure 2**: Orthoimage and interpreted log of the trench excavated across the Aremogna Fault (see Fig. 1 for location). Units A–D and E–L correspond to distinct stratigraphic packages located in the footwall and hanging wall of the fault, respectively, and are overlain by the present-day colluvial cover (unit M). CW1, CW2, and CW3 indicate the three colluvial wedges associated with paleoseismic events Ev4, Ev3, and Ev2, whereas Ev1 (the most recent event) is inferred from the subsequent faulting affecting CW3. The diagram at the bottom shows the chronological ranges of the paleo-earthquakes (orange rectangles) plotted on the time axis, which were determined based on radiocarbon dating of the analyzed samples (small circles in the log, with corresponding calibrated BCE / CE) ages.*

stratigraphic logs, there is a reasonable correlation between the ages of the five surface-rupturing events identified in the newly excavated trenches and those previously documented by other authors. Assuming the identified events ruptured the entire fault system, the number of recognized paleoearthquakes should be regarded as a minimum estimate. This is because the trenches intersect only a subset of the fault strands and subsidiary splays that compose the system, some of which may not have ruptured during all events. In addition, stratigraphic gaps due to erosion and/or limited sediment accumulation imply that portions of the paleoseismic record may be missing.

On this basis, the most recent surface-rupturing earthquake is constrained to the interval between 329 CE and 1227–1494 CE. The penultimate event is defined within a narrower time range and is inferred to have occurred between 326 CE and 435 CE. The third recognized event spans the period 810 BCE to 1370 BCE. The fourth event, based on previously published datasets, is constrained to 3635–3120 BCE, whereas the oldest rupture is interpreted to have occurred between 4230 and 3510 BCE.

By comparing the Holocene paleoseismic history of the ACMFS, as reconstructed in this study and in D'Addezio et al. (2001), with that of the Mt. Morrone Fault reported by Galli et al. (2015) and Puliti et al. (2025), a close chronological correspondence emerges for a major surface-rupturing earthquake. This event produced ≥1 m of coseismic displacement along the Mt. Morrone Fault and approximately ≥0.6 m along the ACMFS and is tentatively dated to the interval 3350–2950 BCE (i.e., ~5300–4900 BP). Although this interpretation remains to be fully constrained by additional chronological and displacement data, it suggests a rupture capable of propagating between adjacent fault systems, thus generating a multi-fault system earthquake.

On the other hand, new surface and subsurface geological data from the Capracotta sheet of the Geological Map of Italy (Servizio Geologico d'Italia, *in press*) appear to exclude any physical continuation of the ACMFS fault planes southeast of the ORL, suggesting that extension in this sector may be accommodated on different, and not necessarily hard-linked, fault systems. Accordingly, the ORL separates two tectonic domains in which active strain is likely partitioned through distinct deformation styles. This contrast is favoured by the presence, southeast of the ORL, of a thick allochthonous sequence dominated by clay–marl deposits that promotes mechanical decoupling with respect to the underlying carbonate succession, as also proposed by Battistelli et al. (2025).

Conversely, northwest of the ORL, the structural barrier effect on southeastward rupture propagation is expressed by an increase in cumulative displacement that is not localized at a single SE tip (as documented, for example, along the Mt. Vettore–Mt. Bove Fault), but is instead distributed across a set of short, subparallel fault strands (see Fig. 1).

These observations support the interpretation of the ORL as a major transverse structural barrier. Rather than representing a simple gap along the active extensional belt of the Apennine axis, the ORL exerts a first-order role as a segmentation boundary and thus directly influences the dimensioning of seismogenic sources, with associated implications for seismic hazard assessment.

REFERENCES

Battistelli, M., Ferrarini, F., Bucci, F., Santangelo, M., Cardinali, M., Boncori, J. P. M., Cirillo D., Carafa M.C. & Brozzetti, F. (2025). Bridging the Gap Between Active Faulting and Deformation Across Normal-Fault Systems in the Central–Southern Apennines (Italy): Multi-Scale and Multi-Source Data Analysis. Remote Sensing, 17(14), 2491.

Brunamonte, Michetti, Serva, & Vittori. (1991). Evidenze Paleosismologiche nell'Appennino Centrale ed implicazioni neotettoniche. Studi Geologici Camerti.

D'Addezio, G., Masana, E., & Pantosti, D. (2001). The Holocene paleoseismicity of the Aremogna-Cinque Miglia Fault (Central Italy). In Journal of Seismology (Vol. 5).

Frezzotti M., & Giraudi C. (1989). Evoluzione geologica tardo-pleistocenica ed olocenica del Piano di Aremogna (Roccaraso-Abruzzo): Implicazioni climatiche e tettoniche. Memorie Della Società Geologica Italiana, 42, 5–19.

Galli, P., Giaccio, B., Peronace, E., & Messina, P. (2015). Holocene paleoearthquakes and early–late Pleistocene slip rate on the Sulmona fault (central Apeninnes, Italy). Bulletin of the Seismological Society of America, 105(1), 1-13.

Pizzi, A., Di Domenica, A., Gallovič, F., Luzi, L., & Puglia, R. (2017). Fault Segmentation as Constraint to the Occurrence of the Main Shocks of the 2016 Central Italy Seismic Sequence. Tectonics, 36(11), 2370–2387. https://doi.org/10.1002/2017TC004652

Puliti, I., Pizzi, A., Gori, S., Falcucci, E., Galadini, F., Moro, M., & Saroli, M. (2025). Paleoseismological evidence of multiple, large-magnitude earthquake surface ruptures on the active Mt. Morrone normal fault, central Apennines, Italy. Solid Earth. Servizio geologico.

INQUA TERPRO Project Cascading Hazards and Mitigation (CHAMP)

Searching for Hidden Local Faults Using a Dense Seismic Array

Protti, M. (1), A. Barbour (2), P. Bodin (3), N. Campos (1), E. Chaves (1), J. Gomberg (2), S. Hajaji (1), W. Jiménez (1), E. Núñez (1), T. Saw i(2), F. Vega (1)

(1) Observatorio Vulcanológico y Sismológico de Costa Rica, Universidad Nacional, Costa Rica.
(2) United States Geological Survey.
(3) University of Washington

Abstract: *To contribute to the identification and 3-D mapping of active faults in and around Cartago in central Costa Rica, scientists from OVSICORI-UNA and the USGS installed and operated an urban, dense. seismic array from July 2024 to April 2025. The network consisted of 70 autonomous, short-period, three-component 'nodal' seismometers on a grid at an average spacing of about two km. Local faults produced moderate magnitude earthquakes that destroyed the city of Cartago and killed hundreds of people in the 19th and 20th centuries and are likely to do so again. We present preliminary results from both manually and AI-located earthquakes. This easily deployed seismic system is well-suited for preparing for, or responding to multiple types of impactful geologic events and may be shared with regional partners as needed.*

INQUA TERPRO Project Cascading Hazards and Mitigation (CHAMP)

paleoseismicity.org

A strategy for refining post-LGM slip rates of fault systems in the Central Apennines, Italy

Pucci, Stefano (1), Riccardo Civico (1), Carlo Alberto Brunori (1), Paolo Marco De Martini (1), Marco Caciagli (1), Tullio Ricci (1)

(1) Istituto Nazionale di Geofisica e Vulcanologia, via di Vigna Murata 605, 00143, Roma.
Email address of corresponding author: stefano.pucci@ingv.it.

Abstract: *In the Central Apennines, a significant discrepancy exists between geodetic extension rates and geological slip rates, likely due to short observational windows and inaccuracies in slip-rate estimates. To address this, we present a high-resolution approach to refine post-Last Glacial Maximum (LGM) displacement variability. Using systematic airborne LiDAR, we generated high-resolution DTMs to image subtle geomorphic offsets, even in vegetated areas. We developed SCARPS (Scarp Analysis and Reconstruction Profile System), a Python-based tool for semi-automatic morphometric analysis. SCARPS extracts along-strike throw distributions by modeling the geometric intersection between the fault plane and the reconstructed LGM footwall surface. Furthermore, we introduce a theoretical framework to evaluate the "zero-age" assumption of LGM markers, defining the boundary between scarp preservation and demolition based on the interplay between fault kinematics and erosion rates. This integrated method provides a robust baseline for improving strain-release models and seismic hazard assessments in complex active fault systems.*

Key words*: Tectonic geomorphology, fault scarp, Last Glacial Maximum, slip rate, Central Apennines.*

INTRODUCTION

In the Central Apennines of Italy, where active extension is accommodated by moderate-to-large earthquakes (M > 5.5), the tectonic moment rate (derived from strain rate maps) is widely observed to exceed the seismic moment release rate calculated from instrumental and historical earthquake catalogues (e.g., D'Agostino, 2014; Nucci et al., 2025). This imbalance in the geodetic-to-seismic budget can be explained by (i) the aseismic release of a portion of the tectonic moment, and/or (ii) the short observational time window relative to the estimated fault recurrence intervals (> 1 kyr) and the completeness of historical catalogues (i.e., the low frequency of large earthquakes; Cinti et al., 2021).

Against this background, extending the observation period into the past using geological data is essential, with the aim of expanding the present-day dataset of on-fault paleoearthquakes and slip rates. Furthermore, given that current geodetic data lack the resolution to distinguish the loading gradient on individual fault systems, a discrepancy between geodetic and geological extension rates is also evident. Geological studies over the past two decades (e.g., Galli et al., 2008) show that Quaternary fault slip rates across the Central Apennines—even for active faults with higher-than-average values (~1 mm/yr)—are significantly below the range required to account for geodetic extension rates. This mismatch may stem from inaccuracies in geological slip rate estimates.

Over the past two decades, fault scarps in the Central Apennines have become prime targets for investigations aiming to determine slip rate (e.g. Roberts and Michetti, 2004; Papanikolaou et al., 2005; FaureWalker et al., 2009). These features serve as archives of cumulative surface-rupturing earthquakes, which are essential for reconstructing paleoseismic records. Both tectonic factors (e.g., slip magnitude, recurrence intervals) and geomorphic processes (e.g., mechanical properties of the bedrock, erosion/deposition rates) influence the preservation of fault scarps and the number of events they record.

Well-preserved Holocene bedrock fault scarps are widely used to represent cumulative post-LGM (Last Glacial Maximum) slip (e.g., Bosi, 1975; Roberts and Michetti, 2004). While some argue these features are primarily erosional (e.g., Kastelic et al., 2017), most authors maintain that intense Pleistocene periglacial erosion—at rates up to 30 times higher than in the Holocene—would have erased any pre-existing scarps (Tucker et al., 2011). Consequently, the transition to post-glacial conditions created a regional morphological marker of smoothed periglacial slopes and glacial sediments, typically dated to the last major glacial retreats (Giraudi and Frezzotti, 1997).

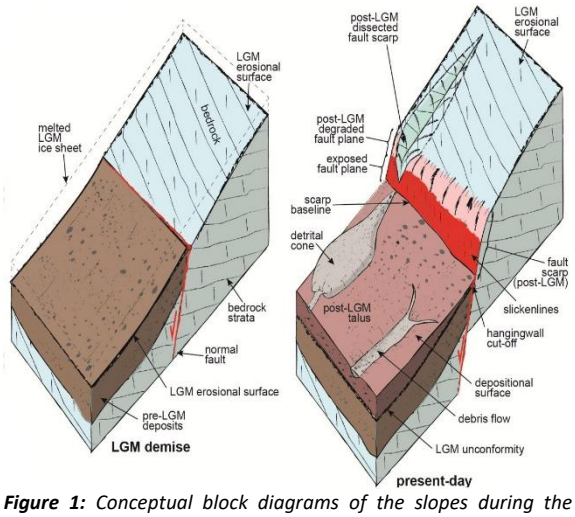

Figure 1: *Conceptual block diagrams of the slopes during the demise of the last glacial maximum (LGM) and present-day. At the demise of the LGM, the hypothesis is that the slope was originally*

quasi-planar and the scarp was generally not exposed as erosion and sedimentation rates outstripped the fault slip rate. At present day, the tectonic scarp records the post-LGM fault slip (from Pucci et al., 2021).

This 'zero-age' assumption has been supported by cosmogenic ^{36}Cl dating of carbonate slip surfaces (e.g., Tesson et al., 2021; Roberts et al., 2025). Although direct dating of preserved LGM hillslopes is nearly absent—with the exception of the Fiamignano fault (~17 ka)—available data confirm that these scarps record cumulative slip since the end of the LGM. However, these dates often yield large uncertainties, ranging between ~10 and ~23 ka (mean: 17.8 ± 4.3 ka; Cowie et al., 2017). Such uncertainty in age estimates may result from erosional processes that, during the transition to full post-glacial conditions, might not have provided a unique regional marker by erasing all pre-existing or forming bedrock fault scarps. In fact, the glacial and periglacial regional markers in the Apennines can be correlated with different post-LGM retreat phases. These phases may significantly predate the 12–18 ka BP interval generally used to calculate throw rates for normal faults.

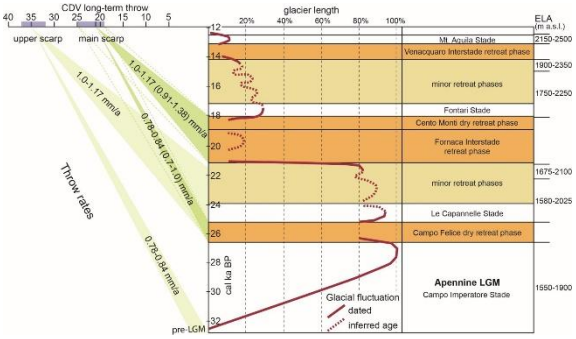

Figure 2: *Chronology of the Apennines LGM and deglaciation phases according to Giraudi (2015). Example of correlation of the post-glacial long-term throws of a fault scarp with different retreat phases indicating possible ages and throw-rates (from Pucci et al., 2021).*

Furthermore, despite significant chronological uncertainties, slip rate estimates remain sparse and are often derived from single measurements that may not be representative of the entire fault. To bridge the knowledge gap regarding along-strike slip variability, it is crucial not only to derive accurate geological extension rates but also to assess fault segmentation and recurrence models

METHODOLOGY

To this end, we propose to acquire micro-topographic data using Airborne LiDAR technology along major normal fault systems in the Central Apennines. These systems were selected based on their high seismic potential and their role within parallel systems that accommodate present-day distributed geodetic strain.

High-resolution digital topography derived from Airborne LiDAR is of critical importance to: 1) enable fine-scale identification and mapping of fault geometry and displaced geological/geomorphological markers; and 2) document post-Last Glacial Maximum fault scarps and along-strike throw distributions for slip rate estimates. Furthermore, the acquired dataset will provide a baseline to: 1) monitor in detail the morphological evolution of fault scarps during interseismic phases; and 2) obtain the pre-earthquake high-resolution imagery necessary to determine near-field ground deformation after a future event through topographic differencing (Nissen et al., 2014). The precise (~0.02 m) and high-resolution (<0.1 m) bare Digital Terrain Models (DTMs) provided the basemap to calculate the cumulative slip distribution along the fault scarp.

For this specific purpose, we developed a workflow employing a Python-based software tool—SCARPS (Scarp Analysis and Reconstruction Profile System)—designed for the semi-automatic morphometric analysis of fault scarps from high-resolution Digital Elevation Models (DEMs). The tool extracts the along-strike fault throw distribution by implementing a geometric methodology, based on the approach of Pucci et al. (2021). This cross-platform, Graphical User Interface-based tool will be released as open-access code to ensure research reproducibility.

The geometric methodology relies on field-derived data collected from the fault plane exposed at the base of the bedrock scarp, specifically: dip direction, dip angle, rake, and slip vector. Additional input consists of three manually traced polylines derived from DTM analysis: the scarp baseline (Line 1); the top of the scarp (Line 2), defined as the upper limit of the degraded fault plane or the lower limit of the post-glacial surface; and the top of the erosional surface at the fault footwall (Line 3) (Fig. 3).

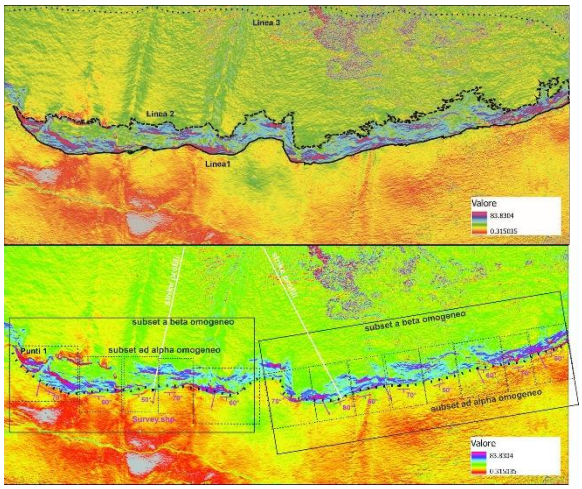

Figure 3: *Slope maps from high-resolution DTM highlighting the fauls scarp features. Upper panel reports lines of data extraction (black): scarp base (solid); lower (dashed) and upper (dotted) limits of the LGM surface. Lower panel shows boxes of sectors with homogeneous structural data (beta=slip vector; alpha=dip angle) to be assigned to the profiles.*

The code extracts high-density, parallel upslope profiles oriented according to the slip vectors and incorporating the structural data of the fault. Starting from the scarp base, each profile intersects Lines 2 and 3 to calculate: 1) the linear regression representing the LGM surface and its associated slope angle; 2) the intersection between the LGM regression line and the fault plane projection; and 3)

the fault throw (T) using the formula: T=S/(1−tan(γ)/tan(α)) (Fig. 4).

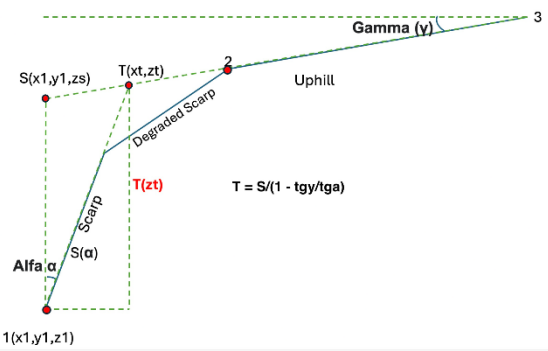

Figure 4: *Conceptual topographic profile showing the throw (T) calculation method. The equations of the two nonparallel lines used to reconstruct the footwall cut-off are reported: γ is the slope angle of the footwall LGM erosional surface at the top of the scarp identified by the regression line; surface offset (S) is its intercept with the vertical axis; α is the dip angle of the fault plane (from Pucci et al., 2021).*

The final numerical parameters are exported to a delimiter-separated text format (*.csv) file and used to generate the following plots: 1) the distribution of throw/slip along the scarp; 2) the reconstructed scarp morphology, showing the along-strike elevation distribution of the base and top; 3) individual cross-sectional profiles; and 4) a synthetic DTM of the non-reclined scarp, reconstructed from footwall cut-off to quantify degradation through topographic differencing.

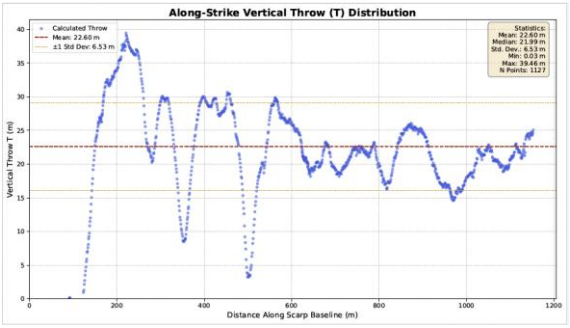

Figure 5: *Diagram of the spatial distribution (along-strike distance) of the calculated throws presented as raw data.*

The cross-fault LGM regional marker—consisting of smoothed periglacial slopes and glacial sediments—underpins the 'zero-age' assumption used to estimate post-LGM slip rates. This marker can be schematized as the result of a balance between coseismic slip and interseismic surface remodelling processes, specifically footwall erosion and hanging wall deposition. In a slope setting where the footwall is detachment-limited (weathering-limited) and the hanging wall is transport-limited, the tectonic escarpment is simultaneously reduced by slope-parallel erosion and buried by sediment accumulation (Fig. 6).

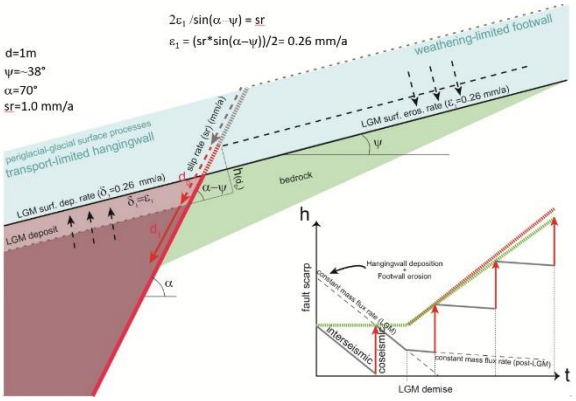

Figure 6: *Conceptual scheme of the cross-fault LGM regional marker of smoothed periglacial slopes with weathering-limited footwall and transport-limited hangingwall. The inset shows the pre- and post-LGM scarp growth model (green line) in the competition between the coseismic slip and the interseismic surface processes remodeling.*

As a result, the 'zero-age' assumption can be described by the equation $2\varepsilon_1/\sin(\alpha-\varphi)=sr$, where ε_1 is the erosional/depositional rate, *sr* is the fault slip rate, α is the fault dip angle and φ is the slope angle. Hence, at a fixed erosion/deposition rate (e.g. LGM estimate of 10-30 time higher than the Holocene; e.g., Whittaker et al., 2008), the tectonic escarpment preservation for a specific slip rate depends on the angular relationship between fault and the affected slope.

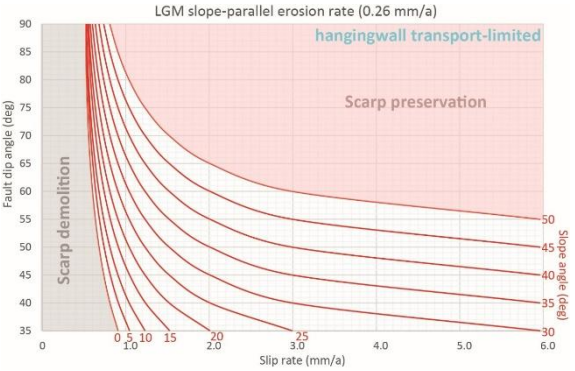

Figure 7: *Diagram showing the shift in the scarp preservation-demolition boundary across various fault-slope geometries and slip rate, assuming a constant erosion rate and a transport-limited hanging wall.*

Based on this framework, we developed diagrams of function curves representing the mathematical relationships between the variables that define the boundary between scarp preservation and demolition (e.g. in Fig. 7). Here is presented a preliminary example of the workflow from the Roccapreturo Fault DTM analysis. Then, we will populate these diagrams with data from morphometric analyses of fault scarps, using ages obtained from cosmogenic dating of the LGM regional marker.

CONCLUSION

To develop reliable strain-release models for the parallel, interacting active fault systems of the Central Apennines,

we reconstructed high-resolution DTMs (HR-DTMs) of bedrock fault scarps using systematic airborne LiDAR. These HR-DTMs facilitate the imaging of subtle geomorphic offsets in faulted landscapes, even in densely vegetated areas, allowing the refinement of the post-LGM slip rate estimates.

We propose a semi-automatic morphometric analysis that retrieves minimum long-term slip via closely spaced cross-profiles derived from both field and DTM data. For this purpose, we developed SCARPS (Scarp Analysis and Reconstruction Profile System), a Python-based tool that calculates the intersection of the two non-parallel lines representing the LGM footwall erosional surface and the fault plane, accounting for scarp degradation and fault kinematics.

Finally, the post-LGM along-strike displacement variability and cosmogenic dating of footwall markers will be evaluated against function-curve diagrams. These diagrams represent the mathematical relationships defining the boundary between scarp preservation and demolition.

Acknowledgements: This work was supported by the INGV RM1 financial fund.

REFERENCES

Bosi, C. (1975). Osservazioni preliminari su faglie probabilmente attive nell'Appennino centrale. Bollettino della Società geologica italiana, 94(4), 827-859.

Cinti, F. R., Pantosti, D., Lombardi, A. M., & Civico, R. (2021). Modeling of earthquake chronology from paleoseismic data: Insights for regional earthquake recurrence and earthquake storms in the Central Apennines. *Tectonophysics*, 816, 229016.

Cowie, P. A., Phillips, R. J., Roberts, G. P., McCaffrey, K., Zijerveld, L. J. J., Gregory, L. C., ... & Wilkinson, M. (2017). Orogen-scale uplift in the central Italian Apennines drives episodic behaviour of earthquake faults. *Scientific Reports*, 7(1), 44858.

D'Agostino, N. (2014). Complete seismic release of tectonic strain and earthquake recurrence in the Apennines (Italy). *Geophysical Research Letters*, 41(4), 1155-1162.

Faure Walker, J., Roberts, G. P., Cowie, P. A., Papanikolaou, I. D., Sammonds, P. R., Michetti, A. M., & Phillips, R. J. (2009). Horizontal strain-rates and throw-rates across breached relay zones, central Italy: Implications for the preservation of throw deficits at points of normal fault linkage. *Journal of Structural Geology*, 31(10), 1145-1160.

Galli, P., Galadini, F., & Pantosti, D. (2008). Twenty years of paleoseismology in Italy. *Earth-Science Reviews*, 88(1-2), 89-117.

Giraudi, C. (2015). The upper Pleistocene deglaciation on the Apennines (peninsular Italy). *Cuadernos de investigación geográfica*, 41(2), 337-358.

Giraudi, C., & Frezzotti, M. (1997). Late Pleistocene glacial events in the central Apennines, Italy. *Quaternary research*, 48(3), 280-290.

Kastelic, V., Burrato, P., Carafa, M. M., & Basili, R. (2017). Repeated surveys reveal nontectonic exposure of supposedly active normal faults in the central Apennines, Italy. *Journal of Geophysical Research: Earth Surface*, 122(1), 114-129.

Nissen, E., Maruyama, T., Arrowsmith, J. R., Elliott, J. R., Krishnan, A. K., Oskin, M. E., & Saripalli, S. (2014). Coseismic fault zone deformation revealed with differential lidar: Examples from Japanese Mw~ 7 intraplate earthquakes. *Earth and Planetary Science Letters*, 405, 244-256.

Nucci, R., Serpelloni, E., Faenza, L., Garcia, A., & Belardinelli, M. E. (2025). Geodetic strain rates and seismicity rates along the Apennines (Italy). *Journal of Geophysical Research: Solid Earth*, 130(2), e2024JB029848.

Papanikolaou, I. D., Roberts, G. P., & Michetti, A. M. (2005). Fault scarps and deformation rates in Lazio–Abruzzo, Central Italy: Comparison between geological fault slip-rate and GPS data. *Tectonophysics*, 408(1-4), 147-176.

Pucci, S., Pizzimenti, L., Civico, R., Villani, F., Brunori, C. A., & Pantosti, D. (2021). High resolution morphometric analysis of the Cordone del Vettore normal fault scarp (2016 central Italy seismic sequence): Insights into age, earthquake recurrence and throw rates. *Geomorphology*, 388, 107784.

Roberts, G. P., & Michetti, A. M. (2004). Spatial and temporal variations in growth rates along active normal fault systems: an example from The Lazio–Abruzzo Apennines, central Italy. *Journal of Structural Geology*, 26(2), 339-376.

Roberts, G. P., Iezzi, F., Sgambato, C., Robertson, J., Beck, J., Mildon, Z. K., ... & Iqbal, M. (2025). Characteristics and modelling of slip-rate variability and temporal earthquake clustering across a distributed network of active normal faults constrained by in situ 36Cl cosmogenic dating of fault scarp exhumation, central Italy. *Journal of Structural Geology*, 195, 105391.

Tesson, J., Benedetti, L., Godard, V., Novaes, C., Fleury, J., & ASTER Team. (2021). Slip rate determined from cosmogenic nuclides on normal-fault facets. *Geology*, 49(1), 66-70.

Tucker, G. E., McCoy, S. W., Whittaker, A. C., Roberts, G. P., Lancaster, S. T., & Phillips, R. (2011). Geomorphic significance of postglacial bedrock scarps on normal-fault footwalls. *Journal of Geophysical Research: Earth Surface*, 116(F1).

Whittaker, A. C., Attal, M., Cowie, P. A., Tucker, G. E., & Roberts, G. (2008). Decoding temporal and spatial patterns of fault uplift using transient river long profiles. *Geomorphology*, 100(3-4), 506-526.

INQUA TERPRO Project Cascading Hazards and Mitigation (CHAMP)

paleoseismicity.org

Trees that Witnessed Earthquakes in the Tien Shan mountains

Rizza, Magali (1,2), Miramont Cécile (3), Dervis Virgile (2), Guibal Frédéric (3), Brisset Elodie (2), Brousset Lenka (3), Guiter Frédéric (3)

(1) Université du Québec à Montréal, Département des sciences de la Terre et de l'atmosphère, Montréal, Canada. Email : rizza.magali@uqam.ca
(2) Aix Marseille Univ., CNRS, IRD, Coll. France, CEREGE, Aix-en-Provence, France
(3) Aix Marseille Univ, Avignon Univ, CNRS, IRD, IMBE, Aix-en-Provence, France

Abstract: *Paleoseismic research is crucial for improving earthquake hazard mitigation in the Tian Shan, a region marked by active faults, frequent strong earthquakes, and landslides. The Zailisky-Kungey Range was shaken by the 1889 Chilik and 1911 Chon-Kemin earthquakes, which triggered widespread slope failures. Yet, their surface ruptures remain poorly constrained due to scarce historical mapping and large dating uncertainties. This study combines drone mapping with dendrochronology on Picea schrenkiana—both dead trunks submerged in dam-lakes and living trees on landslide debris or fault scarps. Along the 1911 fault scarp, tree rings record a decade-long growth decline, confirming severe ground disturbance. Submerged trees show that a lake formed co-seismically in 1911. Conversely, dendrochronological evidence from Kaindy Lake (UNESCO Biosphere Reserve) links its origin to the 1889 earthquake, not 1911, overturning previous interpretations and local belief. Our findings highlight dendrochronology's remarkable potential as a precise paleoseismic tool in complex mountain environments.*

Key words*: Paleoseismology, Dendrogeomorphology, Dammed lake, Sunken Forest, Earthquake.*

INTRODUCTION

The Tian Shan range in Central Asia absorbs much of the shortening between the Eurasian and Indian plates (Tapponnier and Molnar, 1979) and has produced numerous strong historical and instrumental earthquakes (Kalmetieva et al., 2009). It is also marked by many large rock-slope failures that have dammed major rivers (Havenith et al. 2003; Strom and Abdrakhmatov 2018). Most occur on or near active faults and cluster spatially with seismicity (Strom and Korup 2006), supporting the view that major earthquakes triggered them (Delvaux et al. 2001; Havenith et al. 2003; Strom and Abdrakhmatov 2018). Such landslides can thus serve as indirect evidence for dating prehistoric earthquakes, though reactivation and superimposed deposits remain possible.

In the Zailiskey Range—the northernmost Tien Shan range—lies Almaty, one of Kazakhstan's largest and fastest-growing cities (~2 million people). Although recent instrumental seismicity has been mostly moderate (Sloan et al. 2011), the seismic hazard for Almaty is high (Amey et al. 2021). From 1885 to 1978, a series of major earthquakes (Figure 1) struck the Zailisky-Kungey region, causing severe damage, casualties, and widespread slope failures and surface ruptures (Hay 1888; Bogdanovitch et al. 1914; Delvaux et al. 2001; Abdrakhmatov et al. 2016; Arrowsmith et al. 2017). More precisely, five earthquakes with magnitudes Mw > 6.5 occurred in 1887 (Mw = 7.4), 1889 (Mw = 8.3), 1911 (Mw = 7.9), 1970 (Mw = 6.8), and 1978 (Mw = 6.9) within a small geographic area (Abdrakhmatov et al., 2016; Arrowsmith et al., 2017).

Paleoseismological studies have attempted to constrain rupture ages and recurrence intervals (Abdrakhmatov et al. 2016; Arrowsmith et al. 2017; Deev et al. 2016), but radiocarbon and luminescence dating still yield uncertainties too broad to distinguish closely spaced historical events.

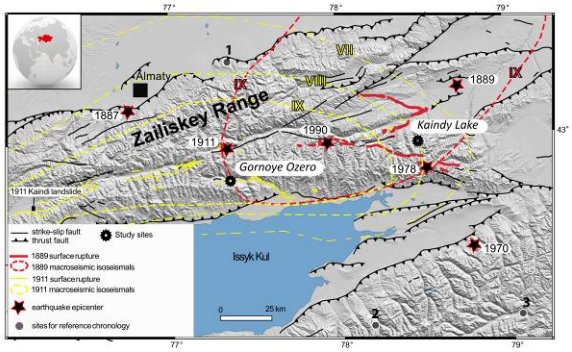

Figure 1: *Modified after Miramont et al., 2025; Macroseismic maps of the 1889 and 1911 earthquakes in the Kungey range. The stars represent the epicenters for selected earthquakes with M > 6.5. The 1889 and 1911 surface ruptures (Abdrakhmatov et al. 2016; Arrowsmith et al. 2017) are represented in color. Isoseismal lines are represented in MSK-64 scale (Januzakov et al. 2003; Bindi et al. 2014). Three of the selected dendrochronological sites for reference chronologies are Solomina-Ulken (1), Schweingruber—Tschongkys (2), and Solomina—Koeliu (3). Data can be found at https://www.ncei.noaa.gov/access/paleo-search.*

The main objective of this study is to test a dendrochronological calibration on a site where the exact date of the earthquake is known, in order to document in detail the types of responses observable in the tree rings of affected trees. We aim to apply this dendrochronological approach to a key question in the region: which fault scarps are associated with the earthquake swarm of July 1889 and January 1911? Indeed, although many scarps have been mapped, it is nearly impossible to distinguish the causative earthquakes in trenches, as they occurred too close in time. Our study examines two sites where lakes formed from earthquake-triggered scarps or landslides in 1889 or 1911. The first, Gornoye Ozero in the Chon-Aksu valley, aligns with the January 3, 1911 surface rupture mapped by Bogdanovich. The second, Lake Kaindy, was created when a landslide blocked the Kaindy River and is now one of Kazakhstan's

top tourist attractions. Whether this rockslide was triggered by the 1889 Chilik or 1911 Kemin earthquake remains debated (Strom and Abdrakhmatov 2018, Miramont et al., 2025).

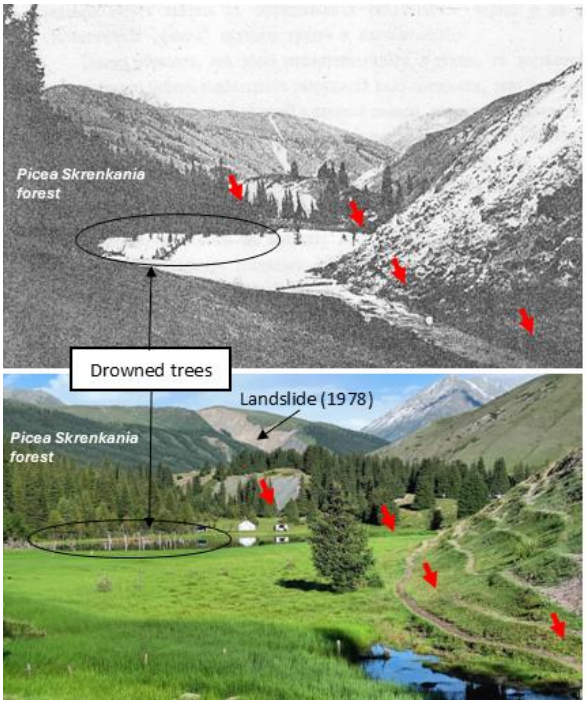

Figure 2: *Photographs of the upper Gornoye Ozero lake in the Chon-Aksu valley. Top photograph: taken in 1911 (Bogdanovitch et al., 1914), showing several trees with their needles still present in the newly formed lake; Bottom: taken a century later (in 2022), showing the submerged dead trees. The location of the surface rupture and the scarp related to the 1911 earthquake is indicated by the red arrows.*

STUDY SITES AND METHOD

Lake Gornoye Ozero: The expedition led by Bogdanovich was the first to make significant observations of the 1911 earthquake, just a few months after it occurred (Bogdanovich et al., 1914). The team produced a detailed map showing landslides and surface ruptures. Along the rupture, watercourses were altered, as shown in a contemporary photograph (Figure 2), where a river was blocked by the fault scarp, forming Lake Gornoye Ozero. The submerged trees with intact needles confirm that the earthquake occurred shortly before the photograph was taken. This site is our "calibration" site for our dendrochronological approach.

Lake Kaindy: Kaindy Lake, in Kolsai National Park—home to rare and endangered species—was added to UNESCO's World Network of Biosphere Reserves in 2021 for its stunning lakes, rich biodiversity, and cultural heritage. Its most striking feature is the dozens of spruce trees (*Picea schrenkiana*) rising from the turquoise water. A rockslide, from the upper right valley slope, blocked the river with an estimated volume of 8 million m^3 (Strom and Abdrakhmatov 2018). Despite its fame, the lake's landslide origin remains poorly documented, with debate over whether it was triggered by the 1889 or 1911 earthquake.

Dendrochronology is a powerful tool for dating past earthquakes and earthquake-triggered geomorphic events, such as landslides (Sheppard and Jacoby 1989; Speer 2010; Bekker 2010; Owczarek et al. 2017; Jacoby et al. 1988, 1997; Dziak et al. 2021). Tree rings record the timing, frequency, and intensity of such events, as earthquakes can disturb growth by shaking roots, causing mortality, reaction wood, or narrow/missing rings. This method has proven particularly effective for dating sunken forests in landslide-dammed lakes.

In this study, we applied dendrochronology at both sites by comparing ring-width patterns from dead submerged trees with nearby living trees. Dead trees were sampled to determine the age of their outer rings, while living trees were collected on the Kaindy landslide and along the Gornoye Ozero fault scarp to provide reference growth patterns.

To accommodate ring width variation around the tree, two increment cores of 5 mm diameter were extracted per tree (living and dead) using increment borers (Grissino-Mayer, 2003*).* All samples were air-dried, mounted, and polished with progressively finer sandpaper up to 400 grit to clearly reveal tree-ring boundaries. Wood cores were then digitized at 1200 dpi. Standard dendrochronological methods were used to develop chronologies. Ring-widths (TRW) were measured using CooRecorder® (Maxwell and Larsson 2021) and a LINTAB® system with 0.01 mm precision. Cross-dating was performed with TSAPWin® software (Rinn 1991–2023). Chronologies were verified through standard statistical tests and visual comparison of raw TRW curves, including the coefficient of coincidence (Gleichläufigkeit, Glk; Eckstein and Bauch 1969), Student t-values using Baillie and Pilcher indices (1973) and Hollstein indices (1980), and the cross-date index (CDI) from TSAP, which combines t-values and Glk (Rinn 1991–2023).

The mean chronologies built for the studied sites were cross-dated with the mean chronologies from the Tian Shan Mountains available in the International Tree-Ring Data Bank (Figure 1).

RESULTS

Lake Gornoye Ozero : In the center of the lake, the upper parts of submerged tree trunks emerge from the lake, and 100% of them show no tree rings formed after 1910, the last recorded radial growth. The mean chronologies (from dead trees and from living trees) are very well synchronized with the mean chronologies from neighboring site (Figure 1). The standardized series clearly show years with pronounced climatic anomalies, such as 1911 and 1917, characterized by severe winters well-documented for the region by Esper et al. (2002). Chon-Aksu trees were exposed to broadly consistent climatic conditions, as reflected by narrow rings during drought or harsh winters in 1885, 1895, 1911, 1917, and 1945, also observed in reference sites (Chen et al., 2013). The year 1911 (harsh winter) shows a narrow ring across multiple reference sites, including Solomina-Ulken, the closest to Chon-Aksu (Figure 1), indicating strong regional climatic coherence. Because both climatic and seismic events can

similarly influence tree-ring widths, a detailed analysis was conducted to disentangle the effects of each factor.
Within the first subset (growing before 1911), trees whose radial growth was not affected by the January 1911 earthquake were identified. However, for trees standing on the fault scarp, while reference trees show rapid growth recovery after 1911, these trees exhibit very narrow rings for several years, from 1911 to 1920, with some only returning to pre-1911 growth levels by 1923. This prolonged and drastic growth reduction strongly suggests the influence of a factor beyond the climatic anomaly of the 1911 winter. These findings provide clear evidence that the 1911 earthquake left a distinct signature in the radial growth of trees at the Chon-Aksu site.

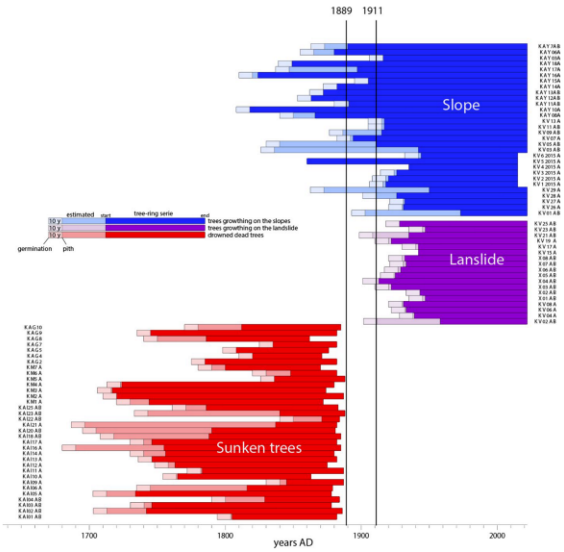

Figure 3: *Bar diagram of cross-dated ring-width series for the Kaindy Lake, showing the correlation between the chronologies and the 1889 and 1911 earthquakes (vertical black lines). Adapted from Miramont et al. (2025).*

Kaindy Lake: Taken together, the living trees provided a reference chronology of 205 yrs, spanning 1818 A.D. to 2022 A.D. with high values for statistical tests. 27 individual chronologies from the dead trees cross-dated were included in a mean chronology labeled, spanning 1717 A.D. to 1888 A.D. with significant values for statistical tests. The sunken Kaindy forest was composed of ~143-year-old trees, which started growing around 1680-1750 AD. Our results show that 65% of the trees from the chronology (sunken trees) have their last measured ring dated between 1882 and 1888 A.D., and we therefore propose that the lake was formed shortly after 1888 A.D (Figure 3). During our sampling campaign, we noticed that some trees still had some bark attached at the base of the trunk, but not higher up where we managed to collect the core samples. From this field observation, we propose that the wood decay is not significant and that the dates of the outermost preserved rings are close to their actual death. Our results indicate that all trees sampled on both stable and active parts of the landslide established after the drowned dead trees. Extrapolated germination dates, spanning 1898 to 1935 A.D., suggest that the landslide occurred prior to 1898, consistent with its formation shortly after the 1889 earthquake (Miramont et al., 2025).

DISCUSSION-CONCLUSION

One challenge in this dendrochronological study was that the 1911 earthquake coincided with a harsh winter, which could have strongly affected tree growth (Chen et al., 2013). The winter of 1911 is also recorded in tree rings from reference sites across the Tien Shan. However, the seismic signal could be distinguished from the climatic signal because trees affected at Chon-Aksu exhibit a pronounced growth decline lasting about a decade from 1911. This prolonged suppression cannot be explained by climate alone, as reference sites show a narrow ring only for that single year. Furthermore, all submerged trees in Gornoye Ozero Lake show no ring formation after 1910, indicating that they died before August–September 1911, when a new ring would normally have formed. After the lake's formation, root systems were suffocated, preventing the trees from producing a ring in 1911, despite needles remaining on the branches, as shown in photographs taken in 1912.
We found similar results with a dataset indicating that Kaindy Lake formed shortly after 1888 A.D. (based on the last rings of the sunken trees) and that the landslide occurred before 1898 A.D. (based on the earliest established trees on the landslide). This time window effectively rules out the 1911 earthquake. The only major earthquake documented in this region between 1888 and 1898 is the 11 July 1889 event (M 8.2) (Kalmetieva et al., 2009; Januzakov et al., 2003). The 1889 A.D. date for the formation of Kaindy Lake contradicts common local beliefs and previously published ages related with the 1911 earthquake. Our results also support the proposition of Abdrakhmatov et al. (2016) that the Saty fault segment, located a few ten kilometers from the Kaindy lake, ruptured during this large historical earthquake.

The two major earthquakes triggered cascading effects, destabilizing the mountainsides and causing a landslide, or topographic scarp,which in turn dammed the rivers flowing through the valleys, leading to the rapid submersion of trees and the formation of the lakes. The study not only revises the history of this iconic Tien Shan landscape, but also confirms that Kaindy and Gornoye Ozero lakes are located within the epicentral zones of the 1889 and 1911 earthquakes, respectively. It further suggests that the nearby surface ruptures previously documented are most likely associated with these events. By combining dendrochronological analyses with paleoseismological investigations, this groundbreaking work deepens our understanding of seismic hazards in a region repeatedly struck by earthquakes since the late 19th century. It also enriches knowledge of the area's natural heritage and supports efforts to protect a unique, fragile, and threatened environment.
As the Tien Shan mountain range remains seismically active, the sequence of events uncovered at both sites could happen again—this time in more densely urbanized

areas. Such cascading hazards could lead to far greater material damage and loss of life.

Acknowledgements: We would like to thank the support of the Institute of seismology of Kazakhstan for accompanying us in the field, and Kolsay Lakes National Park for authorizing us to take samples from the trees. This work received support from the French government under the France 2030 investment plan, as part of the Initiative d'Excellence d'Aix-Marseille Université - A*MIDEX (AMX-19-IET-012) and from the Research Federation ECCOREV (FR 3098; Aix-Marseille Univ., CNRS, INRAE, IRSN, CEA, Univ. Toulon, Univ. Avignon, Univ. Nimes).

REFERENCES

Abdrakhmatov KE, Walker RT, Campbell GE, Carr AS, Elliott A, Hillemann CJ, Hollingsworth, Landgraf A, Mackenzie D, Mukambayev A, Rizza M, Sloan RA (2016) Multisegment rupture in the 11 July 1889 Chilik earthquake (Mw 8.0–8.3), Kazakh Tien Shan, interpreted from remote sensing, field survey, and paleoseismic trenching. Journal of Geophysical Research. Solid Earth, 121(6):4615-4640.

Amey RMJ, Elliott JR, Hussain E, Walker R, Pagani M, Silva V, Abdrakhmatov K, Watson C (2021) Significant seismic risk potential from buried faults beneath Almaty city, Kazakhstan, revealed from high-resolution satellite DEMs. Earth and Space Science 8.

Arrowsmith JR, Crosby CJ, Korzhenkov AM, Mamyrov E, Povolotskaya I, Guralnik B, Landgraf A (2017) Surface rupture of the 1911 Kebin (Chon–Kemin) earthquake, Northern Tien Shan, Kyrgyzstan. Geological Society, London, Special Publications, 432(1):233-253.

Baillie MGL, Pilcher JR (1973) A simple cross-dating program for tree-ring research. Tree-Ring Bulletin 33:7-14.

Bekker MF (2010) Tree Rings and Earthquakes. Wasatch Dendroclimatology Research. Paper 13. In: Stoffel M et al. (ed) Tree Rings and Natural Hazards, Springer Science+Business Media B.V, pp

Bogdanovitch KI, Kark IM, Korolkov BY, Musketov DL (1914) The earthquake in the northern district of the Tien shan. December 1910 (4 January 1911). Commission of the Geology Committee, Leningrad (in Russian).

Chen, F., Yuan, Y., Chen, F.-H., Wei, W., Yu, S., Chen, X., Fan, Z., Zhang, R., Zhang, T., Shang, H., Qin, L., 2013. A 426-year drought history for Western Tian Shan, Central Asia, inferred from tree rings and linkages to the North Atlantic and Indo–West Pacific Oceans. The Holocene 23, 1095–1104.

Deev, E. V., & Korzhenkov, A. M. (2016). Paleoseismological studies in the epicentral area of the 1911 Kemin earthquake (northern Tien Shan). *Russian Geology and Geophysics*, *57*(2), 337-343.

Delvaux D, Abdrakhmatov KE, Lemzin IN, Strom AL (2001) Landslides and surface breaks of the 1911 Ms 8.2 Kemin earthquake, Landslides 42:1583-1592.

Dziak RP, Black BA, Wei Y, Merle SG (2021) Assessing local impacts of the 1700 CE Cascadia earthquake and tsunami using tree-ring growth histories: a case study in South Beach, Oregon, USA. Nat. Hazards Earth Syst. Sci., 21:1971-1982.

Eckstein D, Bauch J (1969) Beitrag zur Rationalisierung eines dendrochronologischen Verfahrens und zur Analyse seiner Aussagesicherheit. Forstwissenschaftliches Centralblatt, 88:230-250.

Esper, J., Schweingruber, F.H., Winiger, M., 2002. 1300 years of climatic history for Western Central Asia inferred from tree-rings. The Holocene 12, 267–277.

Grissino-Mayer HD (2003) A manual and tutorial for the proper use of an increment borer. Tree-Ring Research 59: 63–79

Havenith HB, Strom A, Jongmans D, Abdrakhmatov K, Delvaux D et al. (2003) Seismic triggering of landslides, Part A: Field evidence from the Northern Tien Shan. Natural Hazards and Earth System Sciences 3:135-149.

Hay MB (1888) The earthquakes of May and June, 1887, in the Verny (Vernoe) District, Russian Turkestan, and their consequences. Proceedings of the Royal Geographical Society and Monthly Record of Geography 10:638–646.

Jacoby GC, Shepphard PR, Sieh KE (1988) Irregular recurrence of large earthquakes along the San Andreas Fault: Evidence from Trees. Science 241(4862):196-199.

Jacoby GC, Williams PL, Buckley BM (1992) Tree ring correlation between prehistoric landslides and abrupt tectonic events in Seattle, Washington. Science 258(5088):1621–1623.

Jacoby GC, Bunker DE, Benson BE (1997) Tree-ring evidence for an A.D. 1700 Cascadia earthquake in Washington and northern Oregon. Geology 25:999–1002.

Januzakov K., Omuraliev M., Omuralieva A, Ilyasov B, Grebennikova V (2003). Strong earthquakes of the Tien Shan (within the Kyrgyzstan territory and adjacent regions of the countries of Central Asia). *Ilim, Bishkek*.

Kalmetieva ZA, Mikolaichuk AV, Moldobekov BD, Meleshko AV, Jantaev MM, Zubovich AV, Havenith, HB (2009). Atlas of earthquakes in Kyrgyzstan. *CAIAG, Bishkek*, *76*.

Miramont, C., Rizza, M., Guibal, F., Brisset, E., Brousset, L., Guiter, F., ... & Mukambayev, A. (2025). Tree rings reveal the correlation between the Kaindy Lake submerged forest and the historical 1889 M 8.2 Chilik earthquake (Kazakhstan). *Natural Hazards*, *121*(3), 3533-3558.

Owczarek P, Opała-Owczarek M, Rahmonov O, Mendecki M (2017) 100 years of earthquakes in the Pamir region as recorded in juniper wood: a case study of Tajikistan. J. Asian Earth Sci. 138:173-185.

Sheppard PR, Jacoby GC (1989) Application of tree-ring analysis to paleoseismology: two case studies. Geology 17:226-229.

Sloan RA, Jackson JA, McKenzie D, Priestley K (2011) Earthquake depth distributions in central Asia, and their relations with lithosphere thickness, shortening and extension. Geophysical Journal International 185(1):1-29.

Speer J (2010) *Fundamentals of Tree Ring Research*. Arizona: University of Arizona Press.

Strom A, Abdrakhmatov K (2018) Rockslides and rock avalanches of Central Asia, distribution, morphology, and internal structure, Elsevier, 418 p

Strom AL, Korup O (2006) Extremely large rockslides and rock avalanches in the Tien Shan Mountains, Kyrgyzstan. Landslides, 3(2):125-136.

Tapponnier P, Molnar P (1979) Active faulting and Cenozoic tectonics of the Tien Shan, Mongolia, and Baykal regions. Journal of Geophysical Research: Solid Earth, 84(B7):3425-3459.

INQUA TERPRO Project Cascading Hazards and Mitigation (CHAMP)

Using earthquake cycle models to explore seismic hazard in normal fault systems

Rodriguez Piceda, Constanza (1), Zoë Mildon (1), Jean-Paul Ampuero (2), Martijn van den Ende (2), Billy Andrews (1), Francesco Visini (3), Yifan Yin (4), Claudia Sgambato (5)

(1) School of Geography, Earth and Environmental Sciences, University of Plymouth, Plymouth, UK (zoe.mildon@plymouth.ac.uk).
(2) Université Côte d'Azur, Observatoire de la Côte d'Azur, IRD, CNRS, Géoazur, Nice, France
(3) National Institute of Geophysics and Volcanology (INGV), Italy
(4) MIT Department of Earth, Atmospheric and Planetary Science, Cambridge, MA 02139, United States
(5) Birkbeck, University of London, London, WC1E 7HX, United Kingdom

Abstract: *Physics-based earthquake cycle simulators such as QDYN (a Quasi-Dynamic earthquake simulator) can be used to simulate numerous earthquakes on multiple faults to explore how faults interact and generate earthquakes over longer timescales than available from observations. We have used QDYN to model multiple normal faults, and we drive our simulations with field data from the central and southern Italian Apennines. We explore how the geometry of a normal fault network affects the earthquake behaviour, finding that CV (coefficient of variation of recurrence time) is sensitive to the spacing of across-strike faults, but CV is insensitive to the spacing of along-strike faults. We explore how using slip rates from field data can affect the rupture patterns and recurrence of earthquakes and generate synthetic earthquake catalogues for multiple faults over thousands of years. Ultimately, these catalogues can be used to create new seismic hazard assessment models.*

Key words*: earthquake behaviour, normal fault systems, seismic hazard assessment*

INTRODUCTION

It is becoming common practice to use geological data, such as fault geometry, kinematics and slip rate, as part of probabilistic seismic hazard assessments (Gómez-Novell et al., 2020; Valentini et al., 2017) alongside recurrence intervals and their corresponding coefficient of variation (CV) from historical and paleoseismic records of earthquakes associated with active faults. Evidence from studies imply that natural variations in fault geometry, slip rates and the aperiodicity of earthquakes will affect the resultant seismic hazard (Faure Walker et al., 2019; Roberts et al., 2025). But there is a limitation to such studies because of the relatively short time of historical and paleoseismic earthquake catalogues compared to the recurrence of large earthquakes (10^2 - 10^3 yrs). Physics-based modelling of numerous (>10) seismic cycles, based on rate-and-state friction (Dieterich, 1979; Ruina, 1983), can allow us to explore earthquake dynamics and interaction over longer timescales than is possible from traditional geological observations.

In this study, we present a series of earthquake cycle models, using the software QDYN (Luo et al., 2017), which are based on and driven using data from the normal fault network in the central and southern Apennines of Italy. The Apennines is an area of active extension, which has been ongoing for ~2.5 Ma (Cavinato et al., 2002). Post-glacial Holocene fault scarps are well exposed throughout the region and thus abundant geological data (strike, dip, slip vector and slip rate) can be collected (Faure Walker et al., 2021). We have used these to investigate how fault spacing and slip rate profiles affect earthquake occurrence (recurrence intervals, magnitudes and CV).

METHODS

Fault friction evolves within the models following the classic rate-and-state friction law (Dieterich, 1979; Ruina, 1983). The friction $\mu(\theta, V)$ depends on the slip rate (V) and a state variable (θ).

$$\mu(\theta, V) = \mu_0 + a \ln\left(\frac{V}{V_0}\right) + b \ln\left(\frac{V_0\theta}{D_c}\right)$$

where μ_0 is the reference friction coefficient measured at a reference slip rate V_0; a and b are constants that quantify the instantaneous effect of V and evolution effect of θ on μ, respectively; D_c is the characteristic slip distance over which the fault evolves toward a new steady state.

During steady state, the friction can be described by

$$\mu_{ss} = \mu_0 + (a - b)\ln\frac{V}{V_0}$$

The term (a-b) describes the velocity-dependence of the friction at steady-state. When (a-b) > 0, the material is velocity strengthening, meaning that friction increases with increasing slip rate. Generally these materials display stable aseismic sliding. When (a-b) < 0, the material is velocity-weakening, where friction decreases as slip rate increases. These materials are conditionally stable and can produce earthquake nucleation and rupture propagation if the velocity-weakening part of the fault is larger than the following critical length (Rubin & Ampuero, 2005).

$$L_\infty = \frac{1}{\pi}\left(\frac{b}{b-a}\right)^2 \frac{GD_c}{b\sigma}$$

QDYN solves the equation of elasto-static equilibrium, which relates the stress and the slip rate on a point of a fault, under a quasi-dynamic approximation that accounts for the inertial effects of seismic waves. Faults are loaded using the backslip approach, in which fault elements exert stresses onto the other elements that are proportional to their slip deficit relative to the long-term slip rate V_g (Savage, 1983). To accelerate the computations for the multi-fault simulations, the along-strike interactions are computed as spatial convolutions in the spectral domain using the Fast Fourier Transform, thus we are required to

simplify fault geometries to be planar along-strike and down-dip.

STUDY 1 – IMPACT OF SLIP RATE PROFILES ON EARTHQUAKE STATISTICS (Rodriguez Piceda et al., 2025a)

We use QDYN to explore how variable slip rate profiles, derived from field studies affect the resultant earthquake behaviour and thus seismic hazard. We use the Parasano-Pescina fault in central Italy as our case study (Figure 1a). It has previously been demonstrated that detailed along-strike slip-rate profiles affect the seismicity rates of this fault (Faure Walker et al., 2019). This fault is approximately 7 km long and extends to 15 km depth with a dip of 60°, and there are seven measurements of Holocene (15±3 kyr) slip rates along the fault (Faure Walker et al., 2019). We use this field data to produce a suite of 16 different slip rate profiles, e.g. using all the data (with linear and spline interpolation), triangular, elliptical and boxcar slip profiles, and for each slip profile we run a QDYN model to generate a suite of synthetic earthquakes. We show the results of two models in Figure 1.

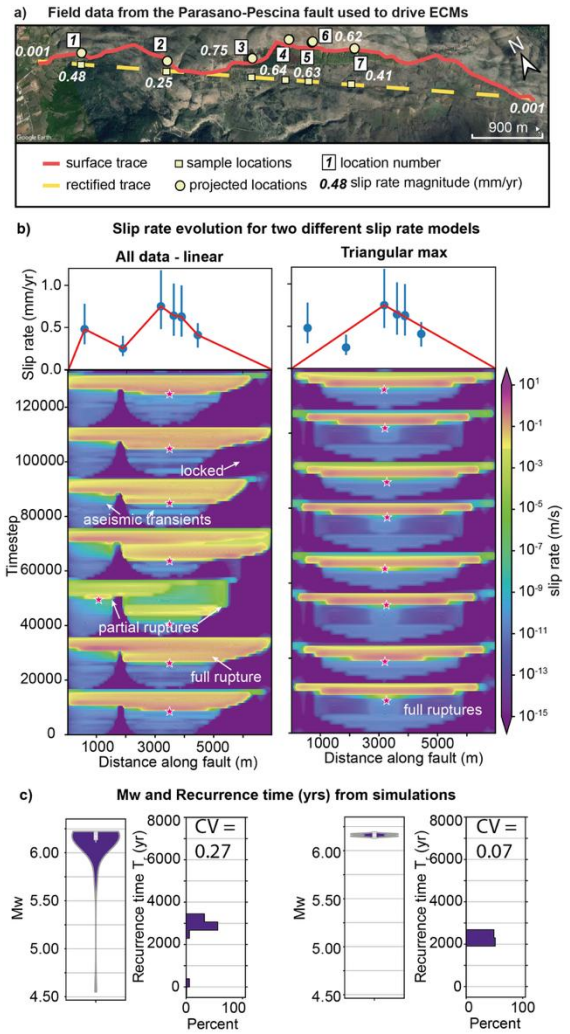

Figure 1: *Earthquake cycle models for the Parasano-Pescina fault (a). b) Slip rate evolution of two models sampled at 7 km depth. Pink stars show nucleation locations. The model using all the field data produces a more complex earthquake history (including partial ruptures) than a simple triangular profile (produces full fault ruptures only). c) Mw, recurrence time and CV of the synthetic earthquake catalogues. The more complex slip rate profile produces a greater range of Mw and a higher CV than the simpler triangular profile. Figure adapted from Rodriguez Piceda et al. (2025a).*

Our models broadly show that the more complex the along-strike slip rate profile used, the more variable the generated earthquake behaviour. Using all the slip rate data produces full fault ruptures, partial fault ruptures, and aseismic transients (Figure 1b), with variable nucleation locations. Contrastingly, simpler profiles, such as the triangular profile (where the peak is the maximum slip rate measured from the field) produce simpler earthquake behaviour of near-regular full fault ruptures with consistent nucleation locations (coincident with the location of maximum slip-rate).

We use the synthetic earthquake catalogues produced by the simulations to calculate the magnitude, recurrence intervals and CV for each slip-rate profile. The more complex slip-rate profiles, such as the "All data-linear" model, produce a range of M_w from 4.5-6.2 (most events exceed M_w 5.75 (Figure 1c)). These models also produce a larger variability in the recurrence time (T_r) and thus a higher value of CV. For the "All data-linear" model, T_r ranges from 0-3,500 years with an average of 2,800 years, giving a CV of 0.27. Simpler slip rate profiles, such as "Triangular max", produce a narrower range of M_w and a smaller range of T_r, resulting in a lower value of CV (~0.07).

Using the simulated synthetic earthquake catalogues, we also calculate the annual probability of exceedance (PoE) for select towns close to the Parasano-Pescina fault. The PoE is different for all models, with variations up to about half an order of magnitude. Comparing simplified slip distributions (triangular, boxcar and elliptical), the PoE is lowest for the "triangular" model and highest for the "boxcar" model.

Comparing the annual PoE for the two models that use all the data – one with linear interpolation and the other with spline interpolation – there is a difference between these models; the spline interpolation produces PoE that are higher than the linear interpolation. This demonstrates that the method of data interpolation affects the predicted hazard.

This study shows that including spatially heterogeneous slip rates in earthquake cycle models introduces variations in slip mode, magnitude frequency distributions and thus impacted seismic hazard calculations.

STUDY 2 – MODELLING MULTI-FAULT SYSTEMS (Rodriguez Piceda et al., 2025b)

Typically, earthquake cycle modelling is used to study one or two faults. We have added new functionalities to QDYN, building on previous studies (Galvez et al., 2019; Yin, 2022), to be capable on modelling numerous faults with variable depths and dips. We have built two simulations, each with seven faults, based on two regions within the actively-extending Italian Apennines, and we use the results of these simulations to investigate how fault network

geometry affects earthquake behaviour and to produce seismic hazard maps.

Fault network geometry (i.e. the spatial arrangement and separation of faults) affects stress interactions between faults which may advance or delay earthquake occurrence. The Apennines is an ideal place to study the effect of fault network geometry due to the abundant field data and different fault configurations. In the Central Apennines, the zone of active extension is ~50 km wide and accommodated on numerous across-strike normal faults. In the Southern Apennines, the zone of active extension is narrower (~25 km) and extension is accommodated on usually one or two faults across-strike. Prior studies (Sgambato et al., 2020, 2023) showed that faults in the southern Apennines develop more regular stress loading histories because there are fewer across-strike faults. They hypothesised that this may lead to more regular earthquake occurrence, but this could not be tested using the historical or paleoseismic record.

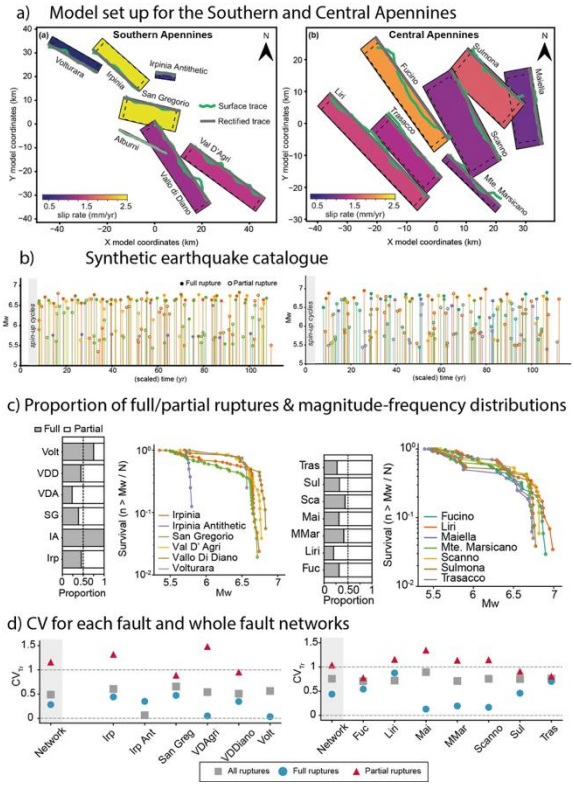

Figure 2: *Earthquake cycle models for the Southern and Central Apennines. a) Model set up, with actual and rectified fault traces, and slip rates used. b) Synthetic earthquake catalogues generated by each model. Colour legends are the same as panel c. c) The proportion of full and partial rupture for each fault, and the magnitude-frequency distribution (shown as survival function) of earthquakes. d) CV of recurrence times for each network and each individual fault. The fault network in the Southern Apennines has more periodic earthquakes and fewer partial-rupture events than in the Central Apennines. Adapted from Rodriguez Piceda et al. (2025b).*

We used earthquake cycle modelling to test this hypothesis by simulating thousands of years of earthquakes on two sets of faults, one representing the Southern Apennines and one for the Central Apennines, (Figure 2a) and then analysing timing and size of earthquakes.

The synthetic catalogues generated for the Southern and Central Apennines have 150 and 154 events respectively, representing approximately 10,000 years of seismicity, with a range of magnitudes between M_w 5.3 and 7. This range of magnitude matches historical and paleoseismic records of earthquake magnitude, and the magnitude – fault length agrees well with scaling relationships (Wells & Coppersmith, 1994). However, our models are unable to produce multi-fault ruptures, such as the 1915 M_w 7.0 Fucino earthquake, which is a limitation of this modelling approach.

Most faults generate both full and partial ruptures (Figure 2b), though there is a higher proportion of partial ruptures generated in the Central Apennines model. This result could be explained by the presence of more across-strike faults leading to greater stress heterogeneities developed through Coulomb stress interactions.

The CV of each fault and fault network can be calculated from the synthetic seismic catalogue. We also calculate CV for all, full and partial ruptures for each fault and network. Generally, partial ruptures have shorter recurrence times than full ruptures that span a greater range of time, from seconds to years. In contrast, the recurrence time of full fault ruptures is longer and has a smaller range of values.

Considering all ruptures in the whole fault networks, CV is 0.8 and 0.5 for the Central and Southern Apennines respectively. This means that earthquakes in the Central Apennines are less periodic than earthquakes in the Southern Apennines. This broadly agrees with the previous conclusions derived from Coulomb stress modelling (Sgambato et al., 2023).

This study demonstrates that physics-based earthquake cycle models can be used to simulate natural fault systems and generate results that can be compared to historical earthquake records, and highlights the potential of using ECM to investigate the seismic hazard of complex fault networks.

DISCUSSION

Our studies have shown that using physics-based earthquake cycle models to simulate numerous earthquake cycles on multiple faults can provide a new approach to thinking about earthquake occurrence, fault interaction and seismic hazard.

It is common practice in SHA to use a single value of CV for an entire region/country, or to use a CV based on a small number of historical/paleoseismic records. Our studies using earthquake cycle models have shown that CV can be affected by the fault network geometry, particularly the number and spacing of faults across-strike from each other.

Secondly, fault-based SHA uses long-term slip rates to derive earthquake rates (e.g. Chartier et al. (2019)), by

calculating the "segment seismic moment conservation" (Field et al., 1999). As earthquake simulators become more popular for SHA (Gerstenberger et al., 2020), our study highlights that care must be taken to consider how the slip rates utilised will affect the rupture properties e.g. the proportion of full versus partial ruptures. Partial ruptures generally create more heterogeneous stress fields than full ruptures, further adding to the complexity of understand the seismic hazard in a region.

Overall our studies demonstrate some different ways that physics-based earthquake cycle models can be used to explore fault interaction, earthquake occurrence and seismic hazard, alongside traditional field-based studies.

Acknowledgements: This research was funded by UK Research and Innovation (UKRI) through the project Quake4D (MR/T041994/1) awarded to Zoë Mildon. This work was carried out using the ARCHER2 UK National Supercomputing Service (https://www.archer2.ac.uk).

REFERENCES

Cavinato, G. P., Carusi, C., Dall'asta, M., Miccadei, E., & Piacentini, T. (2002). Sedimentary and tectonic evolution of Plio-Pleistocene alluvial and lacustrine deposits of Fucino Basin (central Italy). Sedimentary Geology, 148, 29–59. https://doi.org/10.1016/S0037-0738(01)00209-3

Chartier, T., Scotti, O., & Lyon-Caen, H. (2019). SHERIFS: Open-Source Code for Computing Earthquake Rates in Fault Systems and Constructing Hazard Models. Seismological Research Letters, 90(4), 1678–1688. https://doi.org/10.1785/0220180332

Dieterich, J. H. (1979). Modeling of rock friction: 1. Experimental results and constitutive equations. Journal of Geophysical Research - Solid Earth, 84(B5), 2161–2168.

Faure Walker, J. P., Visini, F., Roberts, G. P., Galasso, C., McCaffrey, K., & Mildon, Z. (2019). Variable Fault Geometry Suggests Detailed Fault-Slip-Rate Profiles and Geometries Are Needed for Fault-Based Probabilistic Seismic Hazard Assessment (PSHA). Bulletin of the Seismological Society of America, 109(1), 110–123. https://doi.org/10.1785/0120180137

Faure Walker, J. P., Boncio, P., Pace, B., Roberts, G. P., Benedetti, L., Scotti, O., et al. (2021). Fault2SHA Central Apennines database and structuring active fault data for seismic hazard assessment. Scientific Data, 8(1), 87. https://doi.org/10.1038/s41597-021-00868-0

Field, E. H., Jackson, D. D., & Dolan, J. F. (1999). A mutually consistent seismic-hazard source model for southern California. Bulletin Seismological Society of America, 89, 559–578.

Galvez, P., Somerville, P., Petukhin, A., Ampuero, J. P., & Peter, D. (2019). Earthquake Cycle Modelling of Multi-segmented Faults: Dynamic Rupture and Ground Motion Simulation of the 1992 M w 7.3 Landers Earthquake. Pure Appl. Geophys. https://doi.org/10.1007/s00024-019-02228-x

Gerstenberger, M. C., Marzocchi, W., Allen, T., Pagani, M., Adams, J., Danciu, L., et al. (2020). Probabilistic Seismic Hazard Analysis at Regional and National Scales: State of the Art and Future Challenges. Rev. Geophys., 58(2), 1–49. https://doi.org/10.1029/2019RG000653

Gómez-Novell, O., Chartier, T., García-Mayordomo, J., Ortuño, M., Masana, E., Insua-Arévalo, J. M., & Scotti, O. (2020). Modelling earthquake rupture rates in fault systems for seismic hazard assessment: The Eastern Betics Shear Zone. Eng. Geol., 265(June 2019). https://doi.org/10.1016/j.enggeo.2019.105452

Luo, Y., Ampuero, J.-P., Galvez, P., Van Der Ende, M., & Idinin, B. (2017). Qdyn: A quasi-dynamic earthquake simulator (v1. 1). Retrieved from url: https://github. com/ydluo/qdyn

Roberts, G. P., Iezzi, F., Sgambato, C., Robertson, J., Beck, J., Mildon, Z. K., et al. (2025). Characteristics and modelling of slip-rate variability and temporal earthquake clustering across a distributed network of active normal faults constrained by in situ 36Cl cosmogenic dating of fault scarp exhumation, central Italy. Journal of Structural Geology, 195, 105391. https://doi.org/10.1016/j.jsg.2025.105391

Rodriguez Piceda, C., Mildon, Z. K., Andrews, B. J., Visini, F., Ampuero, J. P., & Ende, M. van den. (2025a). Spatially heterogenous Holocene slip rates drive seismic sequence variability on normal faults. Seismica, 4(2). https://doi.org/10.26443/seismica.v4i2.1682

Rodriguez Piceda, C., Mildon, Z. K., Andrews, B. J., Yin, Y., Ampuero, J.-P., van den Ende, M., et al. (2025b). The role of fault network geometry on the complexity of seismic cycles in the Apennines. EGUsphere, 1–48. https://doi.org/10.5194/egusphere-2025-4694

Rubin, A. M., & Ampuero, J.-P. (2005). Earthquake nucleation on (aging) rate and state faults. Journal of Geophysical Research: Solid Earth, 110(B11). https://doi.org/10.1029/2005JB003686

Ruina, A. (1983). Slip instability and state variable friction laws. Journal of Geophysical Research: Solid Earth, 88(B12), 10359–10370. https://doi.org/10.1029/JB088iB12p10359

Savage, J. C. (1983). A dislocation model of strain accumulation and release at a subduction zone. Journal of Geophysical Research, 88(3), 4984–4996.

Sgambato, C., Faure Walker, J. P., Mildon, Z. K., & Roberts, G. P. (2020). Stress loading history of earthquake faults influenced by fault/shear zone geometry and Coulomb pre-stress. Scientific Reports, 10(1), 12724. https://doi.org/10.1038/s41598-020-69681-w

Sgambato, C., Faure Walker, J. P., Roberts, G. P., Mildon, Z. K., & Meschis, M. (2023). Influence of Fault System Geometry and Slip Rates on the Relative Role of Coseismic and Interseismic Stresses on Earthquake Triggering and Recurrence Variability. Journal of Geophysical Research: Solid Earth, 128(11). Retrieved from https://agupubs.onlinelibrary.wiley.com/doi/full/10.1029/2023JB026496

Valentini, A., Visini, F., & Pace, B. (2017). Integrating faults and past earthquakes into a probabilistic seismic hazard model for peninsular Italy. Nat. Hazards Earth Syst. Sci., 17(11), 2017–2039. https://doi.org/10.5194/nhess-17-2017-2017

Wells, D. L., & Coppersmith, K. J. (1994). New Empirical Relationships among Magnitude, Rupture Length, Rupture Width, Rupture Area, and Surface Displacement. Bulletin of the Seismological Society of America, 84(4), 974–1002.

Yin, Y. (2022). Seismicity and fault interaction through observation and simulation. ETH Zurich.

Surface Failure at Lake Amatitlán Attributed to Liquefaction of Deltaic Sediments During the 1976 Guatemalan Earthquake

Rosenfeld, Joshua H. (1), 2. Byron Mota-Vidaurre (2)

(1) Independent Geologist, Granbury Texas, United States.
(2) Consulting Geologist. Guatemalan Geological Society

Abstract: *On February 4, 1976 seismic waves 50 kilometers from their source triggered liquefaction in recent, non-cohesive deltaic sediments at Lake Amatitlán in the Guatemalan volcanic highlands. Lateral spreading, fractures, sand boils and subsidence occurred mostly within 1.2 square kilometers on the youngest part of the delta of the Río Villalobos extending inland from the shoreline for about 600 meters. Destruction of brick and concrete houses, and a fatality were caused by the surface failure. The regional geography and geologic setting are discussed, and the mechanism and scenario for the failure are presented. Descriptive data and photographs are included to document the event for the community of geotechnical scientists, engineers and developmental planners concerned with seismic hazards. Further work is recommended to accurately determine the subsurface stratigraphy and the control it exerted on ground response.*

INQUA TERPRO Project Cascading Hazards and Mitigation (CHAMP)

Stratigraphy of an inverted Quaternary pull-apart basin along the Motagua fault in Guatemala

Mario Sagüí (1), Sergio Morán-Ical (1), Tina M. Niemi (2), James Murowchick (2), Christoph Grützner (3), and Peter Frenzel (3)

(1) Centro Universitario del Norte, Carrera de Geología, Universidad de San Carlos de Guatemala, 00mariosagui00@gmail.com, sergiomical@yahoo.com
(2) University of Missouri-Kansas City, niemit@umkc.edu, murowchickj@umkc.edu
(3) Institute of Geosciences, Friedrich-Schiller University Jena, Germany, christoph.gruetzner@uni-jena.de, peter.frenzel@uni-jena.de

Abstract: *The Motagua Fault is part of the North American-Caribbean sinistral, strike-slip plate boundary in Guatemala. Limited information is available on its Quaternary history. This study investigates an outcrop of deformed Quaternary sediments at La Laguna, near Sanarate. We described a stratigraphic section and performed, petrographic analyses, x-ray diffraction, and SEM-EDS mapping. We show that the base contains poorly sorted, tectonically brecciated limestone cobbles in a fine calcilutite matrix, overlain by 17 m interbedded cobble conglomerates, bioturbated terrigenous clays, and marls. The XRD analysis indicates clay layers derived from schist bedrock, composed of smectites, quartz, plagioclase, and vermiculite (altered micas). Marl petrography and SEM reveal an abundance of algal laminae, pisoids, acicular calcite, and possible coralline red algae. The data suggest alternating high-energy fluvial sequence or debris flow events and low-energy lacustrine phases. The basin likely formed in a pull-apart structure along a strand of the Motagua fault, now uplifted by compression. Further tectonic and geochronological dating studies are recommended.*

Key words*: Fluvial sequence, lacustrine, Motagua fault, pull-apart basin, Quaternary sediments.*

INTRODUCTION

The Motagua Fault is a sinistral, strike-slip fault and part of the transform boundary between the North American and Caribbean plates in Guatemala. Little is known about the Quaternary history of this boundary. A portion of oceanic lithosphere between the continental Maya and Chortís blocks known as the El Tambor Group, is delimited by the Polochic fault system to the north and by the Motagua fault system to the south (Chiari *et al.*, 2006; Ortega-Gutiérrez *et al.*, 2007).

The El Tambor Group of Late Jurassic-Cretaceous age is composed of an ophiolitic sequence with low-grade volcano-sedimentary and metamorphic rocks of oceanic affinity, including low-grade pillow lavas, greenschists, phyllites, low-grade metasediments, serpentinites, and gabbro (Lawrence, 1975; Martens *et al.*, 2017; Ortega-Gutiérrez *et al.*, 2007).

In this study, we investigate an outcrop of deformed Quaternary sediments that now forms an elongated topographic high within the Motagua fault zone. The goal of this research is to understand the sedimentary conditions during the emplacement of the Quaternary rocks, and to study how the hill is related to fault motion.

The outcrop is exposed along a newly excavated road west of the village of La Laguna near Sanarate (Figure 1). It is about 1 km long, exposing fluvial schist-sourced sequences and limestone-sourced sequences (Figure 2). Its western termination is a limestone breccia quarry. Here, we show the top section of this sequence, where calcareous layers, paleosols, and Ca-enriched debris flows dominate.

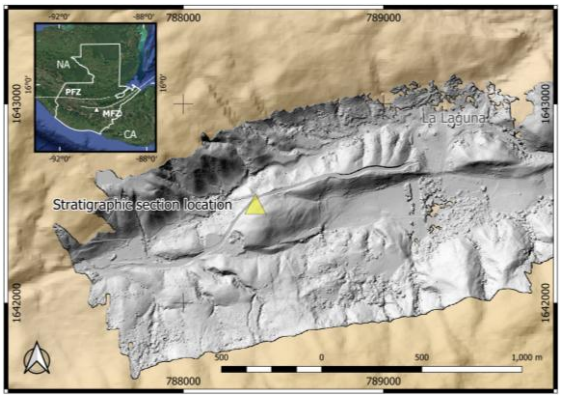

Figure 1: *Location of the outcrop. NA = North American Plate, CA = Caribbean Plate, PFZ = Polochic Fault Zone, MFZ = Motagua Fault Zone, Δ = Studied area.*

OBSERVATIONS

The top section of this fluvial sequence exposes ca. 17 meters of alternating limestone clasts, paleosol layers and debris flow deposits, which are predominantly composed of carbonates (Figure 2a). This section shows different sequences defined by stratigraphic boundaries. We found that mineralogic changes are related to different sedimentation events or depositional conditions. Six samples of this section (sample 10, 7, 8, 9, 6, 5B) were analysed in the laboratory (see Figure 2b for the sampling locations).

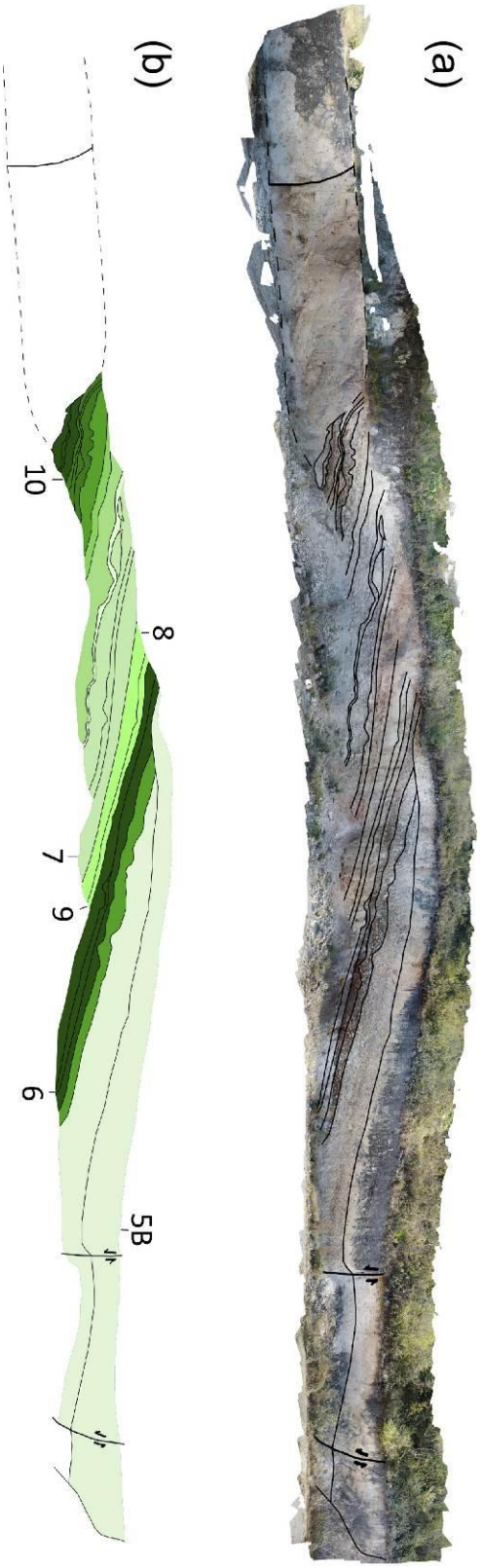

Figure 2: *Top section along the road outcrop. (a) Orthophoto of the outcrop showing main strata and structures. (b) Location of each strata sampled along this section.*

The X-Ray Diffraction (XRD) analyses revealed mineral abundance in % weight. Sample 5B is highly rich in calcite, samples 6 and 10 are rich in saponite. Samples 7-9 show a high content of vermiculite (19% in sample 7, 8% in sample 8, and 3% in sample 9). Quartz, muscovite, plagioclases, and other minerals vary on each sample in different percentages, but siliciclastic minerals are mostly related to samples 7, 8 and 9 (Figure 3).

Mineral / Sample	MS-5B	MS-6	MS-9	MS-8	MS-7	MS-10
Value, Unit	0	0	0	0	0	0
Calcite	95.38(11)	-	-	-	-	-
Calcite, syn	-	-	17.40(6)	56.2(3)	12.74(12)	19.4(3)
Nontronite-15A	3.72(10)	-	-	-	-	-
Quartz low	0.90(5)	-	-	-	-	-
Quartz, syn	-	-	3.82(3)	-	48.1(4)	23.1(3)
a-Si O2	-	21.2(5)	-	-	-	-
a-Si O2, quartz, syn	-	-	-	22.81(16)	-	-
Saponite-15A	-	31.6(7)	-	-	-	17.9(2)
Calcite, Mg-bearing, syn	-	21.6(6)	-	-	-	-
Albite, Ca-bearing	-	-	-	-	16.2(5)	-
Albite, Ca-bearing, syn ordered	-	25.6(17)	-	-	-	-
Vermiculite-2M	-	-	3.34(12)	-	-	-
Vermiculite	-	-	-	7.99(10)	19.45(17)	-
Montmorillonite, Ca-bearing (NR)	-	-	73.20(11)	-	-	-
Andesine	-	-	2.241(15)	-	-	-
Anorthite, Na-bearing	-	-	-	5.49(5)	-	39.6(8)
Pargasite	-	-	-	0.99(5)	-	-
Muscovite-2M1	-	-	-	-	3.5(5)	-

Figure 3: *XRD results (weight fraction % for each sample).*

Laboratory analysis of sample 5B at the top of the sequence revealed the presence of algae, microbial structures, and roots (Figure 4a) into laminated calcareous deposits. The algae is made up of or replaced by microcrystalline quartz (Figure 4b).

The basal 3-m-thick saponite clay-rich in shows periods of moist low-energy conditions that gave rise to bioturbations and low-energy conditions. These sequences were interbedded with high-energy, debris flows containing limestone blocks and mud, ending in medium-energy sequences that contributed to the leaching of siliciclastic sands, forming vermiculite (samples 7, 8, and 9, with decreasing abundance, respectively).

(a)

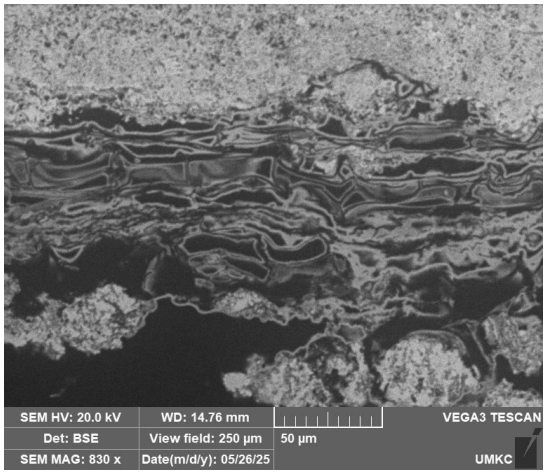

(b)

Figure 4: *SEM-EDS images from sample 5B. (a) Algae, microbial SEM mapped . (b) EDS mapping image of sample 5B.*

After these sequences of constant hydration, a period of weathering began, forming a thick layer of soil (sample 6) intruded by bioturbation and debris flows, which ended at the confluence of tributaries that formed a calcium-rich paleo lagoon with algae and other forms of life (sample 5B). The presence of quartz is likely related to volcanic ash in paleosols. What we interpret as algae could have been adapted to freshwater conditions and been enriched in Ca. These are present at the top of a long-lasting low-energy environment at the depocenter of a pull-apart basin (Figure 5).

DISCUSSION

The appearance of algae on the sequence's top needs to be studied in more detail to explain the paleoenvironment conditions of the pull-apart basin. The taxons of this algae and other microfossils still need to be determined. This would enable a better understanding of the paleoenvironmental conditions of this thick calcareous deposit. Also, the tectonic activity of the area could explain the changes in the clasts' sources. Debris flow deposits and sedimentary structures that are found along this sequence are likely sourced from catchments much farther to the east.

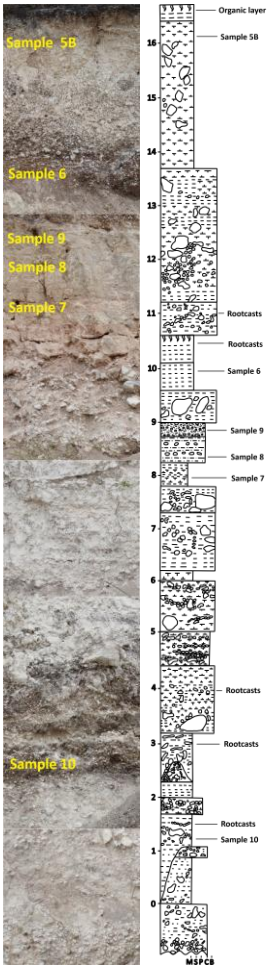

Figure 5: *Stratigraphic section of the upper portion of the outcrop (photos not at scale).*

Acknowledgements: This research was possible by the International Research Experience for Students Geohazards, in collaboration with students and professors from UMKC.

REFERENCES

Chiari, M., Dumitrica, P., Marroni, M., Pandolfi, L., & Principi, G., 2006. Radiolarian biostratigraphic evidence for a Late Jurassic age of the El Tambor Group ophiolites (Guatemala). Ofioliti, 31 (2), 141-150.

Lawrence, D. P., 1975. Petrology and structural geology of the Sanarate-El Progreso area, Guatemala. Graduate Dissertations and Theses, 343.

Martens, U., Tsujimori, T., & Liou, J.G., 2017. Eclogite varieties and petrotectonic evolution of the northern Guatemala Suture Complex. International Geology Review, 59 (5-6), 721-740.

Ortega-Gutiérrez, F., Solari, L., Ortega-Obregón, C., Elías-Herrera, M., Martens, U., Morán-Icál, S., Chiquín, M., Duncan, J., Torres De León, R., & Schaaf, P., 2007. The Maya-Chortís Boundary: A Tectonostratigraphic Approach. International Geology Review, 49 (11), 996-1024.

Are surface ruptures more complex than they should be? Examples that suggest triggered slip is to blame

Gordon Seitz (1)

(1) California Geological Survey, San Mateo, California

Abstract: *Mapped surface rupture traces often exhibit a complex wide zone of cracking along the surface rupture with multiple subparallel minor traces. As modern field methods increasingly incorporate remote sensing the resulting surface rupture maps show greater details and complexity. The rupture patterns are often difficult to reconcile with the rupture patch on the causative fault. In fact, the seismicity may only roughly indicate the rupture trace region.*

I'll discuss ruptures to show how we can incorporate various information such as displacements, kinematics, and seismicity to interpret the origin of the surface cracking which may allow an improved focus on the tectonic surface ruptures versus others. Detailed examples from the Napa M6.0, 2014; Ridgecrest M6.4, 7.1, 2019; and the Monte Cristo M6.5, 2020, will be included.

I suggest that making a greater effort to interpret the origin of individual rupture features may lead to an improved correspondence of rupture maps to earthquakes.

INQUA TERPRO Project Cascading Hazards and Mitigation (CHAMP)

Clustered Multi-Segment Earthquakes and Long-Term Slip History of the Bet Kerem Fault System, Northern Israel

Siman-Tov, Shalev (1), Rawi Dawood (1,2), Gali Shraiber (1,2), Ari Matmon (2)

(1) Geological Survey of Israel, 32 Yesha'ayahu Leibowitz, Jerusalem 9692100, Israel
(2) The Fredy & Nadine Herrmann Institute of Earth Sciences, The Hebrew University of Jerusalem, Edmond J. Safra Campus, Jerusalem 91904, Israel

Abstract: *We investigated the spatiotemporal evolution and seismic behavior of the Bet Kerem Fault System forming the Zurim Escarpment in northern Israel. Using ^{36}Cl exposure dating and U–Pb dating of calcite precipitates, we reconstructed late Quaternary and long-term fault activity. Sixty new ^{36}Cl ages and re-modelled data reveal simultaneous faulting on three segments during 12–11 ka, 8.5–7 ka, and 5–4 ka, each period producing 1.5–6.6 m of slip. U–Pb dating indicates deformation began before ~2.5 Ma, yielding a long-term slip rate of ~0.15 mm/yr. The results suggest that individual segments ruptured together in Mw ~6.5 multi-segment earthquakes, with activity clusters recurring every 3.5–5 ka and separated by ~13 ka of quiescence. These findings reveal supercycle behavior and provide new quantitative constraints on the evolution of intraplate normal-fault systems and on seismic hazard in northern Israel.*

Earthquakes and Their Perception in the Bible and Through History

Štěpančíková, Petra

(1) Institute of Rock Structure and Mechanics, Czech Academy of Sciences, Czechia

Abstract: *During tectonic cycle, new crust is formed at divergent plate boundaries, subduction and mountain building during continental collisions, and is accompanied by earthquakes and volcanism. While these processes can be studied by geoscientists as natural phenomena to better understand Earth's internal structure and dynamics, while others confront their destructive impact on human life and property. The way earthquakes were perceived in antiquity can be learned from the Bible. Based on a compilation of references to earthquakes and related geological phenomena in the Bible, several groups can be distinguished based on their interpretations and perceptions. It appears that these geological events mostly precede or accompany pivotal events, the revelation of God, and apocalyptical visions, and always highlight God´s glory, power and magnificence. Over time, the interpretation of natural disasters has shifted— from attributing responsibility to God, to nature, and finally to humankind in relation to social injustice, where the poorest are the most vulnerable to disasters.*

INQUA TERPRO Project Cascading Hazards and Mitigation (CHAMP)

paleoseismicity.org

New paleoseismological Investigations in the framework of Level III Seismic Microzonation Studies in the L'Aquila Municipality (Central Italy)

Testa, A. (1), D'Annibale S. (2), Francescone M. (1), Iorio M. (3), Mariani M. (1,2), Boncio P. (1), Falcucci E. (2), Galadini F. (2), Gori S. (2), Pizzi A (3).

(1) INGEO Department, Università degli Studi G. d'Annunzio Chieti e Pescara, Via dei Vestini 31, 66100 Chieti, Italy;
(2) Istituto di Geofisica e Vulcanologia, Via di Vigna Murata 605, 00143 Rome, Italy;
(3) Science Department, Università degli Studi Roma Tre, Via della Vasca Navale 84, 00146 Rome, Italy. Alessio.testa@unich.it

Abstract: *As part of Seismic Microzonation studies of the Municipality of L'Aquila, severely affected by the 2009 earthquake (Mw = 6.3; I_o = IX–X MCS), we present a study aimed at improving the understanding of local seismic sources and their potential surface effects. To this end, a comprehensive set of investigations has been carried out, including a review of existing literature and geognostic data, morphotectonic analyses, geological and structural field surveys along the identified fault traces. Furthermore, four paleoseismological trenches were excavated. Although chronological analyses are still in progress, preliminary trench observations have yielded promising results regarding recent surface faulting involving shallow historical deposits, containing pottery shards. These findings provide new insights into the most recent activity of the L'Aquila fault system, contributing to the characterization of active and capable faults. The results of this study will be a key element in defining fault displacement hazard scenarios and fault zoning.*

Key words*: Seismic Microzonation, Active and Capable Faults, Fault Displacement Hazard.*

INTRODUCTION

In the framework of the seismic microzonation of the L'Aquila municipality (Abruzzo, Central Italy), the town council commissioned to the Istituto Nazionale di Geofisica e Vulcanologia (INGV) the study and zonation of the active and capable faults affecting the territory of the town, following the guidelines for level III seismic microzonation in force in Italy (SM Working group, 2015). The INGV researchers in charge of the aforementioned project included in this study the department of Engineering and Geology (INGEO) of the University "G. D'Annunzio" of Chieti-Pescara.

In 2009 L'Aquila was struck by a M 6.3 normal faulting earthquake with maximum IX-X MCS Intensity (Rovida et al., 2022), resulting in 308 deaths (Galli et al., 2009). The causative source was the Paganica fault, belonging to the L'Aquila basin fault system (Fig.1).
Surface ruptures have been documented along the faults, which cross the L'Aquila settlement (Falcucci et al., 2009) with a maximum displacement of 10 cm (Boncio et al., 2010).

In this work we aimed at improving the mapping of local seismic sources and their trace at the surface by means of morphotectonic analysis, structural field surveys and the excavation of paleoseismic trenches, with the goal of defining setback zones in the proximities of the fault traces.
Once defined the fault traces and identified suitable sites we excavated four paleoseismic trenches. The location of the trenches was driven by both geological features and the necessity of investigating specific sites in the vicinity of settlements or infrastructures (e.g., the highway).
Since the work is still in progress, we are here presenting only the two most promising trenches: The San Vittorino 1 trench and the Bazzano trench.

Although we did not receive yet the results of the chronological analyses, preliminary trench observations have yielded promising results regarding recent surface faulting episodes, involving shallow colluvial deposits, containing Roman-era pottery shards.

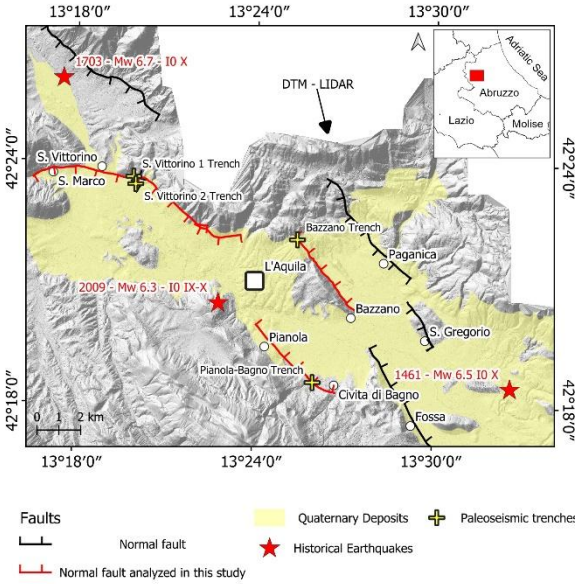

Figure 1: *L'Aquila basin fault system. Faults in red are those analysed in this study. Yellow crosses are the trench sites. Red stars are the historical earthquakes registered in the L'Aquila basin.*

SEISMOTECTONIC SETTING

On 6 April 2009 (01:32 UTC), a Mw 6.3 earthquake struck L'Aquila in the central Apennines. It was preceded by several foreshocks during the previous weeks and followed by an active aftershock sequence (Boncio et al., 2010 and references therein). Focal mechanisms indicate normal faulting consistent with the regional stress field, oriented NE–SW (Chiarabba et al., 2009).

The sequence lies within a system of nearly parallel, SW-dipping active normal faults (Pizzi et al., 2002; Boncio et al., 2004), where late Quaternary and paleoseismic evidence or activity are documented (Galli et al., 2008; Moro et al., 2013). The 6 April 2009 earthquake occurred in an area historically affected by strong seismic events. Among the most significant are the 1349 (Mw 6.5) and 1703 (Mw 6.7) earthquakes (Rovida et al., 2022). Other damaging events that struck the region include those of 1461 (Mw 6.4), 1762 (Mw 5.9), 1916 (Mw 5.2), and 1958 (Mw 5.2), with the 1461 earthquake showing notable similarities to the 6 April 2009 event (Falcucci et al., 2009) (Fig. 1). The pattern of the L'Aquila basin fault system is complex and include NW-SE to WNW-ESE trending synthetic and antithetic fault segments (Fig. 1). The S. Vittorino segment bound the northern edge of the western sector of the basin. In the eastern sector the basin is bounded to the north-east by the Paganica and S. Gregorio fault segments and, to the southwest, by the antithetic Pianola-Bagno and Fossa segments. Right in front of the Paganica segment, the Bazzano antithetic segment lifts a ridge located in the middle of the basin.

METHODS

Even if the fault traces in this area are well known, in order to refine the mapping with respect to the existing maps and to obtain enough detail to identify suitable sites for trenching, we used the LIDAR DTM and DSM from 1945 aerial imagery data available for the L'Aquila basin (Italian Ministry of Environment and Energy Security) to perform an accurate morphotectonic analysis. Then, remote morphotectonic analysis has been supported by specific site inspections and measurements.

The paleoseismological investigations were conducted between spring and autumn 2025 in four sites, in the surrounding of the S. Vittorino, Bazzano and Pianola-Bagno settlements (location in Fig. 1).
First, we dug by backhoe benched trenches, in the selected sites. The trench walls were accurately smoothed, cleaned and equipped with a regular wire grid. The faults and the main stratigraphic contacts were identified, flagged with coloured pins, and logged.
As a basis for the wall logs, four orthophotomosaics were generated from ground-based imagery, processed by structure-from-motion photogrammetry through Agisoft Metashape®.

We collected several samples for radiocarbon dating of both bulk sediment and small charcoals. Moreover, we found and collected several pottery shards for archaeological dating. The radiocarbon dating is still in progress.

As above mentioned, the siting of the trenches was determined not only by geological features but also by land-planning requirements prescribed by the town council. Two trenches were excavated at S. Vittorino: S. Vittorino 1, positioned directly on the outcropping fault plane; and S. Vittorino 2, opened for land-planning reasons across a suspicious scarp that cuts through an area occupied by temporary residential units built after the 2009 earthquake.
The Bazzano trench was located near the highway, in a sector where young slope and colluvial deposits potentially affected by the fault were expected.
Finally, the Pianola-Bagno trench was excavated within the settlement itself, in proximity to the 2009 temporary residential units.
In the next section we will present only the results of the S. Vittorino 1 and Bazzano trenches.

RESULTS

The S. Vittorino 1 trench (Fig. 2) is located at the contact between a fault plane made of slope breccias and colluvial deposits, across a sharp change in slope.
From the youngest to the oldest, the eight stratigraphic units distinguished in this trench are: colluvial units with a sandy-clayey matrix containing angular carbonate clasts (units 1 to 4); possible paleosols (units 5 and 6); fault breccia blocks collapsed from the footwall of the fault (unit 7); carbonate slope breccias (unit 8).
The main fault is located in the NE part of the trench and corresponds to the contact between the slope breccias and units 4, 5, and 6. This fault exhibits a complex, refracted geometry, consisting of several SW-dipping branches that affect the trench up to the surface. The youngest unit affected by the main fault is unit 3.
Moving SW, another SW-dipping fault downthrows the boundary between units 3 and 4 and reaches the surface without forming a corresponding morphological scarp. Two antithetic faults confined within unit 4 are also visible. Between 8 and 9 meters from the SE end of the trench, two nearly vertical faults affect the bottom of unit 4 and are sealed by unit 1.
Finally, another SW-dipping fault is sealed by the base of unit 2, which unconformably overlies unit 6.
The different splays of the main fault (the upper most) are located in a wide area of the trench, within the first 15 m.

The Bazzano trench is located on a NE-facing slope characterized by a steep upper section that gradually flattens towards the bottom. The trench is also located just 300 m north-east of the site where the Bazzano antithetic fault crosses the highway.
Five different stratigraphic units were distinguished in this trench: unit 1 is a very young human-made fill; unit 2 is a young colluvium; unit 3 is a colluvium rich of carbonate clasts and containing pottery shards; unit 4 is a brownish organic fine layer; unit 4 is a brownish matrix supported alluvial gravel with pottery shards; unit 5 is a whitish alluvial gravel.
Three different fault zones were identified. An almost vertical, very localized fault, affecting unit 4 and 5 and sealed by unit 1, located at the base of the steep slope in the lower part of the trench; a fault zone associated with a wide aperture, juxtaposing unit 3 to unit 4, located about 6.5 m from the upper end of the trench; a fault zone made of three different NE-dipping splays with a wide aperture in the upper part, affecting unit 3, located

close to the upper end of the trench.
Even in this case the trench is affected by several fault strands, indicating secondary features that can be found in a 20 m wide area across the trace of the main fault.

DISCUSSION AND CONCLUSIONS

Since the dating analysis is still in progress, we have no constrained ages for the stratigraphic units of the two trenches. Concerning S. Vittorino 1 trench, the stiffness of units 3 to 6 suggests relatively old age. Units 1 and 2 look younger but they are not affected by faulting and in some cases, they just seal tectonic contacts.
On the other hand, the Bazzano trench shows a young stratigraphy including historical layers with pottery shards that can be ascribed to the Roman period.
More in general we can say that in the S. Vittorino 1 trench, we have evidence of surface faulting probably related to old events. Probably because part of the stratigraphy has been eroded. In fact, unit 1 and 2, which seal the faults in the lower part of the trench, are truncated in the upper part of the trench and the relationship between these units and the main fault are not visible anymore.
At the Bazzano trench we have evidence of historical faulting events affecting very young deposits according to the Roman-age pottery found in unit 3 and 4.

The results of radiocarbon dating and more precise evaluation of the pottery fragments will help to constrain the timing of the surface faulting events. This could improve our knowledge of the L'Aquila basin fault system even if it is known to be active (surface faulting associated with the 2009 event).

Another important finding is that at the surface the investigated faults show a complex geometry, being made of several secondary structure within 15-20 meters from the main fault.
In the S. Vittorino 1 trench, secondary faults have been found in the hanging wall of the outcropping fault plane. Concerning the Bazzano trench, the main fault seems to be the one located in the lower part of the trench, but the younger evidence of activity is showed by the upper strands. It means that secondary splays can be found even at the footwall of the main fault (the one characterized by the most evident long-term signature).
This evidence has an important role in the definition of the setback zone in the vicinity of active faults, especially in the proximity of important infrastructure potentially affected by principal or distributed surface faulting hazard (Nurminen et al., 2020).

In conclusion, our studies confirm the location and activity of the S. Vittorino and Bazzano fault segments and their capability to break the surface during strong earthquakes. Even if we have not yet received the results of the dating, at least in the Bazzano trench we have evidence of historical units affected by faulting.
These findings will help to define the location and width of the respect and susceptibility zones in the proximity of the fault traces.

The results of the dating, together with the results of the analysis of the other two trenches will help us to have an even clearer picture of the L'Aquila basin fault system.

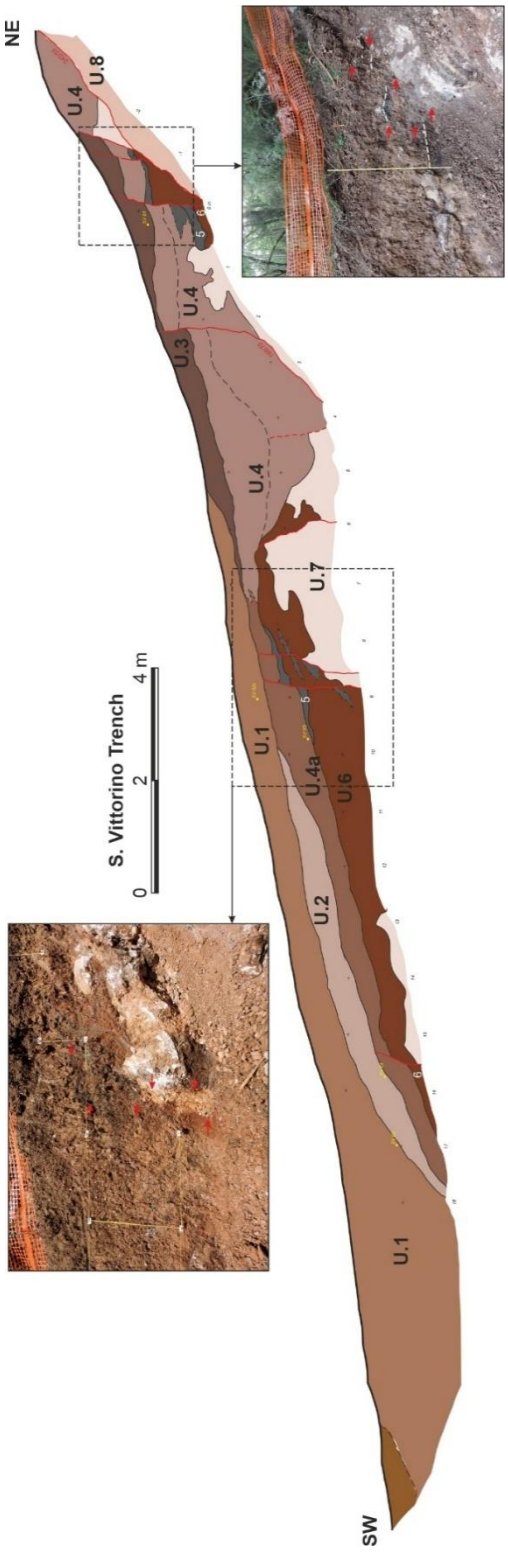

Figure 2: *Log and pictures of the S. Vittorino trench.*

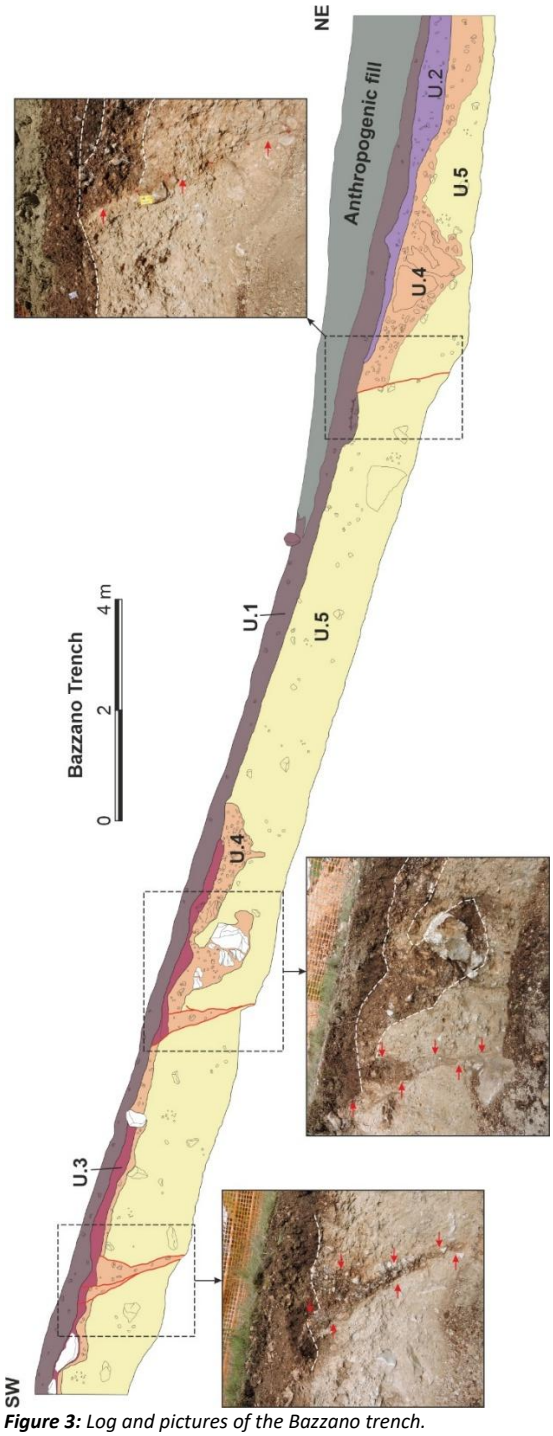

Figure 3: *Log and pictures of the Bazzano trench.*

Acknowledgements: We warmly thank the L'Aquila town council for giving us the opportunity and the financial support for performing this work, in the framework of the seismic microzonation of the town (Agreement between INGV and the Municipality of L'Aquila n. 0024313 - 19 october2023).

REFERENCES

Boncio, P., Pizzi, A., Brozzetti, F., Pomposo, G., Lavecchia, G., Di Naccio, D., Ferrarini, F., 2010. Coseismic ground deformation of the 6 April 2009 L'Aquila earthquake (central Italy, Mw6. 3). Geophys. Res. Lett. 37 (6). https://doi.org/10.1029/2010GL04280.

Boncio, P., G. Lavecchia, and B. Pace (2004), Defining a model of 3D seismogenic sources for seismic hazard assessment applications: the case of central Apennines (Italy), J. Seismol., 8, 407–425, doi:10.1023/B: JOSE.0000038449.78801.05.

Chiarabba, C., et al. (2009), The 2009 L'Aquila (central Italy) MW6.3 earthquake: Main shock and aftershocks, Geophys. Res. Lett., 36, L18308, doi:10.1029/2009GL039627.

Falcucci, E., et al. (2009), The Paganica fault and surface coseismic ruptures due to the April 6, 2009 earthquake (L'Aquila, Central Italy), Seismol. Res. Lett., 80, doi:10.1785/gssrl.80.6.940.

Galli, P., Camassi, R., Azzaro, R., Bernardini, F., Castenetto, S., Molin, D., et al. (2009). Il terremoto aquilano del 6 aprile 2009: Rilievomacrosismico, effetti di superficie ed implicazioni sismotettoniche. Alpine and Mediterranean Quaternary, 22(2), 235–246.

Galli, P., F. Galadini, and D. Pantosti (2008), Twenty years of paleoseismology in Italy, Eart. Sci. Rev., 88, 89–117, doi:10.1016/j.earseirev. 2008.01.001.

Moro, M., Gori, S., Falcucci, E., Saroli, M., Galadini, F., Salvi, S., 2013. Historical earthquakes and variable kinematic behaviour of the 2009 L'Aquila seismic event (central Italy) causative fault, revealed by paleoseismological investigations. Tectonophysics 583, 131–144.

Nurminen F., Boncio P., Visini F., Pace B., Valentini A., Baize S. & Scotti O. (2020) - Probability of occurrence and displacement regression of distributed surface rupturing for reverse fault. Frontiers in Earth Science, https://doi.org/10.3389/feart.2020.581605.

Pizzi, A., F. Calamita, M. Coltorti, and P. Pieruccini (2002), Quaternary normal faults, intramontane basins and seismicity in the Umbria-Marche-Abruzzi Apennine Ridge (Italy): contribution of neotectonic analysis to seismic hazard assessment, Boll. Soc. Geol. It., 1, 923–929.

Rovida, A., Locati, M., Camassi, R., Lolli, B., Gasperini, P., & Antonucci, A. (2022). Catalogo Parametrico dei Terremoti Italiani (CPTI15), versione 4.0. Istituto Nazionale di Geofisica e Vulcanologia (INGV). https://doi.org/10.13127/CPTI/CPTI15.4

Sm Working Group (2015) - Guidelines for Seismic Microzonation, Conference of Regions and Autonomous Provinces of Italy – Civil Protection Department, Rome.

INQUA TERPRO Project Cascading Hazards and Mitigation (CHAMP)

paleoseismicity.org

Complex Spatial-Temporal Rupture Patterns of Reverse Faults: The Dunstan Fault, Otago, New Zealand

Travers, Alexandra (1), Mark Stirling (1), Jonathan GRIFFIN (2), Dan Clark (2)

(1) University of Otago, Dunedin, New Zealand. Email: traal233@student.otago.ac.nz
(2) Geoscience Australia, Canberra, Australia.

Abstract: *The Dunstan Fault is an active reverse fault in Otago, Aotearoa-New Zealand, which is expressed at the surface by multiple parallel fault traces across a zone up to 2.5km wide. We present paleoseismic results from trenches excavated across three of the four major traces preserved on the Devonshire fan section of the Dunstan Fault. These are D3-2025, M2-2025 and D1-2025. There is evidence for one, two and three events respectively in these trenches. Combined with the four-to-six events found in T04/2 trench on the D2 trace (Van Dissen et al., 2007), there has been a maximum of twelve and a minimum of four ground rupturing earthquakes since the deposition of the Devonshire Fan c. 30ka – 70ka (Van Dissen et al., 2007). OSL samples taken from the three trenches will be used to constrain event timings in each trench. These samples are currently being analysed at the Desert Research Institute, Reno. Future work will involve comparing event timings across the different traces, in order to understand whether traces ruptured independently or together in paleoearthquakes. These results will have implications for fault zonation and fault displacement hazard analysis of reverse faults in Aotearoa-New Zealand and beyond.*

Key words*: Paleoseismology, Fault Displacement, Reverse Fault, New Zealand*

INTRODUCTION

The tectonic geomorphology of active reverse faulting is highly variable and often complex (e.g. 1988 Spitak earthquake rupture (Philip et al., 1992), 2016 Kaikoura rupture (Litchfield et al., 2018)). Surface expressions can range from single, well-defined fault scarps to multiple parallel scarps, to zones of deformation dominated by folding. Furthermore, reverse faults are frequently blind, meaning that they have no surface expression (e.g. The 1994 Northridge earthquake rupture occurred on a fault previously unknown (Jones et al., 1994)). With increased infrastructural development directly over active faults (e.g. Franz Josef township on the Alpine Fault) it is necessary to better understand the complex behaviours of reverse fault surface displacement. The Dunstan Fault in Central Otago, New Zealand, exemplifies this complexity (Fig.1). Like many active reverse faults in the region, it is expressed at the surface by multiple parallel fault traces, sometimes spanning a zone up to 2.5 km wide. A key question is whether all traces within this fault zone rupture during a single surface-rupturing earthquake, or if individual traces rupture independently. If the latter, is there a temporal or spatial pattern to these ruptures that could inform future rupture forecasting? Alternatively, what is the likelihood of new surface traces forming in future seismic events?

We present new paleoseismic data from three of the four major traces preserved on the Devonshire fan section of the Dunstan Fault to constrain the timing of past surface-rupturing events on individual traces. These are D1-2025 on the D1 trace, M2-2025 on the M2 trace and D3-2025 on the D3 trace (Fig. 2). The D2 trace was trenched in the mid-2000s and found 4-6 events (Van Dissen et al., 2007).

These results will have implications for our understanding of fault displacement hazard of reverse faults. Current New Zealand Ministry for Environment guidelines recommend a 20-meter fault avoidance zone on either side of an active fault trace, irrespective of fault type (Kerr et al., 2003). In this study we explore the potential to refine fault avoidance zones for multi-trace reverse faults.

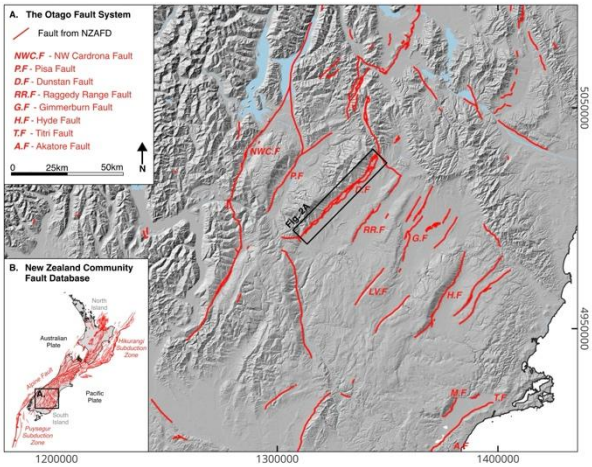

Figure 1: *The Otago Fault System. Faults are from the New Zealand Active Fault Database (Langridge et al., 2016). The Otago Fault system comprises a series of NE striking reverse faults which accomodate compressional strain assosciated with plate boundary tectonics.*

D3-2025 Trench

Seven stratigraphic units were mapped in D3-2025 (Fig. 3). Units 6 and 7 comprise clast supported fluvial boulders and cobbles with interbedded lenses of clay and silt. Though there is limited sedimentological differentiation to be made between these units, they are differentiatied by a continuous bedding plane which runs through the length of the trench. A band of clast-supported fine gravels (unit 4), and a tan silt layer (unit 5) can be traced through the northern part of the trench and act as a key marker horizon. Units 2 and 3 are comprised of poorly sorted

cobbles and gravels, in silt/sand matrix. These deposits resemble debris flows.

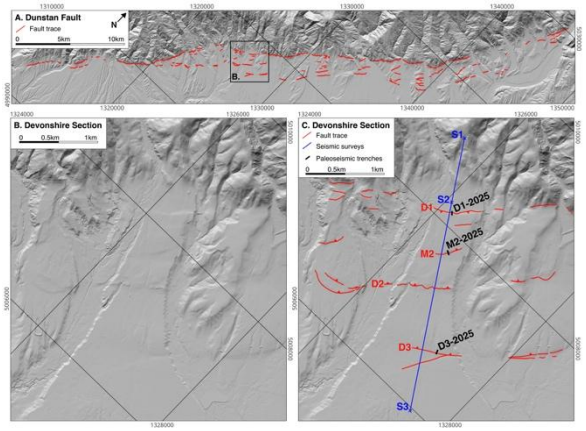

***Figure 2**: (A) Mapped traces of the Dunstan Fault. The traces stretch across a fault zone up to 2.5km wide . (B) The Devonshire Fan field site. (C) The Devonshire Fan field site showing the four major traces (D1, M2, D2, D3) spanning across a ~1.8km fault zone width. Trench locations are indicated. Passive seismic (S1-S3) and active seismic (S2-S3) surveys were conducted but are not discussed in this paper.*

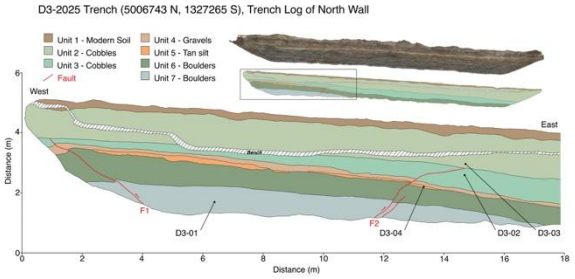

***Figure 3:** Trench log of the North Wall of D3-2025 trench on the D3 trace.*

Two faults, F1 and F2, are observed in D3-2025. F2 is a northwest dipping reverse fault which dips ~45° NW at the base of the trench and shallows to ~9° W further up section. It is characterised by discrete displacement of sedimentary units (Fig. 4D). F1 is a southeast dipping reverse fault which dips ~33° SE. It is characterised by tight folding along the fault plane (Fig. 4C). F1 is interpreted as an antithetic fault to the west dipping Dunstan Fault system. Both F1 and F2 displace units 7 to 3. Units 1 and 2 are undeformed. This implies that both faults ruptured in the D3 trace in the most recent event (MRE) on the D3 trace, post U3 deposition and pre U2 deposition. No events have ruptured D3 since.

Measured fault slip on F1 and F2 is small and similar across all stratigraphic horizons. Thus, there is no evidence for an earlier event on F1 or F2 in the trench exposure. Slip is 9-15cm on F2, using U7, U6 and U4 offsets. Slip on F1 is 9cm, using offsest of U4 by tight folding along the fault plane. These measurements are small in comparison with the total uplift of U6 within the trench exposure, ~95cm. Folding is observed in the western side of the exposure, and is thus assumed to be the predominant cause of uplift in the trench.

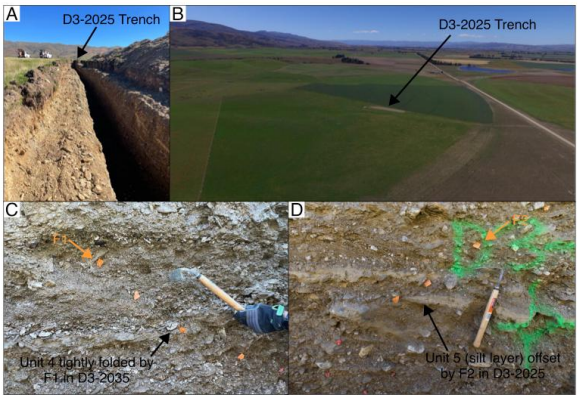

***Figure 4:** (A) Photograph taken northwards looking up at the D3-2025 trench (B) Drone image taken of the D3-2025 trench (C) Photograph of the F1 fault in D3-2025. Tightly folded gravels are indicated (D) Photograph of the F2 fault in D3-2025. The offset silt layer is indicated*

A fault-perpendicular scarp profile taken across D3 has a vertical displacement of ~5m, and displacement is distributed across a ~425m fault perpendicular width (Fig. 5). This is a much greater scale of displacement than is observed in the D3-2025 trench exposure, and suggests that multiple earthquakes, beyond what we obvserve in the trench, have contributed to relief across the D3 scarp. The width of deformation and shape of the hanging wall in the scarp profile suggests that the scarp is prodiminantly a fold scarp. This is supported by our trench results. Thus, events on D3 may not have caused surface rupture, but surface folding instead. If surface displacement of U6 from the trench is assumed to be ~1m (minimum), then it can be hypothesised that up to 5 events (maximum) have caused folding on the D3 trace since Devonshire Fan depsoition.

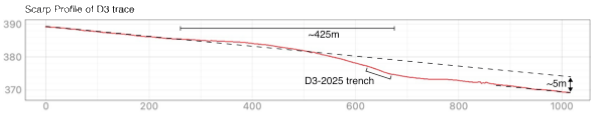

***Figure 5:** Vertically exaggerated scarp profile of D3 trace, with trench location indicated.*

M2-2025 Trench

M2-2025 is comprised of similar alluvium to that observed in D3-2025 (Fig. 6). Units are predominantly comprised of sub-rounded cobble sized clasts, with varying percentages of matrix. These units are interpreted to be debris flow deposits. Unit 7 and unit 9 are lens shaped deposits comprised of finer sands and gravels. These are interpreted to have fluvial origin.

There are two west dipping faults exposed in the trench wall (F1 and F2) which both offset stratigraphic units. F1 and F2 run approximately parallel and shallow up section. The faults are c. 3.75m apart near the base of the trench. F1 dips at 49° at the base of the trench and shallows to 13°

near the top. F2 dips at 45° at the base of the fault and shallows to 29° near the top.

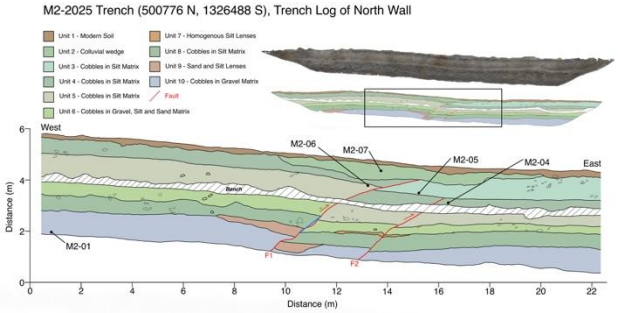

Figure 6: *Trench log of M2-2025 trench, North Wall, on the M2 trace.*

F1 displaces units 10 to 3. The fault is capped by unit 2 (U2). Thus, this event is interpreted to have occured after the deposition of U3 and before the deposition of U2. U2 is a colluvium made up of reworked U3 material, deposited during scarp degredation processes following scarp formation during this event. Units displaced by F1 have experienced just over a metre of slip (measured slip for the top of U8 and U9 are 110cm and 105cm, respectively). Throw is measured from the top of U9 and U8 to be ~50cm and ~66cm respectively. Slip is consistant on F1, thus it was ruptured once in the M2-2025 trench exposure. F2 ruptures units 10 to 4. U3 is not displaced and caps the faulted unit. Thus, a ground rupturing event occured post U4 deposition and pre U3 deposition. Slip on F2 is small and mostly consistant along F2 (15cm and 20cm, measured from U10 and U6 offsets respectively). The small increase in slip up stratigraphy is due to the fault shallowing as it approaches the surface. Vertical displacement is constant: ~14cm. Thus, F2 preserves one ground rupturing event. In total, the M2-2025 trench provides evidence for two ground rupturing events on the M2 trace, which occured on separate faults. The MRE occured on the F1 trace, and the penultimate event occured on the F2 trace.

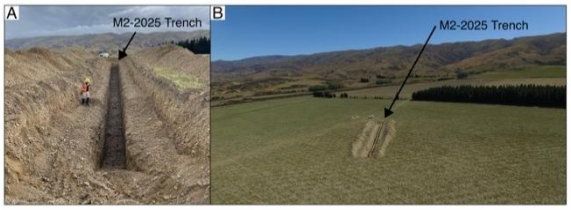

Figure 7: *(A) Photograph taken northwards looking up at the M2-2025 trench (B) Drone image taken of the M2-2025 trench*

Folding is observed in the hanging wall of the M2-2025 trench exposure. Units in the footwall are undeformed and retain horizontal bedding. Folding is observed in units 10 to 4. Thus, we can infer that at least one of these events caused further vertical offset through folding.

A scarp perpendicular profile through M2 has a total vertical displacement of ~2.5m. Unlike the D3-2025 trench, the M2-2025 trench encompasses the majority of deformation at the scarp. Thus, it is expected that total vertical offset within the trench exposure is approximately equivalent to the total vertical offset observed in the scarp profile. The total vertical displacement of the top of U4 is 2.4m across the trench. Although this aligns with the scarp profile, Unit 3 has been completely eroded from the hanging wall. Thus, the scarp profile underestimates total displacement on the M2 scarp. Furthermore, the total vertical displacement of U10 is 1.6m across the trench. Thus there may be evidence for a possible third event in M2, which may be present below the base of the trench.

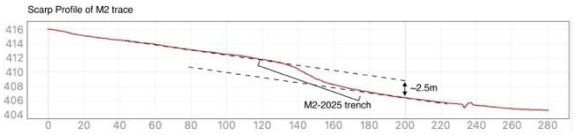

Figure 8: *Vertically exaggerated scarp profile of the M2 trace, with trench location indicated.*

D1-2025 Trench

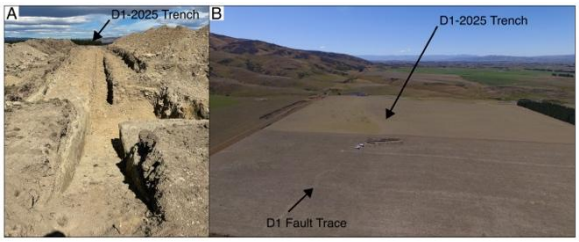

Figure 9: *(A) Photograph taken northwards looking up at the D1-2025 trench. (B) Drone image taken northwards of the D1-2025 trench and the D1 trace on the Devonshire Fan*

The D1-2025 Trench was excavated across the D1 trace which is an uphill facing scarp (Fig. 9). The trench comprises alluvial gravels and cobbles, similar to D3-2025 and M2-2025, but also a series of channel deposits in the west side of the exposure (Fig. 10). These are comprised of well sorted silts, sands and clast supported rounded gravels. These are interpreted to have been deposited against an uphill facing paleo-scarp created by an east dipping reverse fault (F1).

F1 is interpreted as an antithetic reverse fault splaying off the west dipping Dunstan Fault system. It is expressed as a heavily deformed shear zone, c. 15cm wide, from the base of the trench until the top of U9 in the footwall. It is indicated by hatched red shading. Within this section, the 'fault band' dips ~27°E at the base and shallows to ~20° at top of the wider fault zone. The top of F1 is a discrete fault drawn as a line. It steepens again to 43° up section.

Three events are interpreted to have ruptured the F1 trace, from differential offsets and stratigraphy. Units 15, 14 and 13 accommodate more total slip than Unit 11 (~3m from top of U14, ~1.7m from bottom of U11). Thus, it is interpreted that E1 is the oldest event exposed in the

trench, and ruptured units 15, 14 and 13 before any younger units were deposited. Unit 12 is poorly sorted and clast supported colluvium, deposited following E1.

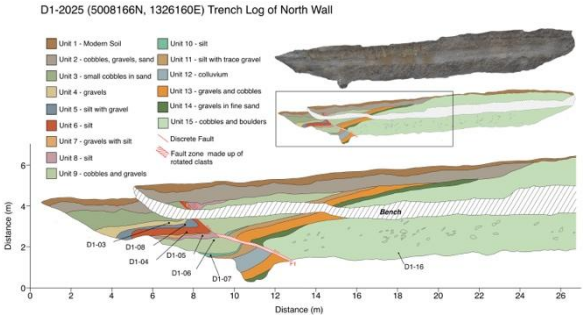

Figure 10: *Trench log of M2-2025 trench, North Wall, on the D1 .*

Units 8 to 4 comprise a series of fine-grained fluvial channel and loess deposits interpreted to have been deposited in the footwall of an uphill facing scarp. Thus, it is interpreted that E2, the second event, ruptured units 15 to 9 on the same F1 fault, creating a scarp for units 8 to 4 to be deposited against.

The MRE is interpreted to have ruptured through the fine grain channel deposits, along F1 again. It displaces units 15 to 3, and is capped by unit 2, a colluvial deposit. This final rupture displaced units along a single fault plane as opposed to a 'fault band' and is accompanied by fault steepening. It is likely that we observe the 'fault band' in the lower units because there have been more rupture events on this section of fault.

Total slip from all three earthquakes is ~3m. Total slip in the MRE and E2 is ~1.7m. Slip in the MRE cannot be resolved because each side of the offset is observed on either side of the bench. As deposition was active along strike of the fault in the offset fluvial channels, it is not accurate to compare either side of the bench. Additionally, the orthomosaic is oblique which would cause further error. However, we can resolve a minimum slip of the MRE, from the base of U8 to the bench, of ~1.4m. U8 is a channel deposit so likely eroded into U9 in the footwall. This would cause an overestimate of slip of U8, so a slip of 1.4m is a reasonable approximation. Thus, it can be hypothesised that there was ~1.3m of slip in E1, ~0.3m of slip in E2 and ~1.4m of slip on the MRE.

A scarp perpendicular profile taken across M2 shows a local vertical uplift at the scarp of ~1.7m (Fig. 11). Total vertical displacement at the scarp is greater than the total uplift of the fan surface (~1.2m) due to localised folding in the hanging wall of the fault. This profile is likely an underestimate of vertical displacement on D1, due to scarp degradation processes observed in the trench (Units 14, 13 and 11 are truncated at their eastern extent by Unit 2). Thus, it is difficult to reconcile displacement observed in the trench with the scarp profile.

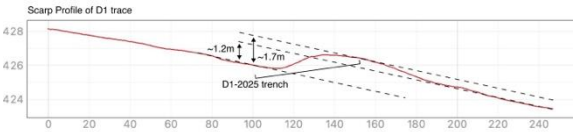

Figure 11: *Vertically exaggerated scarp profile of D1 trace, with trench location indicated.*

Conclusion and Future Work

These trenches provide direct evidence for 6 events on the Devonshire Fan. Previous trenching on the D2 trace found evidence for 4 to 6 events (Van Dissen et al., 2007). Thus there is evidence for a maximum of 12 events on the Devonshire Fan if all traces ruptured separately in each earthquake. OSL age results, currently being analysed at the Desert Research Institute, Reno, will be used to provide age constraints on events. These results will be used to compare event timings between the trenches, to see if multiple traces ruptured in the same events. These results will have implications for magnitude estimations and fault displacement hazard studies.

Acknowledgements: Thanks go to Contact Energy, QuakeCoRE, and Otago University for funding this research. Thank you also to the landowners of the Devonshire area, central Otago.

REFERENCES

Jones, L. M., Aki, K., Boore, D., Celebi, M., Donnellan, A., Hall, J., Harris, R., Hauksson, E., Heaton, T., Hough, S., et al. (1994). The magnitude 6.7 Northridge, California, earthquake of 17 January 1994, *Science 226, no. 5184*, 389-307

Kerr, J., Nathan, S., Van Dissen, R.J., Webb, P., Brunsdon, D., King, A. 2003. Planning for development of land on or close to active faults: a guideline to assist resource management planners in New Zealand. Lower Hutt (NZ): Institute of Geological & Nuclear Sciences. 67 p. Client Report 2002/124. Prepared for the Ministry for the Environment. https://environment.govt.nz/assets/Publications/Files/planning-development-faults-graphics-dec04-1.pdf

Langridge, R. M., Ries, W.F., Litchfield, N. J., Villamor, P., Van Dissen, R. J., Barrell, D. J. A., et al. (2016). The New Zealand active faults database. *New Zealand Journal of Geology and Geophysics, 59*(1), 86-96.

Litchfield, N., Villamor, P., Van Dissen, R., Nicol, A., Barnes, P., Barrell, D., Pettinga, J., Langridge, R., et al. (2018). Surface Rupture of Multiple Crustal Faults in the 2016 7.8 Kaikōura, New Zealand, Earthquake. *Bulletin of the Seismological Society of America* 2018;; 108 (3B): 1496–1520

Philip, H., E. Rogozhin, A. Cisternas, J. C. Bousquet, B. Borisov, and A. Karakhanian (1992). The Armenian earthquake of 1988 December 7: Faulting and folding, neotectonics and palaeoseismicity, *Geophys. J. Int*. 110, no. 1, 141–158

Van Dissen, R., Barrell, D., Langridge, R., Litchfield, N., Villamor, P., & Tonkin, P. (2007). Reassessment of seismic hazard at Clyde Dam, Central Otago: Earthquake geology field investigations and determination of Dunstan Fault rupture characteristics. *GNS Science Consultancy Report 2006/147*

INQUA TERPRO Project Cascading Hazards and Mitigation (CHAMP)

paleoseismicity.org

Subaerially exposed Iceberg Lake sediments: an exceptional record of historical subaqueous earthquake disturbance at the eastern edge of the Alaskan-Aleutian subduction zone

Maarten Van Daele (1), Pieterjan Vercruysse (1), Rob C. Witter (2), Michael G. Loso (3), Drake M. Singleton (4), Sabine Schmidt (5), Kamill Lisson (1), Peter J. Haeussler (2), and Robert L. Wesson (6)

(1) Department of Geology, Ghent University, Krijgslaan 297, S8, Gent, Belgium; maarten.vandaele@ugent.be.
(2) U.S. Geological Survey, Alaska Science Center, Alaska, USA
(3) Wrangell - St Elias National Park & Preserve, National Park Service, Alaska, USA
(4) U.S. Geological Survey, Earthquake Science Center, California, USA
(5) Univ. Bordeaux, CNRS, Bordeaux INP, EPOC, UMR 5805, F-33600 Pessac, France
(6) U.S. Geological Survey, Geologic Hazards Science Center, Colorado, USA

Abstract: *Paleoseismic records are limited in the Yakutat Terrane (eastern edge of the Alaskan-Aleutian subduction zone) due to the extensive ice cover that hinders traditional methods such as trenching of the faults, but lacustrine sediments offer an alternative archive. We investigated lakebed sediments exposed after recent outburst floods (1999 CE) at Iceberg Lake, a glacier-dammed basin whose stratigraphy was revealed after the lake drained and partially eroded. We logged outcrops across the basin and sampled their sediments. Between annually laminated background deposits, we identified sediment gravity flow beds and in-situ soft-sediment deformation structures (convolutions, sand blows, and fractures) interpreted to be earthquake-induced. Our age model links some of the uppermost depositional and deformational events to the 1958, 1964 and 1979 CE earthquakes. These results demonstrate that Iceberg Lake was a sensitive recorder of seismic shaking and its sediments hold strong potential for producing a paleoseismic record for the northern Yakutat Terrane.*

Key words*: south-central Alaska, lacustrine paleoseismology, soft-sediment deformation structures*

INTRODUCTION

The Yakutat Terrane is a structurally complex microplate that occupies the transition between transform and subduction tectonics, at the eastern edge of the Alaskan-Aleutian subduction zone (Fig. 1). It is bounded by the Chugach Saint Elias Fault system (CSEF) to the north, the Queen Charlotte-Fairweather Fault (QCFF) to the northeast, the Transition Fault to the southwest and the Ragged Mountain-Kayak Island zone (RMKI) to the west. The northwestern part of the block is intersected by several faults and fault zones that form the deformation zone (DZ) resulting from the subduction of the Yakutat microplate beneath the North American Plate (Bruhn et al., 2012; Plafker & Thatcher, 2008). Furthermore, the Alaska-Aleutian megathrust extends beneath the Yakutat microplate, and like the 1964 M_w 9.2 Prince William Sound earthquake, earthquakes ~900 and ~1500 yrs ago have caused coastal uplift in the western part of the Yakutat Terrane (Shennan et al., 2014). In contrast to these megathrust earthquakes, comparatively little is known about prehistoric activity of the other faults bordering and crossing the Yakutat Terrane. Historically, the QCFF ruptured in 1958 CE during the M_w 7.9 Lituya Bay earthquake (Doser, 2010), while the CSEF system hosted the 1979 M_w 7.4 Saint Elias earthquake (Estabrook et al., 1992). The largest non-megathrust earthquakes, however, were the two great 1899 M_w 8.1 Yakutat Bay earthquakes, which ruptured thrust faults within the Yakutat Terrane along an extent that is not fully known (Doser, 2010; Plafker & Thatcher, 2008). The only observed paleoseismic evidence in the Yakutat Terrane — other than that of megathrust ruptures — is an uplifted beach near Yakutat Bay with an age of at least 317 cal year BP (Plafker & Thatcher, 2008).

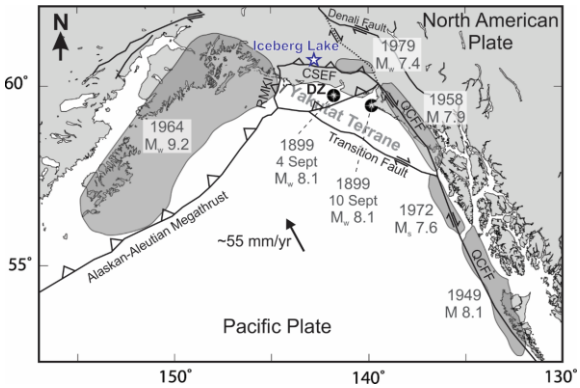

Figure 1: *Tectonic setting of south-central Alaska with the location of Iceberg Lake (blue star) at the northern boundary of the Yakutat Terrane, situated at the eastern edge of the Alaskan-Aleutian subduction zone, at the transition between transform and subduction tectonics. The main faults (black) as well as main historical earthquake ruptures (grey) are adapted from Plafker & Thatcher (2008) and Bruhn et al. (2012). Specific dates are added to differentiate between both 1899 earthquakes. CSEF: Chugach-Saint Elias Fault system; QCFF: Queen Charlotte-Fairweather Fault zone; RMKI: Ragged Mountain-Kayak Island zone; DZ: Deformation Zone occupying the northwestern part of the Yakutat Terrane.*

The scarcity of paleoseismic records in this region is partly due to its extensive ice cover, which hides surface faults (Bruhn et al., 2012). As a result, traditional paleoseismological methods that rely on primary surface rupture are ineffective here. The area's structural complexity and the likelihood of ruptures not reaching the surface further limit their use. Consequently, approaches that target secondary shaking evidence in depositional environments capable of preserving it offer the best opportunity to reconstruct the earthquake history of the eastern Alaskan-Aleutian subduction zone. Lakes provide

such continuous sediment records and have demonstrated to be potentially very accurate recorders of earthquakes in Alaska (Praet et al., 2025). Globally, lake sediments have been shown to record earthquakes through different types of sedimentary features, such as soft-sediment deformation structures (e.g., Lu et al., 2020), microfaults (e.g., Monecke et al., 2006), mass-transport deposits (e.g., Schnellmann et al., 2002) and turbidites (e.g., Moernaut et al., 2014). However, these examples demonstrate that lakes in different environmental settings each record earthquakes in a specific way, and understanding how different lakes and sediment types record earthquake shaking is crucial if we want to exploit these records as accurate and quantitative paleoseismic archives.

Here, we study Iceberg Lake, which offers a unique opportunity to obtain a paleoseismic record for the eastern edge of the Alaskan-Aleutian subduction zone encompassing the last 1,500 yrs. Iceberg Lake is a glacier-dammed lake in the Chugach Mountains, just north of the CSEF (Fig. 1). Since 1999 CE, the lake drained during several glacial-lake outburst floods, exposing the lakebed and thus its sedimentary record (Loso et al., 2004). Subsequent subaerial lakebed erosion resulted in steep-walled cohesive outcrops of several meters in height, which exposed 1,500 yrs of lacustrine deposition (Loso et al., 2006); the entire record is annually laminated (varved), allowing for high-resolution climate reconstructions (Loso et al., 2004; Loso et al., 2006). We revisited the existing data from the early 2000s and subsequently Iceberg Lake itself, where we studied six exposures with a focus on the disturbed layers and sand beds, which we compare to the historical seismic record.

METHODS

Of the six new sites in the Iceberg Lake basin, we focus on "Landslide" (IC22-03) and Site A from Loso et al. (2006). The Landslide site was further exposed by carefully excavating the outcrop to a relatively vertical orientation, using different benches to avoid collapse (Fig. 2). The vertical faces were photographed in high detail to prepare a virtual 3D outcrop model using structure from motion (SfM) (Bilmes et al., 2019) with the Agisoft Metashape Professional software package. We then sampled the stratigraphy by carving out sediments from the outcrop into 50-cm-long, half-open PVC tubes, with 10 cm overlap between consecutive cores. All the cores were scanned with a Siemens SOMATOM Definition Flash medical X-ray computed tomography (CT) scanner at the University Hospital in Ghent. The resolution of these scans is 0.15 x 0.15 x 0.30 mm, and the reconstructed volumes were visualized and processed using the VGSTUDIO 3.3 software. Detailed linescan images of the cores were obtained with a Geotek Multi-Sensor Core Logger (MSCL).

Radionuclide dating (^{137}Cs) was performed at the University of Bordeaux on sediment core ICE01-1A from Loso's Site A. Measurements of ^{137}Cs and ^{232}Th activities (mBq/g) were conducted on freeze-dried samples, utilizing a low-background, high-efficiency, well-shaped gamma-ray detector (CANBERRA). In total, 19 strategically positioned samples of single varves were analyzed in order to pinpoint the onset of ^{137}Cs fallout (1954 CE), peak fallout following atmospheric atomic-bomb testing in 1963-64 CE, and potentially a peak related to the 1986 CE Chernobyl nuclear accident. Varve counting was done between ^{137}Cs marker varves on sediments from both sites (incl. CT data) to complete the age model.

Figure 2: *A) Excavation with shovels of the Landslide site, expanding the outcrop to enhance lateral observations. B) Cleaning a smaller outcrop using a gardening tool. Photos by P. Vercruysse.*

RESULTS

We combined the sedimentological observations at our Landslide site with the chronology at Loso's Site A, which was possible through correlation of the main event beds.

Landslide site

The upper 155 cm at this site consists of sand/silt-clay couplets, and thicker laminated sands and silts. The fine sandy to silty basal bed of the couplets ranges from mms to cms in thickness, but the sharp clay cap is usually in the mm range. These couplets have been interpreted as varves by Loso et al. (2006), and they are locally interrupted by beds that stand out based on their coarse sandy texture, internal structure and/or laterally variable thickness. Each of these beds is identified as an Iceberg Lake Event and numbered ILE-01 to ILE-05. We describe them here from top to bottom.

ILE-01 is a ~30-cm thick light-colored, very fine to fine sand interval. The lower part of this bed includes climbing ripples, while the upper part consists of wavy to planar laminations (Fig. 3). ILE-02 is a lens-shaped fine sandy to silty deposit that locally intercalates the varves at a topographic high in the stratigraphy (Fig. 3C). Below the part where it reaches its maximum thickness of ~20 cm, the sands seem connected to the underlying sand beds through a pipe or dike. We interpret this deposit as a sand blow. ILE-03 is a bed of variable thickness ranging from mm- to cm-scale, with isolated sandy ripples (Fig. 3D). ILE-04 occurs merely 3 varves below ILE-03. It is a silty to fine sandy bed that has a variable thickness (cm-scale) and seems to flatten the undulating stratigraphy below. At the topographic high of ILE-2, ILE-03 has a very similar expression of a sand blow to that of ILE-02 (Fig. 3). ILE-05 consists mainly of light- to brown-grey, planar to (heavily) deformed fine sands and silts, with a total thickness varying between ~30 and ~120 cm (Fig. 3). The sand-silt deposits are interrupted by three laterally continuous clay laminae. Vertically, the deformation increases with depth, with an increase in degree of deformation at each clay lamina. Below the lowest clay lamina, the light-grey sands with locally climbing ripples, are contorted and deformed into

convoluted waves, but are normally faulted at local topographic highs (Fig. 3C). Below ILE-05, the silt-clay couplets (varves) abruptly become thinner and finer-grained with a sporadic sandy summer layer.

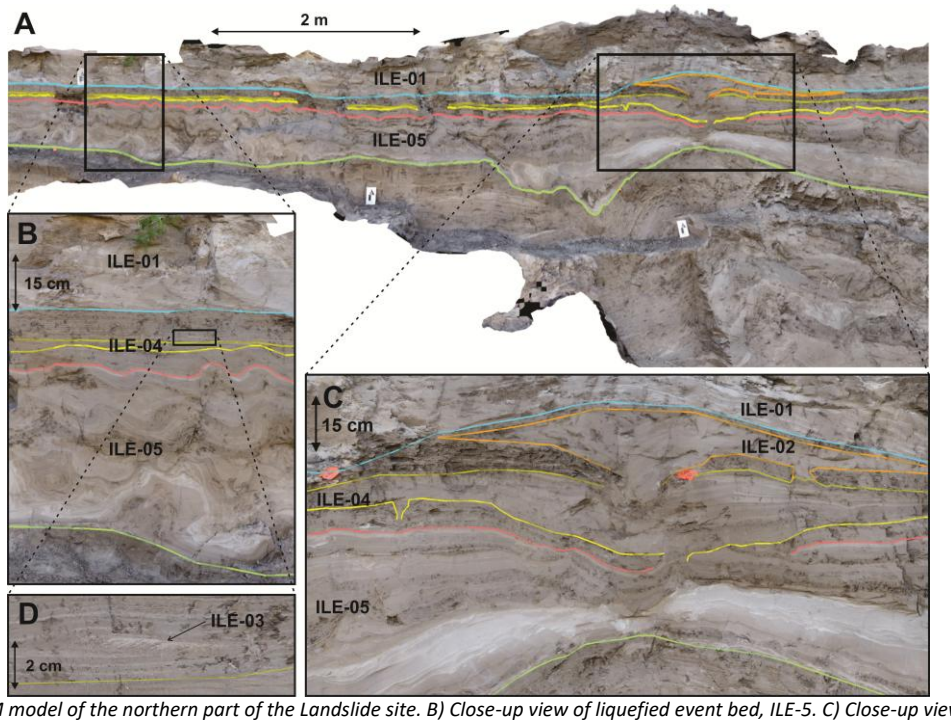

Figure 3: *A) SfM model of the northern part of the Landslide site. B) Close-up view of liquefied event bed, ILE-5. C) Close-up view of area with sand blows, ILE-02 and ILE-04. D) Close-up view of ILE-03 isolated sandy ripple and three varves above the ILE-04 top boundary.*

Loso's Site A

Like at Landslide, Site A from Loso et al. (2006) contains an upper 175 cm (corresponding to 155 cm at Landslide) of sand/silt-clay couplets interrupted by silty to sandy event deposits. The five event deposits are also observed at Site A, but ILE-02, ILE-03, and to some extent ILE-04, have different expressions (Fig. 4). At Site A, ILE-02 is a cm-scale sand bed that is only exceptional in that it is bound by a clay lamina at its base and top, without silt in between. ILE-03 is a ~20 cm thick sand bed with climbing ripples, and ILE-04 is a sandy to silty graded bed, similar to the part that flattens the stratigraphy at the Landslide site.

The ^{137}Cs radionuclide data combined with varve counting reveal the age of these five most recent event deposits. The lowest sample in core ICE01-1A has a negligible amount of ^{137}Cs (Fig. 4), indicating it is older than or of a similar age to the first widely detectable ^{137}Cs fallout around 1954 CE (Hancock et al., 2014). Above that, two peaks can be observed, a main peak centered around ILE-04 and a secondary maximum just above ILE-01. The main peak around ILE-04 can be linked to the 1963-64 CE maximum ^{137}Cs fallout in the Northern Hemisphere (Hancock et al., 2014). Based on varve counts, this further dates the top of ILE-05 to about 1960-61 CE, and ILE-03 to 1967 CE. The secondary ^{137}Cs maximum can be linked to the 1986 CE Chernobyl nuclear accident. As the base of this maximum occurs one varve year above ILE-01, we date this deposit to 1985 CE. ILE-02 occurs six varves below the 1985 CE event, thus dating it to 1979 CE.

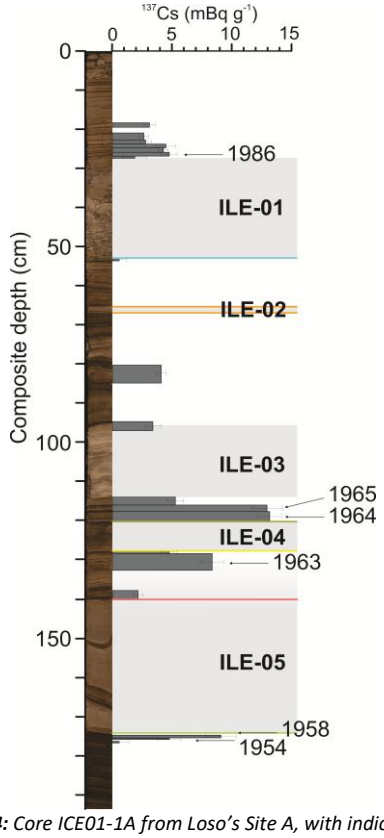

Figure 4: *Core ICE01-1A from Loso's Site A, with indication of event deposits and key varve ages based on ^{137}Cs dating and varve counting.*

DISCUSSION

Based on the primary ^{137}Cs peak, we attribute the ILE-04 graded sands and sand blow to the 1964 M_w 9.2 Prince William Sound earthquake, which locally caused Modified Mercalli Intensities (MMI) of V½-VI (https://earthquake.usgs.gov/earthquakes/eventpage/iscgem869809). The highest ^{137}Cs values are found just above this deposit, which is consistent with the record at the relatively nearby (330 km west) Eklutna Lake, where the actual peak also occurs just above the 1964 turbidite (Boes et al., 2018). The observation that ILE-04 seems to occur early in the varve year (i.e., very shortly after the start of seasonal snow melt) further corroborates the match with the March 27th occurrence of the earthquake. In Landslide, the graded bed of ILE-04 fills and flattens the undulating morphology of varves that drape the top of the strongly internally deformed ILE-05 deposit. Thus, we interpret that the soft-sediment deformation and related liquefaction of ILE-05 also resulted from shaking during the 1964 CE earthquake.

The sands in ILE-05 themselves, were originally deposited from 1958 to 1960 CE and, as evidenced by the suddenly thicker and sandier varves above, were interpreted as relating to a lake-lowering event that occurred in the second half of the 1950s (Loso et al., 2006). However, varve counting from 1964 CE downwards and from ~1954 CE upwards suggests that the initial sand was deposited in the summer of 1958, which corresponds in age to the July 1958 M_w 7.8 Lituya Bay earthquake. Even though this earthquake only caused MMI's of III½ at Iceberg Lake (https://earthquake.usgs.gov/earthquakes/eventpage/iscgem884702), we hypothesize that it may have somehow triggered the preconditioned lake-lowering event, for example by inducing seiche waves that caused a dam breach, or by destabilizing the ice dam.

Finally, the ILE-02 sand blow in Landslide and sand bed in Site A are dated to 1979 CE based on varve counts and the 1986 CE ^{137}Cs peak. In both sites, the sand deposit interrupts a clay cap, which we interpret to mean that it occurred in winter. We therefore link the liquefaction that resulted in the sand blow to the 1979 M_w 7.4 Saint Elias earthquake, which caused MMI's of IV-V at Iceberg Lake (https://earthquake.usgs.gov/earthquakes/eventpage/usp0000z2a).

In summary, the 1964 Prince William Sound and 1979 Saint Elias earthquakes caused liquefaction of thick sand beds that were deposited years to decades prior. Though these sand beds are related to an apparent lake-lowering event, the trigger of that event may have been the 1958 Lituya Bay earthquake. Sand beds with (climbing) ripples deposited in 1967 and 1985 are likely related to a change in the course of the inflowing Chisma Creek or reorganisation of the delta, independent of any seismic trigger.

Acknowledgements: We acknowledge the financial support by the United States Geological Survey-Earthquake Hazards Program (External Grant G22AP0078) and thank the National Park Service for permitting the fieldwork (permit WRST-2022-SCI-0023). Any use of trade, firm, or product names is for descriptive purposes only and does not imply endorsement by the U.S. Government.

REFERENCES

Bilmes, A., D'Elia, L., Lopez, L., Richiano, S., Varela, A., Alvarez, M. d. P., Bucher, J., Eymard, I., Muravchik, M., Franzese, J., & Ariztegui, D., 2019. Digital outcrop modelling using "structure-from- motion" photogrammetry: Acquisition strategies, validation and interpretations to different sedimentary environments. *Journal of South American Earth Sciences* 96, 102325.

Boes, E., Van Daele, M., Moernaut, J., Schmidt, S., Jensen, B.J.L., Praet, N., Kaufman, D., Haeussler, P.J., Loso, M.G., & De Batist, M., 2018. Varve formation during the past three centuries in three large proglacial lakes in south-central Alaska. *GSA Bulletin* 130(5-6), 757-774.

Bruhn, R.L., Sauber, J., Cotton, M.M., Pavlis, T.L., Burgess, E., Ruppert, N., & Forster, R.R., 2012. Plate margin deformation and active tectonics along the northern edge of the Yakutat Terrane in the Saint Elias Orogen, Alaska, and Yukon, Canada. *Geosphere* 8(6), 1384-1407.

Doser, D.I., 2010. A Reevaluation of the 1958 Fairweather, Alaska, Earthquake Sequence. *Bulletin of the Seismological Society of America* 100(4), 1792-1799.

Estabrook, C.H., Nábělek, J.L., & Lerner-Lam, A.L., 1992. Tectonic model of the Pacific-North American Plate Boundary in the Gulf of Alaska from broadband analysis of the 1979 St. Elias, Alaska, earthquake and its aftershocks. *Journal of Geophysical Research: Solid Earth* 97(B5), 6587-6612.

Hancock, G.J., Tims, S.G., Fifield, L.K., & Webster, I.T., 2014, The release and persistence of radioactive anthropogenic nuclides. *Geological Society, London, Special Publications* 395(1), 265-281.

Loso, M.G., Anderson, R.S., & Anderson, S.P., 2004. Post–Little Ice Age record of coarse and fine clastic sedimentation in an Alaskan proglacial lake. *Geology* 32(12), 1065-1068.

Loso, M.G., Anderson, R.S., Anderson, S.P., & Reimer, P.J., 2006. A 1500-year record of temperature and glacial response inferred from varved Iceberg Lake, southcentral Alaska. *Quaternary Research* 66(1), 12-24.

Lu, Y., Wetzler, N., Waldmann, N., Agnon, A., Biasi, G.P., & Marco, S., 2020. A 220,000-year-long continuous large earthquake record on a slow-slipping plate boundary. *Science Advances* 6(48), eaba4170.

Moernaut, J., Van Daele, M., Heirman, K., Fontijn, K., Strasser, M., Pino, M., Urrutia, R., & De Batist, M., 2014. Lacustrine turbidites as a tool for quantitative earthquake reconstruction: New evidence for a variable rupture mode in south central Chile. *Journal of Geophysical Research: Solid Earth* 119, 1607-1633.

Monecke, K., Anselmetti, F.S., Becker, A., Schnellmann, M., Sturm, M., & Giardini, D., 2006. Earthquake-induced deformation structures in lake deposits: A late Pleistocene to holocene paleoseismic record for central Switzerland. *Eclogae Geologicae Helvetiae* 99(3), 343-362.

Plafker, G., & Thatcher, W., 2008. Geological and Geophysical Evaluation of the Mechanisms of the Great 1899 Yakutat Bay Earthquakes. In: *Active Tectonics and Seismic Potential of Alaska* (Freymueller, J.T., Haeussler, P.J., Wesson, R.L., Ekström, G. eds). 215-236.

Praet, N., Van Daele, M., Wils, K., Haeussler, P.J., Witter, R.C., McKay, N.P., Jensen, B.J.L., Moernaut, J., & De Batist, M., 2025. Refining the earthquake history of south-central Alaska through lake records. *Earth-Science Reviews*. 271, 105249.

Schnellmann, M., Anselmetti, F.S., Giardini, D., McKenzie, J.A., & Ward, S. N., 2002. Prehistoric earthquake history revealed by lacustrine slump deposits. *Geology* 30(12), 1131-1134.

Shennan, I., Bruhn, R., Barlow, N., Good, K., & Hocking, E., 2014. Late Holocene great earthquakes in the eastern part of the Aleutian megathrust. *Quaternary Science Reviews* 84(0), 86-97.

INQUA TERPRO Project Cascading Hazards and Mitigation (CHAMP)

The September 19, 1985 Mexico earthquake and its earthquake environmental effects: reassessment of intensity using the ESI-07 scale

Velázquez-Bucio M. M. (1), Ortega-Gutiérrez F. (2), Arroyo Olarte S. (3), Mendoza Carvajal A. de J. (4), Michetti A. M. (5, 6)

(1) Escuela Nacional de Estudios Superiores, Universidad Nacional Autónoma de México, Antigua Carretera a Pátzcuaro No. 8701, C.P. 58190 Morelia, Michoacán, México. magda_vb@yahoo.com.mx
(2) Instituto de Geología, Universidad Nacional Autónoma de México. Ciudad Universitaria, Coyoacán, C. P. 04510, Ciudad de México.
(3) Geografía, Universidad Nacional Autónoma de México. Ciudad Universitaria, Alcaldía Coyoacán, C. P. 04510, Ciudad de México.
(4) Servicio Sismológico Nacional, Universidad Nacional Autónoma de México, Ciudad Universitaria, Coyoacán, C. P. 04510, Ciudad de México.
(5) Dipartimento di Scienza ed Alta Tecnologia, Università degli Studi dell'Insubria, Como, Italy.
(6) Istituto Nazionale di Geofisica e Vulcanologia (INGV), Sezione Osservatorio Vesuviano, Napoli, Italy.

Abstract: *The September 19, 1985, Michoacán earthquake (Mw 8.1), represents a key event in Mexico's seismic history, with devastating consequences and more than 10,000 victims. We apply the ESI-07 Scale to reassess the impact of the event through the analysis of coseismic Earthquake Environmental Effects (EEE), which as of yet have been overlooked. We also analyzed the EEE in Mexico City, where the site amplification focused the intensity assessment mainly on structural damages; however, we concentrate here on the coseismic environmental impact in the epicentral area. The systematic review of scientific literature, technical reports, and institutional archives produced during and after the emergency enabled until now the identification of coastal uplift/subsidence (19), tsunami (20), liquefaction (14), ground cracking (13), landslides/rockfalls (5), and hydrogeological anomalies (7). Integrating the results obtained with available MM scale intensity estimates offers a more complete picture of the impact of this earthquake across the national territory. This analysis contributes to strengthening the methodological approaches for seismic hazard assessment and risk reduction in Mexico.*

Key words*: 1985 Mexico earthquake, earthquake environmental effects, ESI-07 Scale, Seismic hazard.*

INTRODUCTION

The September 19, 1985 (Mw 8.1) earthquake, including the strong "aftershock" two days later (September 21 Mw 7.5), with epicenter along the Pacific coast of the state of Michoacán, represents a turning point in the seismic and social history of Mexico. Its devastating impact, with more than 10,000 causalities and severe damage in Mexico City, transformed national perception of seismic risk and triggered major advances in engineering, civil protection, and earthquake geology research in Mexico. However, four decades after the event, the earthquake environmental effects (EEE) generated along the epicentral region remain poorly documented.

The extreme impact recorded 400 km northeast of the epicenter, in Mexico City, where the amplification of seismic waves due to the site effects focused most intensity assessments on urban structural damage, relegated to the background the environmental effects that now allow us to reconstruct the geological impact of the event on the whole epicentral territory. These EEE produced significant disturbances in the hydrographic network and contributed to the socio-economic and health impacts observed at the time, including epidemiological spread and population migration processes (López Cervantes et al., 1986).

In this context, the application of the Environmental Seismic Intensity scale ESI-07 (Michetti et al., 2007) offers an opportunity to revisit the 1985 earthquake from a comprehensive perspective, based on the analysis of its geologic and environmental effects (Fig. 1).

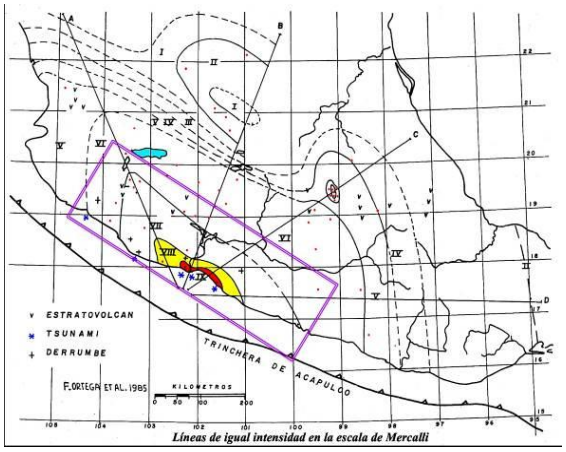

Figure 1: *Modified Mercalli isoseismal map of the September 19, 1985, earthquake, Michoacán, Mexico, including environmental effects; red dots locate intensity data points; this map is unpublished, it was not included in the paper by Corona-Esquivel et al., 1988, but was presented at an official meeting before the H. Congreso General de los Estados Unidos Mexicanos in 1985; it is a good example of the quality of available data that has not been fully exploited for macroseismic intensity assessment until now.*

We focus our analysis on the coast of Michoacán, Guerrero, Colima, and adjacent areas; moreover, we analyzed the EEE in Mexico City, where site amplification conditioned the intensity assessments at the time.

METHODOLOGY

We conducted a systematic review of scientific literature, technical reports, and institutional archives produced during and after the emergency, as well as the compilation

of geological and geomorphological information. We analyzed each record to identify, classify, and georeference into the different types of EEE according to ESI-07 criteria. We assigned an ESI-07 intensity value to each effect, considering its size, location, involved material, and spatial distribution.

PRELIMINARY AND EXPECTED RESULTS

Application of the ESI-07 scale revealed a spatial pattern of intensities ranging from VII to X ESI-07 consistent with the distribution of the identified EEE. The EEE include:
a) Primary effect: tectonic uplift (19 sites);
b) Secondary effects: liquefaction (14), tsunami (20), hydrogeological anomalies (7), ground fracturing (13), landslides, and rockfalls (5).

Primary Effects
Tectonic Uplift. The primary effect associated with the September 19, 1985 earthquake corresponds to tectonic uplift of up to 50 cm, along a segment of at least 32 km (Fig. 2). Bodin and Klinger (1986) and Corona-Esquivel et al. (1988) described in detail evidence of coastal uplift based on the analysis and comparison of a horizontal white band composed of sessile organisms vertically displaced from their pre-earthquake habitat on marine cliffs in Michoacán, Guerrero, and Colima. We assess maximum uplift of ca. 50 cm as intensity ESI-07 = X.

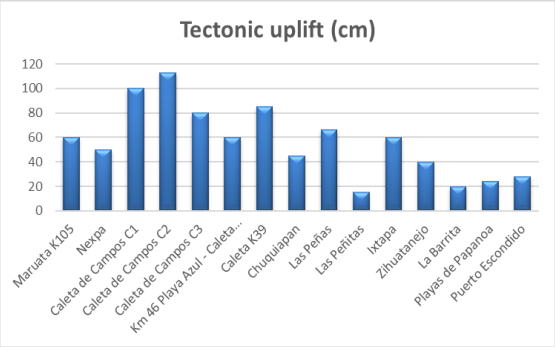

Figure 2: *Tectonic uplift, primary effect of the September 19, 1985 earthquake, registered as vertical displacement of sessile organisms documented by Bodin and Klinger (1986) and Corona-Esquivel et al. (1988) along the Michoacan, Guerrero and Colima, Mexico coast. I ESI-07 = VII – X.*

Secondary Effects
Ground Cracking. Ground cracking was documented mainly in locations near the epicenter, including Lázaro Cárdenas, Playa Azul, and Zihuatanejo, as well as in areas with soft soils of lacustrine or volcaniclastic origin (e.g. Ciudad Guzmán and Mexico City, Fig. 3). Fractures with lateral displacement were also observed in bridges along the main coastal highway.

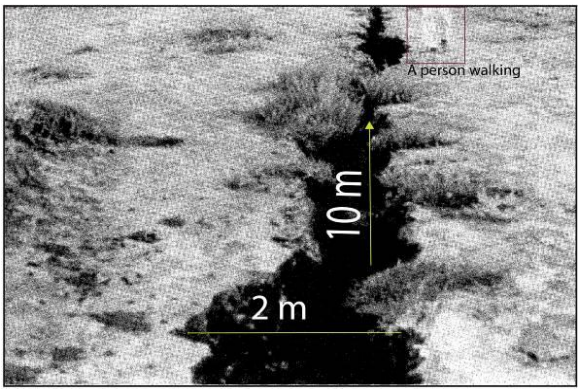

Figure 3: *Severe ground cracking in Mexico City. I ESI-07 = VIII (modified from Ayala and O'Rourke, 1989).*

Liquefaction. Liquefaction processes caused settlements due to compaction of recent alluvial deposits, artificial fills, riverbanks, and beaches. These effects were specially documented in industrial facilities in Lázaro Cárdenas and Ciudad Guzmán. In Lázaro Cárdenas, local witness observed soil liquefaction, mud and sand volcanoes associated with earthquake fountains up to 20 m high (Fig. 4). The pressure from the compression of the ground began to pump water into the sky, shooting up to 20 m high and knocking off the roofs of the houses; they were mud geysers, one crater after another). These effects indicate intensity in the range ESI-07 = VI-X.
It is worth noting that in Mexico City this phenomenon contributed significantly to building collapses in the most affected areas.

Figure 4: *Liquefaction effect, sand volcanoes associated with earthquake fountains up to 20 m high in Lázaro Cárdenas. (Ortega-Gutiérrez et al., 1985). I ESI-07 = VIII – X.*

Landslides and rockfalls. These were concentrated mainly on steep slopes of the Sierra Madre del Sur and on roads with unstable material (Fig. 5). I ESI-07 = VI-IX.

Figure 5: *Landslides along the Sierra Madre del Sur originated near the watershed, in the area of highest terrain instability, and involved the mobilization of thousands of cubic meters of material. I ESI-07 = VIII.*

Toward the mountains, landslides stretching up to more than two thousand meters took the residents by surprise, blanketing their communities in dust. Some lucky ones were carried safely along with their homes for dozens of meters. However, the real tragedy came after the earthquake. Many people died from illnesses. Frightened, people fled their homes, or what remained of them, under pouring rain. Because landslides destroyed the drainage systems, mosquitoes bred in the stagnant water, and people died of malaria, pneumonia, colds, and "fright sickness," simply from the shock of the second earthquake.
Hydrogeological anomalies. Observed effects included variations in flow rates, resurgences, and temporary or permanent disappearance of springs. I ESI-07 = VI-VIII.
Tsunami. The runup reached its greatest heights in locations near the epicenter, with an incursion of up to 500 cm inland in Lázaro Cárdenas (Fig. 6; Abe et al., 1986) and Barra de Potosí, Guerrero (Ocampo-Ríos et al., 2017). The effect was also recorded on coasts outside of Mexico (Abe et al., 1986; USGS, 2025; Fig. X). I ESI-07 = VI-X.

Figure 6: *Heavily deformed railway tracks in the area flooded by the tsunami in Lázaro Cárdenas. (Photo taken from Lomnitz and Castaños, 1985).* I ESI-07 = X.

In the epicentral area, fishermen witnessed the tsunami, and described “shining lights” in the sea, due to bioluminescence caused by turbulence on the seabed. This turbulence caused animals accustomed to a different environment to rise to the surface. Fishermen said they even saw light-emitting animals they had never seen before. These species are typical of very deep areas of the ocean; they need their own light to know where they are. Remarkable tsunami effects occurred in the Zihuatanejo area. The sea advanced inland, and because there is a canal there that distributes water from a dam called La Villita, it began to flow backward, advancing three kilometers. The Balsas River began to rise, and its course, instead of flowing down toward the sea, receded upstream.

Comparison with historical intensities
Comparison between ESI-07 data points distribution and available MM isoseismals of the event shows correspondence in the areas of greatest impact. However, we observe notable differences in the epicentral region, where original maps—mainly based on urban structural damage—underestimated the geological impact of the event. The integration of MM with ESI-07 values provides a finer spatial resolution and a more realistic reconstruction of the earthquake's territorial impact.

Additional expected results
A georeferenced database of recorded and evaluated EEE. ESI-07 and integrated ESI-07 - MM isoseismals, useful for seismic hazard assessments, and territorial planning.
Identification of intensity patterns and ground behavior, derived from the comparison with international earthquakes and with events in different Mexican seismic environments evaluated using the ESI-07 scale.

DISCUSSION

The EEE evaluated in this study are concentrated within the area delimited by isoseismal of intensity VI to IX MM. Reassessment of the 1985 earthquake using the ESI-07 scale indicates an epicentral intensity of X, consistent with the distribution, magnitude, and typology of the EEE in the natural environment. This comparison highlights the need to integrate traditional assessments, generally focused on densely populated areas and structural damage, with estimates derived from the ESI-07 scale, which are particularly valuable in rural, uninhabited, or sparsely populated areas.

The results confirm that the ESI-07 scale is an effective tool for reinterpreting historical events based on the recording of their effects on the natural environment, complementing conventional macroseismic approaches. For the 1985 earthquake, an event for which satellite interferometry, GPS data, and high-resolution optical images are unavailable, the application of ESI-07 allows for a more complete reconstruction of its impact through the analysis of recorded EEE. This provides a more balanced assessment and a solid basis for corroborating or reassessing previously assigned macroseismic intensity.
The affected area also corresponds to a region where geomorphological, historical, and instrumental evidence indicates a high recurrence of major earthquakes,

reflecting a landscape evolution strongly influenced by tectonic activity.

Overall, the results highlight: a) the need to systematically consider the EEE in seismic hazard assessment; and b) the importance of developing a national EEE repository that integrate data from historical and recent events, in order to improve seismic hazard assessment and strengthen risk mitigation strategies.

PRELIMINARY CONCLUSIONS

The review of the EEE generated by the 1985 earthquake and the reassessment of its intensity using the ESI-07 scale provide a more comprehensive understanding of the event's impact. Revisiting the effects of the earthquake after forty years clearly highlights the fact that the devastating impact on the Mexico City metropolitan area has somewhat overshadowed the remarkable environmental effects that occurred in the epicentral area. Based on observed coastal uplift and tsunami runup, we in fact assess ESI-07 epicentral intensity as X, one degree higher than published MM value of IX.

This study lays the groundwork for the development of a national EEE database for Mexico, contributing to improved characterization of seismic effects at regional and national scales.

Furthermore, this work opens the possibility of extending the methodology to other major historical Mexican earthquakes (e.g., 1932, 1973, 1995) in order to improve seismic hazard assessment, better understand impact patterns, and strengthen risk management actions.

REFERENCES

Ayala A.G., O'Rourke M.J. 1989. Effects of the 1985 Michoacan earthquake on water systems and other buried lifelines in Mexico. National Center for Earthquake Engineering Research, Technical Report NCEER-89-0009.

Abe, K., Hakuno, M., Takeuchi, M., Katada, T. 1986. Survey on the Tsunami of the Michoacan, Mexico earthquake of September 19, 1985. Bulletin of the Earthquake Research Institute University of Tokio, Vol. 61, p. 475–481.

Bodin P., Klinger T., 1986. Coastal Uplift and Mortality of Intertidal Organisms Caused by the September 1985 Mexico Earthquake. Science, New Series, Vol. 233, No. 4768, pp. 1071-1073.

Corona-Esquivel, R., Ortega-Gutiérrez, F., Martínez-Reyes, J., Centeno-García, E. 1988. Evidencias de levantamiento tectónico asociado con el sismo del 19 de septiembre de 1985, en la región de Caleta de Campos, estado de Michoacán, Univ. Nal. Autón. México, Inst. Geologia, Revista, vol. 7, núm.1, p. 106-111.

Lomnitz C., Castaños H. 1985. A same-day overflight in the epicentral area of the great Mexico earthquake of 19 September 1985. Bulletin of the Seismological Society of America, Vol. 75, No. 6, pp. 1837-1841.

López Cervantes M., López Carrillo L., Escamilla Cejudo J.A. 1986. Algunas consecuencias de los sismos de septiembre de 1985 en la ciudad de México. Salud Pública Mex 1986; 28:1527-536.

Michetti, A.M., Esposito, E., Guerrieri, L., Porfido, S., Serva, L., Tatevossian, R., Vittori, E., Audemard, F., Azuma, T., Clague, J., Comerci, V., Gürpinar, A., McCalpin, J., Mohammadioun, B., Morner, N.A., Ota, Y., Roghozin, E., 2007. Environmental seismic intensity scale 2007 - ESI 2007, Mem. Descr. Carta Geol. Italia 74, 7–54, Servizio Geologico d'Italia – Dipartimento Difesa del Suolo. APAT, Roma, Italy. http://www.isprambiente.gov.it/en/publications/technical-periodicals/descriptive-memories-of-the-geological-map-of/intensity-scale-esi-2007?set_lang uage=en.

Ocampo-Ríos B.G., Priyadarsi D.R., Macías Ma. C., Jonathan M.P., Lozano-Santacruz R. 2017. Tsunami deposits of September 21st 1985 in Barra de Potosí: comparison with other studies and evaluation of some geological proxies for southwestern Mexico, Geofísica Internacional, 56-1: 57-69, DOI: 10.19155/geofint.2017.056.1.4.

Ortega-Gutiérrez et al. 1985. Oral communication before the National Congress of Mexico, (unpublished manuscript).

USGS, 2025. M 8.0 - 1985 Michoacan, Mexico Earthquake, https://earthquake.usgs.gov/earthquakes/eventpage/usp0002jwe/impact; last visited 29/11/2025

INQUA TERPRO Project Cascading Hazards and Mitigation (CHAMP)

Stress modeling of the March 2022 seismic swarm in the Colca region, southern Peru: implications for dike intrusion and fault activity

Woszczycka, Marta (1), Maciej Mendecki (1), Carlos Benavente (2), Krzysztof Gaidzik (1)

(1) Institute of Earth Sciences, University of Silesia, Sosnowiec, Poland. Email: marta.woszczycka@us.edu.pl
(2) Instituto Geológico, Minero y Metalúrgico INGEMMET, Lima, Peru.

Abstract: *The Colca Region in the Central Andes, southern Peru, is affected by shallow (<20 km) small- to moderate-magnitude earthquakes associated with active normal and strike-slip crustal faults, as well as geothermal and volcanic processes linked to the presently active Sabancaya volcano. In March 2022, a seismic swarm occurred, including two main events (Mw 4.9, Mw 5.5). The hypocenter distribution delineates a distinct SSW-NNE linear structure, atypical for active faults in the region (W-E to NW-SE), but aligned with an older fault zone and spatially close to the magma chamber. This spatial relationship suggests a possible dike intrusion, where magma exploited a pre-existing zone of weakness. Coulomb stress modeling tested scenarios of stress changes from both fault reactivation and dike propagation, with the dike intrusion model best reproducing the observed seismic pattern. Furthermore, the results indicate that stress induced by the topographic load may locally modify the regional stress field, influencing the dike orientation and fault activation in the region.*

Key words*: seismic swarm, crustal fault, dike intrusion, Coulomb stress transfer, Andes*

INTRODUCTION

The Colca region of southern Peru is one of the most active volcanic and tectonic environments in the Central Andes. The Ampato–Sabancaya volcanic complex is characterized by ongoing eruptive activity at Sabancaya since 2016, persistent SO_2 degassing, daily explosions, and repeated cycles of lava-dome formation and destruction. This activity is sustained by a vertically organized magmatic–hydrothermal system that includes a deep magma reservoir beneath Hualca Hualca at approximately 11–18 km depth (Torres et al., 2025). Hydrothermal manifestations such as fumaroles, solfataras, hot springs, and strong self-potential anomalies are widespread and document intense fluid circulation within and around the volcanic complex (Tyc et al., 2022).

Shallow seismicity (<20 km) is abundant and caused mainly through active crustal faults predominantly W–E and NW–SE striking (Benavente et al., 2017; Gaidzik et al., 2020; Gaidzik & Więsek, 2021; Woszczycka et al., 2024), and accommodating N–S to NE–SW extension (Sébrier et al., 1985; Wimpenny et al., 2020). In March 2022, a seismic swarm developed along a well-defined SSW–NNE alignment (Fig. 1), a geometry that contrasts with the dominant mapped fault orientations in the region. The two largest events (Mw 4.9 and Mw 5.5) displayed clear strike-slip mechanisms. The geometry and spatial configuration of the seismicity raise two possible interpretations: reactivation of an older, steep NE-trending crustal structure, or intrusion of a laterally propagating dike that exploited a pre-existing zone of weakness in the upper crust.

To test these alternatives, we analyzed the spatiotemporal evolution of earthquakes recorded between 2021 and 2023, integrated focal mechanisms from regional and global catalogs, and carried out Coulomb stress transfer modeling for both fault-slip and dike-intrusion scenarios of the March 2022 swarm. We also evaluated the influence of the extreme topography of the Ampato–Sabancaya complex, which may rotate local stress orientations and thereby affect both magma pathways and fault behavior.

RESULTS AND DISCUSSION

The March 2022 seismic swarm illustrates the complexity of interpreting seismicity in active volcanic systems. The sequence, which included two moderate-magnitude earthquakes (Mw 4.9 and Mw 5.5), produced a pronounced SSW–NNE alignment of hypocenters that contrasts with the predominant W–E to NW–SE trend of active crustal faults, yet coincides with an older structural trend near the inferred magma storage zone (Fig. 1). Such geometric and spatial relationships permit more than one plausible interpretation, including reactivation of a pre-existing fault or emplacement of a dike along a crustal weakness. In addition, the local stress field may be significantly modified by the large topographic gradients between the volcanic summits and the deeply incised Colca Valley, which can influence intrusion orientations and seismicity patterns (Acocella & Neri, 2009; Albino et al., 2019).

We examine the processes responsible for the March 2022 swarm by combining the spatiotemporal evolution of seismicity with Coulomb stress transfer modeling. By comparing the stress changes produced by different fault-slip and dike-intrusion scenarios, we evaluate which mechanism best explains the geometry and distribution of the earthquakes. The sequence is notable for both its

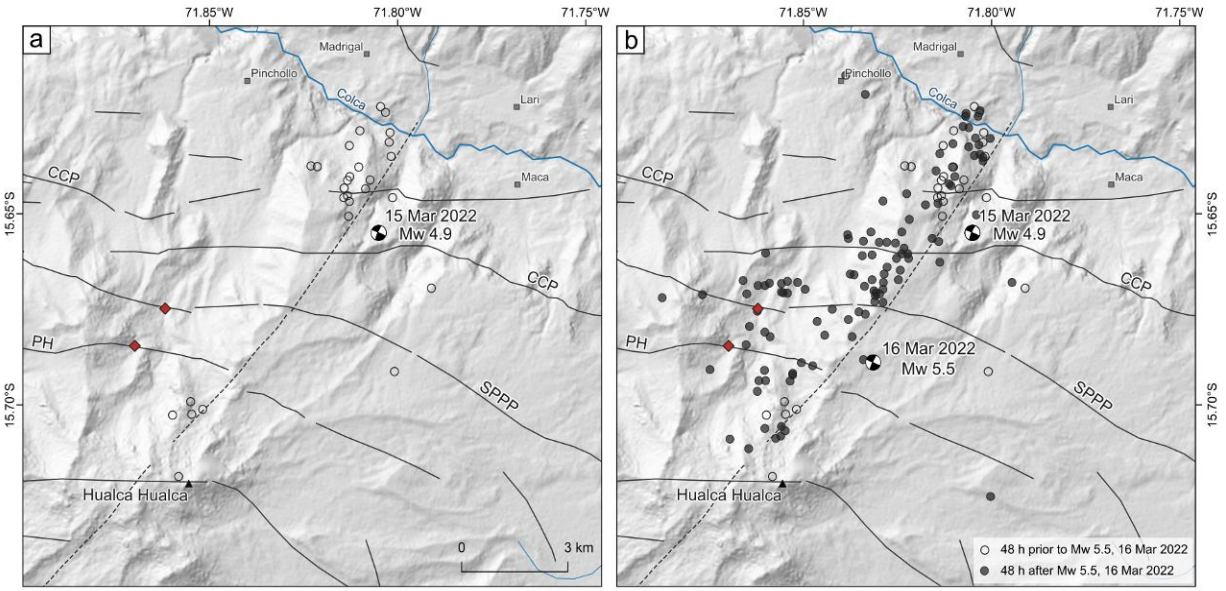

Figure 1: *March 2022 seismic swarm. (a) Earthquakes during the 48 h prior to the 16 March 2022 Mw 5.5 earthquake. (b) Earthquakes during the 48 h after the 16 March 2022 Mw 5.5 earthquake. Solid lines show active faults after Benavente et al. (2017): CCP – Chachas–Cabanaconde–Patapampa, PH – Pungo–Hornilos, SPPP – Solarpampa–Puye Puye–Pillo. Dashed line marks the Hualca Hualca fault (modified after Benavente et al., 2017; Torres et al., 2025). Red diamonds denote thermal springs (after Tyc et al., 2022).*

temporal clustering and its spatial coherence, which differ markedly from other active periods in the region. Seismicity began on 15 March with a Mw 4.9 earthquake, followed by 25 smaller events, and culminated the next day with the Mw 5.5 mainshock, accompanied by 35 additional earthquakes. During the 48 hours before the mainshock, earthquakes were distributed in two distinct clusters – a smaller one near Hualca Hualca and a larger one to the northeast (Fig. 1a). In the 48 hours after the mainshock, seismicity filled the gap between these clusters, forming a continuous SSW–NNE-trending linear structure (Fig. 1b) not observed at any other time in the 2021–2023 record. Hypocenters were concentrated at depths of 3–9 km, with shallower events at the SSW end near Hualca Hualca and progressively deeper events toward the NNE, approximately following the regional topographic gradient between the Hualca Hualca summit (~6025 m a.s.l.) and the Colca valley (~3120 m a.s.l.).

Focal mechanisms for the two main events indicate either right-lateral strike-slip motion on a SSW–NNE plane or left-lateral strike- slip on a WNW–ESE plane. Although the latter orientation corresponds to mapped active faults, the SSW–NNE plane aligns with the seismicity and with the trace of the older, likely Quaternary or pre-Quaternary, Hualca Hualca fault. We therefore modelled stress changes assuming activation of a segment of the SSW–NNE Hualca Hualca fault, as well as WNW–ESE segments of the Solarpampa–Puye Puye–Pillo and Chachas–Cabanaconde–Patapampa faults.

An alternative explanation is that the swarm was triggered by a dike intrusion rather than by purely tectonic failure. This interpretation is supported by the linear distribution of earthquakes, their deviation from the main active faults, and their proximity to the Sabancaya magma reservoir at the SSW end of the structure (MacQueen et al., 2020; Torres et al., 2025). To evaluate this scenario, we estimated the cumulative seismic moment for 15–17 March 2022 of 2.39×10^{17} Nm (Hanks & Kanamori, 1979) and derived an intruded magma volume of 1.04×10^{7} m³ (White & McCausland, 2016). Using hypocenter geometry, we constrained a 14-km-long dike striking N35°E and dipping in accordance with the plunge of seismicity toward the NNE, extending from ~6.5 to 13.25 km depth.

Our Coulomb stress modeling shows that tectonic scenarios involving slip on the candidate fault segments yield small stress changes (generally 0.01–0.1 MPa) and do not reproduce the full extent of the SSW–NNE swarm. The best tectonic correlation (source and receiver faults both oriented 205/83/–178 at 6 km depth) still produced limited and spatially discontinuous positive Coulomb stress change lobes. However, all dike-intrusion models generated two positive lobes oriented NE and SW and two negative lobes oriented NW and SE, with stress magnitudes exceeding 0.1 MPa. Because the dike scenario consistently yielded the highest stress values and the strongest correlation with the earthquake distribution, we computed an optimized model using the best-fitting receiver orientation (205/83/–178). At 6 km depth (representing the mean March 2022 hypocentral depth), the model produced a NNW–SSE-oriented positive stress zone with Coulomb stress change values of up to 3.15 MPa and negative lobes down to –0.80 MPa. The Mw 4.9 and Mw 5.5 events experienced stress changes of 0.12 MPa and 0.47 MPa, respectively (Fig. 2). Nearly all March 2022 hypocenters lie within the positive stress zone northwest of Hualca Hualca, demonstrating strong spatial

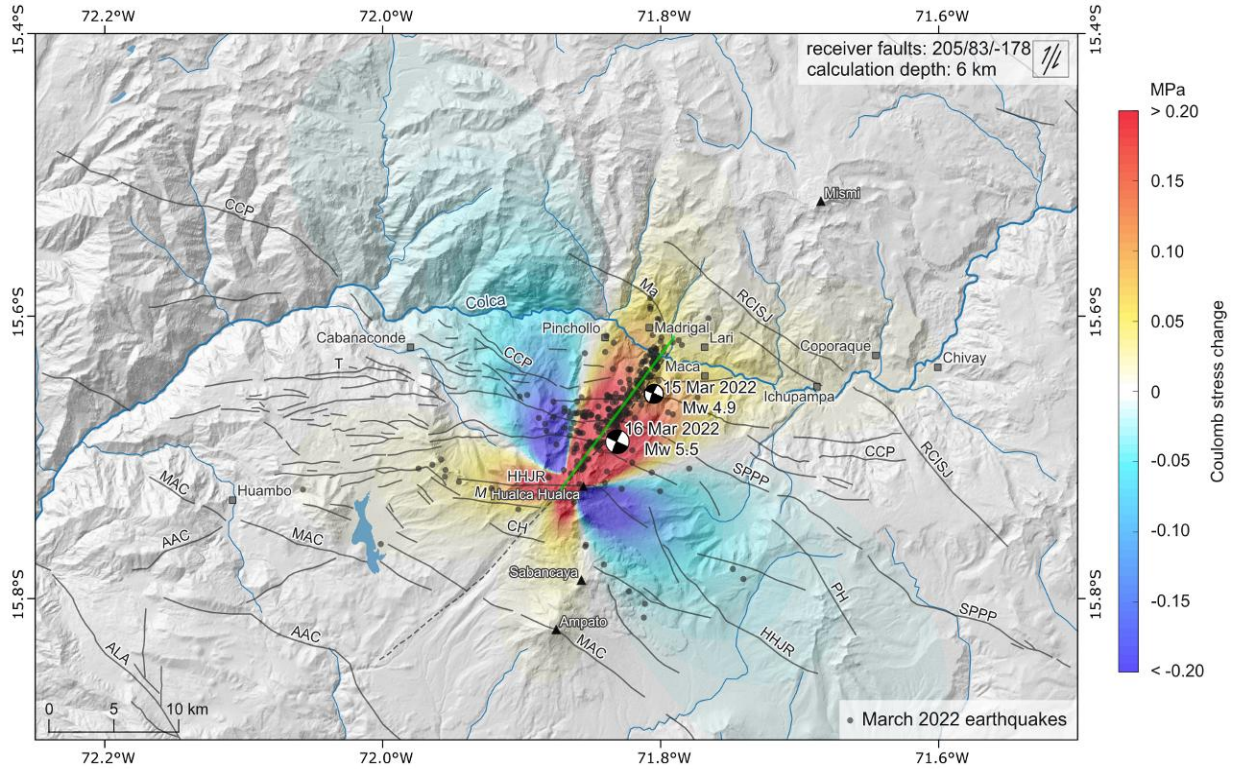

Figure 2: *Coulomb stress change from modeled dike intrusion on specified receiver faults for the March 2022 seismicity. Dike trace is shown in green. Receiver fault geometry, orientation, and calculation depth shown in upper right corner.*

agreement with a dike propagating laterally from the magma chamber beneath the Hualca Hualca volcano.

The spatial overlap between the March swarm, the inferred structural corridor, and the mapped hydrothermal system indicates that magmatic processes likely influenced the sequence. The Colca basin hosts a widespread geothermal system linked to the Sabancaya magma chamber and to permeable faults that channel hot fluids and gases (Tyc et al., 2022). Magma intrusion and gas ascent can increase pore pressure and reduce effective normal stress, weakening the crust and facilitating shear failure (White & McCausland, 2016; MacQueen et al., 2020; Machacca et al., 2023). Thus, even if slip occurred on faults without a dike intrusion, it may have been influenced by magmatic activity and promoted by fluid-assisted weakening.

The March 2022 swarm's SSW–NNE orientation contrasts with the dominant W–E to NW–SE faults. However, N to NE-trending structures have been identified in Mesozoic to Holocene deposits (Gaidzik et al., 2020), and recent activity on similarly oriented faults has been suggested (Torres et al., 2025). To better constrain the local stress state, we examined focal-mechanism axes of major earthquakes from 2021–2023. For normal-faulting events, P-axes (approximating σ_1) are near vertical, so we used T-axes as proxies for σ_3. While regional σ_3 is oriented N–S to NNE–SSW, earthquakes along the March swarm show a locally rotated σ_3 trending NNW–SSE, indicating a localized perturbation northeast of Hualca Hualca.

Given the strong elevation contrast of more than 3000 m between the volcanic summits and the Colca Valley, topographic loading seems to be a natural candidate to explain this local rotation. We therefore computed the stress field (at 6 km depth) induced by the actual topography in our study area. Our topographic loading model, evaluated along the inferred dike strike (N35°E), reveals a σ_3 orientation of approximately N145°E near Hualca Hualca, where σ_3 is nearly horizontal, and becomes progressively steeper toward the northeastern end of the swarm. The corresponding σ_1 has a mean orientation of N152°E and is close to vertical near Hualca Hualca, but becomes increasingly horizontal toward the NE. As topographic stresses decrease from Hualca Hualca toward the Colca Valley, this gradient provides a natural pathway for magma propagation. These results demonstrate that the local stress field is rotated with respect to the regional ~N–S extension: at the southwestern end of the swarm, NW–SE extension associated with a horizontal σ_3 oriented N145°E creates conditions favorable for opening of a NE–SW-oriented dike. Although the inferred dike strike is not perfectly perpendicular to σ_3 (misfit ~20°), this offset can be explained by magma propagating along a pre-existing weakness zone, most plausibly an older, steeply dipping fault.

The role of topography in our case is consistent with broader observations on dike emplacement in volcanic settings. Acocella & Neri (2009) emphasize that dike propagation within volcanoes is controlled primarily by topographic relief and edifice shape, and only secondarily by the regional tectonic field. Moreover, prominent scarps produced by sector collapses can reorient the least compressive stress perpendicular to the scarp, favoring

dike propagation parallel to the scarp margin (e.g., Acocella & Tibaldi, 2005). In our study area, the inferred dike trace follows a local ridge corresponding to the eastern segment of the Hualca Hualca collapse scarp – a horseshoe-shaped caldera morphology open to the north and attributed to failure of the volcano's northern flank (Machacca et al., 2023), precisely where such a locally reoriented stress field would be expected. Our topographic-loading results and the observed dike alignment along the Hualca Hualca collapse scarp are therefore fully consistent with a scenario in which local, edifice-related stresses control the path of a laterally propagating dike.

In many volcanic settings, seismic swarms and migrating hypocenters have been interpreted as the brittle response to dike intrusion, where shear failure is promoted at dike tips by the combined effect of ambient stress and concentrated extensional stresses (e.g., Rubin & Gillard, 1998). In our case, the spatial distribution of earthquakes during the 48 hours preceding the 16 March 2022 mainshock, with clusters at the southwestern and northeastern ends of the swarm, is consistent with failure at the tips of a propagating dike. The strike-slip character of the main March 2022 earthquakes is naturally explained by the stress field expected around a propagating dike. Bonafede & Danesi (1997) showed that dike-induced stresses create a broad region on both sides of the intrusion where the intermediate principal stress (σ_2) is nearly vertical and the maximum compressive stress (σ_1) is oriented perpendicular to the dike plane, creating conditions under which strike-slip faulting is expected to dominate. Their models further demonstrate that fluid-related overpressure at depth and suction near the surface can differentially weaken and strengthen the host rock, promoting shear failure in the deeper, pressurized region. This mechanism would explain the prevalence of strike-slip focal mechanisms during the March 2022 swarm, even within an overall extensional volcanic setting.

CONCLUSIONS

In summary, the stress field in the Colca region most likely reflects the combined influence of regional extension, strong local perturbations imposed by topography, and stress changes associated with seismicity and/or magmatic intrusions. Within this framework, the SSW–NNE March 2022 seismic swarm and its strike-slip focal mechanisms are best explained by a magmatic dike intruding along a pre-existing weakness zone, in a stress field locally rotated by topographic loading and further modified by the intrusion itself. This suggests that local stress perturbations, rather than the regional tectonic field alone, may control seismicity near the Ampato–Sabancaya complex.

Acknowledgements: This research was funded by the National Science Centre (Poland), grant No 2024/53/N/ST10/00772.

REFERENCES

Acocella, V., & Neri, M., 2009. Dike propagation in volcanic edifices: overview and possible developments. Tectonophysics 471(1-2), 67-77.

Acocella, V., & Tibaldi, A., 2005. Dike propagation driven by volcano collapse: a general model tested at Stromboli, Italy. Geophysical Research Letters 32(8).

Albino, F., Biggs, J., & Syahbana, D. K., 2019. Dyke intrusion between neighbouring arc volcanoes responsible for 2017 pre-eruptive seismic swarm at Agung. Nature communications 10(1), 748.

Benavente, C.; Delgado, G.; García, B.; Aguirre, E. & Audin, L., 2017. - Neotectónica, evolución del relieve y peligro sísmico en la región Arequipa. INGEMMET, Boletín Serie C: Geodinámica e Ingeniería Geológica, 64, 370 p., 1 mapa.

Bonafede, M., & Danesi, S., 1997. Near-field modifications of stress induced by dyke injection at shallow depth. Geophysical Journal International 130(2), 435-448.

Gaidzik, K., & Więsek, M., 2021. Seismo-lineaments and potentially seismogenic faults in the overriding plate of the Nazca-South American subduction zone (S Peru). Journal of South American Earth Sciences 109, 103303.

Gaidzik, K., Żaba, J., & Ciesielczuk, J., 2020. Tectonic control on slow-moving Andean landslides in the Colca Valley, Peru. Journal of Mountain Science 17(8), 1807-1825.

Hanks, T. C., & Kanamori, H., 1979. A moment magnitude scale. Journal of Geophysical Research: Solid Earth 84(B5), 2348-2350.

Machacca, R., Lesage, P., Tavera, H., Pesicek, J. D., Caudron, C., Torres, J. L., ... & Burgisser, A., 2023. The 2013–2020 seismic activity at Sabancaya Volcano (Peru): Long lasting unrest and eruption. Journal of Volcanology and Geothermal Research 435, 107767.

MacQueen, P., Delgado, F., Reath, K., Pritchard, M. E., Bagnardi, M., Milillo, P., ... & Miranda, R., 2020. Volcano-tectonic interactions at Sabancaya volcano, Peru: Eruptions, magmatic inflation, moderate earthquakes, and fault creep. Journal of Geophysical Research: Solid Earth 125(5), e2019JB019281.

Rubin, A. M., & Gillard, D. (1998). Dike-induced earthquakes: Theoretical considerations. Journal of Geophysical Research: Solid Earth 103(B5), 10017-10030.

Sébrier, M., Mercier, J. L., Mégard, F., Laubacher, G., & Carey-Gailhardis, E., 1985. Quaternary normal and reverse faulting and the state of stress in the central Andes of south Peru. Tectonics 4(7), 739-780.

Torres, J.-L., Byrdina, S., Romero-Beltran, G., Garambois, S., Rivera, M., Burgisser, A., ... & Rath, V., 2025. Magma storage below Sabancaya volcano (Southern Peru) imaged by broad band magnetotellurics. Manuscript submitted to Journal of Geophysical Research: Solid Earth.

Tyc, A., Gaidzik, K., Ciesielczuk, J., Masías, P., Paulo, A., Postawa, A., & Żaba, J., 2022. Thermal springs and active fault network of the central Colca River basin, Western Cordillera, Peru. Journal of Volcanology and Geothermal Research 424, 107513.

White, R., & McCausland, W., 2016. Volcano-tectonic earthquakes: A new tool for estimating intrusive volumes and forecasting eruptions. Journal of Volcanology and Geothermal Research 309, 139-155.

Wimpenny, S., Benavente, C., Copley, A., Garcia, B., Rosell, L., O'Kane, A., & Aguirre, E., 2020. Observations and dynamical implications of active normal faulting in South Peru. Geophysical Journal International 222(1), 27-53.

Woszczycka, M., Gaidzik, K., Anccasi Figueroa, R. M., Mendecki, M., & Benavente, C., 2024. Unraveling the complex interplay: exploring the relationships between seismic and volcanic activities in the Colca River area using the Coulomb Stress Transfer. Seismological Research Letters 95(4), 2464-2484.

INQUA TERPRO Project Cascading Hazards and Mitigation (CHAMP)

Cite this volume as:

Gordillo, C., Flores, O., Grützner, C., Niemi, T. M., & Obrist-Farner, J. (Eds.), 2026. Proceedings of the 13th International INQUA meeting on Paleoseismology, Active Tectonics and Archaeoseismology - PATA Days 2026. 30 January – 6 February, 2026, Antigua Guatemala, Guatemala. https://doi.org/10.5281/zenodo.20043288.

All abstracts have undergone review. All authors are solely responsible for the content of their abstracts. Previous volumes are avilable at http://pata-days.org.

Previous volumes:

- **Vol. 12:** Proceedings of the 12th International INQUA meeting on Paleoseismology, Active Tectonics and Archaeoseismology (*Easton, G., & González, G., Eds.*), October 6th-11th, 2024, Los Andes, Chile. .
- **Vol. 11:** Proceedings 11th International INQUA Workshop on Paleoseismology, Active Tectonics and Archaeoseismology, PATA Days (*Baize, S., & Rizza, M., Eds*), 25 - 30 September 2022, Aix-En-Provence, France.
- **Vol. 10:** Short abstracts digital volume, 10th International INQUA Meeting on Paleoseismology, Active Tectonics and Archeoseismology, PATA, Hornitos, Chile, November 2021.
- **Vol. 9:** Proceedings of the 9th International INQUA Meeting on Paleoseismology, Active Tectonics and Archeoseismology *(Koukousioura, O., & Chatzipetros, A., Eds.),* 25-27 June 2018, Possidi (Greece).
- **Vol. 8**: Proceedings of the 8th International INQUA Meeting on Paleoseismology, Active Tectonics and Archeoseismology. Handbook and Programme. (*Clark, K. J., Upton, P., Langridge, R., Kelly, K., & Hammond, K., Eds.*), 13-16 November 2017. Lower Hutt (NZ): GNS Science. 441 p. (GNS Science miscellaneous series 110). https://doi.org/10.21420/G2H061.
- **Vol. 7:** Proceeding of the 7th International INQUA Meeting on Paleoseismology, Active Tectonics and Archeoseismology (*McCalpin, J.P., & Gruetzner, C., Eds*.). ISBN 978-0-9974355-2-8, 2016. Published digitally by the Crestone Science Center, Crestone, CO 81131 USA, Guidebook No. 12; 7th International INQUA Meeting on Paleoseismology, Active Tectonics and Archeoseismology, Crestone (USA).
- **Vol. 6:** Abstracts Volume, 6th International INQUA Meeting on Paleoseismology, Active Tectonics and Archeoseismology (*Blumetti, A. M., Cinti, F. R., De Martini, P.M., Galadini, F., Guerrieri, L., Michetti, A. M., Pantosti, D., & Vittori, E., Eds.)*, 19-24 April 2015, Pescina, Fucino Basin, Italy: Miscellanea INGV, Anno 2015_ Numero 27, ISSN 2039-6651, printed in Italy by Instituto Nazionale di Geofisica e Volcanologia, Rome, Italy, 545 p.
- **Vol. 5:** Proceeding of the 5th International INQUA Meeting on Paleoseismology, Active Tectonics and Archeoseismology (*Grützner, C., Choi, J.-H., Edwards, P., & Kim, Y.-S., Eds*.). ISBN 9791195344109 93450. Printed in Korea, 2014. 5th International INQUA Meeting on Paleoseismology, Active Tectonics and Archeoseismology, Busan (Korea).
- **Vol. 4:** Seismic Hazard, Critical Facilities and Slow Active Faults (*Grützner, C., Rudersdorf, A., Perez-Lopez, R., & Reicherter, K., Eds.*). ISBN 978-3-00-0427-96-1. Printed in Germany, 2013. 4th International INQUA Meeting on Paleoseismology, Active Tectonics and Archeoseismology, Aachen (Germany).
- **Vol. 3:** Earthquake Geology and Archeoseismology: Society and Seismic Hazard (*Perez-Lopez, R., Silva, P. G., Rodriguez Pascua, M.A., Garduno Monroy, V. H., Suarez, G., & Reicherter, K., Eds*.). Printed in Mexico, 2012. 3rd INQUA-IGCP 567 International Workshop on Earthquake Geology, Paleoseismology and Archeoseismology, Morelia (Mexico).
- **Vol. 2**: Earthquake Geology and Archeoseismology: Society and Seismic Hazard (*Grützner, C., Perez-Lopez, R., Fernandez-Steeger, T., Papanikolaou, I., Reicherter, K., Silva, P.G., & Vött, A., Eds.*) ISBN: 978-960-466-093-3. Printed in Greece, 2011. 2nd INQUA-IGCP 567 International Workshop, Corinth (Greece).
- **Vol. 1**: Archaeoseismology and Paleoseismology in the Alpine-Himalayan Collisional Zone (*Perez-Lopez, R., Grützner, C., Lario, J., Reicherter, K., & Silva, P.G., Eds.*) ISBN: 978-84-7484-217-3. Printed in Spain, 2009. 1st INQUA-IGCP 567 International Workshop, Baelo Claudia, Cadiz (Spain).